TU Delft

Delft University of Technology

# Band-Edge Energetics Control for Solar Hydrogen Production

Digdaya, Ibadillah

**DOI**
10.4233/uuid:d7bd8ec2-296c-45a1-b1c7-0ee9aac035eb

**Publication date**
2018

**Document Version**
Final published version

**Citation (APA)**
Digdaya, I. (2018). *Band-Edge Energetics Control for Solar Hydrogen Production*. [Dissertation (TU Delft), Delft University of Technology]. https://doi.org/10.4233/uuid:d7bd8ec2-296c-45a1-b1c7-0ee9aac035eb

**Important note**
To cite this publication, please use the final published version (if applicable).
Please check the document version above.

**Copyright**
Other than for strictly personal use, it is not permitted to download, forward or distribute the text or part of it, without the consent of the author(s) and/or copyright holder(s), unless the work is under an open content license such as Creative Commons.

**Takedown policy**
Please contact us and provide details if you believe this document breaches copyrights.
We will remove access to the work immediately and investigate your claim.

*This work is downloaded from Delft University of Technology.*
*For technical reasons the number of authors shown on this cover page is limited to a maximum of 10.*

# Band-Edge Energetics Control for Solar Hydrogen Production

# Band-Edge Energetics Control for Solar Hydrogen Production

## Proefschrift

ter verkrijging van de graad van doctor
aan de Technische Universiteit Delft,
op gezag van de Rector Magnificus prof. dr. ir. T. H. J. J. van der Hagen,
voorzitter van het College voor Promoties,
in het openbaar te verdedigen op woensdag 7 November 2018 om 12:30 uur

door


## Ibadillah Ardhi DIGDAYA

Master of Science in Sustainable Energy Technology,
Technische Universiteit Delft, Nederlands,
geboren te Medan, Indonesië

Dit proefschrift is goedgekeurd door de promotoren.

Samenstelling promotiecommissie bestaat uit:

| | |
|---|---|
| Rector Magnificus, | voorzitter |
| Dr. W. A. Smith, | Technische Universiteit Delft, promotor |
| Prof. dr. B. Dam, | Technische Universiteit Delft, promotor |

| | |
|---|---|
| Onafhankelijke leden: | |
| Prof. dr. A. H. M. Smets, | Technische Universiteit Delft |
| Prof. dr. E. C. Garnett, | Universiteit van Amsterdam |
| Prof. dr. P. E. de Jongh, | Universiteit Utrecht |
| Prof. dr. R. Buonsanti, | École Polytechnique Fédérale de Lausanne |
| Dr. F. F. Abdi, | Helmholtz-Zentrum Berlin |
| Prof. dr. J. J. C. Geerlings, | Technische Universiteit Delft, reservelid |

The work described in this thesis was conducted in Materials for Energy Conversion and Storage (MECS) section, Department of Chemical Engineering, Faculty of Applied Sciences, Delft University of Technology (TU Delft). This work is part of the research programme of the Netherlands Organization for Scientific Research (NWO) and is financed by the BioSolar Cells open innovation consortium, supported by the Dutch Ministry of Economic Affairs, Agriculture and Innovation.










*Printed by:* GVO drukkers & vormgevers B.V.

*Cover artwork:* Resi M. Gautama, Joan Maymi Clariana and Ibadillah A. Digdaya

Copyright © 2018 by I. A. Digdaya
All rights reserved.

ISBN 978-94-6186-978-4

An electronic version of this dissertation is available at
`http://repository.tudelft.nl/`.

*Science is a wonderful thing*
*if one does not have to earn one's living at it.*

Albert Einstein

# Contents


**1 Introduction** **1**
1.1 The energy challenge . . . 1
1.2 Solar fuel: a promising energy storage solution . . . 4
1.3 Organization of this thesis . . . 7
References . . . 9

**2 Fundamentals** **15**
2.1 Physics of semiconductors . . . 15
2.2 Semiconductor junctions . . . 19
2.3 Photoelectrochemical water splitting cells . . . 30
2.4 Solar energy conversion efficiencies . . . 31
2.5 Materials for photoelectrodes . . . 34
References . . . 40

**3 Interfacial engineering of metal-insulator-semiconductor junctions for efficient and stable photoelectrochemical water oxidation** **45**
3.1 Introduction . . . 46
3.2 Experimental details . . . 47
3.3 Results and discussion . . . 49
3.4 Conclusion . . . 58
References . . . 58

**4 General considerations for improving photovoltage in metal-insulator-semicondutor photoanodes** **65**
4.1 Introduction . . . 66
4.2 Experimental section . . . 67
4.3 Results and discussion . . . 69
4.4 Conclusions . . . 79
References . . . 80

**5 Extracting large photovoltages from amorphous silicon carbide photocathodes with a titanium dioxide front surface field layer** **85**
5.1 Introduction . . . 86
5.2 Experimental details . . . 87
5.3 Results and discussion . . . 88
5.4 Conclusion . . . 98
References . . . 98

**6 Engineering the kinetics and interfacial energetics of Ni/Ni–Mo catalyzed amorphous silicon carbide photocathodes in alkaline media 103**
6.1 Introduction . . . 104
6.2 Experimental details . . . 105
6.3 Results and discussion . . . 107
6.4 Conclusion . . . 118
References . . . 118

**A Appendix A 123**
A.1 Corrected current-potential curve . . . 123
A.2 UV-Vis measurement . . . 124
A.3 Equivalent photovoltaic response and open-circuit voltage . . . 124
A.4 Electrochemical impedance spectroscopy and Mott-Schottky analysis . . . 125
A.5 X-ray photoelectron spectroscopy (XPS) analysis . . . 126
A.6 Pourbaix diagram . . . 128
A.7 Cyclic voltammtery and Mott-Schottky plot . . . 128
References . . . 129

**B Appendix B 131**
B.1 Single- and double-diode models . . . 131
B.2 Fit results of dark $j$–$V$ curves . . . 133
B.3 Derivation of the thermionic emission equation corrected for tunneling current . . . 135
B.4 Flat band potentials and barrier heights obtained from Mott-Schottky relationships . . . 137
B.5 Flat band potentials and barrier heights of MIS photoanodes . . . 140
B.6 Photovoltages of MIS photoandoes . . . 144
B.7 Barrier heights and flat band potentials of MIS photoandoes with various $Al_2O_3$ thicknesses . . . 147
References . . . 149

**C Appendix C 151**
C.1 Energy band diagram analysis . . . 151
C.2 Optical band gap . . . 157
C.3 Current-potential characteristics of uncatalyzed photocathodes . . . 158
C.4 Solar photocurrent and irradiance spectra . . . 158
References . . . 159

**D Appendix D 161**

**Summary 171**

**Samenvatting 175**

**Acknowledgements 179**

**Curriculum Vitæ 181**

**List of Publications 183**

# 1

# Introduction

## 1.1. The energy challenge

Ever since the industrial revolution, human demand for transport, heat and electricity has increased significantly and the demand for energy has reached an unprecedented level. Much of this demand is driven by the economic, scientific and technological progress, as well as the exponential growth of human population from 700 million before the industrial era (in the mid 1700s) to 7.6 billion as of February 2018.[1] The global energy consumption in 2015 was 575 quadrillion British thermal units (Quad BTU)[2] or $606 \times 10^{18}$ joules (606 exajoules), which is an average energy consumption rate of 19.2 terrawatts (TW).[2] Currently, 80% of the total primary energy supply is obtained from fossil fuels, such as oil, coal and natural gas.[3] The consumption of fossil fuels is inevitably accompanied by the release of long-lived greenhouse gasses into the atmosphere, mainly carbon dioxide ($CO_2$) that warms the planet. Since the mid-20$^{\text{th}}$ century, the concentration of anthropogenic $CO_2$ in the atmosphere has steadily increased at a rate that is unprecedented, rising the global surface temperature of about +0.9 °C relative to 1951-1980 average temperatures.[4,5]

The synthesis report of the Intergovernmental Panel of Climate Change (IPCC) has previously provided estimates of how much $CO_2$ can be emitted into the atmosphere to stabilize the temperature below a global average of 2 °C above pre-industrial level.[6] This finite quota of cumulative $CO_2$ emissions is known as the carbon budget. The global carbon budget determines the input of $CO_2$ to the atmosphere by emissions from human activities, and the resulting changes in the storage of carbon (carbon sinks) on the land and in the ocean reservoir.[7] For any given emissions, carbon that does not go into the land or ocean will remain in the atmosphere. In 2012, IPCC's report stated that the world had a remaining budget of 1000 $GtCO_2$ to be emitted in order to limit the global warming to less than 2 °C relative to the period 1860–1880 with a likelihood of 66%. This remaining budget has already dropped to about 800 $GtCO_2$ in 2017.[8] Currently, the global emission level is roughly 40 $GtCO_2$ per year (Fig. 1.1a), mostly comes from fossil fuels and

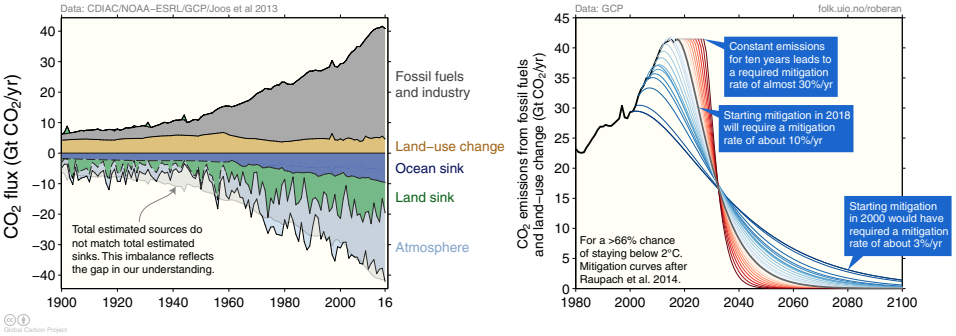



**Figure 1.1:** (a) Combined components of global carbon budget as a function of time, for emissions from fossil fuels and industry and emissions from land-use change, as well as their partitioning among land, ocean and the atmosphere.[7,9] (b) Historical emissions to 2016 and exponential decay pathways such that global cumulative $CO_2$ emission quota is never exceeded. Data and chart from Robbie Andrew at Center for International Climate Research (CICERO) and the Global Carbon Project.[7,10,11]

industry with small contributions from human-driven land-use changes including deforestation, afforestation, logging (forest degradation and harvest activity), shifting cultivation (cutting forest for agriculture and then abandoning) and regrowth of forests following wood harvest or abandonment of agriculture.[7] If the emissions continue at today's rate, the budget will be entirely gone in about 20 years.[7]

To avoid 2 °C warming, global emissions need to stabilize at a peak level and rapidly decline thereafter. If mitigation efforts had been started in 2000, it would have been possible to gradually decrease emissions at a rate of 3% per year (Fig. 1.1b). Starting mitigation in 2018 with the remaining carbon budget will require about 10% of emission reduction per year. If global emissions stay at current level and begin to fall a decade later, the reduction rate would have to be nearly 30% per year. As the world is on the verge of climate catastrophe, with the next few years a crucial period in making decisions about how the planet may survive, it is therefore imperative that the global community to move as quickly as possible to drastically reduce carbon emissions.

By 2050, the world population is projected to reach 9.8 billion,[12] and 30 TW of power supply will be needed to meet the future global demand.[13] Though oil, coal and natural gas reserves will still likely be sufficient to satisfy the world's ravenous appetite for energy, the continued use of fossil fuels will roughly double the current emission by mid-century. With this "business-as-usual" scenario and no new substantial policy to restrain emissions, the global average surface temperature will reach 4 °C above the pre-industrial baseline.[14–16] To avoid devastating consequences, the global community need a vast shift in where they source their energy moving away from fossil fuels toward carbon-neutral sources. Supplying an additional 16 TW by 2050 with all carbon-neutral energy is a challenging task. As has been reported by many literatures, most renewable sources are insufficient to keep up with the fast-growing demand for energy (Fig. 1.2). Hydroelectric power is an

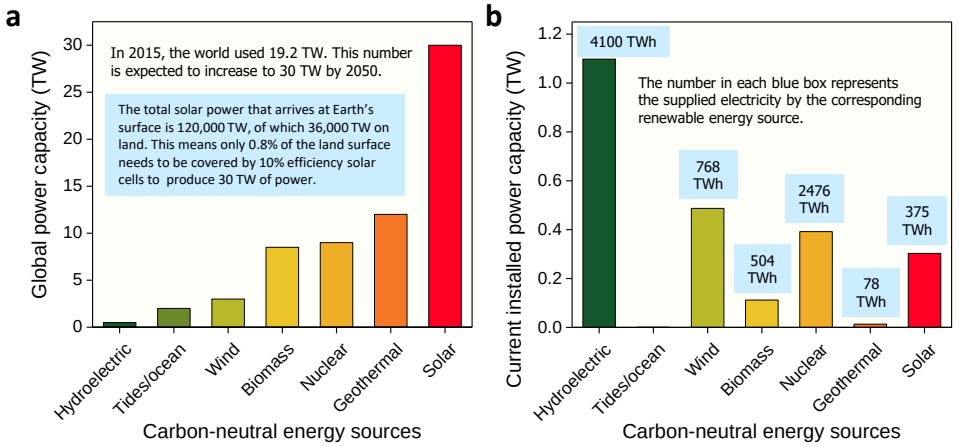



**Figure 1.2:** (a) Globally exploited power of various renewable energy sources.[13,17,19,20] Note that the solar power presented in this figure is calculated based on 0.8% coverage of land surface using 10% efficient solar cells. (b) Current installed power capacity of renewable energy sources in 2016. The number in each blue box represents the supplied electricity by the corresponding renewable energy source. Data are obtained from Ref. 22, except for nuclear power from Ref. 23 and Ref. 24.

excellent source of clean sustainable energy but the remaining practically exploitable hydroelectric sources is less than 0.5 TW.[17] The total energy in all tides and ocean currents amounts less than 2 TW. The energy density of wind is too low,[18] and the total energy of globally extracted wind power from on- and off-shore facilities has been estimated to be 2-4 TW.[19] Geothermal energy has enormous potential but only small fraction can be classified as resources and reserves, with an accessible portion between 12 and 15 TW.[17] The maximum available biomass energy from the agricultural land is 7–10 TW, but obtaining this amount would take the area needed to accommodate a population of 9.2 billion in 2050 and would require harvesting all crops for energy exclusively.[20]

Nuclear power is conceptually a viable carbon-neutral option and has contributed roughly 11% to today's world electricity.[21] The estimated terrestrial uranium resources for nuclear power, however, is limited to only 100 TW-year.[13] Thus if nuclear fission is to supply 10 TW, the terrestrial uranium base resource will be exhausted within a decade. Moreover, delivering a 10-TW value by 2050 would take construction of ten thousand nuclear power plants with a new 1-GW nuclear power plant has to be built every 1.2 days over the next 32 years.[13,20]

Of all the possible carbon-neutral solutions, the energy provided by the sun is by far the most abundant resource on Earth, exceeding all other renewable energy sources combined. A total of 120,000 TW of solar energy strikes the Earth's surface continuously. Energy delivered by the sun in 1.5 hours (648 exajoules) is more than all of the energy currently consumed on the planet in 1 year (606 exajoules in 2015). However, the intermittent nature of the sun renders a high variability of the terrestrial solar resource. The availability of solar power is subjected to day/night cycle, weather condition and seasonal variation. Moreover, the solar energy potentials are

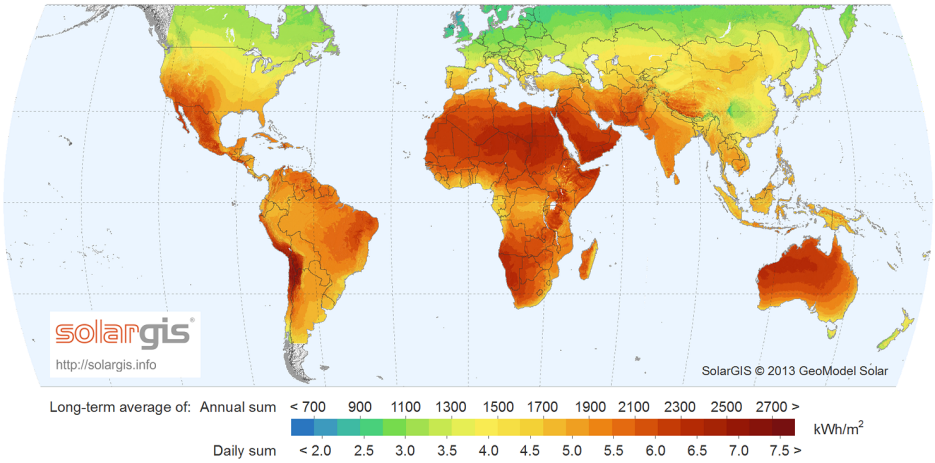



**Figure 1.3:** Solar resource maps showing annual and daily global horizontal irradiance.[25]

geographically constrained to areas close to the equator. For example, Northern Canada, Scandinavia and Russia only have average solar irradiances below 3 kWh $m^{-2}$ per day, whereas some regions in Africa, South America, Northern Australia and the Middle East have average daily solar resources above 7 kWh $m^{-2}$ (Fig. 1.3).

The main challenge of the intermittent solar energy for electricity production is that it is not able to adapt with changes in demands over the same time scales. This is because solar power is non-dispatchable; it only generates electricity when the sun shines. In traditional grid-connected power systems, variation of electricity demand is typically handled by base load and peak load power plants that provide constant power to the minimum level of electricity demand during various period of the day and add supply above that level in times of high demand, respectively. The fluctuation of solar power generation disrupts the grid operation and forces the grid operator to adjust the grid operation ahead of time and to include other power generators in order to compensate for the sudden shortfalls or excesses of solar power production. Thus, penetration of solar electricity in power grids will require supplementary power sources with constant power delivery and minimum variability in order to maintain the balance between electricity supply and demand.

## 1.2. Solar fuel: a promising energy storage solution

As discussed in the previous section, fossil fuels do not provide carbon-neutral solutions to the global energy problem and other renewables are limited in their resource availability and power capacity. Therefore, if solar is to be the primary source of energy, it needs to be stored during times when power generation exceeds the consumption so that it can be deployed for later use and distribution. In principle, storing solar energy offers two main advantages; (i) it allows solar energy to become available 24 hours a day, 7 days a week, thus enabling synchronization between the trend of solar power generation and the demand pattern; (ii) it permits distribution

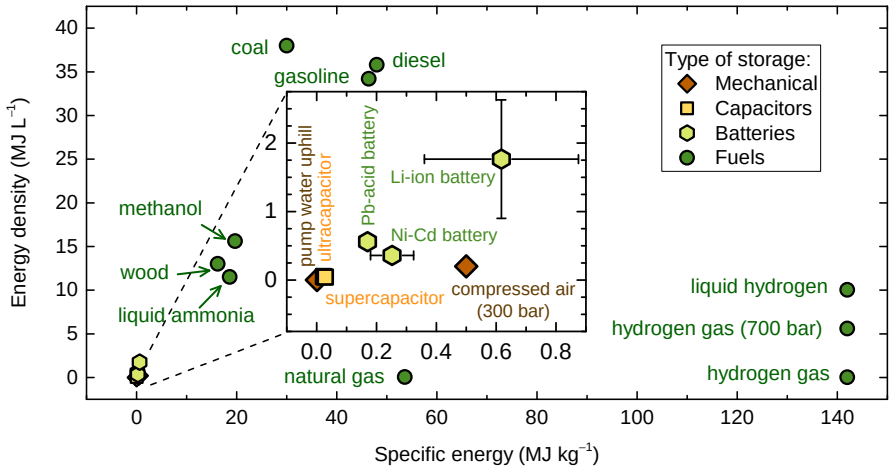



**Figure 1.4:** Specific energy (MJ kg$^{-1}$) and energy density (MJ L$^{-1}$) at 1 bar (unless specified) of various energy storage forms.[13,26–30]

and decentralization of solar energy, improving security of supply and allowing the end users to have control over power utilization.[26] Numerous storage technologies are available today in various forms; (i) mechanical storage systems, such as hydroelectric pump and compressed air; (ii) electrochemical storage mechanisms, such as (super/ultra)-capacitors and batteries; and (iii) chemical energy storage, such as fuels, to name a few (Fig. 1.4).

The ability of a storage system to store energy is often characterized by its volumetric energy density (energy per unit volume) and specific energy (or energy density per unit mass). Mechanical energy storage such as pumped hydroelectric has an absolute poor energy density and is limited by geographic constraints. Compressed air energy storage, although has the potential to provide large-scale solution, has a limited energy storage efficiency because of severe temperature changes due to rapid compression and expansion. Electrochemical storage such as electrochemical batteries and super/ultra-capacitors are low energy storage devices because electrons are stored in atoms composing the electrodes, and thus the volume in which electron and cation reside and transfer is limited to the physical properties of the electrode materials and the electrolyte.[26]

Chemical energy storage in chemical fuels provides the most effective method to storing energy with 2-3 orders of magnitude higher energy density than other energy storage forms (Fig. 1.4). In fuels, the high energy density is achieved by storage of electrons in a smallest possible configuration–chemical bonds between light elements. Examples of chemical fuels include hydrocarbon-based (C–H) fuels such as methanol, natural gas, gasoline and diesel; nitrogen-based (N–H) fuels such as ammonia; and hydrogen (H–H, $H_2$). Whereas hydrocarbons provide the highest volumetric energy density compared to other energy storage forms, they require a source of carbon in their formation and they always produce $CO_2$ upon combustion. In view of

climate concerns outlined in the previous section, $CO_2$ emissions are not desired, and therefore the use of hydrocarbon-based fuels should be avoided as much as possible. Alternatively, $CO_2$ can be directly captured upon combustion (*e.g.* from automobiles, industrial power plants and factories) and be reused as a fuel, thus closing the anthropogenic carbon cycle. A conceptually carbon-neutral approach to convert $CO_2$ to fuels such as methanol and methane using solar energy is by direct/indirect photo(electro)chemical processes. However, this method proceeds at a cost of an extensive energy penalty associated with complex six- or eight-electron transfer reaction steps for $CO_2$ conversion to methanol or methane, respectively.

Hydrogen is a carbon-free chemical fuel that has the highest energy density in mass (almost three times higher than gasoline) but suffers in low volumetric energy density. This is because hydrogen is in the gas phase under normal condition. At room temperature and under atmospheric pressure, hydrogen gas requires almost 3000 times more space than gasoline for an equivalent amount of energy. The volumetric energy density of hydrogen can be increased by storing it in a high-pressure tank at 700 bar (volumetric energy density $\approx$ 5.6 MJ $L^{-1}$), but at an expense of 10-15% energy loss for gas compression.[31] In the liquid form, the volumetric energy density is 2 times larger than the compressed hydrogen, but 30-40% of its energy content will be required for liquefaction.[31] Storing hydrogen in the form of metal hydride is another possible option, but only small fraction of hydrogen atoms can be inserted in each metal atom (gravimetric storage capacity <2%). Alternatively, hydrogen and $CO_2$ can be used to produce carbon monoxide (CO) by the water-gas shift reaction, and a mixture of CO and hydrogen (synthesis gas) can be converted into liquid hydrocarbons, such as methanol and diesel by Fischer-Tropsch process.[32]

Solar energy conversion to hydrogen is perhaps the most attractive route to storing the abundant energy of sunlight. Numerous pathways to produce hydrogen from solar energy are well documented.[30,33,34] This thesis will focus on the photoelectrochemical (PEC) approach in which solar energy is directly converted to hydrogen fuel by means of solar water electrolysis. Indirect methods such as coupled photovoltaic (PV) modules and commercial electrolyzer units are well established and have been demonstrated at various scales.[35–38] In principle, there are at least two main advantages of direct PEC water splitting over PV–electrolyzer. First, PEC systems operate at a much lower current density (10 mA $cm^{-2}$ as compared with 1 A $cm^{-2}$ for commercial electrolyzer), and therefore require lower overvoltages to drive the water electrolysis process, allowing the systems to potentially achieve higher efficiencies. Second, a direct PEC system can be constructed using a single monolithic device, and thus entails fewer additional components than a combination of PV–electrolyzer, which may lead to substantially lower balance-of-system (BOS) cost for hydrogen production.[39] The target hydrogen cost that is set by the U.S. Department of Energy (DOE) is \$2–4/kg and the cost for hydrogen generation with PV–electrolyzer has been estimated to be more than \$8/kg. As has now been documented by literatures, direct PEC technology may offer a route toward competitive hydrogen costs[39,40] and provide a disruptive approach to fuel production from existing energy sources.

To date, various solar hydrogen systems have been proposed and numerous PEC

devices with key light-absorbing materials have been demonstrated experimentally in research laboratories. However, the low solar-to-hydrogen (STH) efficiency and material electrochemical instability have impeded the deployment of PEC technology at industrial scale. This thesis aims to identify the limiting factors that contribute to the low device efficiency and provide engineering solutions to improve the performance of systems that are comprised a single photoabsorber. The selection of light-harvesting components in this study is limited to only technologically important, industrially well-developed, non-oxide photoactive materials such as silicon. Using cost-effective deposition and processsing techniques, this thesis demonstrates various strategies to protect and stabilize otherwise unstable photoabsorbers under PEC operating conditions. This study agrees with the consensus that the STH efficiency of PEC systems that contain a single light-absorber will be low and that the overall solar water electrolysis that proceeds at economically reasonable efficiencies can only be achieved by integrated devices that comprise multiple absorbers with spectrally matched absorption range.[41–46] Although this topic will not be fully addressed in this thesis, a high-performing and electrochemically stable single solar absorber should relax the requirements for the second or the third photoabsorber and thus should always be considered in any design and implementation of solar hydrogen generating systems.

## 1.3. Organization of this thesis

This thesis focuses on the engineering of photoactive materials for sunlight-driven water splitting systems that are efficient, stable and composed from cheap and abundant elements. Two different materials for two different electrochemical half-reactions are independently investigated in this study: (i) crystalline silicon as a photoanode for solar water oxidation, and (ii) amorphous silicon carbide as a photocathode for solar water reduction. Each of these materials will be explored in two interconnected chapters. The general scope of each study includes identification of performance limiting factors, demonstration of effective improvement strategies and stabilization of otherwise chemically-unstable photoelectrodes.

In PEC water splitting, the light collection and charge separation for direct conversion of solar energy to hydrogen and oxygen through water electrolysis is performed by the semiconductor electrode. In chapter 2, a concise view of semiconductor physics will be first introduced. Two semiconductor junction concepts will be discussed: semiconductor-liquid junctions and metal-semiconductor (Schottky) junctions, both of which share mutually similar rectifying characteristics and current transport processes. Additionally, the working principle of PEC water splitting cells and the calculation of solar energy conversion efficiencies are presented. Furthermore, general requirements for suitable water-splitting photoelectrodes are outlined.

Metal-insulator-semiconductor (MIS) junctions are an advanced concept in which the insulating layer plays a critical role in improving the device performance for solar energy conversion. The ability of a solar water splitting electrode to capture and convert sunlight to chemical products is often characterized by the photocurrent and photovoltage. In chapter 3, MIS junction crystalline silicon photoanodes

capable of generating a high photovoltage is demonstrated. A high photovoltage is achieved by engineering the MIS interfaces, including the use of interfacial oxides and applications of two metal components with different functionalities. Dark and illuminated cyclic voltammetry, electrochemical open-circuit potential measurement and Mott-Schottky analysis are used to investigate the device performance. Additionally, depth profiling analysis by x-ray photoelectron spectroscopy (XPS) equipped with ion etching is used to analyze the structural composition of the photoanode. Furthermore, the device stability is evaluated by chronoamperometry test in an alkaline solution under simulated solar illumination.

In chapter 4, the role of the interfacial oxides and metal workfunction for improving MIS junction photovoltage is further explored. The rectifying properties of the MIS devices with different interfacial oxides and various metal contacts are analyzed: (i) by fitting the dark current–voltage curves with the single- and the double-diode models, and (ii) by analyzing capacitance-voltage data using Mott-Schottky relationships. Important parameters such as the dark reverse saturation current, the diode ideality factor and the barrier height are extracted to obtain quantitative information about the influence of the metal workfunction and oxide thickness on the junction properties and the device photovoltage. Additionally, cyclic voltammetry and electrochemical open-circuit potential measurements are used to evaluate the photoanode performance. The theoretical photovoltages are calculated using the thermionic emission and tunneling equations and are compared with the experimentally-measured values. Furthermore, the effects of oxide thickness on the MIS photovoltage are presented.

Amorphous silicon-based semiconductor is a promising photoelectrode material because of its strong absorption coefficient that allows for the use of thin film as the light-absorber and its relatively wide band gap that enables device integration with smaller band gap semiconductors for maximum spectral utilization and high photovoltage generation. In chapter 5, a p-i-n junction photocathode is constructed using a p-type (p) amorphous silicon carbide (a-SiC), an intrinsic-type (i) a-SiC and an amorphous titanium dioxide ($TiO_2$). Two different device structures are compared: p-i a-SiC and p-i a-SiC/$TiO_2$. Mott-Schottky analysis is used to investigate the energetics of both structures and electrochemical open-circuit potential measurement is performed to evaluate the device photovoltages. The $TiO_2$ acts as a front surface field layer that isolates the internal electric field across the p-i-n junction and gives rise to a photovoltage that is higher than the p-i-liquid junction and is independent of the solid-liquid interaction. The surface reaction kinetics of the photocathode surface is improved by depositing two different electrocatalysts: platinum (Pt) and nickel-molybdenum (Ni–Mo). The photoelectrochemical activity and the spectral response of the photocathodes are analyzed by cyclic voltammetry and incident photon-to-current conversion efficiency (IPCE) measurements, respectively. The stability of the photocathodes is examined by chronoamperometry test in an electrolyte solution at pH 4 under simulated 1 sun illumination.

The electrocatalytic activity of Ni–Mo on $TiO_2$ is further evaluated in chapter 6. Scanning electron microscopy (SEM) is used to investigate the surface topography and the catalyst morphology. The resulting deposits of Ni–Mo by electrodeposition

are dispersed nanoparticles with nano-scale gaps that expose the underlying substrate. The incomplete surface coverage of Ni–Mo leads to a low number of active sites that decreases the electron transfer at the interface and reduces the rate of the surface catalytic reaction. To solve this, a thin Ni film is deposited using sputtering prior to the electrodeposition of Ni–Mo. The electrochemical activity of the electrocatalysts is evaluated using cyclic voltammetry in an alkaline electrolyte at pH 14. The catalytic activity of Ni/Ni–Mo is further evaluated on an a-SiC/$TiO_2$ photocathode by cyclic voltammetry under simulated solar irradiation. The device stability is tested by illuminated chronoamperometry in an alkaline electrolyte at pH 14.

## References

[1] Worldometers, *World Population Clock: 7.6 Billion People (2018),* `www.worldometers.info`, accessed: February, 2018.

[2] U.S. Energy Information Administration, *International Energy Outlook 2017,* `www.eia.gov/ieo` (2017).

[3] International Energy Agency, *Key World Energy Statistics 2017,* `www.iea.org` (2017).

[4] U.S. National Aeronautics and Space Administration (NASA), *Global Climate Change: Vital Signs of the Planet,* `https://climate.nasa.gov`, accessed: February, 2018.

[5] U.S. National Centers for Environmental Information, National Oceanic and Atmospheric Administration (NOAA), *Global Climate Report - Annual 2017,* `www.ncdc.noaa.gov`.

[6] Intergovernmental Panel on Climate Change (IPCC), *Climate Change 2014: Synthesis Report. Contribution of Working Groups I, II and III to the Fifth Assessment Report of the Intergovernmental Panel on Climate Change [Core Writing Team, R.K. Pachauri and L.A. Meyer (eds.)],* (2014).

[7] C. Le Quéré, R. M. Andrew, P. Friedlingstein, S. Sitch, J. Pongratz, A. C. Manning, J. I. Korsbakken, G. P. Peters, J. G. Canadell, R. B. Jackson, T. A. Boden, P. P. Tans, O. D. Andrews, V. K. Arora, D. C. E. Bakker, L. Barbero, M. Becker, R. A. Betts, L. Bopp, F. Chevallier, L. P. Chini, P. Ciais, C. E. Cosca, J. Cross, K. Currie, T. Gasser, I. Harris, J. Hauck, V. Haverd, R. A. Houghton, C. W. Hunt, G. Hurtt, T. Ilyina, A. K. Jain, E. Kato, M. Kautz, R. F. Keeling, K. Klein Goldewijk, A. Körtzinger, P. Landschützer, N. Lefèvre, A. Lenton, S. Lienert, I. Lima, D. Lombardozzi, N. Metzl, F. Millero, P. M. S. Monteiro, D. R. Munro, J. E. M. S. Nabel, S.-I. Nakaoka, Y. Nojiri, X. A. Padín, A. Peregon, B. Pfeil, D. Pierrot, B. Poulter, G. Rehder, J. Reimer, C. Rödenbeck, J. Schwinger, R. Séférian, I. Skjelvan, B. D. Stocker, H. Tian, B. Tilbrook, I. T. van der Laan-Luijkx, G. R. van der Werf, S. van Heuven, N. Viovy, N. Vuichard, A. P. Walker, A. J. Watson, A. J. Wiltshire, S. Zaehle,

and D. Zhu, *Global carbon budget 2017,* Earth System Science Data Discussions **2017**, 1 (2017).

[8] G. P. Peters, C. Le Quéré, R. M. Andrew, J. G. Canadell, P. Friedlingstein, T. Ilyina, R. B. Jackson, F. Joos, J. I. Korsbakken, G. A. McKinley, S. Sitch, and P. Tans, *Towards real-time verification of $CO_2$ emissions,* Nature Climate Change **7**, 848 (2017).

[9] F. Joos, R. Roth, J. S. Fuglestvedt, G. P. Peters, I. G. Enting, W. von Bloh, V. Brovkin, E. J. Burke, M. Eby, N. R. Edwards, T. Friedrich, T. L. Frölicher, P. R. Halloran, P. B. Holden, C. Jones, T. Kleinen, F. T. Mackenzie, K. Matsumoto, M. Meinshausen, G.-K. Plattner, A. Reisinger, J. Segschneider, G. Shaffer, M. Steinacher, K. Strassmann, K. Tanaka, A. Timmermann, and A. J. Weaver, *Carbon dioxide and climate impulse response functions for the computation of greenhouse gas metrics: a multi-model analysis,* Atmospheric Chemistry and Physics **13**, 2793 (2013).

[10] Robbie M. Andrew, *It's getting harder and harder to limit ourselves to 2 °C,* `http://folk.uio.no/roberan/t/global_mitigation_curves.shtml`, accessed: February, 2018.

[11] M. R. Raupach, S. J. Davis, G. P. Peters, R. M. Andrew, J. G. Canadell, P. Ciais, P. Friedlingstein, F. Jotzo, D. P. van Vuuren, and C. Le Quéré, *Sharing a quota on cumulative carbon emissions,* Nature Climate Change **4**, 873 (2014).

[12] Population Reference Bureau, *2017 World Population Data Sheet,* `www.prb.org`.

[13] N. S. Lewis and D. G. Nocera, *Powering the planet: Chemical challenges in solar energy utilization,* Proceedings of the National Academy of Sciences **103**, 15729 (2006).

[14] J. Rogelj, D. L. McCollum, B. C. O'Neill, and K. Riahi, *2020 emissions levels required to limit warming to below 2°C,* Nature Climate Change **3**, 405 (2013).

[15] G. P. Peters, R. M. Andrew, T. Boden, J. G. Canadell, P. Ciais, C. Le Quéré, G. Marland, M. R. Raupach, and C. Wilson, *The challenge to keep global warming below 2°C,* Nature Climate Change **3**, 4 (2013).

[16] S. Fuss, J. G. Canadell, G. P. Peters, M. Tavoni, R. M. Andrew, P. Ciais, R. B. Jackson, C. D. Jones, F. Kraxner, N. Nakicenovic, C. Le Quéré, M. R. Raupach, A. Sharifi, P. Smith, and Y. Yamagata, *Betting on negative emissions,* Nature Climate Change **4**, 850 (2014).

[17] United Nations Development Programme, *World Energy Assessment: Energy and the Challenge of Sustainability* (United Nations Department of Economic and Social Affairs, New York, NY, 2017).

[18] D. Abbott, *Keeping the Energy Debate Clean: How Do We Supply the World's Energy Needs?* Proceedings of the IEEE **98**, 42 (2010).

[19] N. S. Lewis, G. Crabtree, A. J. Nozik, M. R. Wasielewski, P. Alivisatos, H. Kung, J. Tsao, E. Chandler, W. Walukiewicz, M. Spitler, R. Ellingson, R. Overend, J. Mazer, M. Gress, J. Horwitz, C. Ashton, B. Herndon, L. Shapard, and R. M. Nault, *Basic Research Needs for Solar Energy Utilization. Report of the Basic Energy Sciences Workshop on Solar Energy Utilization.* (U.S. Department of Energy Office of Science, 2005).

[20] D. G. Nocera, *On the future of global energy,* Daedalus **135**, 112 (2006), https://doi.org/10.1162/daed.2006.135.4.112 .

[21] World Energy Council, *World Energy Resources 2016,* `www.worldenergy.org` (2016).

[22] REN21, *Renewables 2017 Global Status Report,* (2017).

[23] Power Reactor Information System (PRIS), `www.iaea.org/pris`, accessed: February, 2018.

[24] Nuclear Energy Institute (NEI), `www.nei.org`, accessed: February, 2018.

[25] Solargis, *Solar Resource Maps – Global Horizontal Irradiance,* `www.solargis.com`.

[26] T. R. Cook, D. K. Dogutan, S. Y. Reece, Y. Surendranath, T. S. Teets, and D. G. Nocera, *Solar Energy Supply and Storage for the Legacy and Nonlegacy Worlds,* Chemical Reviews **110**, 6474 (2010).

[27] College of the Desert and SunLine Transit Agency, *Hydrogen Fuel Cell Engines and Related Technologies Course Manual. Module 1: Hydrogen Properties, Rev 0, December 2001,* `https://www.energy.gov/eere/fuelcells/hydrogen-fuel-cell-engines-and-related-technologies-course`, accessed: February, 2018.

[28] IOR Energy, *List of Commong Conversion Factors (Engineering Conversion Factors,* `https://web.archive.org/web/20100825042309/http://www.ior.com.au/ecflist.html`, accessed: February, 2018.

[29] Panasonic, *Overview of Lithium Ion Batteries,* `http://www.panasonic.com/industrial/includes/pdf/Panasonic_LiIon_Overview.pdf`, accessed: February, 2018.

[30] R. van de Krol and M. Grätzel, *Photoelectrochemical Hydrogen Production* (Springer, New York, 2012).

[31] N. Armaroli and V. Balzani, *The Hydrogen Issue,* ChemSusChem **4**, 21 (2011).

[32] W. Haije and H. Geerlings, *Efficient Production of Solar Fuel Using Existing Large Scale Production Technologies,* Environmental Science & Technology **45**, 8609 (2011).

[33] K. Rajeshwar, R. McConnell, and S. Licht, *Solar Hydrogen Generation* (Springer, New York, 2012).

[34] C. A. Grimes, O. K. Varghese, and S. Ranjan, *Light, Water, Hydrogen – The Solar Generation of Hydrogen by Water Photoelectrolysis* (Springer, New York, 2012).

[35] A. Đukić and M. Firak, *Hydrogen production using alkaline electrolyzer and photovoltaic (PV) module,* International Journal of Hydrogen Energy **36**, 7799 (2011).

[36] R. Clarke, S. Giddey, F. Ciacchi, S. Badwal, B. Paul, and J. Andrews, *Direct coupling of an electrolyser to a solar PV system for generating hydrogen,* International Journal of Hydrogen Energy **34**, 2531 (2009).

[37] D. Iannuzzi and M. Pagano, *Efficiency of hydrogen based storage systems for stand-alone pv applications: Numerical and experimental results,* in *2009 International Conference on Clean Electrical Power* (2009) pp. 555–561.

[38] A. A. Rahim, A. S. Tijani, M. Fadhlullah, S. Hanapi, and K. Sainan, *Optimization of Direct Coupling Solar PV Panel and Advanced Alkaline Electrolyzer System,* Energy Procedia **79**, 204 (2015).

[39] M. R. Shaner, H. A. Atwater, N. S. Lewis, and E. W. McFarland, *A comparative technoeconomic analysis of renewable hydrogen production using solar energy,* Energy & Environmental Science **9**, 2354 (2016).

[40] B. A. Pinaud, J. D. Benck, L. C. Seitz, A. J. Forman, Z. Chen, T. G. Deutsch, B. D. James, K. N. Baum, G. N. Baum, S. Ardo, H. Wang, E. Miller, and T. F. Jaramillo, *Technical and economic feasibility of centralized facilities for solar hydrogen production via photocatalysis and photoelectrochemistry,* Energy & Environmental Science **6**, 1983 (2013).

[41] J. R. Bolton, S. J. Strickler, and J. S. Connolly, *Limiting and realizable efficiencies of solar photolysis of water,* Nature **316**, 495 (1985).

[42] M. Weber and M. Dignam, *Splitting water with semiconducting photoelectrodes–Efficiency considerations,* International Journal of Hydrogen Energy **11**, 225 (1986).

[43] S. Licht, *Multiple Band Gap Semiconductor/Electrolyte Solar Energy Conversion,* The Journal of Physical Chemistry B **105**, 6281 (2001).

[44] H. Döscher, J. F. Geisz, T. G. Deutsch, and J. A. Turner, *Sunlight absorption in water – efficiency and design implications for photoelectrochemical devices,* Energy & Environmental Science **7**, 2951 (2014).

[45] L. C. Seitz, Z. Chen, A. J. Forman, B. A. Pinaud, J. D. Benck, and T. F. Jaramillo, *Modeling Practical Performance Limits of Photoelectrochemical Water Splitting Based on the Current State of Materials Research,* ChemSusChem **7**, 1372 (2014).

[46] S. Hu, C. Xiang, S. Haussener, A. D. Berger, and N. S. Lewis, *An analysis of the optimal band gaps of light absorbers in integrated tandem photoelectrochemical water-splitting systems,* Energy & Environmental Science **6**, 2984 (2013).

# 2

# Fundamentals

The design and construction of a sunlight-driven electrochemical system that splits water to hydrogen and oxygen requires knowledge and understanding of fundamental aspects of device components and mechanisms underlying photoelectrochemistry. In a photoelectrochemical water splitting cell, the semiconductor is the main component that captures and converts solar energy into an electronic driving force to drive the non-spontaneous reaction of water electrolysis. This chapter aims to present a brief view of semiconductor physics and the working principle of solar water splitting cells utilizing concepts that have been presented in several textbooks and introductory reviews. At the beginning of this chapter, the basic physics of semiconductor devices will be first discussed, and the concept of semiconductor junctions relevant to photoelectrochemical processes will be presented. The working principle of photoelectrochemical water splitting cells and calculations of energy conversion efficiencies will be discussed in the following section. Finally, discussions on fundamental requirements of a semiconductor material for sunlight-driven water splitting will be presented.

## 2.1. Physics of semiconductors

Depending on the electrical conductivity, materials can be categorized as metal, insulator, and semiconductor. The underlying principle of these materials can be understood in terms of quantum states for electrons. In a single isolated atom, electrons reside in atomic orbitals of which energy levels are discrete. According to the Pauli exclusion principle, two electrons cannot occupy the same quantum state simultaneously. If two atoms join together to form a molecule, their atomic orbitals overlap and combine to form the same number of molecular orbitals (bonding and anti bonding) with different energy so that the electron from the former atomic orbital can occupy the new orbital. The number of atoms in solid is very large and thus the number of orbitals is very large. The atomic arrangement in solid gives rise to sets of orbitals that are extremely close together such that their energies are closely spaced and can be viewed as a continuum of allowed states or an energy

band.

A solid has a large number of bands in the electronic band structure, but the most important ones are those that are close to the Fermi level, called the valence band and the conduction band. Fermi level is defined as an energy level of an electron that has half probability of being occupied at any given time. The valence band is a set of closely spaced energy levels that is occupied by valence electrons, and is defined as the highest occupied energy band. Ideally, at absolute zero temperature the valence band is completely filled by electrons. These electrons are effectively immobile, but can be thermally excited into the conduction band at temperatures above absolute zero. The conduction band, on the other hand is the lowest unoccupied energy band in the electronic structure, and is completely empty at absolute zero, thus allowing the electrons to be mobile through the lattice. Because of quantization of energy, the valence and the conduction bands are separated by a forbidden gap (or simply a band gap) in which no electron can exist. Depending on the size of the band gap, materials can be classified in terms of their conductivity. An insulator has a very wide band gap such that thermalization of electrons will not reach the conduction band, and the Fermi level sits at exactly halfway the band gap. For example, a good insulator such as silicon dioxide ($SiO_2$) has a band gap of 9 eV.[1] In a metal, the valence band and the conduction band overlap such that electrons can easily move into the conduction band, which makes it electrically conductive. Figure 2.1 shows the electronic band structure of insulator, metal and semiconductor.

Semiconductors are materials with an electrical conductivity that falls between metals and insulators, with band gaps typically ranging from 0.7 to 3.5 eV. Although the width of the band gap will not allow for room-temperature thermal excitation, it is still within the range of energy provided by sunlight. This unique property of semiconductors is an important feature for solar-energy capture and conversion

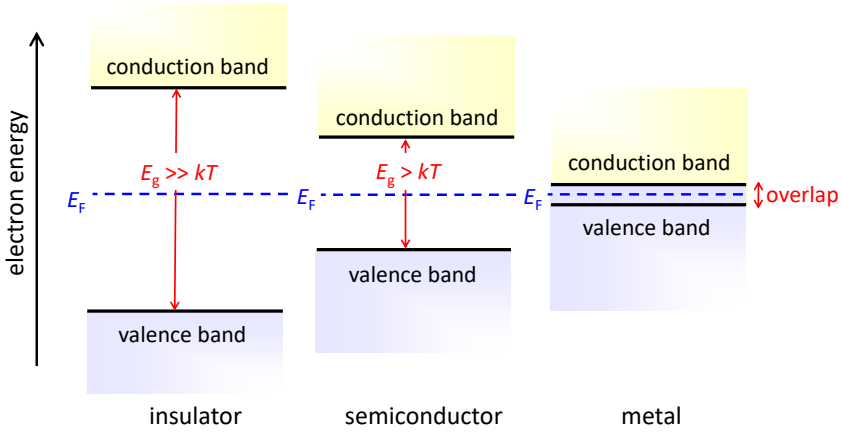



**Figure 2.1:** Energy band diagram of insulator, intrinsic semiconductor and metal. The Fermi level and the band gap are denoted as $E_F$ and $E_g$, respectively. The term $kT$ is thermal energy ($k$ is the Boltzmann's constant and $T$ is the temperature), and has a value of 25.7 eV at room temperature (298 K).

devices such as photovoltaic and photoelectrochemical cells whose charge carriers can be extracted by photoexcitation.

The distribution of electrons in an energy level is a function of the density of states in the valence and conduction bands and the Fermi-Dirac distribution. The density of states $g$ at an energy $E$ in the conduction band close to $E_C$ and in the valence band close to $E_V$ are given by:

$$g_c(E) = \frac{m_e^* \sqrt{2m_e^* (E - E_C)}}{\pi^2 \hbar^3} \tag{2.1a}$$

$$g_v(E) = \frac{m_h^* \sqrt{2m_h^* (E - E_C)}}{\pi^2 \hbar^3} \tag{2.1b}$$

where $m_e^*$ and $m_h^*$ are the effective mass of electrons and holes, respectively, $\hbar$ $(= h/2\pi)$ is the reduced Planck's constant, $h$ is the Planck's constant, $E_C$ and $E_V$ are the energy levels of the conduction and valence band edge, respectively. The Fermi-Dirac distribution function $f(E)$ is given by:

$$f(E) = \frac{1}{1 + \exp\left(\frac{E - E_F}{kT}\right)} \tag{2.2}$$

where $k$ is the Boltzmann's constant ($1.38 \times 10^{-23}$ m$^2$ kg s$^{-2}$ k$^{-1}$) and $E_F$ is the Fermi energy. The term $kT$ is the thermal energy, and at room temperature (298 K) has a value of 25.7 meV.

The conductivity of a material is determined by the concentration of electrons in the conduction band and holes in the valence band. The total population of electrons in the conduction band and holes in the valence band is obtained by integrating the product of the density of states and the Fermi-Dirac distribution function across the whole energy band, as given by:

$$n = \int_{E_C}^{E_{top}} g_c(E) f(E) \, dE \tag{2.3a}$$

$$p = \int_{E_{bottom}}^{E_V} g_v(E) \left[1 - f(E)\right] dE \tag{2.3b}$$

For non-degenerate semiconductors, the difference between the Fermi level and the conduction band edge or the valence band edge is greater than $3kT$ ($E_C - E_F$ or $E_F - E_V > 3kT$). Equation 2.3 can be simplified by substituting the density of states and the distribution function, as given by:

$$n = N_C \exp\left(\frac{E_F - E_C}{kT}\right), \qquad E_C - E_F \geq 3kT \tag{2.4a}$$

$$p = N_V \exp\left(\frac{E_V - E_F}{kT}\right), \qquad E_F - E_V \geq 3kT \tag{2.4b}$$

where $N_C$ and $N_V$ are the effective density of states in the conduction band and the valence band, respectively, and are given by:

$$N_C = 2\left(\frac{2\pi m_e^* kT}{h^2}\right)^{3/2} \tag{2.5a}$$

$$N_V = 2\left(\frac{2\pi m_h^* kT}{h^2}\right)^{3/2} \tag{2.5b}$$

Pure semiconductors (also called intrinsic semiconductors) are not desired for many optoelectronic applications because of their low concentration of free carriers which results in poor conductivity. Alternatively, the density of electrons and holes in an intrinsic semiconductor can be manipulated by substituting the host atoms with dopant impurities in the lattice. Semiconductors with dopant impurities are called extrinsic semiconductors. Depending on the number of valence electron in the dopant atom, the impurities can serve either as donors or acceptors. One of many semiconductor materials that is commonly doped is silicon (Si). Each Si atom has four valence electrons, and they are covalently bonded with other Si atoms. To increase the electron concentration, some of the Si atoms are substituted with atoms that have five valence electrons, such as phosphorus (P). When introducing phosphorus into the Si lattice, four valence electrons in the phosphorus atom readily form bonds with the neighboring four Si atoms (Fig. 2.2a). The fifth valence electron cannot take part in forming a bond and becomes weakly bound to the phosphorus atom. Consequently, the excess electron can easily be liberated by absorption of thermal energy at room temperature, and once free, the electron can move throughout the lattice. Phosphorus atoms that substitute Si atoms and donate free electrons are called donors. A semiconductor that has excess free electrons

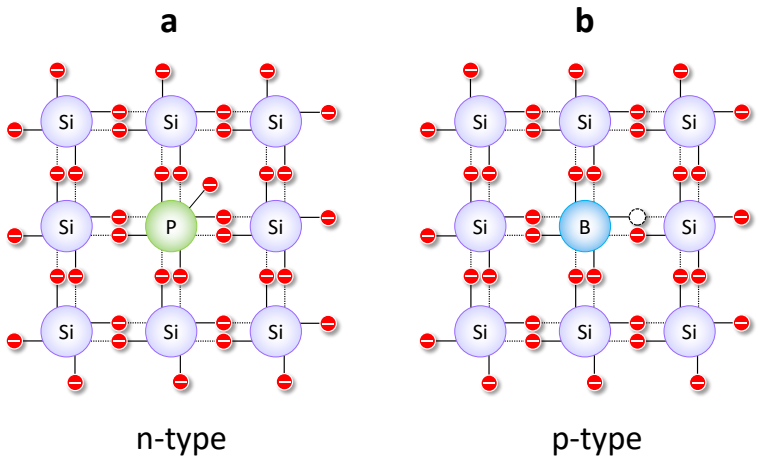



**Figure 2.2:** Doping process of silicon (Si): (a) A phosphorus atom (P) with five valence electrons substitutes a Si atom the lattice, resulting a free electron. (b) A boron (B) atom with three valence electrons substitutes a Si atom, resulting a hole.

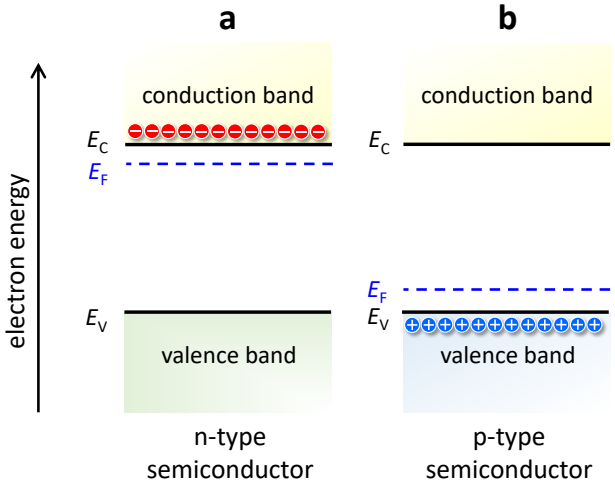



**Figure 2.3:** Energy band diagram of extrinsic semiconductors: (a) n-type, and (b) p-type.

(electrons are the majority carriers) is called an n-type semiconductor. Conversely, free holes can be introduced into the Si lattice by substituting some of the Si atoms with atoms that have three valence electrons, such as boron (B). Boron atom cannot form a bond with all the four neighboring Si atoms, leaving a hole in the lattice, but it readily accepts an electron from the nearby Si atom (Fig. 2.2b). Because of their behavior that accepts electrons, boron impurities in the Si lattice are called acceptors. A semiconductor that has excess free holes (holes are the majority carriers) is called a p-type semiconductor.

The energy band diagram of an n-type semiconductor and a p-type semiconductor are shown schematically in Fig. 2.3. Because of a large concentration of electrons in the n-type semiconductor, the Fermi level ($E_F$) resides near the conduction band edge ($E_C$). Conversely, the large population of holes in the p-type semiconductor places the Fermi level near the valence band edge ($E_V$).

## 2.2. Semiconductor junctions

This section will focus on semiconductor junction concepts that are generally used for solar water splitting electrodes. The physics of the traditional semiconductor-liquid junctions will be first introduced, followed by an innovative concept such as metal-semiconductor junctions. Lastly, the energetics of semiconductor junctions and the current transport mechanisms across the junction will be discussed.

### Semiconductor-liquid junctions

When a semiconductor is brought into contact with liquid, charge transfer will occur between the semiconductor and the solution (Fig. 2.4a) until an equilibrium is reached. The flow of charge carriers from the semiconductor to the solution leads to the depletion of free carriers near the semiconductor-liquid interface and gives rise

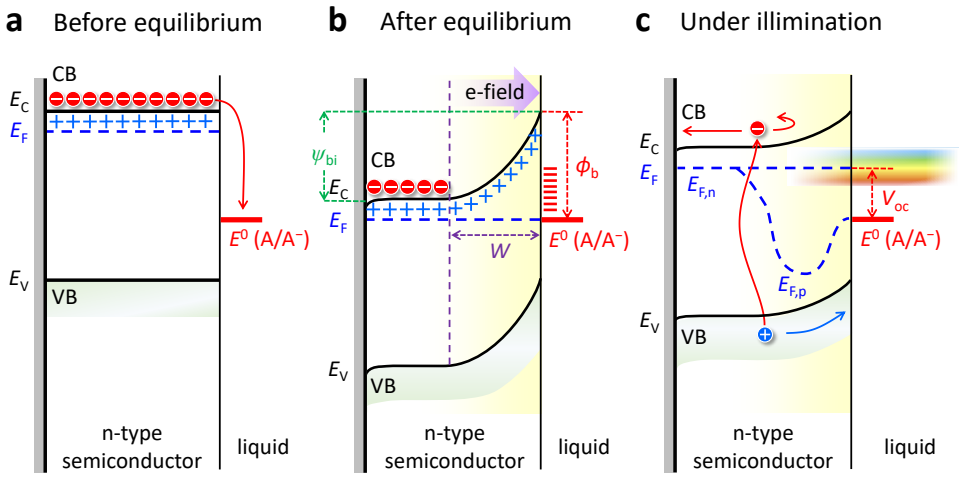



**Figure 2.4:** Energy band diagram of a semiconductor-liquid junction in a solution containing a redox couple (A/A$^-$), having an electrochemical potential $E^0$ (A/A$^-$) (a) before equilibrium, (b) after equilibrium with the redox couple, and (c) under illumination. The barrier height ($\phi_b$) is given by the difference between the conduction band edge ($E_{CB}$) and $E^0$ (A/A$^-$). Under illumination, the non-equilibrium concentration of photogenerated charge carriers are represented by the quasi-Fermi level of electron ($E_{F,n}$) and hole ($E_{F,p}$). The voltage of a semiconductor-liquid junction electrode generated due to charge excitation under illumination is given by the difference between ($E_{F,n}$) and $E^0$ (A/A$^-$).

to a region that is free of mobile charges called the space-charge region. The region outside the space-charge region maintains its charge neutrality, and is called the quasi-neutral region. After equilibration, the electrochemical potential (*i.e.*, Fermi level, $E_F$) has a constant position and is the same across the semiconductor-liquid junction.

The electrostatic potential difference between the boundaries of the space-charge region is called the diffusion potential or the built-in voltage ($\psi_{bi}$). The magnitude of $\psi_{bi}$ represents the maximum attainable photovoltage, and is determined by the initial difference in electrochemical potentials between the the semiconductor and the solution. Because of the electrostatic potential difference, an internal electric field is established inside the space-charge region. The strength of electric field is zero outside the space-charge region and maximum ($\xi_{max}$) at the semiconductor-liquid interface. Assuming the conduction and the valence band edges are pinned at the semiconductor-liquid interface, $\xi_{max}$ is a function of applied voltage ($V$) as given by:

$$\xi_{max} = \sqrt{\frac{2qN_D}{\epsilon_0\epsilon_s}\left(\psi_{bi} - V - \frac{kT}{q}\right)} \tag{2.6}$$

where $\epsilon_0$ is the vacuum dielectric permittivity, $\epsilon_s$ is the dielectric permittivity of the semiconductor, $N_D$ is the donor concentration, and $q$ is the elementary charge ($1.6 \times 10^{-19}$ C). Separation of charge carriers generated by light absorption in the semiconductor takes place in the space-charge region by this electric field.

For an n-type semiconductor, the space-charge region will have an excess positive charge as a result of the ionized dopant atoms that are no longer compensated by the mobile charges (Fig. 2.4b). The solution, on the other hand, will have an excess negative charge. The distribution of positive charges in the semiconductor is spread across the the space-charge region, while negative charges in the solution are concentrated in a much narrower region (4–6 Å)[2] called the Helmholtz layer. The width of the space-charge region ($W$) in the semiconductor is a function of the applied voltage as given by:

$$W = \sqrt{\frac{2\epsilon_0\epsilon_s}{qN_D}\left(\psi_{bi} - V - \frac{kT}{q}\right)} \tag{2.7}$$

The theoretical limit of internal energy that can be extracted from photogenerated charge carriers at a semiconductor-liquid junction is determined by the potential energy barrier at the semiconductor-liquid interface. For an n-type semiconductor, the height of this barrier ($\phi_b$) is given by the initial difference between the energy level of the conduction band edge and the electrochemical potential of the liquid. To enable maximum generation of photovoltage from a semiconductor-liquid junction, the barrier should be as high as possible. Intuitively, the barrier height of a semiconductor-liquid junction can be tuned by varying the electrochemical potential of the redox couple in the solution. In a photoelectrochemical water splitting cell, however, the electrochemical potential of the redox couple is fixed by the desired chemistry. For example, the redox pair of interest for an n-type semiconductor photoanode is $O_2/H_2O$, and for a p-type semiconductor photocathode is $H^+/H_2$.

Alternatively, the interfacial energetics of a semiconductor-liquid junction can be optimized by adjusting the pH of the liquid solution. For water oxidation, the dependence of $E^0$ ($O_2/H_2O$) on the pH is expressed by:

$$E^0(O_2/H_2O) = 1.23\ \text{V} - 0.059\ \text{V} \times \text{pH} \qquad (\text{V } \textit{vs.}\ \text{NHE}) \tag{2.8}$$

Equation 2.8 suggests that $E^0$ ($O_2/H_2O$) will shift −59 mV per pH unit with respect to the band edges of the semiconductor. This approach, however, is not practically useful because semiconductor surfaces in contact with water tend to form hydroxyl groups that adsorb/desorb protons depending on the pH of the solution. The protonation/deprotonation of these surface groups generates a potential drop across the Helmholtz layer that shifts the band edges following the movement of the water redox potentials (−59 mV per pH unit). As the band edges stay constant relative to the electrochemical potential of the redox couple, the energetics of a semiconductor-liquid junction remain pH-independent in water.

The upper limit of photovoltage that can be generated by a semiconductor-liquid junction under illumination is reduced by the amount of various losses due to recombination events occurring in various regions of the semiconductor. As a result, the actual photovoltage does not reach the maximum achievable value given by the built-in voltage described above. In principle, the photovoltage of an illuminated semiconductor-liquid junction electrode is given by the difference between the quasi-Fermi level of electron ($E_{F,n}$) and hole ($E_{F,p}$) (Fig. 2.4c). The quasi-Fermi level

represents the electrochemical potential of one type of carrier at a time (*i.e.*, either electron or hole), and according to Fermi-Dirac distribution, describes the concentration of electrons and holes in the semiconductor under non-equilibrium conditions. In the absence of significant surface capacitance and band edge movement due to illumination, the degree of quasi-Fermi level splitting, thus the photovoltage, can simply be estimated by the change of open-circuit potential in the dark and under illumination.

Under illuminated open-circuit condition, there is no net current flow through the junction, and the degree of splitting of electron and hole quasi-Fermi levels equals to the open-circuit voltage ($V_{oc}$). For semiconductors with a flat surface, the theoretical expression for $V_{oc}$ of an illuminated semiconductor-liquid junction is given by the diode equation:

$$V_{oc} = \frac{nkT}{q} \ln\left(\frac{j_{ph}}{j_0} + 1\right) \approx \frac{nkT}{q} \ln\left(\frac{j_{ph}}{j_0}\right) \tag{2.9}$$

where $n$ is the diode ideality factor, $k$ is the Boltzmann's constant ($1.38 \times 10^{-23}$ $m^2$ kg $s^{-2}$ $k^{-1}$), $T$ is the temperature (in K), $q$ is the elementary charge ($1.6 \times 10^{-19}$ C), $j_{ph}$ is the light-limited photocurrent density and $j_0$ is the dark reverse saturation current density. $j_0$ is a fundamental parameter that depends on the complex recombination processes in the semiconductor. The value of $n$ is a measure of the junction quality and the type of recombination in the semiconductor. For an ideal junction where recombination events are limited by the recombination of minority carriers in the bulk, $n$ is equal to 1. If other recombination mechanisms occur, such as recombination in the space-charge region and/or on the surface, $n$ will be greater than unity. A high $n$ value is typically a signal of a high recombination, and is usually accompanied with a high value of $j_0$. Therefore, a high $n$ will lead to a lower $V_{oc}$.

In the absence of mass transport limitations in the electrolyte and charge transfer losses due to recombination at the semiconductor-liquid interface, electronic transport mechanisms in a semiconductor-liquid junction electrode are similar to those in a metal-semiconductor junction. These topics will be discussed in detail in the following section.

### Metal-semiconductor junctions

The barrier formation at a metal-semiconductor contact is similar to that at a semiconductor-liquid junction, except that the electrostatic potential difference arises from the workfunction difference between the metal ($\Phi_m$) and the semiconductor ($\Phi_s$). If the workfunction of the metal exceeds that of an n-type semiconductor, the bands will bend upward (Fig. 2.5a). Conversely, if the metal workfunction is lower than that of the n-type semiconductor, the bands will bend downward (Fig. 2.5b). According to the Schottky-Mott theory, the height of the potential barrier ($\phi_b$) for an n-type semiconductor in contact with a metal is given by:[3,4]

$$\phi_b = \Phi_m - \chi_s \tag{2.10}$$

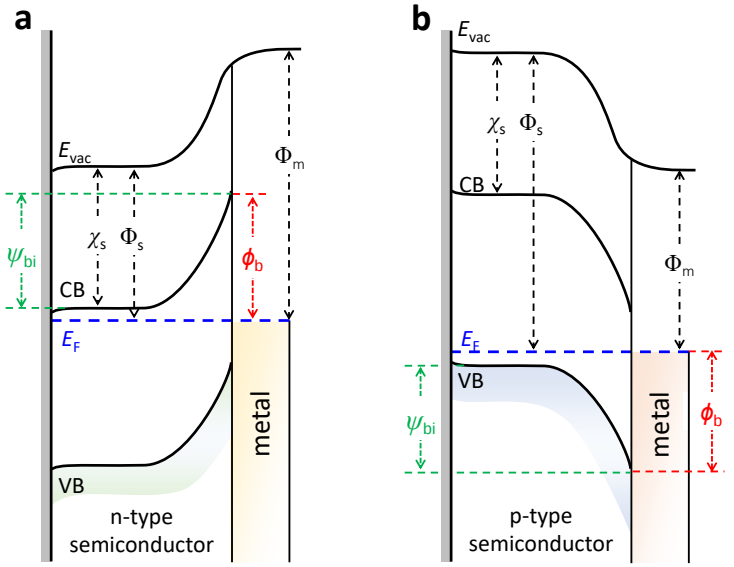



**Figure 2.5:** Energy band diagram of a metal-semiconductor junction using (a) an n-type semiconductor, and (b) a p-type semiconductor.

where $\chi_s$ is the electron affinity of the semiconductor, and is defined as the distance between the the conduction band edge and the vacuum level. For a p-type semiconductor, the barrier height is given by the sum of electron affinity and the semiconductor band gap ($E_g$) minus the metal workfunction:

$$\phi_b = (\chi_s + E_g) - \Phi_m \tag{2.11}$$

The actual barrier height of a metal-semiconductor contact, however, does not in practice obey the Schottky-Mott rule described in Eq. 2.10 or Eq. 2.11. Bardeen was the first to propose the surface state model to explain this observation.[5] It was initially assumed that the surface states arise due to impurity levels or surface imperfection in which the electrons are localized around the foreign atoms or surface defects in the crystal lattice. At the present time, it is generally accepted that the existence of surface states is a result of unpaired atoms at the semiconductor surface that are not able to form bond with the neighboring atoms (*i.e.*, dangling bonds), and their energies are usually distributed across the surface band gap. According to the Bardeen's model, if the density of the surface levels is sufficiently high ($> 10^{13}$ $cm^{-2}$), there will be a double layer at the free surface of the semiconductor that alters the potential difference between the metal and the semiconductor.

Cowley and and Sze showed that the barrier height of a metal-semiconductor contact agrees with the Bardeen's model only if there is a thin interfacial oxide layer of a few angstroms that is transparent to electrons, as given by:[6]

$$\phi_b = \gamma(\Phi_m - \chi_s) + (1-\gamma)(E_g - \Phi_0) \tag{2.12}$$

where $E_g$ is the band gap and $\Phi_0$ is the charge neutrality level. The semiconductor surface is electrically neutral if the surface states occupy up to $\Phi_0$. The term $\gamma$ is given by:

$$\gamma = \frac{\epsilon_i}{\epsilon_i + q\delta D_s} \tag{2.13}$$

where $\epsilon_i$ is the dielectric permittivity of the interfacial oxide, $\delta$ is the thickness of the oxide, and $D_s$ is the density of the surface states per unit area per electron volt. In the absence of surface states, $D_s = 0$, $\gamma = 1$, and Eq. 2.12 becomes $\phi_b = \Phi_m - \chi_s$, in accord with the Schottky-Mott approximation described in Eq. 2.10. If the density of surface states is very high, $\gamma$ becomes very small and the barrier height approaches $E_g - \Phi_0$.

Heine later argued that surface states cannot exist in the surface band gap for most metal-semiconductor intimate contacts.[7] Surface states formed by dangling bonds are typically shallow, and reside near the valence and the conduction band edges, which means they will be buried by the total valance and conduction bands. Heine pointed out that when a metal is brought into contact with a clean semiconductor surface, the wave functions of metal electrons exponentially decay and penetrate into regions where the metal conduction band overlaps the band gap of the semiconductor. The resulting states are later known as metal-induced-gap states (MIGS).[8] These gap states tend to pin the Fermi level and control the barrier height of the metal-semiconductor contact, resulting in a junction behavior that defies from the Schottky-Mott theory.

### Current transport mechanisms

The current mechanism in a metal-semiconductor contact is mainly due to the transport of majority carriers. There are four fundamental electronic transport processes through a metal-semiconductor junction (Fig. 2.6a):[9,10]

(a) emission of electrons from the semiconductor over the top of the potential barrier into the metal,
(b) quantum mechanical tunneling through the barrier,
(c) recombination of the space charge region,
(d) recombination in the neutral region (hole injection).

The inverse processes occur under reverse bias (Fig. 2.6b).

The electronic transport across a metal-semiconductor junction under forward bias voltage is governed by electron diffusion to the space-charge region, followed by emission of electrons to the metal.[9] Although both mechanisms occur in sequence, the thermionic emission theory proposed by Bethe assumes that the current is limited by the emission process (process a, Fig. 2.6a).[11] The net current flow across a metal-semiconductor junction is given by the sum of the thermionic emission current from the semiconductor to the metal ($j_{S\to M}$), and the reverse current from the metal to the semiconductor ($j_{M\to S}$). The forward current from the semiconductor to the metal is determined by electrons with energies sufficient to overcome the potential

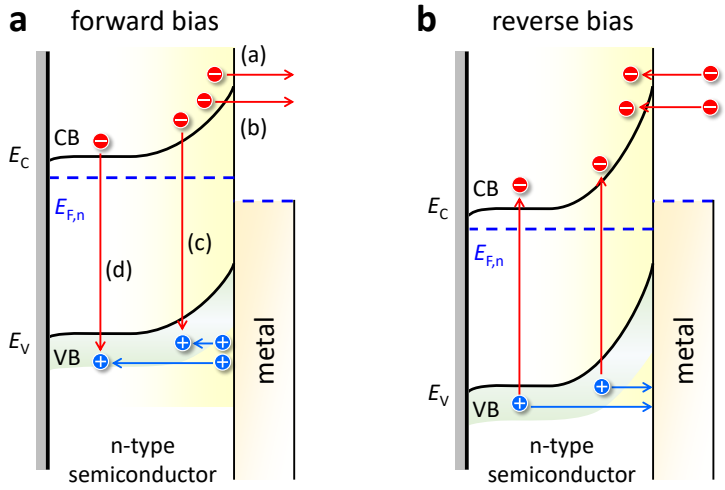



**Figure 2.6:** Current transport mechanisms of a metal-semiconductor (n-type) junction (a) under forward bias (adapted from Ref. 9), and (b) under reverse bias.

barrier. Thus, $j_{S\to M}$ depends on the height of the potential barrier at the junction $(-q\phi_b)$ and the applied voltage $(V)$, as given by:

$$\begin{aligned} j_{S\to M} &= \frac{4\pi m_e^* q}{h^3}(kT)^2 \exp\left(\frac{-q\phi_b}{kT}\right)\exp\left(\frac{qV}{kT}\right) \\ &= A^* T^2 \exp\left(\frac{-q\phi_b}{kT}\right)\exp\left(\frac{qV}{kT}\right) \end{aligned} \tag{2.14}$$

where $A^*$ $(= 4\pi m_e^* q k^2/h^3)$ is the effective Richardson's constant for thermionic emission. The term $\exp(qV/kT)$ is called the Boltzmann's factor.

The potential barrier for electrons that move from the metal to the semiconductor remains the same under bias, and therefore the reverse current flow to the semiconductor is unaffected by the applied voltage $(V = 0)$. Thus, $j_{M\to S}$ is given by:

$$j_{M\to S} = -A^* T^2 \exp\left(\frac{-q\phi_b}{kT}\right) \tag{2.15}$$

The total current density under forward bias is then given by the sum of Eq. 2.14 and Eq. 2.15:

$$\begin{aligned} j_{TE} &= j_{S\to M} + j_{M\to S} \\ &= A^* T^2 \exp\left(\frac{-q\phi_b}{kT}\right)\left[\exp\left(\frac{qV}{kT}\right) - 1\right] \\ &= j_{TE,0}\left[\exp\left(\frac{qV}{kT}\right) - 1\right] \end{aligned} \tag{2.16}$$

where $j_{TE,0}$ $(= A^* T^2 \exp(-q\phi_b/kT))$ is the reverse saturation current density for thermionic emission.

Under reverse bias, the barrier height increases by the amount of applied voltage and forces electrons to move in the opposite direction. Consequently, the forward thermionic emission current ($j_{S\rightarrow M}$) becomes negligible. The potential barrier for the reverse thermionic emission current ($j_{M\rightarrow S}$) on the other hand remains constant at any applied bias voltage. At sufficiently high reverse bias, the Boltzmann's factor becomes very small and the current density saturates at $-j_{TE,0}$.

Another current mechanism, such as quantum mechanical tunneling through the potential barrier (process b, Fig. 2.6a) is less dominant for non-degenerate semiconductors and is only significant for heavily doped semiconductors in which the dopant concentration is very high ($> 10^{17}$ cm$^{-3}$) and the difference between the conduction/valence band and the Fermi level is less than $3kT$. This is because the tunneling probability of electrons in the forward direction increases with thinner and lower potential barrier. Hole injection current (process d, Fig. 2.6a), on the other hand, is generally considered to be negligible for low-current operation under forward bias, because the injection ratio between the electron and hole ($j_p/j_n$) is very small.[12,13] In principle, the hole injection current is given by the same mechanism as the thermionic emission, except that it is proportional to $\exp(-q\phi_{bp}/kT)$ , where $\phi_{bp}$ is the barrier height for holes and is equal to the difference between the Fermi level and the top of the valence band edge in the bulk of the semiconductor.[9] Under forward bias, the hole barrier height $\phi_{bp}$ typically exceeds the electron barrier height $\phi_{bn}$, such that the hole injection ratio is very small and can be neglected.

The current flow due to carrier recombination in the space-charge region (process c, Fig. 2.6a) typically occurs when the potential barrier is high and becomes important at low forward biases.[14] Under high forward bias, the recombination current in the space-charge layer is negligible compared to the thermionic emission current. The recombination in the space-charge region is assumed to take place at the trap centers near the middle of the energy gap through capture processes (Fig. 2.7a), and is called the Shockley-Read-Hall recombination.[15,16] The origin of these sites is generally attributed to crystal lattice disorder, impurity atoms located interstitially or substitutionally or surface defects.[14] If the traps are initially filled with electrons, injected holes in the valence band can move up to these trap states and recombine with the electrons before they are thermally emitted to the conduction band, leaving the traps empty. Subsequently, the electrons in the conduction band can be captured in the empty trap states, causing the electron current to flow through the external circuit.

Any recombination event occurring under bias may lead to the departure from an ideal diode behavior. The non-ideality of a diode is generally represented by the diode ideality factor ($n$). A diode is considered ideal if the recombination is limited by minority carriers, and has an $n$ value of unity. For a metal-semiconductor junction with a high barrier, majority carriers can also recombine in the space-charge region, resulting an $n$ value that is greater than one. The current density arising from recombination of charge carriers is given by the following expression:

$$j_{rec} = j_{rec,0} \exp\left(\frac{qV}{nkT}\right) \tag{2.17}$$

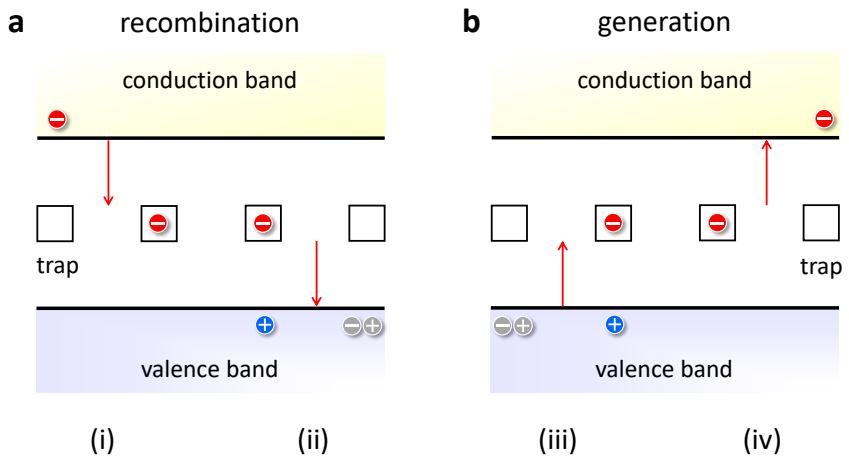



**Figure 2.7:** Processes of Shockley-Read-Hall (SRH) (a) recombination, and (b) generation. Four sub-processes in SRH generation/recombination include (i) electron capture, (ii) hole capture, (iii) hole emission and (iv) electron emission.

The $n$ value is usually 2 for recombination in the space-charge region that involves recombination of both carrier types (majority and minority carriers). The $j_{rec,0}$ is the recombination saturation current density, and is given by:

$$j_{rec,0} = \frac{qn_i x'}{2\tau} \tag{2.18}$$

where $n_i$ is the intrinsic carrier concentration which is proportional to $\exp(-qE_g/2kT)$, $\tau$ is the effective carrier lifetime in the space-charge region, and $x'$ is the effective width of the space-charge region. The value of $x'$ is usually lower than the space-charge width ($W$), but an upper estimate for $j_{rec,0}$ can be obtained by substituting $x'$ with $W$.[10]

In the space-charge layer, both types of carriers are generated through the emission processes (Fig. 2.7b). Under reverse bias these carriers are rapidly swept out of the region by the large electric field, resulting in current flow in the external circuit which is called the generation current. The generation current is assumed to be constant throughout the space-charge region, as given by:[14]

$$j_{gen} = -\frac{qn_i W}{2\tau} = -j_{gen,0} \tag{2.19}$$

Equation 2.18 and 2.19 suggest that the recombination saturation current is equal to the generation saturation current ($j_{rec,0} = j_{gen,0} = j_{gen/rec,0}$). The total current due to generation/recombination in the space-charge region is then given by:

$$\begin{aligned} j_{gen/rec} &= j_{rec} + j_{gen} \\ &= j_{gen/rec,0}\left[\exp\left(\frac{qV}{2kT}\right) - 1\right] \end{aligned} \tag{2.20}$$

It may be noted that the generation current is important under reverse bias condition where the recombination is very small because of the large electric field. Under moderate forward bias, carrier recombination in the space-charge region becomes the dominant conduction mechanism. At very high forward bias voltage, the recombination current is extremely small in comparison to the thermionic emission current, so that its contribution to the total current is negligible.

For a metal-semiconductor junction with a high barrier, the total current is given by the sum of the thermionic emission current (Eq. 2.16) and the generation/recombination current in the space-charge region (Eq. 2.20):

$$\begin{aligned} j_n &= j_{\mathrm{TE}} + j_{\mathrm{gen/rec}} \\ &= j_{\mathrm{TE},0}\left[\exp\left(\frac{qV}{kT}\right) - 1\right] + j_{\mathrm{gen/rec},0}\left[\exp\left(\frac{qV}{2kT}\right) - 1\right] \end{aligned} \tag{2.21}$$

The generation-recombination processes in a rectifying junction can be identified by examining the diode properties through the current–voltage ($j$–$V$) characteristics in the dark. Each region in the dark $j$–$V$ curve (Fig. 2.8a) represents the dominant current transport mechanism under a certain range of applied bias: (i) generation-recombination in the space-charge region, (ii) thermionic emission, (iii) series resistance effect, and (iv) reverse leakage current due to generation and recombination. In an ideal case, a straight line in the forward bias region is indicative of an exponential voltage dependence of current, and for a metal-semiconductor junction, the forward current is limited by thermionic emission. If recombination exists in the space-charge layer, the curve will deviate from linear at low forward biases and the resulting current in this region will be appreciably higher than the thermionic emission current. In the reverse bias region, the generation current is more dominant

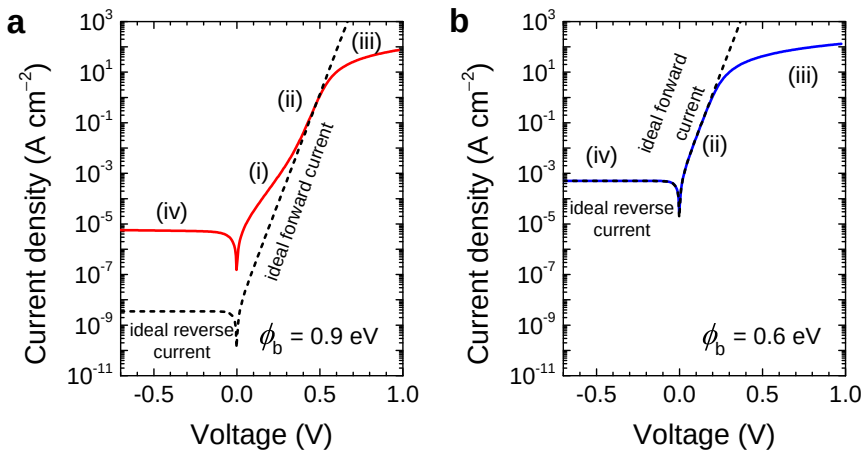



**Figure 2.8:** Current–voltage ($j$–$V$) characteristics of silicon diodes; (a) with a barrier height of 0.9 eV and (b) with a barrier height of 0.6 eV. The ideal current-potential curves that exclude the generation-recombination in the space-charge region and no series resistance are shown as the dashed lines.

than the recombination current because all the excited carriers are swept out of the space-charge layer by the strong electric field. The generation-recombination current is only important if the barrier is sufficiently high. For a rectifying junction with a low barrier, the current due to generation and recombination in the space-charge layer is extremely small, and therefore these processes cannot be distinguished from the thermionic emission current in the dark $j$–$V$ curve (Fig. 2.8b).

The photocurrent for a metal-semiconductor junction under illumination is a result of generation of minority carriers in the semiconductor that move to the metal. For an n-type semiconductor, the theoretical expression for the hole photocurrent density is given by:

$$j_p = \frac{4\pi m_h^* q(kT)^2}{h^3} \exp\left(\frac{-q\phi_{\mathrm{bp}}}{kT}\right) = j_{\mathrm{sc}} \tag{2.22}$$

where $m_h^*$ is the effective hole mass in the semiconductor, $\phi_{\mathrm{b},p}$ is the barrier height for holes (the difference between Fermi level and the top of the valence band $\phi_{\mathrm{bp}} = E_{\mathrm{V}} - E_{\mathrm{Fp}}$), and $j_{\mathrm{sc}}$ is the short-circuit current (defined as the photocurrent at zero voltage).

The total current of a metal-insulator semiconductor junction under illumination is therefore given by:

$$\begin{aligned} j &= j_p - j_n \\ &= j_{\mathrm{sc}} + j_{\mathrm{gen}} - j_{\mathrm{TE}} - j_{\mathrm{rec}} \\ &= j_{\mathrm{sc}} - j_{\mathrm{TE},0}\left[\exp\left(\frac{qV}{kT}\right) - 1\right] + j_{\mathrm{gen/rec},0}\left[\exp\left(\frac{qV}{2kT}\right) - 1\right] \end{aligned} \tag{2.23}$$

Under open-circuit condition, there is no net current flow through the junction, and therefore, the photovoltage can be obtained by setting the total current to zero. For large voltages such as the open-circuit voltage ($V_{\mathrm{oc}}$), the current due to generation and recombination is very small in comparison with the other current transport mechanisms in Eq. 2.23. Neglecting ($j_{\mathrm{gen/rec}}$), $V_{\mathrm{oc}}$ is then given by the following expression:

$$\begin{aligned} V_{\mathrm{oc}} &= \frac{kT}{q}\ln\left(\frac{j_{\mathrm{sc}}}{j_{\mathrm{TE},0}} + 1\right) \approx \frac{kT}{q}\ln\left(\frac{j_{\mathrm{sc}}}{j_{\mathrm{TE},0}}\right) \\ &= \frac{kT}{q}\left[\ln\left(\frac{j_{\mathrm{sc}}}{A^* T^2}\right) + \frac{q\phi_{\mathrm{b}}}{kT}\right] \end{aligned} \tag{2.24}$$

Note that the Eq. 2.14, 2.16 and 2.23 have assumed that the thermionic emission current flows through an ideal diode in which the current is limited by the recombination of minority carriers, and therefore the ideality factor ($n$) is 1. If other recombination processes occur, the Boltzmann's factor should be corrected to $\exp(qV/nkT)$, and $n$ value will deviate from unity. The theoretical expression for $V_{\mathrm{oc}}$ should then also be corrected for the non-ideal diode behavior by introducing an ideality factor, as given by:

$$V_{\mathrm{oc}} = \frac{nkT}{q}\left[\ln\left(\frac{j_{\mathrm{sc}}}{A^* T^2}\right) + \frac{q\phi_{\mathrm{b}}}{kT}\right] \tag{2.25}$$

## 2.3. Photoelectrochemical water splitting cells

A photoelectrochemical water splitting cell, in the simplest form, consists of a photoelectrode and a metal counter electrode in an aqueous electrolyte solution. Central to the operation of solar water splitting is the semiconducting electrode (photoelectrode) that absorbs and converts incident photons to electron-hole pairs. Electrons and holes are separated by the electrid field in the space-charge region of the semiconductor and are then used to drive the water splitting reaction. The electrochemical half-reaction that occurs on the semiconductor surface depends on the doping characteristic of the semiconductor. For a photoelectrochemical system involving an n-type semiconducting light-absorber (*i.e.*, a photoanode), the photogenerated holes ($h^+$) are transported to the semiconductor-electrolyte interface where water ($H_2O$) is oxidized to oxygen ($O_2$), and the photogenerated electrons ($e^-$) are transported via an external circuit to the metal cathode where water is reduced to hydrogen ($H_2$), as illustrated in Fig. 2.9. The n-type semiconductor is commonly used as a photoanode because the electric field that is formed by equilibration of the Fermi level with the redox couple in the solution gives rise to a band bending that allows photogenerated minority carriers (holes) to move into the solution and oxidize water, and repels the majority carrier (electrons) so that they move in the opposite direction to the counter electrode and reduce water. A solar water splitting cell utilizing a p-type semiconducting electrode behaves in an analogous manner, except that electrons are the minority carriers and holes are the majority carriers, and thus water is reduced on the semiconductor surface and is oxidized at the counter metal electrode.

At standard temperature (298 K), under atmospheric pressure condition (1 bar) and at standard concentration (1 mol $L^{-1}$), the change of Gibbs free energy required to split a $H_2O$ molecule to one $H_2$ and 1/2 $O_2$ equals to $\Delta G = 237.2$ kJ $mol^{-1}$, or equivalent to an electrochemical cell voltage of $\Delta E^0 = 1.23$ eV. For an alkaline elec-

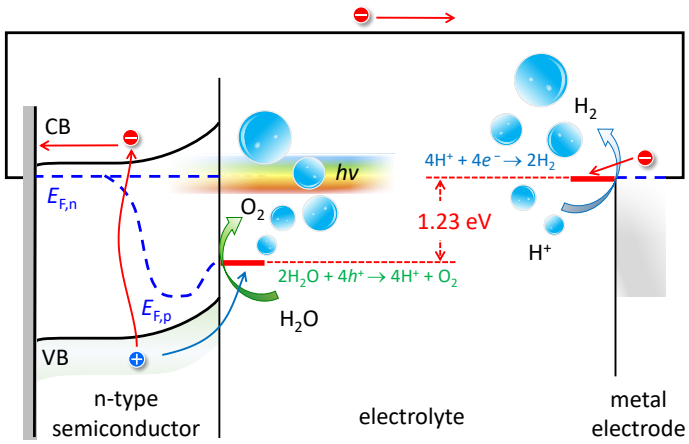



**Figure 2.9:** Schematic of photoelectrochemical water splitting cells under illumination consisting of an n-type semiconductor and a metal counter electrode in an electrolyte solution.

trolyte, the water reduction and oxidation processes occurring in an electrochemical water splitting cell are given by the following reactions:

$$4H_2O + 4e^- \rightleftharpoons 2H_2 + 4OH^- \qquad E^0_{red} = -0.828 \text{ V } \textit{vs.} \text{ NHE} \tag{2.26a}$$

$$4OH^- + 4h^+ \rightleftharpoons 2H_2O + O_2 \qquad E^0_{ox} = -0.401 \text{ V } \textit{vs.} \text{ NHE} \tag{2.26b}$$

where NHE is the normal hydrogen electrode reference in a three-electrode electrochemical configuration. For an acidic electrolyte, the expressions for water reduction and oxidation (redox) reactions are modified to the following:

$$4H^+ + 4e^- \rightleftharpoons 2H_2 \qquad E^0_{red} = 0.000 \text{ V } \textit{vs.} \text{ NHE} \tag{2.27a}$$

$$2H_2O + 4h^+ \rightleftharpoons 4H^+ + O_2 \qquad E^0_{ox} = -1.229 \text{ V } \textit{vs.} \text{ NHE} \tag{2.27b}$$

The overall water splitting reaction can therefore be written as the following:

$$H_2O \xrightarrow{\text{sunlight}} 2H_2 + O_2 \qquad \Delta E^0_{redox} = 1.23 \text{ V} \tag{2.28}$$

To effectively split water, the semiconductor should be able to absorb light with energies greater than 1.23 eV. Ideally, a photoelectrochemical cell can spontaneously drive the water splitting reaction if the semiconductor component has a sufficiently large energy gap and having conduction band and valence band edges straddle the electrochemical potentials of hydrogen evolution $E^0$ ($H^+/H_2$) and oxygen evolution $E^0$ ($O_2/H_2O$). The minimum requirement for the semiconductor band gap is determined by the thermodynamic potential needed to split water (1.23 eV) plus the free energy losses in the semiconductor (0.4–0.6 eV)[17] and the kinetic overpotentials for charge-transfer to drive the catalytic reactions of water oxidation and water reduction. As a result, the energy demand for solar water splitting at the semiconductor electrode is between 1.6–2.4 eV per electron-hole pair generated.[18]

## 2.4. Solar energy conversion efficiencies

The solar-to-hydrogen (STH) efficiency is an important measure for evaluating the performance of a photoelectrochemical system. Under solar irradiation, the STH efficiency of a photoelectrochemical water splitting cell is defined by the amount of evolved hydrogen gas divided by the solar energy input. Quantification of the amount of the hydrogen gas can be done by mass spectroscopy or gas chromatography[19], or by following water displacement in inverted burette.[20] The calculation of STH efficiency ($\eta_{STH}$) for this method is given by:

$$\eta_{STH} = \frac{\Phi_{H_2} G^0_{f,H_2}}{P_{light}} \tag{2.29}$$

where $\Phi_{H_2}$ is the rate of hydrogen evolution at illuminated area (mol $s^{-1}$ $m^{-2}$), $G^0_{f,H_2}$ is the Gibbs free energy for hydrogen formation (237 kJ $mol^{-1}$), and $P_{light}$ is the

power density of the illumination (100 mW $cm^{-2}$). For a reliable measurement, the products of water splitting reactions should be stoichiometric ($H_2$:$O_2$ = 2:1), with no other reaction due to sacrificial donor or acceptor,[19] and the light intensity and spectral distribution should match the standard AM1.5 G spectrum.[21]

Alternatively, the efficiency of a photoelectrochemical cell can be calculated by measuring the output current density under irradiation ($j_{photo}$) in a two-electrode configuration. Assuming all photogenerated electrons and holes are used to drive the water splitting reactions, no corrosion reaction at the photoelectrode and the metal counter electrode, and a Faradaic efficiency of unity, the STH efficiency of a solar water splitting cell is equal to the ratio of the electrical power output ($P_{electrical}$) and the input power from the illumination ($P_{light}$), as given by:

$$\eta_{STH} = \frac{P_{electrical}}{P_{light}} = \frac{j_{photo} V_{redox}}{P_{light}} \tag{2.30}$$

At standard condition, $V_{redox}$ is 1.23 V, and is equivalent to the change of Gibbs free energy energy for water splitting at 237 kJ $mol^{-1}$. In the presence of applied bias ($V_{app}$), in an illuminated three-electrode cell, the STH efficiency is obtained by modifying Eq. 2.30 to the following:

$$\eta_{STH} = \frac{j_{photo}\left(1.23\ \text{V} - V_{app}\right)}{P_{light}} \tag{2.31}$$

The solar energy conversion efficiency of an individual photoelectrode can be calculated from the current-voltage ($j$–$V$) measurement using a potentiostat in a three-electrode cell under illumination. The characterization of photoelectrode performance involves parameters analogous to those of solid-state photovoltaic cells, such as the short-circuit current density ($j_{sc}$) and the open-circuit voltage ($V_{oc}$), only they are referenced to the equilibrium potential of the half-reaction performed by the corresponding photoelectrode (*i.e.*, $E^0(H^+/H_2)$ for a photocathode or $E^0(O_2/H_2O)$ for a photoanode).[23] For a semiconductor-liquid junction electrode cell, $j_{sc}$ is referred to as the photocurrent density at $E^0$ ($A/A^-$) (denoted as $j_{E^0\ (A/A^-)}$, where $E^0$ ($A/A^-$) is the Nernstian potential of the half-reaction of interest), and $V_{oc}$ is referred to as the difference between the potential of the photocurrent onset ($V_{onset}$) and $E^0$ ($A/A^-$).

The efficiency of the photoelectrochemical half-cell can then be calculated by the following relationship:

$$\eta = \frac{P_{max}}{P_{light}} = \frac{j_{mp} V_{mp}}{P_{light}} \tag{2.32}$$

where $P_{max}$ is the maximum power, $j_{mp}$ and $V_{mp}$ are the photocurrent and the voltage at the maximum power point, respectively and *ff* is the fill factor. The *ff* is defined as the "squareness" of the $j$–$V$ curve which equals to the ratio between the maximum power output divided by the product of the short-circuit current density and the open-circuit voltage. For solar water splitting cells, the characteristic of *ff* is closely related to the bulk recombination of the semiconductor, surface recombination of electrons or holes, and the series resistance of the solution.

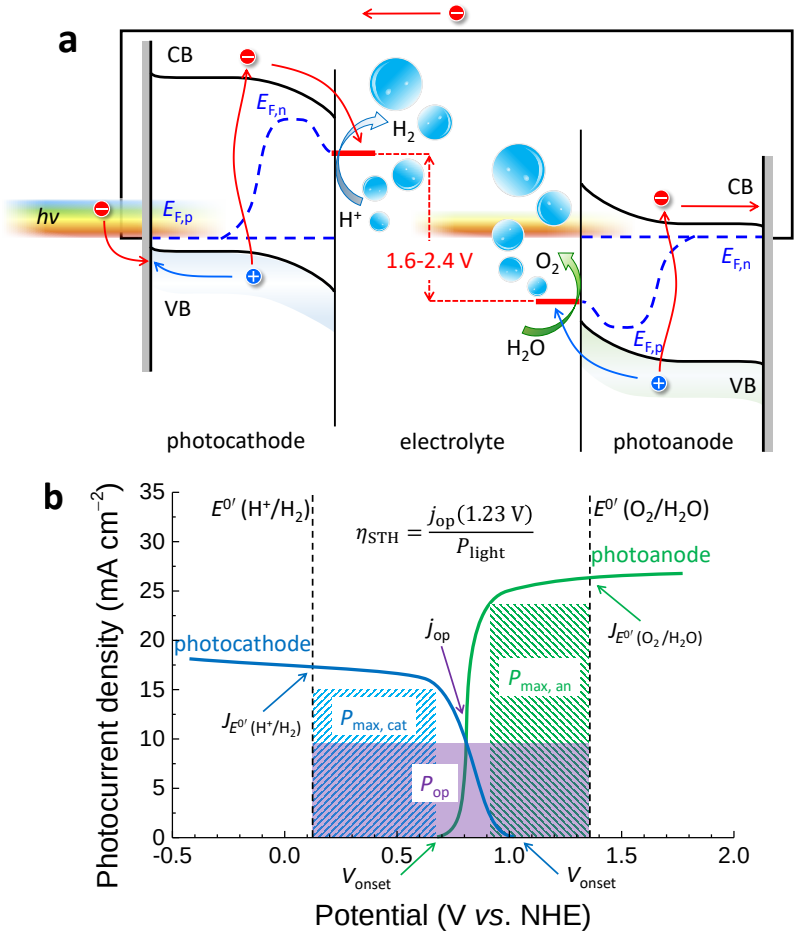



**Figure 2.10:** (a) Representative energy band diagram a dual photoelectrode system consisting of a photocathode and a photoanode, illuminated side-by-side. (b) Current density-voltage ($j$–$V$) characteristics of an illuminated dual photoelectrode cell, adapted from Ref. 22. The maximum power of the photocathode is denoted as $P_{max,\ cat}$ and the maximum power of the photoanode is denoted as $P_{max,\ an}$. The overall system efficiency is given by the product of the operating photocurrent density ($j_{op}$) and 1.23 V divided by the input power from the illumination ($P_{light}$).

It should be emphasized that the individual photoelectrode efficiency represents only half of the water splitting reaction and does not reflect the overall STH efficiency. The utility of single half-cell calculation is that the photoelectrode materials can be evaluated independently for optimization of a tandem structure that uses multiple band gap absorbers in a Z-scheme water splitting system.[24] A Z-scheme system is a device architecture in which a photoanode and a photocathode are arranged in a side-by-side configuration, optically and electrically connected in series, independently performing water oxidation and water reduction reactions, respectively (Fig. 2.10a). Such a system requires at least two photoabsorbers with spectrally matched band gaps (one photoelectrode should have a smaller or larger band gap than the other) for maximum spectral utilization and optimum photocurrent generation. The operating photocurrent of a complete cell can be estimated from the intersection of the overlapping $j$–$V$ curves of the photoelectrodes (Fig. 2.10b). The efficiency of a tandem system reaches maximum if the two curves intersect near the maximum power point of a photoelectrode, *i.e.,* $P_{\text{max, an}}$ for the photoanode, or $P_{\text{max, cat}}$ for the photocathode. The series electrical connection of two photoelectrodes will increase the photovoltage of the overall system, and thus, a dual photoelectrode cell is expected to produce a sufficiently large photovoltage to satisfy the necessary potential requirement to split water and to overcome the overpotential losses associated with the thermodynamic limits of the semiconductor and the kinetic limits of the surface reaction.

## 2.5. Materials for photoelectrodes

The main component of a photoelectrochemical water splitting cell is the semiconducting electrode that absorbs and converts light into energetic charge carriers which are then used to split water to hydrogen and oxygen. In order to efficiently drive the water splitting reaction, the semiconductor should meet the following requirements:

- strong light absorption in a broad spectrum,
- band edges position that straddle the water reduction and oxidation potentials,
- efficient charge transport in the semiconductor,
- fast surface reaction kinetics,
- high electrochemical stability.

The spectral region in which the semiconductor absorbs light is determined by the band gap. Only light with energies greater than the band gap of the semiconductor will be absorbed and converted to photogenerated charge carriers. The energy of light with a particular wavelength ($\lambda$) or photon ($E_{\text{photon}}$) is given by:

$$E_{\text{photon}} = \frac{hc}{\lambda} \tag{2.33}$$

where $h$ is the Planck's constant ($6.626 \times 10^{-34}$ J s) and $c$ is the speed of light ($2.99 \times 10^{8}$ m s$^{-1}$). In electron-volt (eV) unit, the term $hc$ can be rewritten as $hc/q$, where $q$ is the elementary charge ($1.6 \times 10^{-19}$ J). Therefore, the product of $hc$ is equal to $1.24 \times 10^{-6}$ eV m, or 1240 eV nm. The absorption edge of a semiconductor

($\lambda_{\text{abs. edge}}$) in the solar spectrum is given by the wavelength at which the energy of photon equals the band gap ($E_g$) of the semiconductor, as expressed by:

$$\lambda_{\text{abs. edge}}\ (\text{nm}) = \frac{1240\ (\text{eV nm})}{E_g\ (\text{eV})} \tag{2.34}$$

The absorption edge, hence the band gap of the semiconductor determines the maximum number of photon that can be absorbed and converted to usable electrical current. The light-generated current per wavelength ($I(\lambda)$) produced by a semiconductor is given by the following relation:

$$\begin{aligned} I(\lambda) &= qE(\lambda)\frac{\lambda}{hc} \\ &= qN_{\text{photon}}(\lambda) \end{aligned} \tag{2.35}$$

where $E(\lambda)$ is the spectral irradiance and $N_{\text{photon}}(\lambda)$ is the spectral photon flux. Assuming all photons in the absorption spectrum are absorbed and contribute to current generation, the maximum photocurrent density ($j$) generated by a semiconductor is given by the integration of the spectral current over the absorption spectrum:

$$j = \int I(\lambda)\mathrm{d}\lambda \tag{2.36}$$

Figure 2.11a shows the photon flux of solar spectrum (AM1.5G) and the maximum photocurrent density generated by the semiconductors.

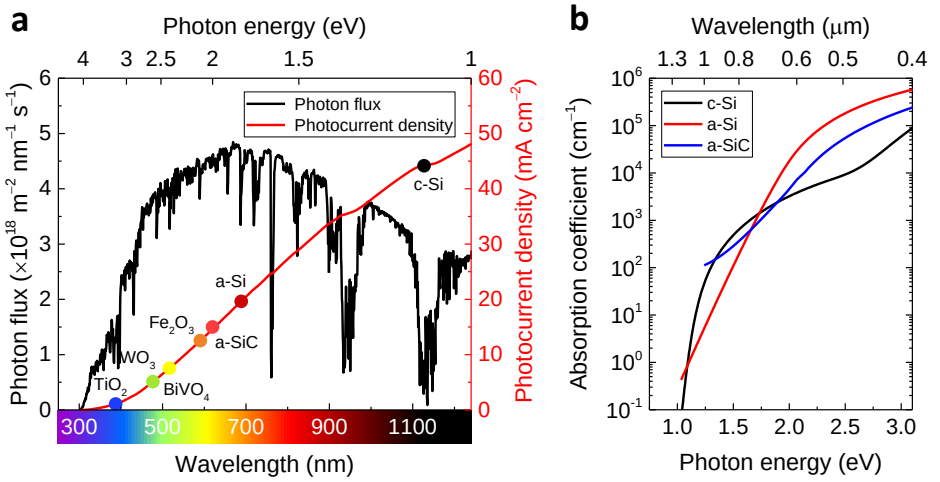



**Figure 2.11:** (a) Spectral photon flux of AM1.5G spectrum and maximum photocurrent densities generated by the semiconductors: titanium oxide ($TiO_2$), tungsten oxide ($WO_3$), bismuth vanadate ($BiVO_4$), iron oxide ($Fe_2O_3$), amorphous silicon carbide (a-SiC), amorphous silicon (a-Si) and crystalline silicon (c-Si). (b) Absorption coefficient of c-Si, a-Si and a-SiC as a function photon energy.

In addition to the ability to absorb light in a wide spectral range, the semiconductor should have a strong light absorption. The optical property of a semiconductor is usually characterized by the absorption coefficient. Figure 2.11b depicts that the absorption coefficient of amorphous silicon (a-Si) is 100 times larger than that of crystalline silicon (c-Si) in the visible part of the spectrum. This implies the a-Si requires 100 times less thickness than the c-Si does in order to absorb the same amount of photon in the same spectrum. The higher absorption coefficient of a-Si is related to the localized defect states within the a-Si that arise from the disorder of atomic structure and behaves like a direct band gap semiconductor. The high absorption coefficient is an important characteristic that distinguishes direct band gap semiconductors from the indirect ones, which can lead to important savings in both materials and energy for device manufacturing.

The electrical property of a material is often characterized by its conductivity. For a semiconductor, the electrical conductivity is an important measure that determines the electronic charge transport. A low photogenerated current may originate from the narrow band gap or the weak optical absorption of the semiconductor, but it may also be due to the recombination of photogenerated electron-hole pairs as a result of the poor conductivity. The semiconductor conductivity is proportional to the product of carrier concentration and mobility:

$$\sigma = qn\mu_e + qp\mu_h \tag{2.37}$$

where $q$ is the elementary charge, $n$ is the electron concentration, $p$ is the hole concentration, $\mu_e$ is the electron mobility and $\mu_h$ is the hole mobility.

Charge transport mechanism via band transport such as in crystalline silicon (Si) and gallium arsenide (GaAs) typically leads to a higher effective carrier mobility than that via low-mobility extended state conduction by traps such as in amorphous silicon (a-Si), or by carrier hopping between metals such as in metal oxide semiconductors. Table 2.1 lists the charge carrier mobility and lifetime of selected semiconductors.

**Table 2.1:** Charge carrier mobilities and lifetimes of selected semiconductors.

| Material | Mobility ($cm^2\ V^{-1}\ s^{-1}$) | | Carrier lifetime (s) | References |
|---|---|---|---|---|
| | electron | hole | | |
| $TiO_2$ (anatase) | | 0.1–0.3 | 20–80 ns | [25–28] |
| $WO_3$ | 10 | | 1–9 ns | [29,30] |
| $BiVO_4$ | 0.044 | | 40 ns | [31] |
| $\alpha$-$Fe_2O_3$ | 0.1 | 0.2 | 3 ps | [32,33] |
| a-Si | 10–20 | 1–5 | 5–10 ns | [34] |
| c-Si | 1450 | 500 | 1 ms | [10] |
| GaAs | 8000 | 400 | 10 ns | [10] |

Extrinsic factors such as recombination centers due to impurity atoms or lattice defects often play a vital role in the electronic transport in a semiconductor. The average time for an excess minority carrier to recombine with the majority carrier

in the lattice is expressed by the lifetime ($\tau$), which is related to the minority-carrier diffusion length ($L_D$):

$$L_D = \sqrt{D\tau} \tag{2.38}$$

where diffusivity ($D$) is related to the minority carrier mobility ($\mu_h$ for n-type semiconductors or $\mu_e$ for p-type semiconductors) through the Einstein equation:

$$D = \mu \frac{kT}{q} \tag{2.39}$$

The semiconductor electrode should facilitate sufficiently fast charge transfer at the semiconductor-electrolyte interface to prevent carrier accumulation and surface recombination. Most semiconductor surfaces are not catalytically active for water oxidation (oxygen evolution reaction, OER) or water reduction (hydrogen evolution reaction, HER). However, the charge transfer kinetics can be improved by adding catalytically active species, or catalysts on the semiconductor surface. Efficient catalysts for water splitting often involve precious metals such as iridium oxide ($IrO_x$) and ruthenium oxide ($RuO_x$) for OER, and platinum for HER. Nickel- and cobalt-based compounds, however have proven to be non-noble metal-based alternatives that exhibit comparable catalytic activity and chemical stability for both OER and HER (Fig. 2.12).

In general, the role of catalyst on a semiconductor surface is to lower the overpotential to drive the reaction by facilitating fast charge transfer at the solid-liquid interface, of which the effect is usually manifested by the substantial shift of photocurrent onset potential in the illuminated current-potential curve. It has been found recently that the true nature of how the catalyst improves the photoelectrochemical performance of a photoelectrode is not only by enhancing the kinetics of surface reaction but also by reducing the rate of surface recombination, in a similar manner to the passivation effect on semiconductor surfaces or interfaces.[36,37] The contributions of improved charge transfer and reduced carrier recombination vary

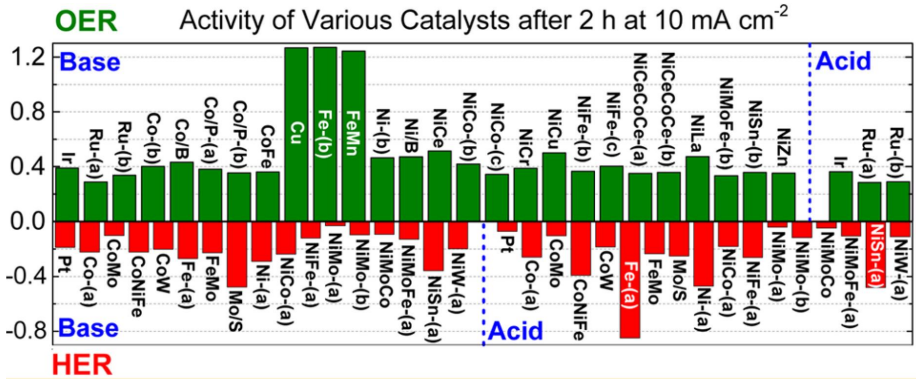



**Figure 2.12:** Oxygen evolution reaction (OER) and hydrogen evolution reaction (HER) electrocatalyst and their overpotentials to achieve a current density of 10 mA $cm^{-2}$.[35]

depending on the complex interaction at the semiconductor-catalyst interface. For example, metallic silver (Ag) on the gallium nitride (GaN) photocathode surface can reduce the same rate of surface recombination as when Pt is used, but the photocurrent onset potential of the GaN with Pt remains superior than that with Ag.[36] This implies that Pt facilitates better charge transfer kinetics than Ag does, and therefore in such a structure, Pt behaves both as a catalyst and a surface passivation layer. In contrast, nickel iron oxide ($NiFeO_x$) which is known as a water oxidation catalyst merely serves as a passivation layer on an iron oxide ($Fe_2O_3$) photoanode that reduces the rate of surface recombination without increasing the rate of charge transfer at the liquid interface.[37]

Having conduction band and valence band edges that straddle the water reduction and oxidation potentials is particularly important for semiconductor-liquid junction photoelectrodes whose energetics strongly depend on the interplay between the semiconductor and the electrolyte. This requirement entails the semiconductor band gap to be at least equal to the water redox potential (1.23 eV) so that photogenerated electrons and holes have sufficient driving force to drive the overall water splitting reaction. In practice, the minimum band gap is also determined by the energy required to overcome the thermodynamic losses in the semiconductor and the kinetic losses to enable sufficiently fast reaction at various points in the electro-

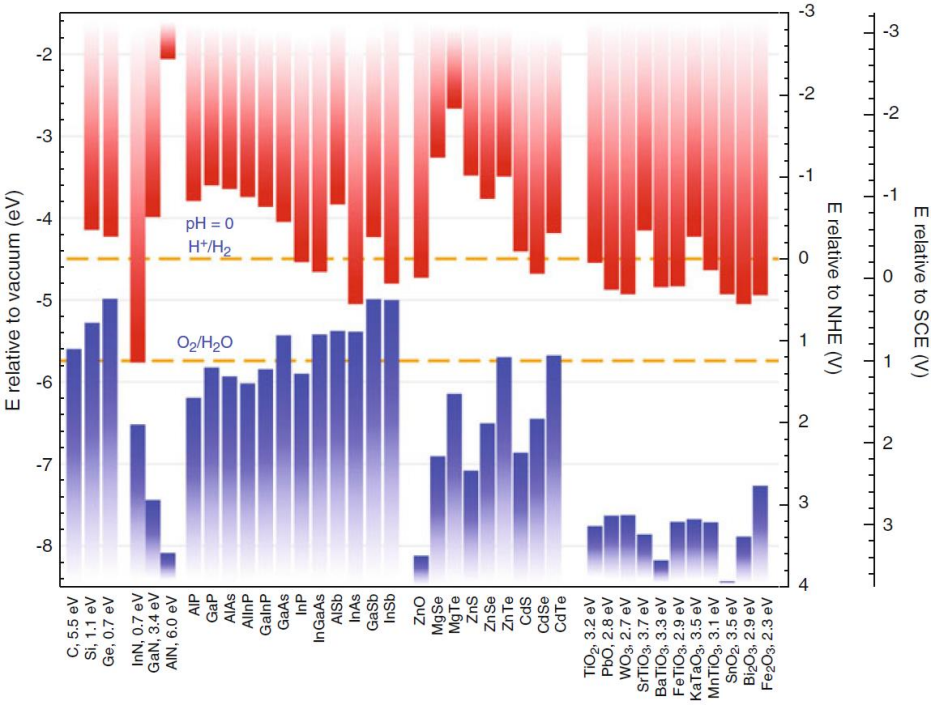



**Figure 2.13:** Band edges position of selected semiconductors at pH 14 with respect to water oxidation and reduction potentials as well as some other redox potentials, reproduced from Ref. 38.[39–41]

chemical system (0.4–0.6 eV). As a result, the band gap of the semiconductor should ideally be in the range between 1.6 and 2.4 eV. Figure 2.13 shows that the band edge positions of some metal oxides and large gap semiconductors favor both the water reduction and oxidation potentials. However, the band gaps of these materials are mostly greater than 3 eV, which can limit their ability to produce high photocurrent. Non-oxide semiconductors such as Si, Ge and some of III-V compounds have excellent electronic and optical properties for high photocurrent generation but their band gaps are too small to produce sufficient photovoltage for spontaneous overall water splitting reaction. The limited selection of materials with suitable band gaps and appropriate band edge positions motivates the use of multiple semiconductors with different energy gaps, as described previously in section 2.4.

The chemical stability of the semiconductor in an aqueous solution under photoelectrocatalytic conditions is critical to ensure a long operation of water splitting reaction. Many semiconductors either dissolve in the electrolyte or oxidize, forming a surface oxide layer that prevents electronic charge transfer across the semiconductor-liquid interface. Because of the nature of the oxide compound, most metal oxide semiconductors are stable under photoanodic conditions, but are prone to cathodic decomposition or photo-induced corrosion. Under irradiation, the photoelectrochemical stability of a semiconductor depends on the alignment of material reduction or oxidation potential with respect to the water reduction or oxidation potential, respectively.[42] For example, an n-type semiconductor photoanode is photoelectrochemically stable if the material oxidation potential $\phi^{ox}$ is below the water oxidation potential ($E^0$ ($O_2/H_2O$)) or the valence band minimum (Fig. 2.14a). Likewise, a p-type semiconductor photocathode is stable under illumination if the material reduction potential $\phi^{re}$ lies above the water reduction potential ($E^0$ ($H^+/H_2$)) or the conduction band minimum (Fig. 2.14b). Figure 2.15 shows $\phi^{ox}$ and $\phi^{re}$ relative to the normal hydrogen electrode (NHE) and vacuum level of a series of semiconductors

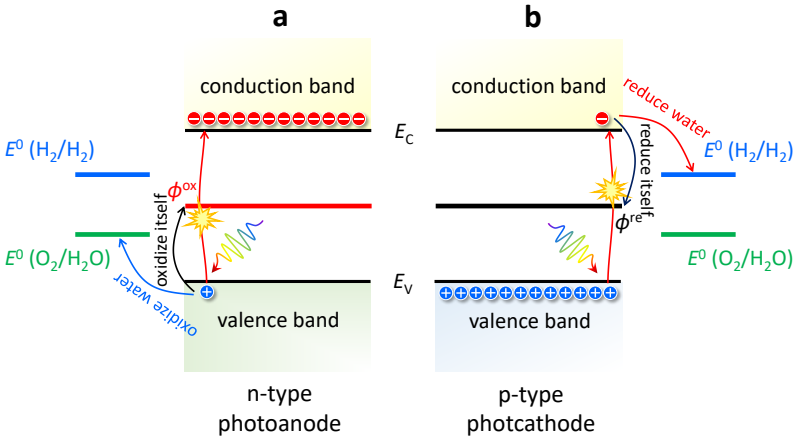



**Figure 2.14:** Band alignment of (a) n-type photoanode with respect to water redox potentials and material oxidation potential ($\phi^{ox}$) and (b) p-type photoanode with respect to water redox potentials and material reduction potential ($\phi^{re}$), adapted from Ref. 42.

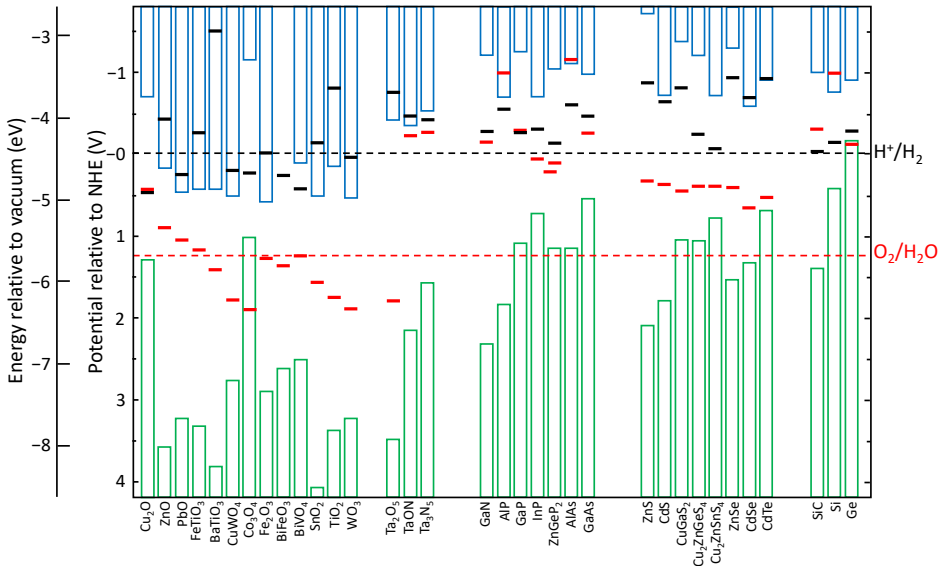



**Figure 2.15:** Calculated oxidation potential ($\phi^{ox}$, red bars) and reduction potential ($\phi^{re}$, black bars) relative to the normal hydrogen electrode (NHE) and vacuum level of selected semiconductors in a solution at pH 0, at ambient temperature (298.15 K) and pressure (1 bar).[42]

in a solution at pH 0.

## References


[1] E. Vella, F. Messina, M. Cannas, and R. Boscaino, *Unraveling exciton dynamics in amorphous silicon dioxide: Interpretation of the optical features from 8 to 11 ev,* Inorganic Chemistry **44**, 6900 (2005).

[2] K. Rajeshwar, *Encyclopedia of Electrochemistry,* (Wiley-VCH Verlag GmbH & Co. KGaA, 2007) Chap. Fundamentals of Semiconductor Electrochemistry and Photoelectrochemistry.

[3] W. Schottky, *Halbleitertheorie der Sperrschicht,* Naturwissenschaften **26**, 843 (1938).

[4] N. F. Mott, *Note on the contact between a metal and an insulator or semiconductor,* Proceedings of the Cambridge Philosophical Society **34**, 568 (1938).

[5] J. Bardeen, *Surface States and Rectification at a Metal Semi-Conductor Contact,* Physical Review **71**, 717 (1947).

[6] A. M. Cowley and S. M. Sze, *Surface States and Barrier Height of Metal-Semiconductor Systems,* Journal of Applied Physics **36**, 3212 (1965).

[7] V. Heine, *Theory of Surface States,* Physical Review **138**, A1689 (1965).

[8] S. G. Louie and M. L. Cohen, *Electronic structure of a metal-semiconductor interface,* Physical Review B **13**, 2461 (1976).

[9] E. H. Rhoderick, *Metal-semiconductor contacts,* IEE Proceedings I - Solid-State and Electron Devices **129**, 1 (1982).

[10] S. M. Sze and K. K. Ng, *Physics of Semiconductor Devices* (Wiley, 2007).

[11] H. A. Bethe, *Theory of the boundary layers of crystal rectifiers* (Radiation Laboratory, Massachusetts Institute of Technology, 1942).

[12] D. L. Scharfetter, *Minority carrier injection and charge storage in epitaxial Schottky barrier diodes,* Solid-State Electronics **8**, 299 (1965).

[13] A. Y. C. Yu and E. H. Snow, *Minority carrier injection of metal-silicon contacts,* Solid-State Electronics **12**, 155 (1969).

[14] C.-T. Sah, R. Noyce, and W. Shockley, *Carrier generation and recombination in p-n junctions and p-n junction characteristics,* Proceedings of the IRE **45**, 1228 (1957).

[15] W. Shockley and W. T. Read, *Statistics of the Recombination of Holes and Electrons,* Physical Review **87**, 835 (1952).

[16] R. N. Hall, *Electron-Hole Recombination in Germanium,* Physical Review **87**, 387 (1952).

[17] L. C. Seitz, Z. Chen, A. J. Forman, B. A. Pinaud, J. D. Benck, and T. F. Jaramillo, *Modeling practical performance limits of photoelectrochemical water splitting based on the current state of materials research,* ChemSusChem **7**, 1372 (2014).

[18] J. R. Bolton, S. J. Strickler, and J. S. Connolly, *Limiting and realizable efficiencies of solar photolysis of water,* Nature **316**, 495 (1985).

[19] A. Kudo and Y. Miseki, *Heterogeneous photocatalyst materials for water splitting,* Chemical Society Reviews **38**, 253 (2009).

[20] R. van de Krol and M. Grätzel, *Photoelectrochemical Hydrogen Production*, edited by R. van de Krol and M. Grätzel, Electronic Materials: Science & Technology, Vol. 102 (Springer US, Boston, MA, 2012).

[21] American Society for Testing and Materials (ASTM), *Reference Solar Spectral Irradiance: Air Mass 1.5G173-03,* (http://rredc.nrel.gov/solar/spectra/am1.5).

[22] M. G. Walter, E. L. Warren, J. R. McKone, S. W. Boettcher, Q. Mi, E. A. Santori, and N. S. Lewis, *Solar water splitting cells,* Chemical Reviews **110**, 6446 (2010).

[23] R. H. Coridan, A. C. Nielander, S. A. Francis, M. T. McDowell, V. Dix, S. M. Chatman, and N. S. Lewis, *Methods for comparing the performance of energy-conversion systems for use in solar fuels and solar electricity generation,* Energy & Environmental Science **8**, 2886 (2015).

[24] M. Grätzel, *Photoelectrochemical cells,* Nature **414**, 338 (2001).

[25] P. Odier, J. D. Baumard, D. Panis, and A. M. Anthony, *Thermal emission, electrical conductivity, and hall effect for defects study at high temperature ($T \geqslant 1250$ K) in refractory oxides ($Y_2O_3$, $TiO_2$),* Journal of Solid State Chemistry **12**, 324 (1975).

[26] T. Bak, M. K. Nowotny, L. R. Sheppard, and J. Nowotny, *Mobility of Electronic Charge Carriers in Titanium Dioxide,* Journal of Physical Chemistry C **112**, 12981 (2008).

[27] N. A. Deskins and M. Dupuis, *Intrinsic Hole Migration Rates in $TiO_2$ from Density Functional Theory,* Journal of Physical Chemistry C **113**, 346 (2009).

[28] K. Ozawa, M. Emori, S. Yamamoto, R. Yukawa, S. Yamamoto, R. Hobara, K. Fujikawa, H. Sakama, and I. Matsuda, *Electron–hole recombination time at $TiO_2$ single-crystal surfaces: Influence of surface band bending,* The Journal of Physical Chemistry Letters **5**, 1953 (2014).

[29] J. M. Berak and M. J. Sienko, *Effect of oxygen-deficiency on electrical transport properties of tungsten trioxide crystals,* Journal of Solid State Chemistry **2**, 109 (1970).

[30] M. A. Butler, *Photoelectrolysis and physical properties of the semiconducting electrode $WO_3$ ,* Journal of Applied Physics **48**, 1914 (1977).

[31] F. F. Abdi, T. J. Savenije, M. M. May, B. Dam, and R. van de Krol, *The Origin of Slow Carrier Transport in $BiVO_4$ Thin Film Photoanodes: A Time-Resolved Microwave Conductivity Study,* The Journal of Physical Chemistry Letters **4**, 2752 (2013).

[32] A. J. Bosman and H. J. van Daal, *Small-polaron versus band conduction in some transition-metal oxides,* Advance in Physics **19**, 1 (1970).

[33] A. G. Joly, J. R. Williams, S. A. Chambers, G. Xiang, and W. P. Hess, *Carrier dynamics in $\alpha$-$Fe_2O_3$ (0001) thin films and single crystals probed by femtosecond transient absorption and reflectivity,* Journal of Applied Physics **99**, 053521 (2006).

[34] M. Zeman, *Advanced Amorphous Silicon Solar Cell Technologies,* in *Thin Film Solar Cells Fabrication, Characterization and Applications*, edited by J. Poortmans and V. Arkhipov (John Wiley & Sons, Ltd, Chichester, 2006) Chap. Advanced A, pp. 173–236.

[35] C. C. L. McCrory, S. Jung, I. M. Ferrer, S. M. Chatman, J. C. Peters, and T. F. Jaramillo, *Benchmarking Hydrogen Evolving Reaction and Oxygen Evolving Reaction Electrocatalysts for Solar Water Splitting Devices,* Journal of the American Chemical Society **137**, 4347 (2015).

[36] J. E. Thorne, Y. Zhao, D. He, S. Fan, S. Vanka, Z. Mi, and D. Wang, *Understanding the role of co-catalysts on silicon photocathodes using intensity modulated photocurrent spectroscopy,* Physical Chemistry Chemical Physics **19**, 29653 (2017).

[37] J. E. Thorne, J.-W. Jang, E. Y. Liu, and D. Wang, *Understanding the origin of photoelectrode performance enhancement by probing surface kinetics,* Chemical Science **7**, 3347 (2016).

[38] J. W. Ager, *Lecture Notes in Energy 32,* in *Solar to Chemical Energy Conversion*, edited by M. Sugiyama, K. Fujii, and S. Nakamura (Springer International Publishing Switzerland, 2016) Chap. Photoelectrochemical Approach for Water Splitting, pp. 249–260.

[39] W. Walukiewicz, *Intrinsic limitations to the doping of wide-gap semiconductors,* Physica B: Condensed Matter **302–303**, 123 (2001).

[40] C. G. Van de Walle and J. Neugebauer, *Universal alignment of hydrogen levels in semiconductors, insulators and solutions,* Nature **423**, 626 (2003).

[41] T. Bak, J. Nowotny, M. Rekas, and C. Sorrell, *Photo-electrochemical hydrogen generation from water using solar energy,* International Journal of Hydrogen Energy **27**, 991 (2002).

[42] S. Chen and L.-W. Wang, *Thermodynamic oxidation and reduction potentials of photocatalytic semiconductors in aqueous solution,* Chemistry of Materials **24**, 3659 (2012).

# 3

# Interfacial engineering of metal-insulator-semiconductor junctions for efficient and stable photoelectrochemical water oxidation

Solar-assisted water splitting can potentially provide an efficient route for large-scale renewable energy conversion and storage. It is essential for such a system to provide a sufficiently high photocurrent and photovoltage to drive the water oxidation reaction. Here we demonstrate a photoanode that is capable of achieving a high photovoltage by engineering the interfacial energetics at the metal-insulator-semiconductor interfaces. We evaluate the importance of using a bimetal thin-film structure to separate its function as a Schottky contact from its function as a protective and catalytic overlayer. We also illustrate the improvement of the photovoltage upon incidental oxidation of the metal surface layer in an alkaline electrolyte. Additionally, we analyze the role of interfacial insulating layers on the alleviation of Fermi level pinning and the resulting photovoltage. Finally, we report the advantage of using a thin bilayer metal structure as a simple protection route for metal-insulator-semiconductor photoanodes by showing over 200 hours of operational stability.

Parts of this chapter have been published in I. A. Digdaya, G. W. P. Adhyaksa, Bartek J. Trześniewski, E. C. Garnett and W. A. Smith, *Nature Communications*, 2017, **8**, 15968. [1]

## 3.1. Introduction

Photoelectrochemical (PEC) water splitting has been envisioned as a sustainable approach to produce clean and renewable fuels by the direct conversion of solar to chemical energy.[2–4] One important step during the PEC process is charge separation in the space-charge region that is formed due to the electrostatic potential difference across a semiconductor junction.[5] A buried semiconductor junction can be established by variations in doping (homojunction), offsets in the conduction and the valence bands (heterojunction), or by differences in Fermi level at a metal-semiconductor interface (Schottky junction).[6–11] When an n-type semiconductor is brought into contact with a high workfunction metal, the electron Fermi-level falls close to the valence band at the interface and creates a potential barrier that repels the majority carriers and selectively conducts the minority carriers.[12] The height of the potential barrier determines the built-in voltage and sets an upper limit on the maximum attainable photovoltage of a Schottky junction. Semiconductor surface termination by metal, however, creates electronic states near midgap that tend to pin the Fermi level of the semiconductor, diminishing the barrier height, and thus reducing the achievable photovoltage. This problem can be effectively solved by inserting a thin insulator layer that separates the semiconductor from the metal contact at the interface.[13–15]

Metal-insulator-semiconductor (MIS) junction concepts have attracted considerable attention in photovoltaic (PV) and PEC research because of the simplicity of device fabrication and processing that only requires a metal and a thin passivating tunnel dielectric, as well as the versatility of obtaining the desired barrier height by the wide selection of metals with various workfunctions.[16,17] The major challenge in implementing MIS structures on solar energy conversion devices is that the required metal coverage to form a homogeneous Schottky junction can significantly increase the light reflection, reducing the light absorption in the semiconductor, and therefore decreasing the photocurrent output.[18] Despite this unfavorable architecture, advanced nanoscale-structuring of metal contacts have been successful to partially circumvent the optical problem by allowing light to transmit to the photoabsorber through the contactless surface while still enabling charge collection through nanostructured metal contacts.[19–22]

The key advantage of MIS junction for PEC devices is the fact that metals have a high density of states to facilitate efficient collection and transport of charges. This means that any collected minority carriers can be readily transferred to the electrolyte through the metallic catalyst to drive the electrochemical reaction instead of flowing through the external circuit as in PV cells. This simple route allows the ability to use thin metals (*i.e.*, a few nanometers) as the charge collector as well as the carrier conduction mediator.[23–26] The thin metal contact allows the reaction to occur throughout the whole surface, and thus enabling the photogenerated current from the semiconductor to flow perpendicular to the metal film. Additionally, the complete coverage of the metal film on the semiconductor surface forms a buried junction and allows the Fermi level of the metal to float and adjust with the current density and kinetics of the electrochemical reaction. Furthermore, a thin metal contact allows for a significant light transmission to the absorber, thus enabling a

high generation of photocurrent.

Despite the great advantage of the MIS structure for PEC water splitting electrodes, there remains a major trade-off between the high efficiency and the long-term durability. Therefore, many efforts have concentrated on protecting the photoelectrodes either using stable oxide insertion layers[20,21,23] or corrosion-resistant overlayers.[27–29] Another protection scheme can be achieved by tuning the metallic component of the MIS structure. Nickel (Ni) is an attractive material that has all the functionalities required for MIS photoanodes: high workfunction for high barrier formation and thus high photovoltage generation, high catalytic activity for water oxidation and high chemical stability in strongly alkaline solutions.[30,31] Prior work has shown that a thin Ni film (2 nm) was sufficient to create a Schottky junction with the semiconductor and readily oxidized to nickel oxide ($NiO_x$) in a strongly alkaline solution, forming $Ni/NiO_x$/electrolyte interfaces that increased the effective workfunction of the surface.[28] Such a thin Ni layer, however, was not able to completely protect the underlying absorber in a highly corrosive electrolyte at pH 14. As a result, the MIS photoanode showed a degradation of performance after 24 hours of operation in 1 M KOH electrolyte. On the other hand, it was also found that the device with a thicker Ni (*i.e.*, 5 nm) was able to avoid corrosion in 1 M KOH, but suffered from a low photovoltage due to the low Schottky barrier formed by the n-$Si/SiO_x$/Ni.[28]

Herein we demonstrate an MIS photoanode for water oxidation that yield a high efficiency and a high stability by engineering the interfaces at the MIS contact. Specifically, we introduce a high quality aluminum oxide ($Al_2O_3$) tunnel layer in conjunction with a chemically-grown silicon oxide ($SiO_x$) layer that substantially alleviate the Fermi-level pinning and allow for a high Schottky barrier formation at the MIS junction. Additionally, we use a bilayer metal structure to decouple its function as a Schottky contact from its other function as a water oxidation catalyst. We investigate the role of the bilayer metal structure in the energetics at the MIS interface that is responsible for the high photovoltage of the photoanode. Finally, using a simple yet effective protection strategy, we demonstrate a more than 200-hour operation of an MIS photoanode that shows constant high photocurrents in a strongly alkaline solution.

## 3.2. Experimental details

### Chemicals

All chemicals were used as received: potassium hydroxide pellets (KOH, Alfa Aesar, 85%), hydrogen peroxide ($H_2O_2$, 30% (w/w) in $H_2O$, Sigma-Aldrich), sulfuric acid ($H_2SO_4$, 99.999%, Sigma-Aldrich), hydrofluoric acid (HF, 48%, Sigma-Aldrich), hydrochloric acid (HCl, 37%, Sigma-Aldrich), potassium hexacyanoferrate(II) trihydrate ($K_4Fe(CN)_6.3H_2O$, ≥99%, Sigma-Aldrich), potassium hexacyanoferrate(III) ($K_3Fe(CN)_6$, ≥99%, Sigma-Aldrich). Water with resistivity 18.2 MΩ cm from Milli-Q integral ultrapure water (Merck Millipore).

### Preparation of substrates

Phosphorus-doped (n-type, (100)-oriented, single-side polished, resistivity 0.1–0.3 Ω cm, thickness 525 μm) and degenerately boron-doped ($p^+$-type, (100)-oriented, single-side polished, resistivity <0.005 Ω cm) Si wafers were purchased from Si-Mat. The n-type Si wafers were first cleaned in a piranha solution containing a mixture of $H_2SO_4$ and $H_2O_2$ (3:1 by volume ratio) at 120 °C for 20 min to remove organic contaminants. The n-type Si wafers were then dipped into a buffered HF etchant (2%) for 2 min at room temperature to strip the native oxide on the Si wafer surface. Next, the Si wafers were immersed in a Radio Corporation of America (RCA) Standard Clean-2 (SC-2) solution consisting of $H_2O$, HCl and $H_2O_2$ (5:1:1 by volume ratio) at 75 °C for 10 min to regrow the oxide layer ($SiO_{x,RCA}$). Finally, the Si wafers were rinsed using deionized water and dried using $N_2$ gas. The same procedure was applied on the $p^+$-type Si wafers.

### Atomic-layer deposition of aluminium oxides

Atomic layer deposition (ALD) of aluminum oxides ($Al_2O_3$) was conducted in a home-built thermal ALD system (developed at AMOLF) at 250 °C at a base pressure of 0.01–0.05 mbar. The ALD cycle consisted of a 10 ms pulse of $H_2O$, a 18 s $N_2$ purge, a 10 ms pulse of trimethylaluminum (TMA), and another 18 s $N_2$ purge to complete the cycle. The deposition rate was approximately 1.25 Å per cycle. Eight ALD cycles were used to deposit 1 nm thick $Al_2O_3$ on the n-type $Si/SiO_{x,RCA}$ substrate. The thickness of the $Al_2O_3$ was estimated by ellipsometer (J.A. Woollam) using dielectric models for $Al_2O_3$ and Si native oxide on a Si substrate.

### Sputter-deposition of metals

Platinum (Pt) was deposited using Prevac radio frequency (rf) magnetron sputtering from a Pt target (Mateck, 99.95%, 2 inch diameter, 5 mm thickness). The Ar flow was kept at 15 sccm and the working pressure was held at 3 μbar. The rf power was kept at 25 W and the deposition rate was approximately, 0.138 Å $s^{-1}$. The deposition time was 144 s, and the thickness of the deposited Pt film was 2 nm. Nickel (Ni) was deposited in the same Prevac sputter chamber from a pure Ni target (Mateck, 99.95%, 2 inch diameter). The Ar flow was maintained at 15 sccm and the working pressure was 3 μbar. The rf power was 100 W and the deposition rate was approximately 0.2 Å $s^{-1}$. Ni was sputter-deposited for 200 s, resulting a 4-nm thick Ni film.

### Preparation of electrodes

The back side of n-Si wafers was scratched using sand paper to remove the oxide layer, followed by cleaning the residue using ethanol. The ohmic back contacts were formed by rubbing the back side surface of n-Si wafers with a Ga-In eutectic alloy (75.5:24.5 wt%, 99.9% metal basis, Alfa Aesar). The ohmic back contact of the $p^+$-Si wafer was formed by sputtering Pt.

### (Photo)electrochemical measurements

Photoelectrochemical measurements of the photoanode were conducted in a three electrode configuration in 1 M KOH electrolyte solution under simulated solar irradiation using a Newport Sol3A Class AAA solar simulator (type 94023A-SR3) with 450 Watt xenon short arc lamp. A mercury/mercury oxide (Hg/HgO in 1 M KOH, Radiometer Analytical XR440, Hach) electrode was used as the reference electrode, and Ni coil was used as the counter electrode. The Hg/HgO electrode was calibrated using a silver/silver chloride (Ag/AgCl, in saturated KCl and AgCl, Radiometer Analytical XR300, Hach) reference electrode with a well-known potential with respect to the standard hydrogen potential ($V^{0}_{\mathrm{Ag/AgCl}\ \textit{versus}\ \mathrm{SHE}} = 0.199$ V), and had a potential of 0.9281 V *versus* the reversible hydrogen electrode (RHE) in 1 M KOH solution. The exposed area of the working electrode was 0.2826 $\mathrm{cm}^{-2}$. During the measurement, the electrolyte was continuously agitated using a magnetic stir bar. Cyclic voltammetry, electrochemical open-circuit, electrochemical impedance spectroscopy and chronoamperometry measurements were performed using a potentiostat PARSTAT MC (Princeton Applied Research, AMETEK). The cyclic voltammetry data was recorded at a constant scan rate of 50 mV $\mathrm{s}^{-1}$ and the chronoamperometric data was collected at constant potential of 1.7 V *versus* RHE.

### Electrochemical impedance spectroscopy

Electrochemical impedance spectroscopy (EIS) of the photoanode was performed in 50 mM $K_3Fe(CN)_6$, 350 mM $K_4Fe(CN)_6$ and 1 M KCl in a three electrode measurement using a Pt wire in a fritted glass tube as the reference electrode and a Pt coil as the counter electrode. The measurements were performed using a potentiostat PARSTAT MC (Princeton Applied Research, AMETEK) and the experimental setup was kept in the dark during the measurement.

### X-ray photoelectron spectroscopy

X-ray photoelectron spectroscopy (XPS) experiments were performed using the Thermo Scientific K-alpha apparatus (Thermo Scientific), equipped with an Al K-alpha X-ray source and a flood gun. Parameters used for the characterization were: spot size of 400 µm, pass energy of 50 eV, energy step size of 0.1 eV, dwell time of 50 ms and 10 scans in the vicinity of the binding energy of the investigated elements. For depth profiling experiment, a careful ion etching procedure was conducted using low ion energy beam at 500 eV.

## 3.3. Results and discussion

### Photoelectrochemical performance

The schematic structure of the MIS photoanode is shown in Fig. 3.1. The PEC performance of the MIS photoanodes was evaluated by cyclic voltammetry in 1 M potassium hydroxide (KOH) under simulated solar illumination in a three-electrode configuration without correction for resistance losses in the electrolyte solution. Figure 3.2 shows the evolution of current–voltage ($j$–$V$) characteristics of the n-$Si/SiO_{x,\mathrm{RCA}}/Al_2O_3/Pt/Ni$ photoanode over the course of 18 hours in 1 M KOH.

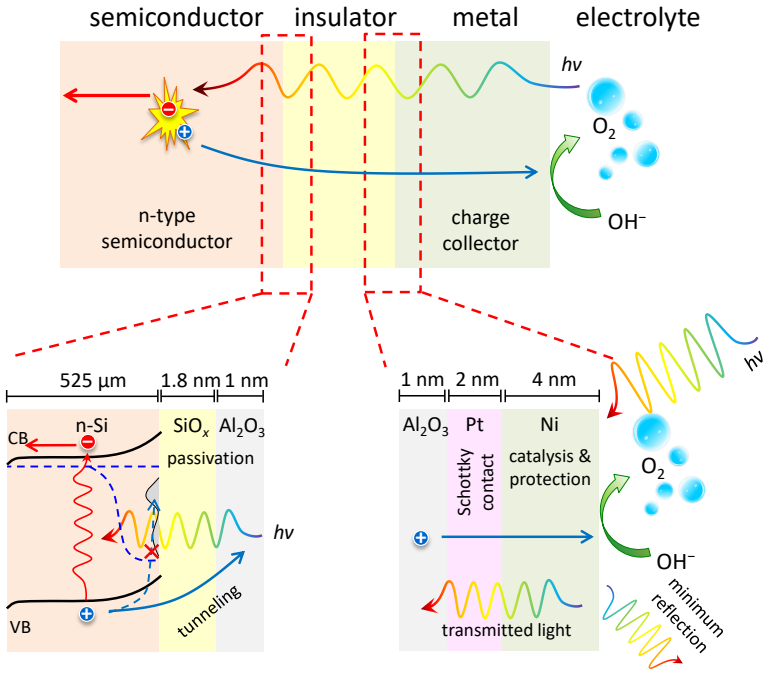



**Figure 3.1:** Schematic of planar MIS photoanodes for water oxidation and magnification of the interfaces, showing the functionality of each layer

The initial photocurrent onset potential (defined as the potential required to achieve an anodic current of 100 µA $cm^{-2}$) was −56 mV, and cathodically shifted to −168 mV relative to the formal potential for water oxidation ($E^{0\prime}$ ($O_2/OH^-$) = 1.23 V *versus* a reversible hydrogen electrode, RHE) after 3 hours in 1 M KOH electrolyte. The photocurrent onset potential further shifted to −233 mV relative to $E^{0\prime}$ ($O_2/OH^-$), and the photocurrent density of the photoanode was 19.2 mA $cm^{-2}$ at $E^{0\prime}$ ($O_2/OH^-$) after 18 hours in contact with 1 M KOH. The series resistance of the system was 4.24 Ω $cm^{-2}$, as measured using electrochemical impedance spectroscopy (EIS), and the photocurrent density at $E^{0\prime}$ ($O_2/OH^-$) after compensation for the series resistance was 25 mA $cm^{-2}$ (Fig. A.1, Appendix A). The dark current was measured to be close to zero, implying that the high observed current under illumination was indeed related to the photogeneration of charge carriers. The saturated photocurrent density of the photoanode was increased from 25.5 mA $cm^{-2}$ during the first scan to 28.5 mA $cm^{-2}$ after 18 hours in contact with 1 M KOH electrolyte (hereafter we define a prolonged contact with KOH electrolyte in the absence of an applied potential as the aging process[32]). The increase of the limiting photocurrent density is attributed to the oxidation of the thin Ni (4nm) to the more transparent $NiO_x$ or $Ni(OH)_2$ during the aging process that reduces the light reflection (Fig. A.2, Appendix A), and thus allowing for more light transmission to the absorber layer. The photovoltage of this structure was estimated by comparing the onset potential of the photoanode

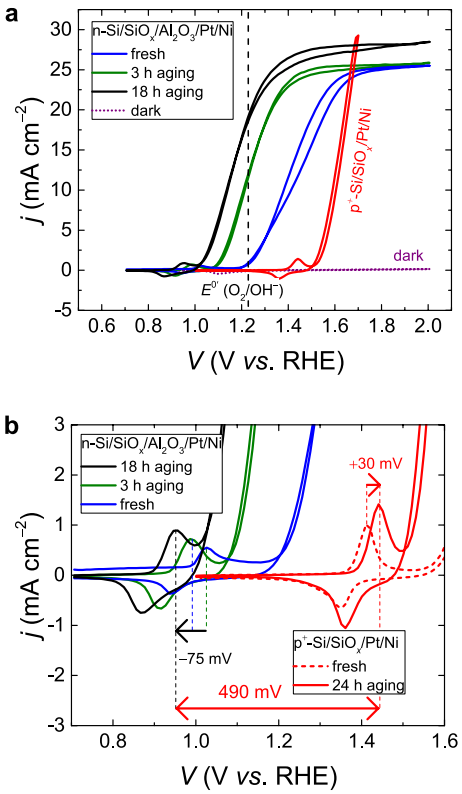



**Figure 3.2:** (a) Three-electrode (photo) current density *versus* applied voltage ($j$–$V$) curves of n-Si/SiO$_{x,\mathrm{RCA}}$/Al$_2$O$_3$/Pt/Ni photoanode during aging in 1 M KOH under simulated AM1.5 illumination. A total of three illuminated voltammetry scans are shown: one for initial fresh sample (blue line), one after 3 hours (green line) and one after 18 hours (black line) of aging in the electrolyte. The dark voltammetry scan of the n-Si/SiO$_{x,\mathrm{RCA}}$/Al$_2$O$_3$/Pt/Ni is shown as the dotted purple line. For comparison, the $j$–$V$ behavior of the non-photoactive p$^+$-Si/SiO$_{x,\mathrm{RCA}}$/Al$_2$O$_3$/Pt/Ni is shown (red line). The black vertical dashed line indicates the potential for water oxidation, $E^{0\prime}$ (O$_2$/OH$^-$). (b) The magnification of Fig. 3.2a, showing the shift of the redox peaks of Ni over the course of 18 hours.

under illumination and the non-photoactive p$^+$-Si/SiO$_{x,\mathrm{RCA}}$/Al$_2$O$_3$/Pt/Ni (here the degenerate p$^+$-Si simply served as a conductive substrate), and was measured to be 490 mV. The equivalent PV response analysis[22,33] indicated that the $j$–$V$ behavior of the n-Si/SiO$_{x,\mathrm{RCA}}$/Al$_2$O$_3$/Pt/Ni photoanode after 18 hours of aging in 1 M KOH is equivalent to that of a PV cell with an open-circuit voltage ($V_{\mathrm{oc}}$) of 496 mV, a short-circuit current density $j_{\mathrm{sc}}$ of 28.06 mA cm$^{-2}$, a fill factor (*ff*) of 0.64 and an energy-conversion-efficiency of 8.87% that is electrically connected in series with a dark electrolysis cell (Appendix A.3 and Fig. A.3, Appendix A).

Figure 3.2b shows the magnification of Fig. 3.2a that highlights the current onset potential region of the electrodes. The initial oxidation peak of Ni within the n-Si/SiO$_{x,\mathrm{RCA}}$/Al$_2$O$_3$/Pt/Ni photoanode was −390 mV relative to the initial Ni oxidation peak in the non-photoactive p$^+$-Si/SiO$_{x,\mathrm{RCA}}$/Pt/Ni, suggesting that

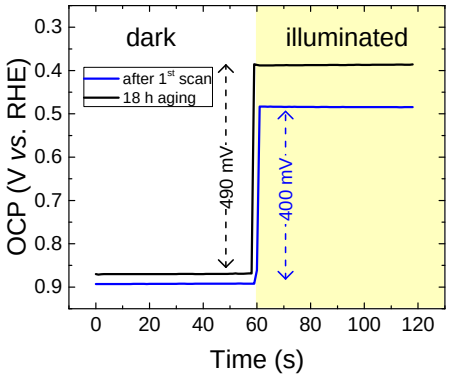



**Figure 3.3:** Open-circuit potential *versus* the reference electrode (scaled in RHE) of the n-$Si/SiO_{x,RCA}/Al_2O_3/Pt/Ni$ photoanode after the first voltammetry scan and after 18-hour aging in 1 M KOH measured in the dark and under illumination. The change in OCP between the dark and illuminated conditions indicates the photovoltage of the photoanode.

the initial photovoltage of the photoanode during the first scan was 385 mV. After 18 hours in contact with KOH, the redox peaks of the non-photoactive $p^+$-$Si/SiO_{x,RCA}/Al_2O_3/Pt/Ni$ electrode anodically shifted by +30 mV. This potential shift is attributed to the incorporation of Fe into the $Ni(OH)_2$ on the Ni surface during aging process in a non-purified KOH electrolyte,[32,34] which is responsible for the catalytic activation of Ni for the oxygen evolution reaction. In contrast, the redox peaks of Ni within the n-$Si/SiO_{x,RCA}/Al_2O_3/Pt/Ni$ photoanode shifted cathodically by −75 mV relative to the initial scan, indicating that the photovoltage of the photoanode indeed increased during the aging process in KOH. The increase of the photovoltage of the photoanode was further ascertained by comparing the electrochemical open-circuit potential (OCP) of the photoanode against a reference electrode (scaled in RHE) in the dark and under illumination (Fig. 3.3). The change in the OCP between the dark and illuminated conditions indicates the photovoltage of the photoanode. The change of OCP of the sample after the first scan was 400 mV, and increased to 490 mV after 18 hours in the electrolyte, in an excellent agreement with the increased photovoltage observed from the $j$–$V$ measurements shown in Fig. 3.2.

The energetics at the MIS junction were evaluated by electrochemical impedance spectroscopy (EIS) in a solution containing electrochemically reversible, one-electron $Fe(CN)_6^{3-/4-}$ redox couple and Mott-Schottky analysis of the inverse square of the space-charge capacitance–voltage ($C_{sc}^{-2}$–$V$) of the electrode.[10,11] The space-charge capacitances ($C_{sc}$) of the semiconductor were obtained by fitting the impedance data with an equivalent electronic circuit that consisted of a parallel resistor and a parallel capacitor, corresponding to the resistive and capacitive behaviors in the space-charge region of the semiconductor (Fig. A.4, Appendix A). The flat band potential ($E_{fb}$) was estimated by taking the value of the intercept between the extrapolated linear region of the inverse square of the space-charge capacitance ($C_{sc}^{-2}$) with the $x$-axis in the Mott–Schottky plot in Fig. 3.4. The $E_{fb}$ of the fresh n-

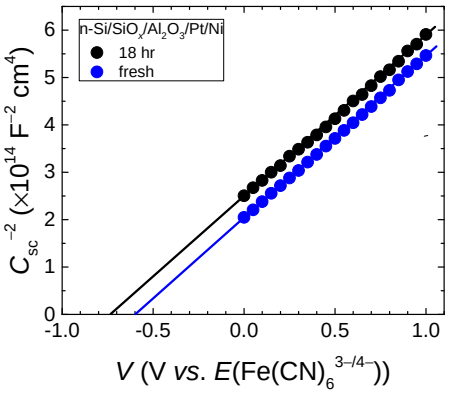



**Figure 3.4:** Mott–Schottky plots of the inverse square of the space-charge capacitance as a function of applied voltage ($C_{sc}^{-2}$–$V$) relative to the redox potential of $Fe(CN)_6^{3-/4-}$ for the n-$Si/SiO_{x,RCA}/Al_2O_3/Pt/Ni$ photoanode before (blue) and after 18 hours of aging (black).

$Si/SiO_{x,RCA}/Al_2O_3/Pt/Ni$ was −0.6 V *versus* $Fe(CN)_6^{3-/4-}$ and the $E_{fb}$ of the aged electrode was −0.73 V *versus* $Fe(CN)_6^{3-/4-}$. The slope of the linear region of the $C_{sc}^{-2}$–$V$ curve was 3.35 ± 0.02 × $10^{14}$ $F^{-2}$ $cm^4$ $V^{-1}$ for both samples, corresponding to a donor density ($N_D$) of 3.54 × $10^{16}$ $cm^{-3}$ (Appendix A.4), which also implies a corresponding resistivity ($\rho$) of ~0.185 Ω cm, in accordance with the range specified by the manufacturer of the Si wafer (0.1–0.3 Ω cm). The calculated barrier height of the Si within the fresh and the aged n-$Si/SiO_{x,RCA}/Al_2O_3/Pt/Ni$ photoanode was 0.77 and 0.9 eV, respectively (Appendix A.4). Such a large barrier height should give rise to a strong inversion layer near the Si surface, and thus would result in a large photovoltage, mainly due to the associated increase of band bending, and the subsequent improvement of charge-carrier extraction as well as separation inside the semiconductor.

To confirm the composition of the n-$Si/SiO_{x,RCA}/Al_2O_3/Pt/Ni$ after the aging treatment, X-ray photoelectron spectroscopy (XPS) experiments were performed using low energy ion etching with an average etching rate of approximately 3 Å per step. Figure 3.5a shows the Ni 2$p$ XPS peaks of the electrode starting from step 0 (no etching) to step 10 (approximate depth of 3 nm). The results indicated that in an alkaline solution the Ni surface mostly transformed to $Ni(OH)_2$, and prolonged aging partially modified the bulk Ni into $NiO_x$, as observed after three steps and five steps of etching, respectively. Strong Ni 2$p$ signals corresponding to the metallic Ni were observed and became dominant as the etching depth increased to ten steps. These XPS spectra substantiate that the initial metallic Ni film (thickness of 4 nm) was transformed into a $Ni/NiO_x/Ni(OH)_2$ composite after 18 hours in contact with aqueous KOH solution. Figure 3.5b shows the XPS depth profiling analysis of the electrode on the basis of Ni 2$p$, Pt 4$f$, Al 2$s$ and Si 2$p$ XPS spectra. The Al 2$s$ signal was used in this analysis due to the difficulty to identify the Al 2$p$ signals that overlapped with the Pt 4$f$ (Appendix A.5). In total, 36 etching steps were performed and the full elemental scan can be found in Fig. A.5, Appendix A. Consistent with

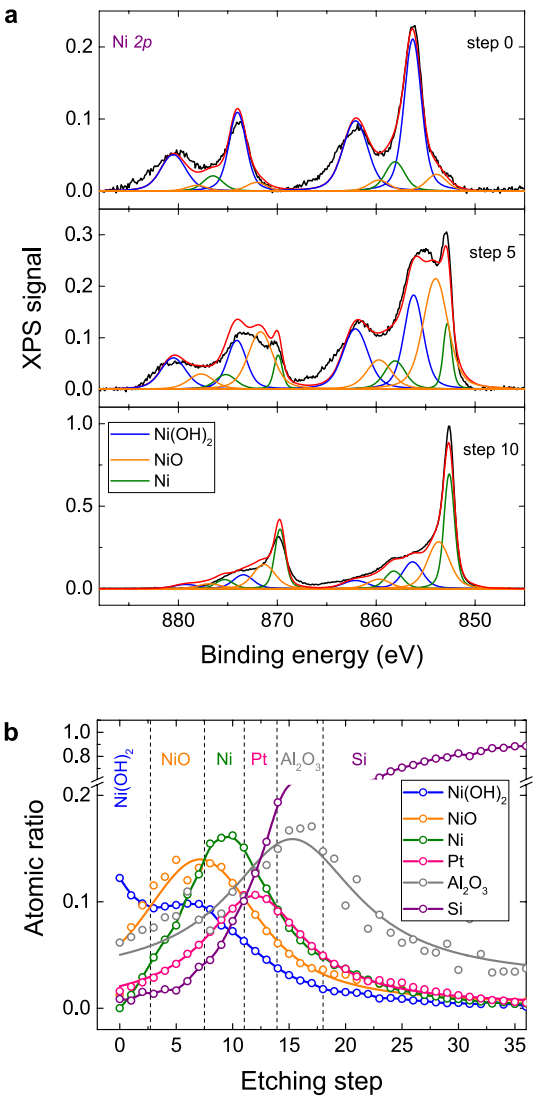



**Figure 3.5:** X-ray photoelectron spectroscopy (XPS) spectra of n-Si/$SiO_{x,RCA}$/$Al_2O_3$/Pt/Ni after 18-hour aging. (a) Ni 2*p* signals as a function of etching step; step 0 (no etching), step 5 and step 10 (approximate depth of 3 nm), showing variation of Ni phases. (b) Depth profiling analysis of the composite system. The XPS signals corresponded to Ni 2*p*,Pt 4*f*,Al 2*s* and Si 2*p*. The Al 2*s* signal was used in this analysis due to the overlapping peak locations of the Al 2*p* and the Pt 4*f*. The sample was etched using ion beam with an average etching rate of approximately 3 Å per step.

the previous study, the Ni surface film in contact with 1 M KOH did not oxidize further to a depth of more than ±2.5 nm,[28] as indicated by the dominant signal of metallic Ni at etching step 10 (approximate depth of 3 nm), as well as the absence of NiO or $Ni(OH)_2$ signals at the Pt interface. This implies that the $Al_2O_3$ and Si underneath were still fully protected by the Ni surface layer after 18 hours in KOH under open-circuit condition in the absence of illumination. Without Ni and Pt, $Al_2O_3$ easily corroded in KOH electrolyte,[35] as also indicated by the absence of Al $2p$ signal in Fig. A.6, Appendix A.

The improvement of the barrier height of the n-Si/$SiO_{x,RCA}$/$Al_2O_3$/Pt/Ni photoanode after 18 hours of aging in KOH solution is closely related to the inability of the 2 nm Pt to completely screen charge at the Si interface, so that the effective screening is also affected by the increased workfunction of the Ni surface layer that is oxidized by a strongly alkaline electrolyte. Previous studies have shown that the effective metal screening and the associated barrier height in a bimetal Schottky structure depends on the inner metal thickness.[21,36] The XPS depth profiling analysis equipped with ion etching in Fig. 3.5 shows that the Ni film is partially transformed into $Ni(OH)_2$ and $NiO_x$ on the surface after 18 hours in 1 M KOH. According to the Pourbaix diagram (Fig. A.7, Appendix A), Ni readily oxidizes to $NiO_x$ even in a weak base (pH>7), and therefore prolonged contact with a pH 14 solution may accelerate and exacerbate the oxidation process of Ni. The $NiO_x$ and $Ni(OH)_2$ phases are known to have a large workfunction in the range of 5.2–5.6 eV,[37,38] close to the vacuum workfunction of Pt. Although Pt has a sufficiently high workfunction to produce a large Schottky barrier, its effective workfunction may differ from the ideal value, and is usually lower when in contact with a dielectric material than when in vacuum. The decrease of the metal workfunction is essentially due to the existence of intrinsic states at the MIS interface whose energy level is at the so-called charge neutrality level.[39,40] These interface-induced gap states tend to pin the metal Fermi level and alter the effective metal workfunction relative to its vacuum value. The magnitude of the Fermi level shift depends on the pinning strength of the thin dielectric layer and/or the underlying semiconductor, *i.e.*, the pinning factor that ranges from 0 for perfect pinning and 1 for no pinning. By using the Schottky-Mott rule, the $E_{fb}$ of −0.6V *versus* $Fe(CN)_6^{3-/4-}$ for the fresh sample implies a corresponding barrier height of 0.77 eV and an effective workfunction of Pt/Ni bilayer structure of 4.82 eV on the n-Si/$SiO_{x,RCA}$/$Al_2O_3$. On the other hand, the oxidized $NiO_x$ on Pt within the aged sample is isolated from $Al_2O_3$, and thus is not affected by the pinning at the MIS interface and would likely to maintain its high workfunction for Schottky junction formation with the underlying Si, as illustrated in Fig. 3.6.

The effect of the interfacial metallic layer was analyzed by comparing the $j$–$V$ curves and the Mott–Schottky plots of the MIS electrode with bilayer Pt (2 nm)/Ni (4nm) contact and the MIS electrode with Ni (6 nm) contact after 18 hours of aging treatment in aqueous KOH solution, shown in Fig. 3.7a and b. The vacuum workfunction of Ni is known to vary from 5.22 to 5.35 eV depending on the crystal facet, and the vacuum workfunction of Pt is 5.64 eV for polycrystalline films. After 18 hours, the onset potential of the n-Si/$SiO_{x,RCA}$/$Al_2O_3$/Ni was −160 mV

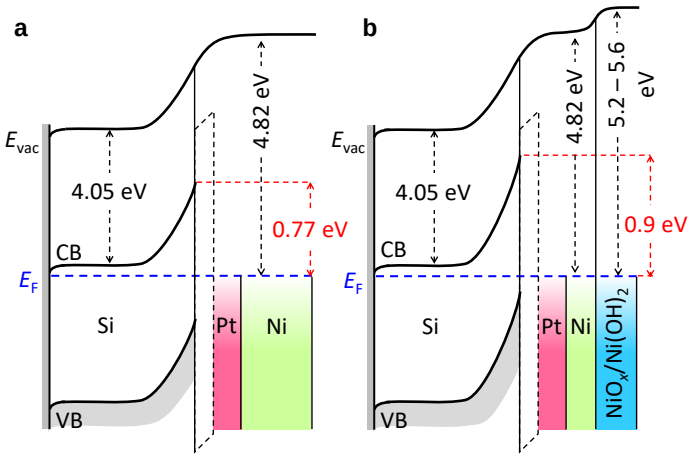



**Figure 3.6:** Representative energy band diagrams of the n-Si/$SiO_{x,RCA}$/$Al_2O_3$/Pt/Ni (a) before and (b) after prolonged aging of in 1 M KOH solution.

relative to $E^{0\prime}$ ($O_2$/$OH^-$), and the photovoltage was 410 mV (Fig. A.8, Appendix A). The initial $E_{fb}$ of the n-Si/$SiO_{x,RCA}$/$Al_2O_3$/Ni was −0.5V *versus* $Fe(CN)_6^{3-/4-}$ (Fig. A.9, Appendix A) and shifted to −0.6 V *versus* $Fe(CN)_6^{3-/4-}$ after 18 hours of aging. Considering the Ni surface layer already oxidized to $NiO_x$ after 18 hours in 1 M KOH, and did not oxidize further than 2.5 nm, the lower photovoltage and $E_{fb}$ observed in n-Si/$SiO_{x,RCA}$/$Al_2O_3$/Ni than the n-Si/$SiO_{x,RCA}$/$Al_2O_3$/Pt/Ni suggests that the inner metal still partially screened charge and its workfunction contributed substantially to the effective barrier height in a multilayer Schottky structure.

Figure 3.7a also compares the *j*–*V* characteristics of the samples with and without the $Al_2O_3$ interlayer. In the absence of $Al_2O_3$ at the interface, the onset potentials were −60 and +22 mV relative to $E^{0\prime}$ ($O_2$/$OH^-$) and the photovoltages were only 310 and 230 mV for MIS photoanodes with the $SiO_{x,RCA}$ and the $SiO_{x,native}$, respectively. Mott–Schottky analysis (Fig. 3.7c) indicated that the $E_{fb}$ was only −0.56 V *versus* $Fe(CN)_6^{3-/4-}$ for the n-Si/$SiO_{x,RCA}$/Pt/Ni and −0.46 V *versus* $Fe(CN)_6^{3-/4-}$ for the n-Si/$SiO_{x,native}$/Pt/Ni, and there were no substantial changes between the initial conditions and after 18-hour aging. The constant $E_{fb}$ and the low photovoltage of the n-Si/$SiO_x$/Pt/Ni photoanode, despite the high workfunction of the surface layers, is ascribed to the strong pinning of the Fermi level at Si/$SiO_x$/Pt interfaces. Fundamentally, Fermi level pinning arises in response to incomplete termination of the Si surface, resulting in an asymmetric bonding situation, *i.e.*, dangling bonds, that introduces energy states inside the surface band gap.[41,42] These energy states tend to pin the Fermi level of the semiconductor, and dictates the barrier height by their energy levels instead of by the metal workfunction. Additionally, chemical reaction at Si/$SiO_x$/metal interfaces can also create extrinsic defect states that cause Fermi level pinning of both the semiconductor and the metal. On the other hand, $Al_2O_3$ is known for its high level of chemical passivation that is capable of

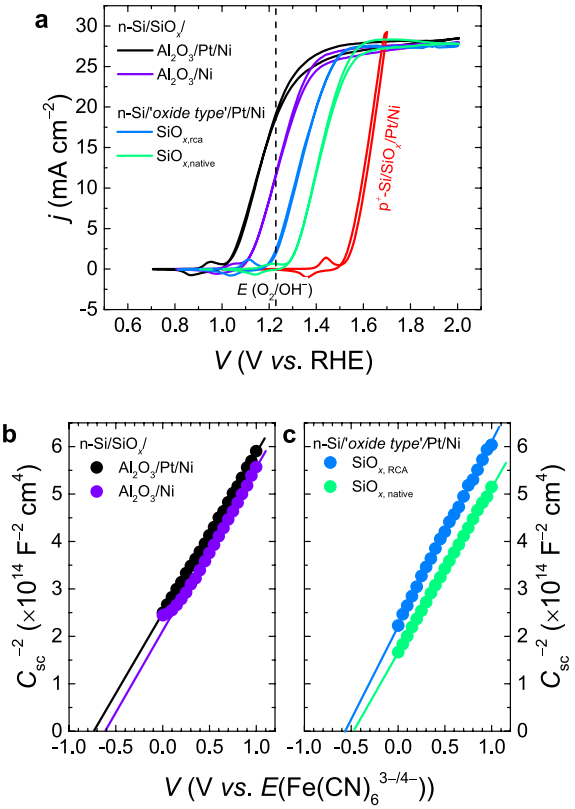



**Figure 3.7:** (a) Representative *j*–*V* behaviors of the n-Si/$SiO_{x,RCA}$/$Al_2O_3$/Pt (2 nm)/Ni (4nm) and n-Si/$SiO_{x,RCA}$/$Al_2O_3$/Ni (6 nm). For comparison, the samples without $Al_2O_3$ are also shown; with the $SiO_{x,RCA}$ and $SiO_{x,native}$.(b) Mott–Schottky plots of n-Si/$SiO_{x,RCA}$/$Al_2O_3$/Pt (2 nm)/Ni (4nm) and n-Si/$SiO_{x,RCA}$/$Al_2O_3$/Ni (6 nm). (c) Mott–Schottky plots of n-Si/$SiO_{x,RCA}$/Pt/Ni and n-Si/$SiO_{x,native}$/Pt/Ni. All the plots shown are samples measured after 18 hours of aging treatment in 1 M KOH solution.

saturating dangling bonds on the Si surface, and thus has been used extensively for surface passivation of Si.[43,44] Therefore, the high observed photovoltage of the n-Si/$SiO_{x,RCA}$/$Al_2O_3$/Pt/Ni MIS structure can be attributed to the high quality of surface chemical passivation induced by the chemically-grown $SiO_{x,RCA}$ and $Al_2O_3$ stack combination.

The stability of the n-Si/$SiO_{x,RCA}$/$Al_2O_3$/Pt/Ni photoanode was evaluated by a chronoamperometry test at a fixed applied potential of 1.7 V *versus* RHE in 1 M KOH electrolyte under simulated solar illumination, and is shown in Fig. 3.8a. The initial photocurrent density was 28 mA cm$^{-2}$ and periodically dropped due to the unavoidable bubble formation during continuous measurement. Gas bubbles were constantly generated and detached on the electrode surface, causing fluctuations in the observed photocurrent. The 4 nm Ni (or Ni/$NiO_x$/$Ni(OH)_2$ upon transformation) surface film was able to protect the underlying photoanode under illumination

and at a constant applied voltage without any noticeable decay of photocurrent for more than 200 hours in 1 M KOH solution. Linear sweep voltammetry scans were recorded periodically during the chronoamperometry test (Fig. 3.8b) and showed no anodic shift in the $j$–$V$ characteristics during 200 hours of operation. Without Pt and Ni, the $Al_2O_3$ layer was not stable in highly alkaline solutions (Fig. A.6, Appendix A),[35] and thus penetration of a highly concentrated KOH could potentially delaminate the catalyst overlayers, which would subsequently cause a rapid degradation of the device performance. The constant current observed during the chronoamperometry measurement indicated that the $Al_2O_3$ underneath was not adversely affected by the strongly corrosive electrolyte, and demonstrated the effectiveness of the ultrathin bilayer Pt/Ni film for photoelectrode protection against corrosion.

This work clearly demonstrates the use of an MIS Si photoelectrode to achieve a sufficiently high photovoltage for solar water-oxidation half reaction, and therefore does not reflect the ability to spontaneously split water. To successfully realize a bias-free water splitting, the photoanode should be combined with the second or third semiconductor in a series or tandem arrangement. In such an integrated system, a considerable fraction of light would be absorbed by the top junction, and therefore, our device would ideally produce less than the photocurrent reported in this work. However, the narrow band gap of Si and the high photovoltage as well as the high photocurrent output of our MIS electrode could potentially simplify the design and fabrication of a highly efficient PEC device for solar water splitting.

## 3.4. Conclusion

In summary we have successfully fabricated an MIS photoanode and demonstrated a high photovoltage and stability for solar water oxidation. The high photovoltage was achieved by engineering the semiconductor–insulator and insulator–metal interfaces using a thin $Al_2O_3$ dielectric layer and using a high workfunction metal Pt as well as an active water oxidation catalyst Ni, respectively. The incidental oxidation of Ni in 1 M KOH electrolyte resulted in an increase in its workfunction that subsequently improved the effective barrier height at the MIS junction as well as the degree of band bending near the Si surface, thereby increasing the photovoltage with a value close to the conventional $np^+$ Si buried junction. Additionally, we have shown the role of the interfacial oxide layers on the alleviation of Fermi level pinning, which is partially responsible for the shift of photocurrent onset potential, and thus the observed photovoltage. Finally we have demonstrated a simple yet effective strategy to achieve a high efficiency MIS photoanode that is chemically stable for more than 200 hours of PEC operation in a highly corrosive environment.

## References

[1] I. A. Digdaya, G. W. P. Adhyaksa, B. J. Trzesniewski, E. C. Garnett, and W. A. Smith, *Interfacial engineering of metal-insulator-semiconductor junctions for efficient and stable photoelectrochemical water oxidation,* Nat. Commun. **8**, 15968 (2017).

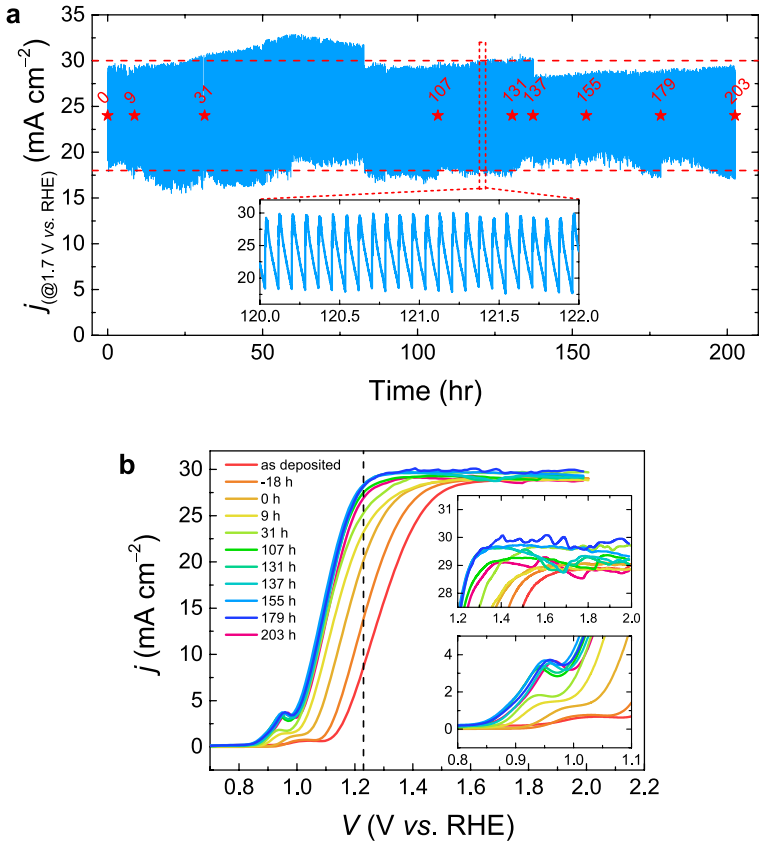



**Figure 3.8:** (a) Chronoamperometic current *versus* time ($j$–$t$) curve of the n-Si/$SiO_{x,RCA}$/$Al_2O_3$/Pt/Ni photoanode measured at a constant applied voltage of 1.7 *versus* RHE in 1 M KOH solution under simulated solar illumination. The inset shows current fluctuations due to bubble formation during the measurement. (b) Representative $j$–$V$ behavior of the n-Si/$SiO_{x,RCA}$/$Al_2O_3$/Pt/Ni photoanode in contact with 1 M KOH under simulated solar illumination collected periodically during 200 hours of operation. Insets show the magnification of the evolution of photocurrent (top) and Ni redox waves (bottom).

[2] N. S. Lewis and D. G. Nocera, *Powering the planet: Chemical challenges in solar energy utilization,* Proc. Natl Acad. Sci. USA **103**, 15729 (2006).

[3] J. Turner, G. Sverdrup, M. K. Mann, P.-C. Maness, B. Kroposki, M. Ghirardi, R. J. Evans, and D. Blake, *Renewable hydrogen production,* Int. J. Energy Res. **32**, 379 (2008).

[4] B. A. Pinaud, J. D. Benck, L. C. Seitz, A. J. Forman, Z. Chen, T. G. Deutsch, B. D. James, K. N. Baum, G. N. Baum, S. Ardo, H. Wang, E. Miller, and T. F. Jaramillo, *Technical and economic feasibility of centralized facilities for solar hydrogen production via photocatalysis and photoelectrochemistry,* Energy Energy Environ. Sci. **6**, 1983 (2013).

[5] W. A. Smith, I. D. Sharp, N. C. Strandwitz, and J. Bisquert, *Interfacial band-edge energetics for solar fuels production,* Energy Environ. Sci. **8**, 2851 (2015).

[6] K. Sun, M. T. McDowell, A. C. Nielander, S. Hu, M. R. Shaner, F. Yang, B. S. Brunschwig, and N. S. Lewis, *Stable Solar-Driven Water Oxidation to $O_2$ (g) by Ni-Oxide-Coated Silicon Photoanodes,* J. Phys. Chem. Lett. **6**, 592 (2015).

[7] B. Mei, A. A. Permyakova, R. Frydendal, D. Bae, T. Pedersen, P. Malacrida, O. Hansen, I. E. L. Stephens, P. C. K. Vesborg, B. Seger, and I. Chorkendorff, *Iron-treated nio as a highly transparent p-type protection layer for efficient Si-based photoanodes,* J. Phys. Chem. Lett. **5**, 3456 (2014).

[8] X. Yu, P. Yang, S. Chen, M. Zhang, and G. Shi, *NiFe Alloy Protected Silicon Photoanode for Efficient Water Splitting,* Adv. Energy Mater. **7**, 1601805 (2017).

[9] S. Hu, M. R. Shaner, J. A. Beardslee, M. Lichterman, B. S. Brunschwig, and N. S. Lewis, *Amorphous $TiO_2$ coatings stabilize Si, GaAs, and GaP photoanodes for efficient water oxidation,* Science **344**, 1005 (2014).

[10] X. Zhou, R. Liu, K. Sun, D. Friedrich, M. T. McDowell, F. Yang, S. T. Omelchenko, F. H. Saadi, A. C. Nielander, S. Yalamanchili, K. M. Papadantonakis, B. S. Brunschwig, and N. S. Lewis, *Interface engineering of the photoelectrochemical performance of Ni-oxide-coated n-Si photoanodes by atomic-layer deposition of ultrathin films of cobalt oxide,* Energy Environ. Sci. **8**, 2644 (2015).

[11] X. Zhou, R. Liu, K. Sun, K. M. Papadantonakis, B. S. Brunschwig, and N. S. Lewis, *570 mV photovoltage, stabilized n-Si/$CoO_x$ heterojunction photoanodes fabricated using atomic layer deposition,* Energy Environ. Sci. **9**, 892 (2016).

[12] R. Singh, M. Green, and K. Rajkanan, *Review of conductor-insulator-semiconductor (CIS) solar cells,* Sol. Cells **3**, 95 (1981).

[13] D. Connelly, C. Faulkner, P. A. Clifton, and D. E. Grupp, *Fermi-level depinning for low-barrier Schottky source/drain transistors,* Appl. Phys. Lett. **88**, 012105 (2006).

[14] W. Mönch, *On the alleviation of fermi-level pinning by ultrathin insulator layers in schottky contacts,* J. Appl. Phys. **111**, 73706 (2012).

[15] A. Agrawal, J. Lin, M. Barth, R. White, B. Zheng, S. Chopra, S. Gupta, K. Wang, J. Gelatos, S. E. Mohney, and S. Datta, *Fermi level depinning and contact resistivity reduction using a reduced titania interlayer in n-silicon metal-insulator-semiconductor ohmic contacts,* Appl. Phys. Lett. **104**, 112101 (2014).

[16] M. A. Green, F. D. King, and J. Shewchun, *Minority carrier mis tunnel diodes and their application to electron- and photo-voltaic energy conversion—i. theory,* Solid State Phenom. **17**, 551 (1974).

[17] H. Steinkemper, M. Hermle, and S. W. Glunz, *Comprehensive simulation study of industrially relevant silicon solar cell architectures for an optimal material parameter choice,* Prog. Photovoltaics Res. Appl. **24**, 1319 (2016).

[18] R. Hezel, R. Meyer, and A. Metz, *A new generation of crystalline silicon solar cells: Simple processing and record efficiencies for industrial-size devices,* Sol. Energy Mater. Sol. Cells **65**, 311 (2001).

[19] S. Z. Oener, J. van de Groep, B. Macco, P. C. P. Bronsveld, W. M. M. Kessels, A. Polman, and E. C. Garnett, *Metal-insulator-semiconductor nanowire network solar cells,* Nano Lett. **16**, 3689 (2016).

[20] L. Ji, M. D. McDaniel, S. Wang, A. B. Posadas, X. Li, H. Huang, J. C. Lee, A. A. Demkov, A. J. Bard, J. G. Ekerdt, and E. T. Yu, *A silicon-based photocathode for water reduction with an epitaxial $SrTiO_3$ protection layer and a nanostructured catalyst,* Nat. Nanotechnol. **10**, 84 (2014).

[21] D. V. Esposito, I. Levin, T. P. Moffat, and A. A. Talin, *$H_2$ evolution at Si-based metal-insulator-semiconductor photoelectrodes enhanced by inversion channel charge collection and H spillover,* Nature Materials **12**, 562 (2013).

[22] J. C. Hill, A. T. Landers, and J. A. Switzer, *An electrodeposited inhomogeneous metal-insulator-semiconductor junction for efficient photoelectrochemical water oxidation,* Nat. Mater. **14**, 1150 (2015).

[23] Y. W. Chen, J. D. Prange, S. Dühnen, Y. Park, M. Gunji, C. E. D. Chidsey, and P. C. McIntyre, *Atomic layer-deposited tunnel oxide stabilizes silicon photoanodes for water oxidation,* Nat. Mater. **10**, 539 (2011).

[24] A. G. Scheuermann, J. P. Lawrence, K. W. Kemp, T. Ito, A. Walsh, C. E. D. Chidsey, P. K. Hurley, and P. C. McIntyre, *Design principles for maximizing photovoltage in metal-oxide-protected water-splitting photoanodes.* Nat. Mater. **15**, 99 (2016).

[25] A. G. Scheuermann, J. D. Prange, M. Gunji, C. E. D. Chidsey, and P. C. McIntyre, *Effects of catalyst material and atomic layer deposited $TiO_2$ oxide thickness on the water oxidation performance of metal-insulator-silicon anodes,* Energy Environ. Sci. **6**, 2487 (2013).

[26] A. G. Scheuermann, J. P. Lawrence, A. C. Meng, K. Tang, O. L. Hendricks, C. E. D. Chidsey, and P. C. McIntyre, *Titanium Oxide Crystallization and Interface Defect Passivation for High Performance Insulator-Protected Schottky Junction MIS Photoanodes,* ACS Appl. Mater. Interfaces **8**, 14596 (2016).

[27] T. Zhu and M. N. Chong, *Prospects of metal–insulator–semiconductor (MIS) nanojunction structures for enhanced hydrogen evolution in photoelectrochemical cells: A review,* Nano Energy **12**, 347 (2015).

[28] M. J. Kenney, M. Gong, Y. Li, J. Z. Wu, J. Feng, M. Lanza, and H. Dai, *High-Performance Silicon Photoanodes Passivated with Ultrathin Nickel Films for Water Oxidation,* Science **342**, 836 (2013).

[29] N. Y. Labrador, X. Li, Y. Liu, H. Tan, R. Wang, J. T. Koberstein, T. P. Moffat, and D. V. Esposito, *Enhanced Performance of Si MIS Photocathodes Containing Oxide-Coated Nanoparticle Electrocatalysts,* Nano Lett. **16**, 6452 (2016).

[30] C. C. L. McCrory, S. Jung, J. C. Peters, and T. F. Jaramillo, *Benchmarking heterogeneous electrocatalysts for the oxygen evolution reaction,* J. Am. Chem. Soc. **135**, 16977 (2013).

[31] C. C. L. McCrory, S. Jung, I. M. Ferrer, S. M. Chatman, J. C. Peters, and T. F. Jaramillo, *Benchmarking Hydrogen Evolving Reaction and Oxygen Evolving Reaction Electrocatalysts for Solar Water Splitting Devices,* J. Am. Chem. Soc. **137**, 4347 (2015).

[32] L. Trotochaud, S. L. Young, J. K. Ranney, and S. W. Boettcher, *Nickel-iron oxyhydroxide oxygen-evolution electrocatalysts: the role of intentional and incidental iron incorporation.* J. Am. Chem. Soc. **136**, 6744 (2014).

[33] R. H. Coridan, A. C. Nielander, S. a. Francis, M. T. McDowell, V. Dix, S. M. Chatman, and N. S. Lewis, *Methods for comparing the performance of energy-conversion systems for use in solar fuels and solar electricity generation,* Energy Environ. Sci. **8**, 2886 (2015).

[34] M. S. Burke, L. J. Enman, A. S. Batchellor, S. Zou, and S. W. Boettcher, *Oxygen Evolution Reaction Electrocatalysis on Transition Metal Oxides and (Oxy)hydroxides: Activity Trends and Design Principles,* Chem. Mater. **27**, 7549 (2015).

[35] G. C. Correa, B. Bao, and N. C. Strandwitz, *Chemical stability of titania and alumina thin films formed by atomic layer deposition,* ACS Applied Materials & Interfaces **7**, 14816 (2015).

[36] X. Wu and E. S. Yang, *Effective Metal Screening and Schottky-Barrier Formation in Metal-GaAs Structures,* IEEE Electron Device Lett. **11**, 315 (1990).

[37] P. Schulz, S. R. Cowan, Z.-l. Guan, A. Garcia, D. C. Olson, and A. Kahn, *NiO X /MoO 3 Bi-Layers as Efficient Hole Extraction Contacts in Organic Solar Cells,* Adv. Funct. Mater. **24**, 701 (2014).

[38] M. T. Greiner, M. G. Helander, Z.-B. Wang, W.-M. Tang, and Z.-H. Lu, *Effects of Processing Conditions on the Work Function and Energy-Level Alignment of NiO Thin Films,* J. Phys. Chem. C **114**, 19777 (2010).

[39] Y.-C. Yeo, T.-J. King, and C. Hu, *Metal-dielectric band alignment and its implications for metal gate complementary metal-oxide-semiconductor technology,* J. Appl. Phys. **92**, 7266 (2002).

[40] J. Robertson, *Band offsets of wide-band-gap oxides and implications for future electronic devices,* J. Vac. Sci. Technol. B Microelectron. Nanom. Struct. **18**, 1785 (2000).

[41] O. F. Sankey, R. E. Allen, and J. D. Dow, *Si/transition-metal Schottky barriers: Fermi-level pinning by Si dangling bonds at interfacial vacancies,* Solid State Commun. **49**, 1 (1984).

[42] C. R. Helms and E. H. Poindexter, *The silicon-silicon dioxide system: Its microstructure and imperfections,* Reports Prog. Phys. **57**, 791 (1994).

[43] G. Dingemans, R. Seguin, P. Engelhart, M. C. M. van de Sanden, and W. M. M. Kessels, *Silicon surface passivation by ultrathin $Al_2O_3$ films synthesized by thermal and plasma atomic layer deposition,* Phys. Status Solidi RRL **4**, 10 (2010).

[44] G. Dingemans and W. M. M. Kessels, *Status and prospects of $Al_2O_3$-based surface passivation schemes for silicon solar cells,* J. Vac. Sci. Technol. A: Vacuum, Surfaces, and Films **30**, 040802 (2012).

# 4

# General considerations for improving photovoltage in metal-insulator-semicondutor photoanodes

Metal-insulator-semiconductor (MIS) junction photoelectrode is a simple alternative to the traditional semiconductor-liquid junction and the conventional p-n junction electrodes. Highly efficient MIS photoanodes often require interfacial surface passivating oxides and high workfunction metals to produce a high photovoltage. Herein we investigate and analyze the effect of oxide interlayers and metal workfunctions to the barrier height and the photovoltage of the MIS junction silicon photoanode. We use two metal components in a bimetal thin-film structure and observe the modulation of effective barrier height and the resulting photovoltage as a function of the inner metal. The MIS photoanode shows a strong linear dependence between the photovoltage and the inner metal workfunction, with the highest photovoltage achieved by the device that uses platinum inner metal. Additionally, we found that coupling a thin aluminum oxide with a chemically-grown silicon oxide and controlling the oxide thickness can significantly improve the photovoltage of an MIS junction photoanode.

Parts of this chapter have been published in I. A. Digdaya, Bartek J. Trześniewski, G. W. P. Adhyaksa, E. C. Garnett and W. A. Smith, *The Journal of Physical Chemistry C*, 2018, **122**, 5462. [1]

## 4.1. Introduction

Sunlight-driven photoelectrochemical (PEC) water splitting is a promising approach to store intermittent solar energy by enabling a renewable and sustainable production of hydrogen, which can be later directly consumed as a transportation fuel or utilized as a feedstock in industrial and stationary power sectors.[2] At the heart of a PEC system is the semiconducting photoelectrode that absorbs and transforms light into photoexcited charge carriers, which are then directly used to drive non-spontaneous electrochemical reactions such as electrolysis of water. One important step in the PEC processes is charge separation driven by an electric field at the semiconductor interface which can be formed by bringing a semiconductor into contact with an electrolyte (semiconductor-liquid junction), with an opposing-type semiconductor (p-n homo- or hetero-junction), or with a metal (Schottky junction, *e.g.*, metal-semiconductor junction or metal-insulator-semiconductor junction).

Metal-insulator-semiconductor (MIS) structures have been the focus of great interest for solar energy conversion devices because of their simple fabrication, low-temperature processing and the potential for achieving higher efficiencies than the traditional p-n junction. For diffused p-n silicon junctions, the photovoltage, thus the device efficiency, is limited by Auger recombination in the highly doped emitter region with an upper limit of 720 mV for devices thicker than the minority carrier diffusion length.[3,4] The MIS junction concept has an advantage over the conventional p-n junction in that the buried rectifying junction is formed with a carrier selective metal contact, thus eliminating the need for a highly doped emitter in the structure, and thereby allowing the device to potentially attain a photovoltage of greater than 720 mV.

A significant development in MIS photoelectrodes has set a record photovoltage of 630 mV,[5] close to that obtained from the p-n junction electrode.[6] The keys to achieving a high photovoltage MIS photoelectrode include the use of thin tunnel oxides and the application of appropriate metal contacts with suitable workfunctions.[7] For n-type semiconductor photoanodes, the metal workfunction should be sufficiently high to ensure a strong inversion near the semiconductor surface,[7] which is a prerequisite for a large generation of photovoltage. However, most high workfunction metals such as platinum (Pt) and iridium (Ir) are too scarce for large-scale applications and too expensive for industrial commercialization. Conversely, p-type semiconductor photocathodes benefit from the need for low workfunction metals such as titanium (Ti) and aluminum (Al) to form a rectifying junction and create a strong inversion. Although low workfunction metals are relatively cheap, these metals exhibit poor catalytic activity, and thus require an additional catalytic overlayer such as Pt to improve the reaction kinetics on the photocathode surface.[8,9]

Another important factor that determines a high photovoltage in an MIS junction photoelectrode is the thin tunnel oxide at the metal-semiconductor interface. The interfacial oxide should have a surface passivation ability to minimize carrier recombination, and a minimum charge extraction barrier to allow for facile electronic transport.[6] In addition, the oxide layer should have dielectric properties that maintain the workfunction mismatch between the metal and the semiconductor to enable a large photovoltage generation across the MIS junction. The native silicon

oxide ($SiO_x$) and the chemically-grown $SiO_x$ are commonly used as an interfacial insulating layer in MIS photoelectrodes.[10–12] Apart from simplicity, the motivation of using these types of oxides is often the assumption that they have the same passivation properties as the high-quality thermal silicon dioxide ($SiO_2$), a surface passivation material that has been used extensively in photovoltaic research and industries.

In the previous chapter, we have introduced an ultrathin layer of aluminum oxide ($Al_2O_3$) in conjunction with the chemically-grown $SiO_x$ at the metal-semiconductor interface, and observed significant improvements of photovoltage which was attributed to the excellent surface passivation induced by $Al_2O_3$ and the simultaneous increase of barrier height.[1] While this is partially true, in this chapter, we aim to expand upon the previous analysis and seek to identify the additional contribution that results in photovoltage enhancement upon the introduction of a supplementary oxide. Additionally, we explore the application of less-precious metal contacts and analyze their impact on the performance and trade-offs associated with the use of lower workfunction metals. We first investigate the junction properties of MIS structures using various metal contacts with different workfunctions by performing dark current–voltage measurements. Using the diode models for MIS junctions, we extract the important parameters such as the dark reverse saturation current and the ideality factor that determine the photovoltage of an MIS photoanode. We additionally determine the barrier heights using capacitance-voltage method and Mott-Schottky analysis, and compare the experimental values with the theoretical models for MIS contacts. Furthermore, we demonstrate how the interfacial oxides and the workfunction of each metal affect the Schottky barrier height at the MIS junction. In separate experiments, we fabricate MIS photoanodes by depositing ultrathin bimetal contacts with various inner metals and show how the outer metal modulates the effective barrier height of the MIS photoanodes. Using the extracted parameters from the Schottky diode modeling, we then compare the experimentally-measured photovoltages with the theoretically-determined values. Finally, we demonstrate how tuning the thickness of the $Al_2O_3$ interface layer and using the appropriate inner metal contact can improve the photovoltage of an MIS photoanode.

## 4.2. Experimental section

### Chemicals

All chemicals were used as received: potassium hydroxide pellets (KOH, Alfa Aesar, 85%), hydrogen peroxide ($H_2O_2$, 30% (w/w) in $H_2O$, contains stabilizer, Sigma-Aldrich), sulfuric acid ($H_2SO_4$, 99.999%, Sigma-Aldrich), hydrofluoric acid (HF, ACS reagent 48%, Sigma-Aldrich), hydrochloric acid (HCl, reagent grade, 37%, Sigma-Aldrich), potassium hexacyanoferrate(II) trihydrate ($K_4Fe(CN)_6 \cdot 3H_2O$, ≥99% puriss. p.a., ACS reagent, Sigma-Aldrich), potassium hexacyanoferrate(III) ($K_3Fe(CN)_6$, ≥99% puriss. p.a., ACS reagent, Sigma-Aldrich). Water with resistivity 18.2 MΩ cm from Milli-Q integral ultrapure water (Merck Millipore).

### Preparation of substrates

Phosphorus-doped (n-type, (100)-oriented, single-side polished, resistivity 0.1-0.3 Ω cm, thickness 525 μm) and degenerately boron-doped ($p^+$-type, (100)-oriented, singe-side pol-

ished, resistivity < 0.005 Ω cm) Si wafers were purchased from Si-Mat. The n-type Si wafers were first cleaned in a piranha solution containing a mixture of $H_2SO_4$ and $H_2O_2$ (3:1 by volume ratio) at 120 °C for 20 minutes to remove organic contaminants. The n-type Si wafers were then dipped into a buffered HF etchant (2%) for 2 minutes at room temperature to strip the native oxide on the Si wafer surface. Next, the Si wafers were immersed in a Radio Corporation of America (RCA) Standard Clean-2 (SC-2) solution consisting of $H_2O$, HCl and $H_2O_2$ (5:1:1 by volume ratio) at 75 °C for 10 minutes to regrow the oxide layer ($SiO_x$). The same procedure was applied on the $p^+$-type Si wafers.

#### Atomic-layer deposition of aluminum oxides

Atomic-layer deposition (ALD) of aluminum oxides ($Al_2O_3$) was conducted in a home-built thermal ALD system (developed at AMOLF) at 250 °C at a base pressure of 0.01-0.05 mbar. The ALD cycle consisted of a 10 ms pulse of $H_2O$, a 18 s of $N_2$ purge, a 10 ms pulse of trimethylaluminum (TMA), and another 18 s of $N_2$ purge to complete the cycle. Eight ALD cycles were used to deposit 1 nm thick $Al_2O_3$ on an n-Si/$SiO_x$ substrate. In selected experiments, 24, 32 and 80 ALD cycles were used to deposit 2.7 nm, 3.9 nm and 8 nm layers of $Al_2O_3$, respectively. The thickness of the $Al_2O_3$ was estimated by ellipsometer (J.A. Woollam) using dielectric models for $Al_2O_3$ and Si native oxide on a Si substrate.

#### Sputter-deposition of metals

Platinum (Pt), nickel (Ni) and cobalt (Co) were deposited using Prevac radio frequency (rf) magnetron sputtering from a Pt, Ni and Co target, respectively (Mateck, 99.95%, 2 inch diameter, 5 mm thickness). The Ar flow was kept at 15 sccm and the working pressure was held at 3 μbar. For Pt deposition, the rf power was kept at 25 W and the deposition rate was approximately, 0.138 Å $s^{-1}$. For Ni and Co depositions, the rf power was 100 W, and the deposition rates were 0.2 Å $s^{-1}$ and 0.16 Å $s^{-1}$, respectively. Ti was deposited in AJA sputter chamber from a Ti target (Mateck, 99.95%, 2 inch diameter) using a direct current (dc) power. The Ar flow was maintained at 15 sccm and the working pressure was 3 μbar. The dc power for Ti deposition was 10 W.

#### Preparation of MIS devices

MIS devices were fabricated by depositing an $Al_2O_3$ layer onto n-Si wafers using ALD. The front Schottky contact of each MIS device was formed by depositing different metals, such as Pt, Ni, Co and Ti, each with a thickness of 60 nm. In separate experiments, a set of photoanodes were fabricated by depositing 2-nm thick inner metals (Pt, Ni, Co or Ti), followed by depositing 4 nm of Ni capping layer using low-power sputtering to ensure uniform deposition and homogeneous coverage. The back side of the n-Si wafers was scratched using sand paper to remove the oxide layer, followed by cleaning the residue using ethanol. Next, the ohmic back contact was formed by rubbing the back side surfaces of the Si wafers with an Ga-In alloy (75.5:24.5 wt%, 99.9% metal basis, Alfa Aesar). The ohmic back contact of the $p^+$-Si electrode was formed by sputtering Pt.

#### (Photo)electrochemical measurements

Photoelectrochemical measurement of the photoanode was conducted in a three electrode configuration in 1 M KOH electrolyte solution under simulated AM1.5 solar irradiation (100 mW $cm^{-2}$) using a Newport Sol3A Class AAA solar simulator (type 94023A-SR3) with 450 Watt xenon short arc lamp. A mercury/mercury oxide (Hg/HgO in 1 M KOH, Radiometer Analytical XR440, Hach) electrode was used as the reference electrode, and Ni coil was used as the counter electrode. The Hg/HgO electrode was calibrated using a sil-

ver/silver chloride (Ag/AgCl, in saturated KCl and AgCl, Radiometer Analytical XR300, Hach) reference electrode with a well-known potential with respect to the standard hydrogen potential ($V^0_{\mathrm{Ag/AgCl}\ \textit{versus}\ \mathrm{SHE}} = 0.199$ V), and had a potential of 0.9222 V *versus* the reversible hydrogen electrode (RHE) in 1 M KOH solution. The exposed area of the working electrode was 0.2826 $cm^2$. During the measurement, the electrolyte was continuously stirred using a magnetic stir bar. Cyclic voltammetry, electrochemical open-circuit, electrochemical impedance spectroscopy and chronoamperometry measurements were performed using a potentiostat PARSTAT MC (Princeton Applied Research, AMETEK). The cyclic voltammetry data were recorded at a constant scan rate of 50 mV $s^{-1}$ and the chronoamperometric data were collected at a constant potential of 1.7 V *versus* RHE.

#### Impedance spectroscopy

Solid-state impedance spectroscopy of MIS devices were performed by connecting of the front metal contact with the back metal contact. Impedance spectroscopy of MIS photoanodes with thin bimetal contacts were performed electrochemically in solution containing 50 mM $K_3Fe(CN)_6$, 350 mM $K_4Fe(CN)_6$ and 1 M KCl in a three electrode measurement using a Pt wire placed in a fritted glass tube as the reference electrode and a Pt coil as the counter electrode. The experimental setup was kept in the dark during the measurement.

## 4.3. Results and discussion

#### Schottky barrier height and effective pinning factor of MIS junction

The junction properties at the metal-insulator-semiconductor interfaces can be examined by modeling the current-potential ($j$–$V$) curves in the dark. A simple and realistic dark $j$–$V$ characteristic can be described by an implicit diode equation that takes into account the parallel resistance ($R_\mathrm{p}$) and the series resistance ($R_\mathrm{s}$) in Eq. 4.1:

$$j = j_0 \left[\exp\left(\frac{q\left(V - R_\mathrm{s} j\right)}{nkT}\right)\right] + \frac{V - R_\mathrm{s} j}{R_\mathrm{p}} \tag{4.1}$$

where $j$ is the dark current density, $j_0$ is the dark reverse saturation current density, $n$ is the diode ideality factor, $q$ is the elementary charge ($1.6 \times 10^{-19}$ C), $k$ is the Boltzmann's constant ($1.38 \times 10^{-23}$ $m^2$ kg $s^{-2}$ $K^{-1}$), $T$ is the temperature (293 K) and $V$ is the applied voltage. For an MIS junction with a large barrier height, the generation and recombination current in the space-charge region[13] can be more accurately modeled by adding a second diode in parallel connection with the first in an equivalent circuit (Fig. B.1, Appendix B) which is represented by the double-diode equation in (Eq. 4.2):

$$j = j_{01} \left[\exp\left(\frac{q\left(V - R_\mathrm{s} j\right)}{n_1 kT}\right)\right] + j_{02} \left[\exp\left(\frac{q\left(V - R_\mathrm{s} j\right)}{n_2 kT}\right)\right] + \frac{V - R_\mathrm{s} j}{R_\mathrm{p}} \tag{4.2}$$

Here, $j_{01}$ is the dark reverse saturation current density from the thermionic emission, $n_1$ is the diode ideality factor at high forward biases, $j_{02}$ is the dark saturation current density from trap-assisted recombination and generation processes at the space-charge region and $n_2$ is the diode ideality factor for recombination and generation current at low voltage biases.

Figure 4.1a shows the semi-logarithmic dark $j$–$V$ curves of the n-Si/$SiO_x$/$Al_2O_3$/'*metal*' systems. The symbols (open circles) indicate the measured data and the lines represent the fit results derived from Eq. 4.1 and Eq. 4.2. Positive applied voltages ($V > 0$) in the $j$–$V$ curve represent the forward bias region and negative voltages ($V < 0$) represent the reverse bias region. Four different metal contacts were investigated in our MIS structures; Pt, Ni,

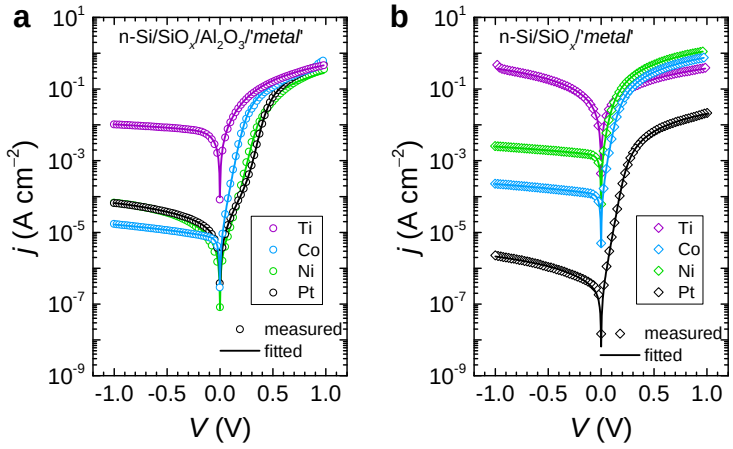



**Figure 4.1:** Dark $j$–$V$ curves of (a) the n-Si/$SiO_x$/$Al_2O_3$/'*metal*' and (b) the n-Si/$SiO_x$/'*metal*' systems. The thickness of each metal contact is 60 nm. Symbols represent the measured data and straight lines represent the fit results. Tabulated values of the extracted parameters are provided in Table B.1 and B.2, Appendix B.

Co and Ti with corresponding workfunctions of 5.6, 5.2, 5.0 and 4.3 eV, respectively.[14] The thickness of each metal was 60 nm, and the ellipsometrically-measured thickness of the oxide layers were approximately 1.8 nm for the chemical $SiO_x$ and 1 nm for the $Al_2O_3$. All the investigated devices exhibited rectifying behavior, as indicated by the weak voltage dependence of the reverse current, and the exponential increase of forward current with increasing applied voltage. The n-Si/$SiO_x$/$Al_2O_3$ with Pt and Ni contacts showed four distinct regions in each corresponding dark $j$–$V$ curve: a reverse bias region, two linear regions with different slopes at low and high forward biases, and a current limited region at very high forward biases. The four regions in the dark $j$–$V$ were simultaneously fitted using a two-diode model described in the Eq. 4.2. The n-Si/$SiO_x$/$Al_2O_3$ with Co and Ti contacts displayed only one linear curve in the intermediate region of forward bias, and thus the fitting procedure was performed using a single-diode model in Eq. 4.1. Figure 4.1b depicts representative dark $j$–$V$ characteristics of the n-Si/$SiO_x$/'*metal*' systems. All devices demonstrated a linear line in the intermediate forward bias region, and thus the $j$–$V$ responses were fitted using a single-diode equation. The n-Si/$SiO_x$ with Pt, Co and Ni contacts behaved as rectifying junctions, whereas the n-Si/$SiO_x$/Ti behaved as an ohmic contact, as indicated by the symmetry of $j$–$V$ curve in the forward and the reverse bias regions. From the fit results, the mean ideality factors were $n = 1.1$ for the n-Si/$SiO_x$/$Al_2O_3$/'*metal*' and $n = 1$ for the n-Si/$SiO_x$/'*metal*' systems.

The utility of Fig. 4.1a and b is that the barrier height can be extracted from the dark $j$–$V$ curve. In an intimate metal-semiconductor structure where thermionic emission is the dominant current transport mechanism,[15] the barrier height can be directly derived from the dark reverse saturation current using the classical thermionic emission theory. However, in the presence of an oxide layer at the interface, the current transport across the MIS junction is also governed by carrier tunneling through the oxide. To account for the contribution of tunneling conduction, the dark reverse saturation current of an MIS junction is given by the thermionic emission equation corrected for tunneling (see Appendix B.3 for the derivation of the equation):[16,17]

$$j_0 = A^* T^2 \exp\left(\frac{-q\phi_b}{kT}\right) \exp\left(-\sqrt{\chi}\delta\right) \tag{4.3}$$

where $A^*$ is the Richardson's constant (120 A cm$^{-2}$ K$^{-2}$ for Si), $\phi_b$ is the barrier height, $\chi$ (in eV) is the mean barrier height presented by the tunnel oxide (*i.e.*, the conduction band offset between the semiconductor and the oxide) and $\delta$ is the thickness of the oxide (in Å). The term $\exp(-\sqrt{\chi}\delta)$ is the transmission coefficient for electron tunneling through a one-dimensional rectangular barrier, and $\sqrt{\chi}\delta$ is the tunnel exponent (there is a constant (not shown) with a value ≈1 and units eV$^{-1/2}$ Å to make the exponent dimensionless).[16,17] Rearranging Eq. 4.3, the barrier height of an MIS junction is given by:

$$\phi_b = \frac{kT}{q}\left(\ln\left(\frac{A^* T^2}{j_0}\right) - \sqrt{\chi}\delta\right) \tag{4.4}$$

From Eq. 4.4, it is clear that the barrier height has a strong dependence on the $\sqrt{\chi}\delta$. In real situations where the interfacial oxide is very thin (*i.e.*, $\delta < 30$ Å), the experimental value of $\sqrt{\chi}\delta$ is appreciably different, and typically can be much lower than the theoretical quantity. This discrepancy has been largely attributed to the non-uniformities of the oxide layer and the inhomogeneous distribution of the oxide thickness.[18,19] Additionally, barrier lowering due to image charges (*i.e.*, image-force lowering) and the gradual disappearance of the band structure of a few atomic layers can also reduce the $\sqrt{\chi}\delta$.[20]

For an MIS junction consisting of multiple interfacial oxides such as in the devices shown in this work, the effective tunnel exponent $(\sqrt{\chi}\delta)_{\text{eff}}$ is not accurately known, and the barrier height cannot be explicitly derived from the dark reverse saturation current. Alternatively the barrier height can be estimated from Mott-Schottky analysis of the inverse square of the space-charge capacitance–voltage ($C_{sc}^{-2}$–$V$) of the electrode, measured using impedance spectroscopy (Fig. B.4, Appendix B). Independent determination of the barrier height allows the approximation of the $(\sqrt{\chi}\delta)_{\text{eff}}$ for multiple interfacial oxides using Eq. 4.4. Using the experimentally determined barrier heights from the Mott-Schottky relationship (Table B.4, Appendix B) and $j_0$ values from the fit results of Fig. 4.1b, and putting them into Eq. 4.4, the $\sqrt{\chi}\delta$ for MIS devices with an $SiO_x$ (1.8 nm) interlayer was estimated to be 1.2, close to the value reported previously for wet-chemical $SiO_2$ with the same thickness.[20] Using the same approach, the calculated values for $(\sqrt{\chi}\delta)_{\text{eff}}$ were approximately 1.6 for the n-Si/$SiO_x$ (1.8 nm)/$Al_2O_3$ (1 nm) in contact with Pt, Ni and Co, and 4 for the n-Si/$SiO_x$ (1.8 nm)/$Al_2O_3$ (1 nm) with Ti metal contact. The higher $(\sqrt{\chi}\delta)_{\text{eff}}$ for the n-Si/$SiO_x$/$Al_2O_3$/Ti is presumably due to the formation of an additional oxide layer as a result of oxidation at the $Al_2O_3$/Ti interface. High-workfunction metals such as Pt are resistant to oxidation, but low-workfunction metals such as Ti are extremely reactive and their surfaces may readily oxidize upon contact with an underlying oxide. Previous study has indicated that the tunnel barrier of the n-Si/$SiO_2$/metal system increases when a lower workfunction metal such as Al is used in comparison to the higher workfunction Au.[20] This may also be the case for the n-Si/$SiO_x$/$Al_2O_3$/Ti, considering both Ti and Al have similarly low workfunctions.

Figure 4.2a and b show the experimentally determined barrier height as a function of the metal workfunction for the n-Si/$SiO_x$/$Al_2O_3$/'*metal*' systems (solid circles) and the n-Si/$SiO_x$/'*metal*' systems (solid diamonds), respectively. For comparison, the barrier heights calculated using the previously determined $\sqrt{\chi}\delta)_{\text{eff}}$ and $j_0$ values in Eq. 4.4 are also presented as hollow stars. The barrier height of the n-Si/$SiO_x$/Ti was not obtained from the space-charge capacitance determination using impedance measurement due to a high leakage current, but a value close to 0.37 ± 0.02 eV is expected based on the calculation

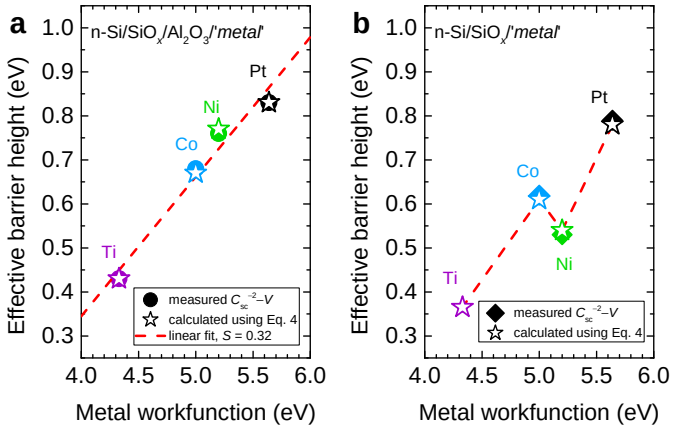



**Figure 4.2:** Effective barrier height as a function of the metal workfunction of (a) n-Si/$SiO_x$/$Al_2O_3$/'*metal*', and (b) n-Si/$SiO_x$/'*metal*' systems. Solid symbols are determined from Mott-Schottky analysis of the inverse square of the space-charge capacitance–voltage ($C_{sc}^{-2}$–$V$) of the electrode, measured using impedance spectroscopy, and open symbols are extracted using Eq. 4.4 from the fit results of Fig. 4.1. Mott-Schottky plots are shown in Fig. B.4, Appendix B.

using Eq. 4.4. An excellent linearity between the barrier height and the metal workfunction was observed on the n-Si/$SiO_x$/$Al_2O_3$/'*metal*' systems with a slope of 0.32. In the absence of $Al_2O_3$ insertion layer, a linear relation with nearly the same slope was only apparent on the n-Si/$SiO_x$ in contact with Pt, Co and Ti, while a large deviation was observed when using a Ni contact which exhibited a lower barrier height than that expected from the linear trend with the metal workfunction. In general, with the exception of the n-Si/$SiO_x$/Ni, the incorporation of 1-nm-thick $Al_2O_3$ increased the barrier height by 0.05 ± 0.01 eV.

The slope of the linear trend between the barrier height and the metal workfunction ($S = d\phi_b/d\Phi_m$) is indicative of the effective pinning factor for the MIS contact that ranges from 0 for perfect pinning to 1 for no pinning.[21] In an MIS structure, Fermi level pinning effect typically arises from two distinct contributions: (i) the existence of interfacial trap states at semiconductor-oxide interface and (ii) the movement of the metal Fermi level due to occupation of intrinsic states at the surface of the oxide layer by metal electrons (*i.e.*, metal Fermi level pinning). While the former tends to pin the semiconductor Fermi level to the interface states, the latter tends to alter the effective value of metal workfunction which, in most cases, differs appreciably from the value in vacuum. It should be noted that the $S$ parameter of a dielectric material (*i.e.*, the oxide layer) should be distinguished from the effective $S$ parameter of an MIS structure as a whole because interface states exist both at the metal-insulator and the insulator-semiconductor interfaces.[22] For example, the $Al_2O_3$ has been reported to have a dielectric $S$ parameter between 0.63 and 0.69,[23] but the effective $S$ parameter of an MIS junction employing an $Al_2O_3$ interfacial dielectric would be considerably different.

Previous empirical and experimental studies have shown that intimate contact between an n-Si and a metal results in a nearly complete pinning of the Fermi level with an effective $S$ parameter as small as 0.075.[24,25] The effective $S$ parameter of 0.32 for the n-Si/$SiO_x$/$Al_2O_3$/'*metal*' systems, therefore, underlines the ability of the oxide layers to alleviate the pinning of Fermi level within the n-Si-based MIS junction. In addition to intrinsic states, extrinsic defect states may also arise from the interfacial reaction between the

metal and the oxide, and may contribute to the modification of metal workfunction.[23] The existence of extrinsic defect states within an MIS contact is typically indicated by a large deviation of barrier height from the linear trend with varying metal workfunction.[22,23] We note however, that of all the MIS devices investigated herein, such a deviation only occurs on the n-Si/$SiO_x$/Ni. As the barrier height of other n-Si/$SiO_x$/'*metal*' systems exhibits a positive linear scaling with increasing metal workfunction, it may suggest that the distribution of the extrinsic defect states arising from the interfacial chemical reaction is metal-dependent. By introducing the $Al_2O_3$ interfacial layer, such a deviation can be eliminated, thus suggesting that the formation of defect-related states is considerably hindered.

#### Schottky barrier height and effective pinning factor of MIS photoanodes with thin bimetal contacts

In an effort to directly evaluate the effect of $Al_2O_3$ interlayer on the photoanode, a series of bimetallic MIS electrodes were fabricated by depositing 2 nm of various inner metals to serve as the Schottky contact, and 4 nm of Ni outer metal to serve as the catalyst and protection overlayer. The front metal contacts were designed very thin to avoid significant optical losses for high photocurrent generation without compromising the protection ability to prevent corrosion and to promote catalytic reaction of water oxidation. Because of the inability to directly probe the ultrathin metal contact (*i.e.*, total thickness of 6 nm), impedance measurements for barrier height determination were performed electrochemically in a solution containing electrochemically reversible, one-electron ferri/ferrocyanide ($Fe(CN)_6^{3-/4-}$) redox couple (Fig. B.5, Appendix B). Afterwards, all electrodes were subjected to contact with 1 M of potassium hydroxide (KOH) solution for at least 24 hours (from hereafter called the aging process). Impedance measurements were then repeated to estimate the barrier heights of all electrodes.

Figure 4.3a shows the effective barrier height of the n-Si/$SiO_x$/$Al_2O_3$/'*inner metal*'/Ni photoanodes as a function of inner metal workfunction. Barrier height shifts were observed on MIS electrodes with thin bimetal contact in comparison to structures with a thick single layer metal contact. For example, the barrier height of the n-Si/$SiO_x$/$Al_2O_3$/Pt (2 nm)/Ni (4 nm) was slightly lower than the n-Si/$SiO_x$/$Al_2O_3$/Pt (60 nm) (Fig. B.6, Appendix B). In bimetal Schottky structures, the shift of barrier height is closely related to the ineffective metal screening by the ultrathin inner metal, which is largely affected by the outer metal workfunction. The theoretical Thomas-Fermi screening length is 0.7 Å for most metals[26] but previous experimental study has shown that the extent of inner metal band bending in a bimetal Schottky diode can exceed 1.5 nm.[27] Considering the thickness of our inner metal is only 2 nm, the bimetal effective workfunction is expected to shift toward the value of the outer metal workfunction. Additionally, we also cannot rule out the possibility that interfacial diffusion of inner metal may occur either to the underlying oxide or to the outer metal (*i.e.*, metal interdiffusion), which can potentially alter the effective workfunction of the bimetal structure.

Figure 4.3a also indicates that the effective barrier height of all electrodes increased after aging process. Such an increase of barrier height is ascribed to the transition of workfunction of the surface layer due to incidental oxidation of Ni to nickel oxide/nickel dihydroxide (NiO/$Ni(OH)_2$) after prolonged contact with KOH electrolyte.[1,10] The vacuum workfunction of NiO or $NiO_x$ is typically between 5.2 and 5.6 eV, and depending on the processing conditions and/or post-treatments, the value can be as high as 6.7 eV.[28,29] Furthermore, the thickness of the surface layer should increase as a result of Ni lattice expansion upon transformation to $NiO_x$.[12,30] Such an increase of surface layer thickness

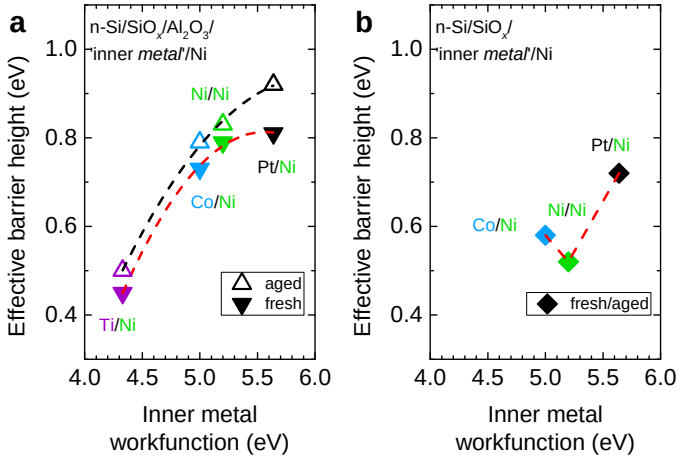



**Figure 4.3:** Effective barrier height as a function of inner metal workfunction of the n-Si/'*oxide*'/bimetal photoanodes with (a) both $SiO_x/Al_2O_3$, and (b) only $SiO_x$ interfacial layer. Barrier heights are determined from Mott-Schottky analysis of the inverse square of the space-charge capacitance–voltage ($C_{sc}^{-2}$–$V$) of the electrode, measured using impedance spectroscopy. The thickness of each inner metal is 2 nm and the thickness of the Ni outer metal is 4 nm. Mott-Schottky plots are shown in Fig. B.5, Appendix B.

is then expected to extend the modulation of the bimetal effective workfunction, and thus the shift of the barrier height of a Schottky junction. Measurement results and analysis of a test device employing a sputtered NiO from a NiO target on the n-Si/$SiO_x$/$Al_2O_3$/Pt structure also concurred with the conjecture that the barrier height of the MIS electrode was indeed larger when a NiO front surface layer was used in place of Ni film (Fig. B.7, Appendix B).

Figure 4.3b shows the effective barrier height of the n-Si/$SiO_x$/'*inner metal*'/Ni without an $Al_2O_3$ interlayer. No substantial variation of barrier height was apparent between the fresh and the aged electrodes. The effective barrier height of the n-Si/$SiO_x$ with thin bilayer metal contacts exhibited a non-ideal scaling when changing inner metal workfunction in a fashion similar to those observed with a single thick metal contact (Fig. 4.2b), regardless of the presence of the secondary outer metal, even after oxidation of Ni surface layer in KOH. Impedance characterization technique failed to measure the capacitance of the n-Si/$SiO_x$/Ti/Ni for barrier height determination due to the non-rectifying behavior of the junction which resulted in a high leakage current, but a barrier height of close to 0.37 eV is expected based on the assumption of a similar trend in Fig. 4.2b and Fig. 4.3b. Given the fact that the effective barrier heights of all n-Si/$SiO_x$/'*inner metal*'/Ni electrodes remain constant despite the oxidation of the outer Ni, which should increase due to increasing effective workfunction of the surface layer, the Fermi level seems to strongly pin at the interface states that are most likely to be metal-dependent.

### PEC performance of MIS photoanodes

The photoelectrochemical activity of the MIS photoanodes was examined by performing cyclic voltammetry in 1 M KOH solution under simulated solar irradiation. Figure 4.4a shows $j$–$V$ curves of the illuminated n-Si/$SiO_x$/$Al_2O_3$/'*inner metal*'/Ni photoanodes after

the aging process in 1 M KOH electrolyte. Among all inner metals investigated in this work, the most negative photocurrent onset potential (defined as the potential required to achieve an anodic current of 100 μA $cm^{-2}$) was achieved by the photoanode with Pt inner metal (−270 mV relative to the formal potential for water oxidation, $E^{0\prime}$ ($O_2/OH^-$) = 1.23 V *versus* a reversible hydrogen electrode, RHE) and the most positive potential of photocurrent onset was observed on the photoanode with inner Ti (+140 mV relative to $E^{0\prime}$ ($O_2/OH^-$). In the absence of light, the photoanodes with inner Pt, Ni and Co exhibited nearly zero current, whereas a non-negligible dark current was observed on the photoanode with inner Ti. This non-zero dark current is consistent with the lower barrier height of the n-Si/$SiO_x$/Ti/Ni which increases the leakage current under reverse bias condition in a solid-state measurement or under anodic potential bias in an electrochemical measurement.

Figure 4.4b depicts *j*–*V* curves of the n-Si/$SiO_x$/'*inner metal*'/Ni photoanodes. Without $Al_2O_3$, all MIS photoanodes showed significant positive shifts of photocurrent onset potential for water oxidation. Even with Pt as the inner metal, the was only −50 mV relative to $E^{0\prime}$ ($O_2/OH^-$). A considerable dark leakage current was observed on the photoanode with only Ni contact due to the low barrier height of the n-Si/$SiO_x$/Ni, in agreement with the thermionic emission theory described in Eq. 4.3. The photoactivity of the photoanode, generally indicated by the photocurrent plateau at sufficiently positive potentials, was not apparent on the n-Si/$SiO_x$/Ti/Ni. Both illuminated and dark *j*–*V* responses were identical, and showed a behavior typically displayed by a non-photoactive electrode for water oxidation. These results clearly indicate that the photovoltage of the n-Si/$SiO_x$/Ti/Ni was indeed zero.

Figure 4.4c summarizes the photovoltage of the n-Si/$SiO_x$/$Al_2O_3$/'*inner metal*'/Ni photoanodes as a function of the inner metal workfunction. The photovoltage was determined from the difference in anodic current onset potential between the illuminated photoanode and the non-photoactive $p^+$-Si/$SiO_x$/Ni in Fig. 4.4a and b. Electrochemical open-circuit measurements in the dark and under illumination were also performed before and after aging in KOH to confirm the photovoltage (Fig. B.8, Appendix B), and revealed identical values as those measured using the aforementioned approach. The photovoltage of the n-Si/$SiO_x$/$Al_2O_3$/'*inner metal*'/Ni photoanodes showed a positive linear scaling with increasing inner metal work function. Consistent with the increase of barrier height, the photovoltage of all MIS photoanodes increased upon oxidation of Ni surface layer in KOH. The highest photovoltage was achieved by the n-Si/$SiO_x$/$Al_2O_3$/Pt/Ni after aging, reaching a value of 520 mV. In the absence of $Al_2O_3$ interlayer, all photoanodes exhibited lower photovoltages, and showed almost no photovoltage shift after prolonged contact in KOH (Fig. 4.4d), in close agreement with their barrier heights that remained constant upon aging (Fig. 4.3b).

During the aging process in KOH solution, all photoanodes remained stable, and the total metal thickness of 6 nm did not seem to allow for electrolyte permeation to the underlying oxide layers. Previous report has shown that the as-deposited $Al_2O_3$ by ALD is chemically unstable in 1 M KOH and undergoes rapid dissolution upon contact with a strongly alkaline solution.[31] The dissolution of $Al_2O_3$ may lead to the delamination of the metal overlayers, which may result in the degradation of photovoltage and subsequently the deactivation of the photoelectrode. The X-ray photoelectron spectroscopy (XPS) depth profiling on the device consisting of n-Si/$SiO_x$ (1.8 nm)/$Al_2O_3$ (1 nm)/Pt (2 nm)/Ni (4 nm) has indicated that the Pt/Ni overlayers had transformed into Pt/Ni/NiO/Ni$(OH)_2$ and that the $Al_2O_3$ remained intact in the structure after 18 hours in 1 M KOH.[1] Without metal overlayers, no XPS peak corresponding to $Al_2O_3$ was observed after 1 hour in 1 M KOH, indicating that the $Al_2O_3$ had rapidly dissolved in an alkaline solution.[1]

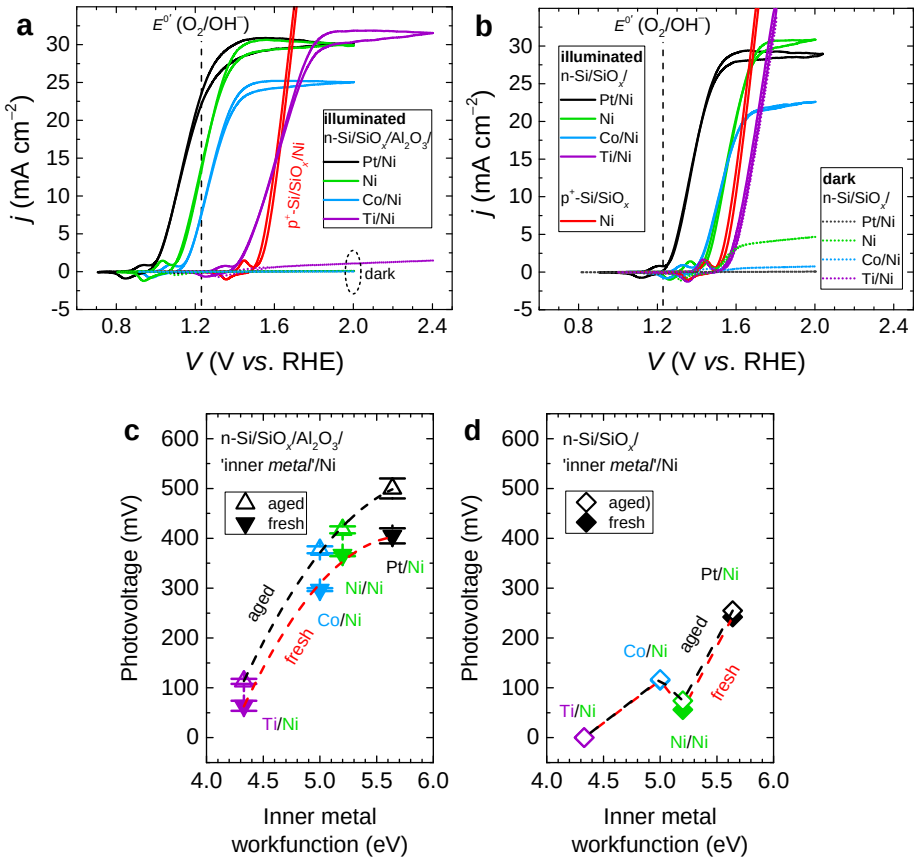



**Figure 4.4:** Representative current–potential ($j$–$V$) characteristics of (a) n-Si/$SiO_x$/$Al_2O_3$/'*inner metal*'/Ni, and (b) n-Si/$SiO_x$/'*inner metal*'/Ni photoanodes after aging, measured in 1 M KOH solution under simulated solar illumination (solid lines). Dark currents are indicated by the dotted lines of the same color. The vertical dashed line indicates the formal potential for water oxidation ($E^{0\prime}$ ($O_2$/$OH^-$) = 1.23 V *versus* the reversible hydrogen electrode (RHE)). The $j$–$V$ behavior of the non-photoactive p$^+$-Si/$SiO_x$/Ni is also shown. The photovoltage as a function of inner metal workfunction of (c) n-Si/$SiO_x$/$Al_2O_3$/'*inner metal*'/Ni, and (d) n-Si/$SiO_x$/$Al_2O_3$/'*inner metal*'/Ni photoanodes. The thickness of the inner metal and the outer Ni are 2 nm and 4 nm respectively.

The theoretical photovoltage ($V_{\mathrm{ph}}$) of an MIS photoanode can be calculated using the following equation:

$$V_{\mathrm{ph}} = \frac{nkT}{q} \ln\left(\frac{j_{\mathrm{ph}}}{j_0}\right) \tag{4.5}$$

where $j_{\mathrm{ph}}$ is the light-limited photocurrent density. The relation between the photovoltage and the barrier height can be obtained by substituting Eq. 4.3 with Eq. 4.5:

$$V_{\mathrm{ph}} = \frac{nkT}{q} \left(\ln\left(\frac{j_{\mathrm{ph}}}{A^* T^2}\right) + \frac{q\phi_{\mathrm{b}}}{kT} + \sqrt{\chi}\delta\right) \tag{4.6}$$

The mean parameters are assumed to be the same as previously obtained for MIS devices with thick metal contacts: $n = 1$ and $\sqrt{\chi}\delta = 1.2$ for the n-Si/$SiO_x$/'*inner metal*'/Ni, and $n$ = 1.1 and $(\sqrt{\chi}\delta)_{\text{eff}} = 1.6$ for the n-Si/$SiO_x$/$Al_2O_3$/'*inner metal*'/Ni photoanodes. As indicated in Fig. 4.5, the theoretical model (Eq. 4.6) predicts the photovoltages accurately for the given barrier heights, except for the n-Si/$SiO_x$/$Al_2O_3$/Ti/Ni (*i.e.*, the two red circles at the bottom left corner, because the the tunnel exponent for this particular structure is slightly higher (*i.e.*, $(\sqrt{\chi}\delta)_{\text{eff}} = 4$), but using this value will actually give accurate results, see Fig. B.9, Appendix B). Clearly, the increase of photovoltage upon the addition of $Al_2O_3$ onto the $SiO_x$ interface layer is related to the lower dark reverse saturation current, which depends not only on the barrier height, but also on the oxide thickness. In the absence of an oxide interlayer, the photovoltage will be substantially lower (hypothetical relation between the photovoltage and the barrier height of metal-semiconductor photoanodes without an interfacial oxide is indicated by the dashed blue line).

Equation 4.6 also suggests that the photovoltage will increase with a higher ideality factor. From the fit results of dark $j$–$V$ curves in Fig. 4.1, the mean ideality factor of the n-Si/$SiO_x$/$Al_2O_3$/'*metal*' is indeed higher than that of the same structure without $Al_2O_3$ (*i.e.*, $n_{SiO_x/Al_2O_3} = 1.1$, $n_{SiO_x} = 1$). This is because the ideality factor increases with increasing oxide thickness, as expressed by:[17,32]

$$n = 1 + \left(\frac{\delta}{\epsilon_i}\right) \frac{(\epsilon_s / W) + qD_{it,s}}{1 + (\delta/\epsilon_i)\, qD_{it,m}} \tag{4.7}$$

where $\epsilon_i$ is the dielectric permittivity of the interfacial oxide, $\epsilon_s$ is the dielectric permittivity of the semiconductor, $W$ is the space-charge width of the semiconductor. The $D_{it,s}$ and $D_{it,m}$ are the density of interface states in equilibrium with the semiconductor and the metal, respectively. For an MIS structure with a very thin oxide, such as the n-Si/$SiO_x$ (1.8 nm)/'*metal*' systems investigated in this work, the charge exchange between the interface states and the metal is relatively easier than with the semiconductor, and thus the

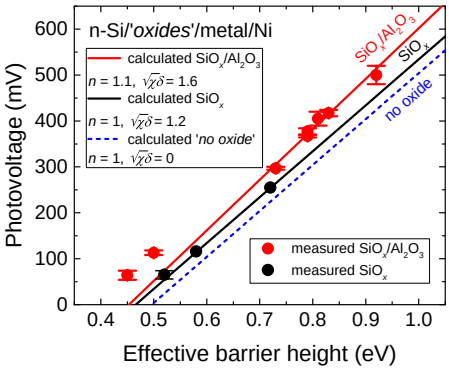



**Figure 4.5:** Measured photovoltage as a function of the effective barrier height of MIS photoanodes using only $SiO_x$ (black circles) and $SiO_x/Al_2O_3$ (red circles) interfacial layers. For comparison, the calculated photovoltage as a function of barrier height using Eq. 4.6 is shown (black and red lines). Parameters used for MIS systems using only $SiO_x$ include an ideality factor, $n = 1$ and a tunnel exponent, $\sqrt{\chi}\delta = 1.2$. For MIS devices with $SiO_x/Al_2O_3$, the $n = 1.1$ and the $(\sqrt{\chi}\delta)_{\text{eff}} = 1.6$. For comparison the hypothetical photovoltage of metal-insulator photoanode without an interfacial oxide is shown (blue dashed line).

population of interface states is controlled by the metal, so that $D_{\mathrm{it,s}}$ is almost negligible. In a situation where $D_{\mathrm{it,m}}$ is very large, the ideality factor will be close to unity. For thicker oxides, such as the n-Si/$SiO_x$ (1.8 nm)/$Al_2O_3$ (1 nm)/'*metal*' systems, charge exchange between the interface states and the metal decreases by the total oxide thickness, and thus the interface states will partially equilibrate with the semiconductor. In a simple formalism where $D_{\mathrm{it,}}$ equals to the sum of $D_{\mathrm{it,s}}$ and $D_{\mathrm{it,m}}$,[33] introducing an $Al_2O_3$ to the existing $SiO_x$ will increase $D_{\mathrm{it,s}}$ by the same amount that reduces $D_{\mathrm{it,m}}$. As a result, the ideality factor will depart from unity.

So far, the analysis presented above have assumed that the barrier height and the ideality factor remain constant under illumination. In practice, their values in the dark can be different from those under illumination. In the former case, the potential drop in the oxide layer is partly controlled by charging/discharging of interface states with applied bias, whereas in the latter case the potential drop is influenced by the injection of minority carriers into the interface states. Considering the excellent agreement between the experimental and theoretically calculated values of our device photovoltage, the change of barrier height and ideality factor should be negligibly small under illumination. Further complications that are not discussed here arise from the fact that the interfacial oxide can either increase or decrease the barrier height, depending on the polarity of the charge induced by the oxide. The $Al_2O_3$ is known to exhibit a fixed negative charge,[34–36] and if used with an n-type semiconductor can lead to a field-effect passivation of the underlying surface. This can also be the origin of the barrier height shift (Fig. B.10, Appendix B) and thus the photovoltage improvement of the n-Si/$SiO_x$/$Al_2O_3$/'*metal*'/Ni photoanodes.

Figure 4.6a and b shows that increasing the oxide thickness improved the MIS junction photovoltage. For the n-Si/$SiO_x$/$Al_2O_3$/Pt/Ni photoanode, the photovoltage reached a maximum value of 538 mV as the $Al_2O_3$ thickness increased to 2.7 nm. Further increase of $Al_2O_3$ thickness diminished the photovoltage due to the decrease of barrier height (Fig. B.10, Appendix B). As the $Al_2O_3$ became much thicker, the tunneling barrier also increased to such an extent that it suppressed the photocurrent. We note that the behavior of our device is distinct as compared to the previously reported n-Si/$SiO_2$/$Al_2O_3$/Ir photoanode whose photovoltage rapidly drops with a small increase of $Al_2O_3$ thickness.[5,37] A relatively high photocurrent observed with an $Al_2O_3$ thickness of 3.9 nm (measured by ellipsometer) indicates that our $Al_2O_3$ is rather conductive. A high leakage current has been frequently observed on $Al_2O_3$ films deposited by thermal ALD, and has been experimentally attributed to the hydrogen incorporation during the deposition in a system involving hydrogen-containing oxygen precursor such as $H_2O$.[38–41] According to density functional theory (DFT) calculations, interstitial hydrogen in $Al_2O_3$ can introduce a defect level near midgap that enables electronic conduction through the oxide.[42] The carrier lifetime in this energy level is brief, and therefore the tunneling conductivity is sensitive to oxide thickness. Since our $Al_2O_3$ films were deposited by thermal ALD and using $H_2O$ oxygen precursor, therefore, it is reasonable that the same mechanism of defect-mediated conduction within the hydrogen-contaminated $Al_2O_3$ film governs the carrier transport, which allows for the passage of high photocurrent within thick tunnel oxide interlayers.

Improvements of photovoltage by controlling the interfacial $SiO_2$ thickness have been observed in Schottky junction solar cells[43–45] and MIS photoelectrodes.[11,12] However, many of these devices require a high precision of interfacial oxide thickness with subnanometer accuracy to improve the photovoltage without compromising the tunneling current in the oxide layer. For highly resistive oxides such as $SiO_2$, a small thickness increase of a few angstrom can lead to significant carrier recombination and photocurrent suppression, which will result in a reduced fill factor and a drop of photovoltage. On

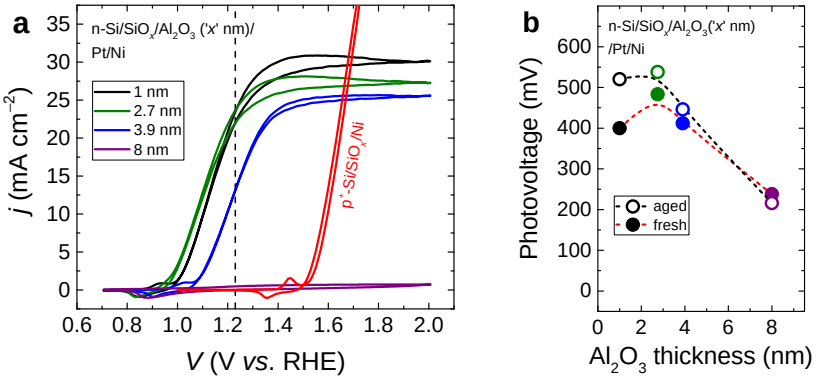



**Figure 4.6:** (a) Representatives $j$–$V$ curves, and (b) photovoltages of the n-Si/$SiO_x$/$Al_2O_3$/Pt/Ni photoanodes with various $Al_2O_3$ thicknesses. The photovoltage was determined by comparing the anodic current onset potential of the MIS photoanodes under illumination and the non-photoactive $p^+$-Si/$SiO_x$/Ni electrode in the dark.

the other hand, the leaky characteristic of our $Al_2O_3$ offers the flexibility and a better control to optimize the oxide interlayer thickness without losing too much photocurrent. Other interfacial oxide materials that show similar tunneling properties include titanium dioxide ($TiO_2$),[5,6,37,46] graphene oxide (GO)[47] and cobalt oxide ($CoO_x$).[48] This highlights the importance of using a conductive tunnel dielectric to achieve a highly efficient MIS photoelectrode.

## 4.4. Conclusions

In summary we have demonstrated the role of interfacial oxides and metal workfunction in improving the photovoltage of MIS junction photoanodes. The use of a thin chemically-grown $SiO_x$ at the metal-semiconductor interface is evidently not sufficient to favorably shift the Schottky barrier height. Depending on the metal used, the thin $SiO_x$ can facilitate the formation of extrinsic defect states that reduces the metal effective workfunction and subsequently decreases the barrier height. Adding supplementary oxide such as $Al_2O_3$ to the interfacial $SiO_x$ can eliminate the development of extrinsic defect states and simultaneously increase the barrier height which is advantageous for increasing the photovoltage. The improvement of photovoltage upon the addition of interfacial oxide is also found to be partly a result of the reduced dark reverse saturation current which is not solely determined by the MIS barrier height but also by the oxide thickness. With an optimum thickness, the interfacial oxides reduce the majority-carrier thermionic emission current without significantly affecting the minority carrier-injection, thereby improving the photovoltage of the MIS photoanode.

The results and analysis presented herein also attempt to serve as guidelines for designing bimetal-insulator-semiconductor photoanodes with realistically achievable photovoltages. The photovoltage dependence on inner metal workfunction indicates that a high workfunction metal such as Pt is fundamentally required to achieve a highly efficient MIS photoanode with bilayer metal contacts. Using a lower workfunction inner metal substantially sacrifices the photovoltage in a trade-off for a lower cost inherent to the natural

abundance of the low-workfunction metals. Most high workfunction metals such as Pt and Ir are indeed scarce, but the seek for Schottky contact candidates should not be limited to only materials in the metallic form. Transition metal oxides such as molybdenum trioxide ($MoO_3$), chromium trioxide ($CrO_3$), vanadium pentoxide ($V_2O_5$), tungsten trioxide ($WO_3$) and NiO are relatively cheap and known to have high workfunctions, exceeding the workfunction of noble metals.[29,49] Therefore, research directions should be guided toward the development and the use of these metal oxides as carrier-selective contacts for buried, rectifying junction photoanodes. Some of these oxides may have poor chemical stability and inferior catalytic activity, but with the rapid advancements in the protection and catalytic layer research and their successful implementations in a wide variety of photoelectrodes, a cheap, chemically stable and highly efficient photoanode can be achieved with all earth-abundant materials.

## References


[1] I. A. Digdaya, G. W. P. Adhyaksa, B. J. Trzesniewski, E. C. Garnett, and W. A. Smith, *Interfacial engineering of metal-insulator-semiconductor junctions for efficient and stable photoelectrochemical water oxidation,* Nature Communications **8**, 15968 (2017).

[2] N. Armaroli and V. Balzani, *The Hydrogen Issue,* ChemSusChem **4**, 21 (2011).

[3] M. Green, *Limits on the open-circuit voltage and efficiency of silicon solar cells imposed by intrinsic Auger processes,* IEEE Transactions on Electron Devices **31**, 671 (1984).

[4] *Non p-n junction solar cells using carrier selective contacts*, Vol. 8620 (2013).

[5] A. G. Scheuermann, J. P. Lawrence, A. C. Meng, K. Tang, O. L. Hendricks, C. E. D. Chidsey, and P. C. McIntyre, *Titanium Oxide Crystallization and Interface Defect Passivation for High Performance Insulator-Protected Schottky Junction MIS Photoanodes,* ACS Applied Materials & Interfaces **8**, 14596 (2016).

[6] A. G. Scheuermann, J. P. Lawrence, K. W. Kemp, T. Ito, A. Walsh, C. E. D. Chidsey, P. K. Hurley, and P. C. McIntyre, *Design principles for maximizing photovoltage in metal-oxide-protected water-splitting photoanodes,* Nature Materials **15**, 99 (2015).

[7] R. Singh, M. Green, and K. Rajkanan, *Review of conductor-insulator-semiconductor (CIS) solar cells,* Solar Cells **3**, 95 (1981).

[8] D. V. Esposito, I. Levin, T. P. Moffat, and a. A. Talin, *H2 evolution at Si-based metal–insulator–semiconductor photoelectrodes enhanced by inversion channel charge collection and H spillover,* Nature Materials **12**, 562 (2013).

[9] L. Ji, M. D. McDaniel, S. Wang, A. B. Posadas, X. Li, H. Huang, J. C. Lee, A. A. Demkov, A. J. Bard, J. G. Ekerdt, and E. T. Yu, *A silicon-based photocathode for water reduction with an epitaxial $SrTiO_3$ protection layer and a nanostructured catalyst,* Nature Nanotechnology **10**, 84 (2014).

[10] M. J. Kenney, M. Gong, Y. Li, J. Z. Wu, J. Feng, M. Lanza, and H. Dai, *High-Performance Silicon Photoanodes Passivated with Ultrathin Nickel Films for Water Oxidation,* Science **342**, 836 (2013).

[11] F. A. L. Laskowski, M. R. Nellist, R. Venkatkarthick, and S. W. Boettcher, *Junction behavior of n-Si photoanodes protected by thin Ni elucidated from dual working electrode photoelectrochemistry,* Energy Environ. Sci. **10**, 570 (2017).

[12] T. Han, Y. Shi, X. Song, A. Mio, L. Valenti, F. Hui, S. Privitera, S. Lombardo, and M. Lanza, *Ageing mechanisms of highly active and stable nickel-coated silicon photoanodes for water splitting,* J. Mater. Chem. A **4**, 8053 (2016).

[13] *Carrier generation and recombination in p-n junctions and p-n junction characteristics*, Vol. 45 (1957).

[14] H. B. Michaelson, *The work function of the elements and its periodicity,* Journal of Applied Physics **48**, 4729 (1977).

[15] *Metal-semiconductor contacts*, Vol. 129 (1982).

[16] H. Card, *Photovoltaic properties of MIS-Schottky barriers,* Solid-State Electronics **20**, 971 (1977).

[17] H. C. Card and E. H. Rhoderick, *Studies of tunnel MOS diodes I. Interface effects in silicon Schottky diodes,* Journal of Physics D: Applied Physics **4**, 319 (1971).

[18] Z. Hurych, *Influence of non-uniform thickness of dielectric layers on capacitance and tunnel currents,* Solid-State Electronics **9**, 967 (1966).

[19] P. Bhatnagar, K. Sharma, V. Ojha, and G. Srivastava, *A modified expression for the tunnelling exponent in Schottky barriers,* Solar Cells **5**, 301 (1981).

[20] H. Card, *Potential barriers to electron tunnelling in ultra-thin films of $SiO_2$,* Solid State Communications **14**, 1011 (1974).

[21] W. Mönch, *Role of virtual gap states and defects in metal-semiconductor contacts,* Physical Review Letters **58**, 1260 (1987).

[22] W. Mönch, *On the alleviation of Fermi-level pinning by ultrathin insulator layers in Schottky contacts,* Journal of Applied Physics **111**, 073706 (2012).

[23] Y.-C. Yeo, T.-J. King, and C. Hu, *Metal-dielectric band alignment and its implications for metal gate complementary metal-oxide-semiconductor technology,* Journal of Applied Physics **92**, 7266 (2002).

[24] A. Agrawal, J. Lin, M. Barth, R. White, B. Zheng, S. Chopra, S. Gupta, K. Wang, J. Gelatos, S. E. Mohney, and S. Datta, *Fermi level depinning and contact resistivity reduction using a reduced titania interlayer in n-silicon metal-insulator-semiconductor ohmic contacts,* Applied Physics Letters **104**, 112101 (2014).

[25] R. Islam, G. Shine, and K. C. Saraswat, *Schottky barrier height reduction for holes by Fermi level depinning using metal/nickel oxide/silicon contacts,* Applied Physics Letters **105** (2014), 10.1063/1.4901193.

[26] N. F. Mott and H. Jones, *The theory of the properties of metals and alloys*, Vol. 111 (Dover, 1958).

[27] X. Wu and E. S. Yang, *Effective Metal Screening and Schottky-Barrier Formation in Metal-GaAs Structures,* IEEE Electron Device Letters **11**, 315 (1990).

[28] M. T. Greiner, M. G. Helander, Z.-B. Wang, W.-M. Tang, and Z.-H. Lu, *Effects of Processing Conditions on the Work Function and Energy-Level Alignment of NiO Thin Films,* The Journal of Physical Chemistry C **114**, 19777 (2010).

[29] M. T. Greiner and Z.-H. Lu, *Thin-film metal oxides in organic semiconductor devices: their electronic structures, work functions and interfaces,* NPG Asia Materials **5**, e55 (2013).

[30] L. De Los Santos Valladares, A. Ionescu, S. Holmes, C. H. W. Barnes, A. Bustamante Domínguez, O. Avalos Quispe, J. C. González, S. Milana, M. Barbone, A. C. Ferrari, H. Ramos, and Y. Majima, *Characterization of Ni thin films following thermal oxidation in air,* Journal of Vacuum Science & Technology B, Nanotechnology and Microelectronics: Materials, Processing, Measurement, and Phenomena **32**, 051808 (2014).

[31] G. C. Correa, B. Bao, and N. C. Strandwitz, *Chemical Stability of Titania and Alumina Thin Films Formed by Atomic Layer Deposition,* ACS Applied Materials & Interfaces **7**, 14816 (2015).

[32] S. M. Sze and K. K. Ng, *Physics of Semiconductor Devices* (Wiley-Interscience, 2007).

[33] H. C. Card and E. H. Rhoderick, *Studies of tunnel MOS diodes II. Thermal equilibrium considerations,* Journal of Physics D: Applied Physics **4**, 320 (1971).

[34] G. Dingemans and W. M. M. Kessels, *Status and prospects of Al2O3-based surface passivation schemes for silicon solar cells,* Journal of Vacuum Science & Technology A: Vacuum, Surfaces, and Films **30**, 040802 (2012).

[35] D. K. Simon, P. M. Jordan, T. Mikolajick, and I. Dirnstorfer, *On the Control of the Fixed Charge Densities in $Al_2O_3$-Based Silicon Surface Passivation Schemes,* ACS Applied Materials & Interfaces **7**, 28215 (2015).

[36] F. Werner, B. Veith, D. Zielke, L. Kühnemund, C. Tegenkamp, M. Seibt, R. Brendel, and J. Schmidt, *Electronic and chemical properties of the c-Si/$Al_2O_3$ interface,* Journal of Applied Physics **109**, 113701 (2011).

[37] A. G. Scheuermann, K. W. Kemp, K. Tang, D. Q. Lu, P. F. Satterthwaite, T. Ito, C. E. D. Chidsey, and P. C. McIntyre, *Conductance and capacitance of bilayer protective oxides for silicon water splitting anodes,* Energy Environ. Sci. **9**, 504 (2016).

[38] K. B. Jinesh, J. L. van Hemmen, M. C. M. van de Sanden, F. Roozeboom, J. H. Klootwijk, W. F. A. Besling, and W. M. M. Kessels, *Dielectric properties of thermal and plasma-assisted atomic layer deposited $Al_2O_3$ thin films,* Journal of The Electrochemical Society **158**, G21 (2011).

[39] L. Aarik, T. Arroval, R. Rammula, H. Mändar, V. Sammelselg, B. Hudec, K. Hušeková, K. Fröhlich, and J. Aarik, *Atomic layer deposition of high-quality $Al_2O_3$ and Al-doped $TiO_2$ thin films from hydrogen-free precursors,* Thin Solid Films **565**, 19 (2014).

[40] S.-C. Ha, E. Choi, S.-H. Kim, and J. Sung Roh, *Influence of oxidant source on the property of atomic layer deposited $Al_2O_3$ on hydrogen-terminated Si substrate,* Thin Solid Films **476**, 252 (2004).

[41] A. C. Kozen, M. A. Schroeder, K. D. Osborn, C. J. Lobb, and G. W. Rubloff, *Examining the role of hydrogen in the electrical performance of in situ fabricated metal-insulator-metal trilayers using an atomic layer deposited $Al_2O_3$ dielectric,* Applied Physics Letters **102**, 173501 (2013).

[42] D. R. Jennison, P. A. Schultz, and J. P. Sullivan, *Evidence for interstitial hydrogen as the dominant electronic defect in nanometer alumina films,* Physical Review B **69**, 041405 (2004).

[43] J. P. Ponpon and P. Siffert, *Open-circuit voltage of mis silicon solar cells,* Journal of Applied Physics **47**, 3248 (1976).

[44] Y. Song, X. Li, C. Mackin, X. Zhang, W. Fang, T. Palacios, H. Zhu, and J. Kong, *Role of interfacial oxide in high-efficiency graphene–silicon Schottky barrier solar cells,* Nano Letters **15**, 2104 (2015).

[45] H. C. Card and E. S. Yang, *MIS-Schottky theory under conditions of optical carrier generation in solar cells,* Applied Physics Letters **29**, 51 (1976).

[46] S. Hu, M. H. Richter, M. F. Lichterman, J. Beardslee, T. Mayer, B. S. Brunschwig, and N. S. Lewis, *Electrical, Photoelectrochemical, and Photoelectron Spectroscopic Investigation of the Interfacial Transport and Energetics of Amorphous $TiO_2$/Si Heterojunctions,* The Journal of Physical Chemistry C **120**, 3117 (2016).

[47] L. Yang, X. Yu, M. Xu, H. Chen, and D. Yang, *Interface engineering for efficient and stable chemical-doping-free graphene-on-silicon solar cells by introducing a graphene oxide interlayer,* Journal of Materials Chemistry A **2**, 16877 (2014).

[48] X. Zhou, R. Liu, K. Sun, K. M. Papadantonakis, B. S. Brunschwig, and N. S. Lewis, *570 mV photovoltage, stabilized n-Si/$CoO_x$ heterojunction photoanodes fabricated using atomic layer deposition,* Energy & Environmental Science **9**, 892 (2016).

[49] M. T. Greiner, M. G. Helander, W.-M. Tang, Z.-B. Wang, J. Qiu, and Z.-H. Lu, *Universal energy-level alignment of molecules on metal oxides.* Nature materials **11**, 76 (2012).

# 5

# Extracting large photovoltages from amorphous silicon carbide photocathodes with a titanium dioxide front surface field layer

A thin film heterojunction photocathode is fabricated by depositing a natural n-type titanium dioxide ($TiO_2$) onto a p-type-intrinsic (p-i) amorphous silicon carbide (a-SiC). Using this device structure, the junction photovoltage increases from 0.41 V for the p-i-liquid junction a-SiC photocathode to 0.77 V for the p-i-n junction a-SiC photocathode. The introduction of the $TiO_2$ on the p-i a-SiC produces an internal electric field that increases the operating photovoltage, and subsequently improves the drift mechanism of photogenerated charge carriers across the intrinsic layer. The enhancement of the photovoltage leads to a cathodic shift of photocurrent onset potential and exhibits a photocurrent density of $-8.57$ mA cm$^{-2}$ at the formal potential for the hydrogen evolution reaction. The a-SiC photocathode with a $TiO_2$ surface layer shows a high stability for 12 hours of operation under photoelectrocatalytic conditions. This high performance and very thin photocathode is very promising for integration with smaller band gap solar absorbers to form multijunction devices for highly efficient bias-free solar water splitting systems.

Parts of this chapter have been published in I. A. Digdaya, L. Han, T. W. F. Buijs, M. Zeman, B. Dam, A. H. M, Smets and W. A. Smith, *Energy Environ. Sci.*, 2015, **8**, 1585–1593. [1]

## 5.1. Introduction

Photoelectrochemical (PEC) water splitting has the potential to be a large-scale, sustainable, and efficient route to produce solar fuels (*e.g.*, hydrogen) by harnessing and storing the power of the sun. One of the most attractive features of this technology is that the light absorbing materials can be directly integrated with catalysts to produce a monolithic device, thereby making it more simple and cost-effective than using separate photovoltaic (PV) cells and electrolyzers.[2,3] In order to make this approach competitive with conventional hydrogen production from fossil fuels, *i.e.*, steam-methane reforming, the materials for PEC water splitting need to be made from cheap earth-abundant elements using a low-cost and scalable processing technique.

In recent years, major efforts have focused on single-crystal silicon- (c-Si) based photoelectrodes,[4–11] due to the natural abundance of Si, its excellent light absorbing and electronic properties and its low-cost and high throughput processing. While these photocathodes show a notably high photocurrent density, a practical device realization with c-Si remains a challenge due to the inability of the narrow band gap of c-Si (*i.e.*, 1.1 eV) to meet the thermodynamic requirements to split water (1.23 V),[12] plus the necessary overpotentials to drive the reaction (>0.8 V).[13] A more attractive and realistic approach to overcome these large potentials is to create a tandem device that contains more than one light absorbing material, which has several benefits such as increased spectral utilization, higher operating voltage, and more flexibility with respect to the band edge positions relative to the water redox potentials.[14–17] Thin film fabrication techniques such as plasma enhanced chemical vapor deposition (PECVD) have the necessary versatility to control the optoelectronic properties of Si and allow for multi-junction devices to be deposited in succession to form homo- and heterojunction films. Therefore, developing thin-film-silicon-based tandem structures with an operating voltage of at least 1.9 V is one of the most attractive and promising approaches to achieve a low-cost bias-free solar water-splitting device.

Amorphous silicon carbide (a-SiC) photocathodes have received a growing interest due to their earth abundant composition, their simple and scalable thin film deposition technique, and their relative high stability in a mildly acidic environment under cathodic bias conditions.[18–23] Moreover, a-SiC has a tunable band gap energy from 1.8 eV to 2.3 eV,[24] which allows the integration of multi-junction PV cells with smaller band gaps (*i.e.*, 1.1–1.8 eV) to form tandem light absorbers for maximum spectral utilization. Prior work has integrated a-SiC photocathodes with thin-film silicon PV junctions consisting of amorphous silicon and nanocrystalline silicon (a-Si/nc-Si) to provide an additional photovoltage, resulting in a significant anodic shift of the photocurrent onset potential.[25] However, the low charge carrier collection and the slow reaction kinetics on the a-SiC surface limit the overall performance of such a triple-junction system to well below their theoretical potential.

Initial reports have indicated that the photovoltage of a-SiC photocathodes consisting of a p-type and an intrinsic a-SiC (p-i a-SiC) is poor, mainly because of the non-ideal band edges whose alignment strongly depends on the interaction between the a-SiC and the electrolyte.[18–23] Such a dependence can be eliminated by introducing an n-type layer onto the p-i structure to form a buried rectifying p-i-n junction. Titanium dioxide ($TiO_2$) is one of the most investigated n-type materials for PEC water splitting due to its wide band gap and its high resistance against corrosion in aqueous solutions. For this reason it has been widely used as either a photoabsorber or a protection layer for unstable narrow band gap photoelectrodes.[26–33]. $TiO_2$ has also been used in conjunction with p-type semiconductors, such as p-type Si,[34] cuprous oxide ($Cu_2O$),[35,36] and gallium phosphide (GaP),[37] to create a heterojunction that provides a sufficiently strong internal electric field

for efficient photogenerated charge separation.

We herein demonstrate the use of a thin amorphous $TiO_2$ grown by atomic layer deposition (ALD) on a p-type-intrinsic (p-i) a-SiC, to form a p–i–n heterojunction photocathode for solar hydrogen evolution. This p–i–n structure produces a large photovoltage relative to the p-i a-SiC, which is attributed to the improved interfacial energetics of the buried solid-state junction. We place a hydrogen evolution catalyst on the p–i–n heterojunction photocathode, and report a significant shift in the photocurrent onset potential while obtaining a high photocurrent at the formal potential for hydrogen evolution under simulated solar illumination. Finally we show that the p-i a-SiC photocathode with a $TiO_2$ front surface layer is stable and able to maintain a continuous operation under PEC condition in near-neutral electrolyte solution.

## 5.2. Experimental details

### Fabrication of a-SiC photocathodes

The a-SiC photocathodes were deposited onto a textured Asahi VU-type fluorine-doped tin oxide (FTO) substrate using a radio frequency plasma enhanced chemical vapor deposition (RF-PECVD) multi-chamber tool. The substrate was kept at 170 °C during the deposition. The ultrathin boron doped hydrogenated amorphous silicon carbide (a-SiC(B)) was used as the p-type layer (10 nm), decomposed from $SiH_4$,$CH_4$ and $B_2H_6$ diluted $H_2$ gas flow under controlled pressure. The thin intrinsic layer (100 nm) was deposited in a separate chamber to avoid cross-contamination. A $H_2$ treatment in a low RF power density is followed in the same chamber in order to passivate the p-i interface. A stripe of 300 nm Al was coated on the pre-covered region of the sample to serve as a metal contact using a Provac electron beam evaporator in rotation mode. As the final step, electrical contact was made using a silver wire and graphite paste.

### Atomic layer deposition of $TiO_2$

Thin amorphous $TiO_2$ layers (25 nm) were deposited onto a-SiC films using a homemade thermal atomic layer deposition (ALD) system. No special treatment was done to preclean the a-SiC surface before the $TiO_2$ deposition. The $TiO_2$ ALD was carried out at a substrate temperature of 150 °C using tetrakis(dimethylamido)-titanium (TDMAT) and $H_2O$ ($T_{H_2O}$ = 25 °C) as the Ti and O precursors, respectively. The pulsing times are 5 s and 10 ms for Ti and O precursors, respectively. Each precursor was purged for 30 seconds after pulse. The growth rate was 0.8 Å per cycle as measured by ellipsometry.

### Catalyst depositions

Nickel molybdenum (Ni–Mo) catalyst was deposited by electrodeposition as described previously in other report,[11] only nickel sulfate was used instead of nickel sulfamate. The electrodeposition bath consisted of 1.3 M $Ni_2SO_4$, 0.5 M $H_3BO_3$, and $Na_2MoO_4$. No pH adjustment was carried out. The electrodeposition of Ni–Mo catalyst on the photocathodes was performed potentiostatically at −1.5 V *versus* a silver/silver chloride (Ag/AgCl) reference electrode for the p-i a-SiC and at −1.1 V *versus* Ag/AgCl for the p-i a-SiC/$TiO_2$ until 500 mC $cm^{-2}$ of charge has passed. During the deposition, the photocathodes were shone with the standard AM1.5 illumination (100 mA $cm^{-2}$) by a Newport Sol3A Class AAA solar simulator (type 94023A-SR3) equipped with 450 Watt xenon short arc lamp. Finally, the electrodes were rinsed with milli-Q water. Pt catalysts were sputter-deposited in a PREVAC sputter chamber using radio frequency (RF) power at 100 W from a pure Pt target for 18 s, resulting in approximately 1-nm-thick Pt islands.

### Photoelectrochemical measurements

The a-SiC photocathodes were photoelectrochemically tested using a potentiostat (EG&G PAR 283) in a three-electrode system, where the a-SiC photocathode with an exposed surface area of 0.283 $cm^{-2}$ acted as the working electrode, a coiled platinum or nickel wire sealed by a fritted-glass gas dispersion tube (Sigma-Aldrich) as the counter electrode and an Ag/AgCl electrode (in saturated KCL and AgCl, Radiometer Analytical XR300, Hach) as the reference electrode. The electrolyte used was an aqueous 0.5 M potassium hydrogen phthalate (KHP, Alfa Aesar, 99.99%) solution (pH 4). The Ag/AgCl reference electrode was converted to the reversible hydrogen electrode (RHE) and had a potential of 0.436 V *versus* RHE in 0.5 M KHP solution at pH 4. Linear sweep voltammetry measurements were carried out at a scan rate of 50 mV $s^{-1}$ with 25 mV incremental steps. Photocurrent measurements were performed under simulated AM1.5 solar irradiation (100 mW $cm^{-2}$) using a Newport Sol3A Class AAA solar simulator (type 94023A-SR3) with a 450 Watt xenon short arc lamp. The light enters the photocathode through the FTO-coated glass substrate. During the measurement, the electrolyte was continuously stirred using a magnetic stir bar and was constantly purged with a mixture of $Ar/H_2$ (95/5) to remove oxygen from the solution and to fix the $H^+/H_2$ Nernst potential. All current–potential curves were presented as measured without correction. Monochromatic photocurrent measurements were performed with a 200 W quartz tungsten-halogen lamp coupled with a grating monochromator (Acton SpectraPro 150i). The illumination intensities of the tungsten-halogen lamp were measured using a calibrated photodiode (Ophir PD300-UV). An electronic shutter (Uniblitz LS6) was used, and a long-pass glass filter (Schott) was placed between the monochromator and the sample to remove the second-order diffracted light. The shutter was actuated every 10 seconds, and the photocurrent was taken as the difference between the current when the shutter opened and closed (3 seconds integration time).

### Electrochemical impedance spectroscopy

Electrochemical impedance spectroscopy (EIS) measurements were separately performed on the p-i a-SiC electrodes and the amorphous $TiO_2$ film in the same electrolyte solutions as for the photoelectrochemical testing using a potentiostat PARSTAT 4000 (AMETEK, Princeton Applied Research). Mott–Schottky measurements were performed at a fixed frequency of 6 kHz for the p-i a-SiC and 500 Hz for the $TiO_2$ at an AC potential amplitude of 10 mV. The potential was scanned anodically from 0.75 to 1.1 V *versus* RHE for the a-SiC and cathodically from 0.5 to 0 V *versus* RHE for the $TiO_2$.

## 5.3. Results and discussion

### a-SiC photocathodes

The traditional p-i-liquid junction photocathode studied in this work consisted of a p-type (p) layer and an intrinsic (i) layer of a-SiC in contact with an electrolyte solution. The p-i-n junction photocathode was fabricated by depositing an amorphous $TiO_2$ (25 nm) with natural n-type conductivity onto the p-i a-SiC structure. The doped layer of a-SiC contains a high defect density–up to three orders of magnitude higher than in the intrinsic layer, that results in as short carrier diffusion length in the doped a-SiC.[38] To avoid substantial recombination losses, the p-type layer of a-SiC photocathode is usually designed to be very thin. The main absorber layer of the p-i-n junction photocathode is the intrinsic (undoped) layer, in which charge carriers are generated and separated by the internal electric field that is set up by the p-type and the n-type layers. The electric field forces the photogenerated electrons to drift toward the electrolyte and pushes holes to drift toward the p-type layer.

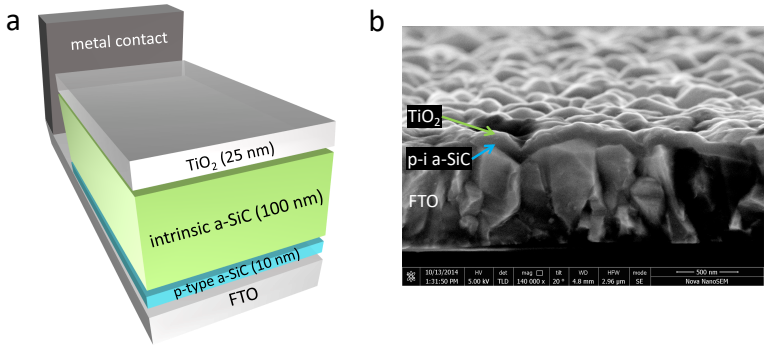



**Figure 5.1:** (a) Schematic structure of the p-i a-SiC/$TiO_2$ photocathode and (b) the corresponding cross-sectional scanning electron microscopy (SEM) image.

A schematic representation and the cross-sectional scanning electron microscope (SEM) image of the p-a-SiC/$TiO_2$ photocathode are shown in Fig. 5.1a and b, respectively.

### Interfacial energetics

The band-edge energetics of the p-i a-SiC and the p-i a-SiC/$TiO_2$ photocathodes were investigated independently by electrochemical impedance spectroscopy using a three-electrode configuration in a potassium hydrogen phthalate (KHP) electrolyte solution. Figure 5.2a and b show Mott-Schottky plots of the inverse square of the space-charge capacitance *versus* potential ($C_{sc}^{-2}$–$V$) of the p-i a-SiC and the $TiO_2$ electrode, respectively. The intercept between the extrapolated linear region of the $C_{sc}^{-2}$–$V$ curve and the $x$-axis indicates the flat band potential ($E_{fb}$) of the electrode. The estimated $E_{fb}$ of the p-i a-SiC was +1.17 V *versus* the reversible hydrogen electrode (RHE) and the slope in the linear region of the $C_{sc}^{-2}$–$V$ yielded an acceptor concentration of $1.46 \times 10^{17}$ $cm^{-3}$ for the p-type a-SiC and suggested a Fermi level position at 105.26 meV above the valence band edge. Given a value of 4.44 eV for the $H^+/H_2$ redox energy below the vacuum level[39] and a band gap of 2.0 eV for the a-SiC (Fig. C.4, Appendix C), the electron affinity of the a-SiC ($\chi_{a\text{-SiC}}$) was estimated to be 3.71 eV, close to the value reported by literatures.[40,41] The approximated $E_{fb}$ of the $TiO_2$ was −0.11 V *versus* RHE and the electron concentration in the $TiO_2$ calculated from the slope of $C_{sc}^{-2}$–$V$ was $1.62 \times 10^{20}$ $cm^{-3}$. The $TiO_2$ Fermi level was estimated to be placed at 40.54 meV below the conduction band edge. Using a band gap of 3.2 eV for the $TiO_2$ (Fig. C.4, Appendix C), the electron affinity of the $TiO_2$ ($\chi_{TiO_2}$) was approximated to be 4.29 eV (details of the calculation are described in Appendix C.1).

Figure 5.3 shows the electrochemical open-circuit potentials (OCP) *versus* a reference electrode (in RHE scale) of the p-i a-SiC and the p-i a-SiC/$TiO_2$ electrodes in an electrolyte solution, measured in the dark and under illumination. In the absence of light, the Fermi level of the electrodes is expected to be in thermodynamic equilibrium with the surface layer that is pinned at the electronic states at the surface. The development of surface states on metal oxide semiconductors such as $TiO_2$ typically arises from surface termination by hydroxyl group upon dissociative adsorption of water molecules.[12] For the a-SiC, surface hydroxylation may occur on the oxidized surface as a result of water exposure in an electrochemical environment.[42–46] Both p-i a-SiC and p-i a-SiC/$TiO_2$ displayed the same equilibrium potential at +0.48 ± 0.02 V *versus* RHE in the dark condition, indicating the same surface states position for both a-SiC and $TiO_2$. Under illumination, the OCP shifted

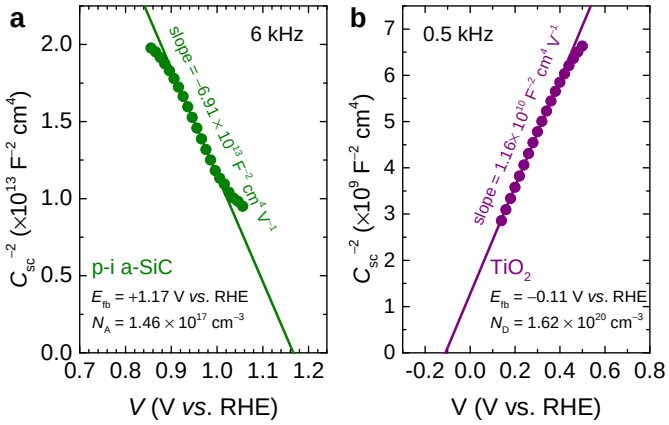



**Figure 5.2:** Mott-Schottky plots of the inverse square of the space-charge capacitance *versus* potential ($C_{sc}^{-2}$–$V$) of the (a) p-i a-SiC and (b) $TiO_2$. Impedance spectroscopy measurements were performed electrochemically in 0.5 M KHP electrolyte solution at pH 4.

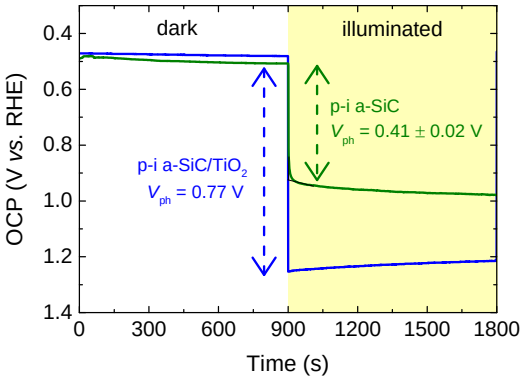



**Figure 5.3:** Electrochemical open-circuit potentials (OCP) *versus* a reversible hydrogen electrode (RHE) of the of the p-i a-SiC and the p-i a-SiC/$TiO_2$ photocathodes, monitored as a function of time under open circuit conditions in the dark and under illumination. OCP measurements were conducted in 0.5 M KHP electrolyte solution at pH 4.

anodically to +0.91 ± 0.02 V *versus* RHE and +1.25 V *versus* RHE, indicating open-circuit photovoltages of +410 ± 20 mV and 770 mV for the p-i a-SiC and the p-i a-SiC/$TiO_2$ photocathodes, respectively. Thus, the increase of photovoltage upon the introduction of a $TiO_2$ front surface layer onto the p-i a-SiC was 360 ± 20 mV.

To illustrate the band alignment of the p-i a-SiC and the p-i a-SiC/$TiO_2$ electrodes, energy band diagrams are constructed using the values obtained from the Mott-Schottky analysis (Fig. 5.4). Details of the calculation are provided in Appendix C.1. Few assumptions are made for the p-i a-SiC: (i) the space-charge region of the p-type a-SiC is extended to the intrinsic layer, (ii) no band movement during cathodic biasing of electrochemical impedance spectroscopy, (iii) the conduction and valence band edges are pinned at the solid-liquid interface. The flat band potential and the calculated acceptor concentration

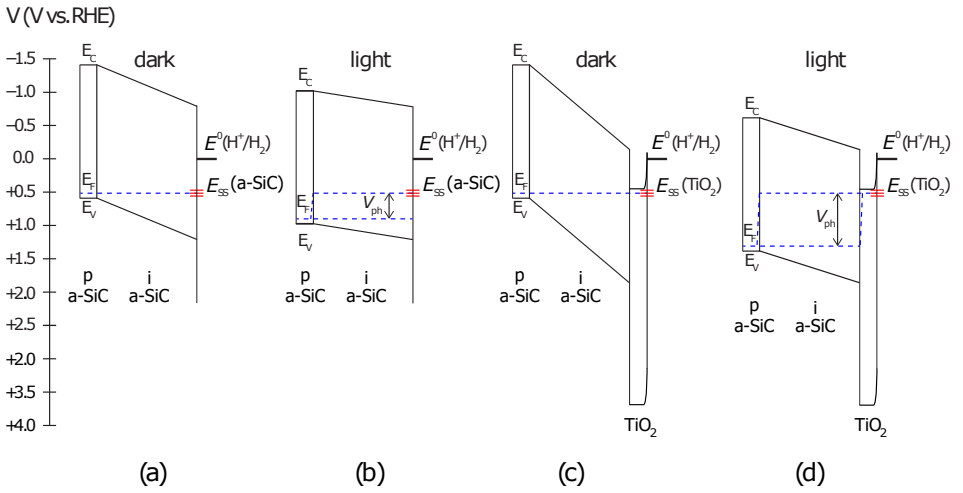



**Figure 5.4:** Energy band diagram of the p-i a-SiC photocathode under open circuit condition: (a) in the dark, (b) under illumination, and the p-i a-SiC/$TiO_2$ photocathode: (c) in the dark, (d) under illumination. The band edges of the p-i a-SiC and the $TiO_2$ are estimated using the Mott–Schottky analysis and are assumed to be pinned at the solid-liquid interface.

indicate that the valence band edge of the p-i a-SiC resides approximately at 1.27 V more positive than $E^{0\prime}$ ($H^+/H_2$) at the solid-liquid interface. Considering a dark electrochemical open-circuit potential of +0.48 relative to $E^{0\prime}$ ($H^+/H_2$) which also represents the Fermi level position of the p-i a-SiC under equilibrium in the electrolyte, the barrier height of the p-i-liquid junction a-SiC was estimated to be 0.79 eV. The width of the space-charge region of the p-i a-SiC was calculated to be 88.90 nm, close to the approximate thickness of the intrinsic layer of the a-SiC (100 nm), thus confirms the validity of our measurement and calculation (details of the calculation is described in Appendix C.1). For the p-i a-SiC/$TiO_2$ heterostructure, the density of interface states is assumed to be very small such that no Fermi level pinning takes place at the heterointerface. Using the electron affinity values calculated from the flat band potentials relative to the vacuum level and the band gaps of the a-SiC and the $TiO_2$, the conduction band and the valence band offsets at the a-SiC/$TiO_2$ interface are approximated to be 0.57 eV and 1.77 eV, respectively. The initial difference of Fermi levels between the p-i a-SiC and the $TiO_2$ under flat band conditions yields a maximum barrier height of 1.38 eV for the p-i a-SiC/$TiO_2$ photocathode with the given acceptor concentration of the p-i a-SiC and donor concentration of the $TiO_2$. From the energy band analysis, it is clear that the introduction of $TiO_2$ on the p-i a-SiC may result in a larger barrier height, which can produce a higher photovoltage than the p-i a-SiC electrode that does not have $TiO_2$ front surface field layer.

### Photoelectrochemical characterization

The PEC performance of the p-i a-SiC and the p-i a-SiC/$TiO_2$ photocathodes was evaluated by cyclic voltammetry in 0.5 M KHP electrolyte at pH 4 under simulated solar irradiation in a three-electrode configuration without correction for resistance losses in the solution. Figure 5.5 shows illuminated current–voltage ($j$–$V$) characteristics of the p-i a-SiC and p-i a-SiC/$TiO_2$ photocathodes coated with platinum (Pt) and nickel-molybdenum (Ni–Mo) hydrogen evolution catalysts, recorded during the first scan of cyclic voltammetry.

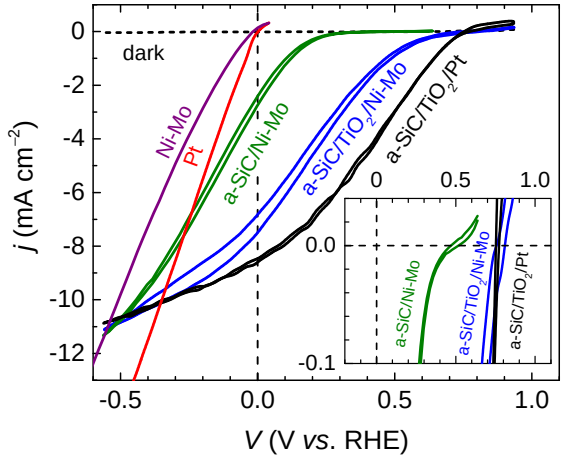



**Figure 5.5:** Representative current–voltage ($j$–$V$) characteristics of p-i a-SiC/$TiO_2$/Pt, p-i a-SiC/$TiO_2$Ni–Mo and p-i a-SiC/Ni–Mo photocathodes in contact with 0.5 M KHP electrolyte solution and under simulated solar illumination, taken from the first scan of cyclic voltammetry in a three-electrode configuration. The dark $j$–$V$ characteristics of the non-photoactive Pt and Ni–Mo on FTO glass substrates are also shown. The vertical dash line indicates the formal potential for hydrogen evolution, $E^{0\prime}$ ($H^+/H_2$).

A closer inspection in the inset of Fig. 5.5 reveals that the photocurrent onset potentials (defined as the potential required to achieve a cathodic current of −10 μA $cm^{-2}$) were +760 ± 10 mV, +767 ± 33 mV and +410 ± 10 mV relative to the formal potential for hydrogen evolution ($E^{0\prime}$ ($H^+/H_2$) = 0 V *versus* RHE) for the p-i a-SiC/$TiO_2$/Pt, p-i a-SiC/$TiO_2$/Ni–Mo and p-i a-SiC/Ni–Mo photocathodes, respectively. Thus, the presence of $TiO_2$ front surface field layer on the p-i a-SiC resulted in an anodic shift of photocurrent onset potential of 321 ± 18 mV relative to the p-i a-SiC photocathode that did not have a $TiO_2$ layer. Equivalent photovoltaic response analysis by subtracting the $j$–$V$ data of the photoelectrodes from the dark electrolysis $j$–$V$ curves of the non-photoactive electrodes with the corresponding catalysts (Pt and Ni–Mo, each deposited on an FTO-coated glass substrate) indicated photovoltages of 760 ± 10 mV, 784 ± 33 mV and 427 ± 10 mV, for the p-i a-SiC/$TiO_2$/Pt, p-i a-SiC/$TiO_2$/Ni–Mo and p-i a-SiC/Ni–Mo photocathodes, respectively, in close agreement with the values measured using the dark and illuminated electrochemical open-circuit method. The photocurrent density of the p-i a-SiC/$TiO_2$ electrode with Pt catalyst was −8.57 ± 0.07 mA $cm^{-2}$ at $E^{0\prime}$ ($H^+/H_2$) and the photocurrent density of the same structure with Ni–Mo catalyst was −7.16 ± 0.33 mA $cm^{-2}$ at $E^{0\prime}$ ($H^+/H_2$). In the absence of $TiO_2$ front surface layer, the photocurrent density was substantially lower ($j_{ph}$ = −2.58 mA $cm^{-2}$ at $E^{0\prime}$ ($H^+/H_2$)), mainly because of the more negative photocurrent onset potential of the p-i a-SiC/Ni–Mo relative to the p-i-a-SiC/$TiO_2$/Ni–Mo. The dark current for all photocathodes was measured to be close to zero, implying that the observed photocurrent was indeed related to photogeneration of charges.

The anodic shift in the potential of photocurrent onset, thus the increase of photovoltage for the p-i a-SiC/$TiO_2$ relative to the p-i a-SiC with the same Ni–Mo catalyst is related to the improved interfacial energetics of the photocathode upon the introduction of $TiO_2$ front surface layer. The low barrier height of the p-i a-SiC structure is attributable to the non-ideal alignment of band edges relative to $E^{0\prime}$ ($H^+/H_2$), which is most likely

due to pinning of Fermi level at localized defect states at the solid-liquid interface. In the absence of significant interface states and potential drop across the Helmholtz layer, the barrier height of a p-i liquid junction a-SiC photocathode can be approximated by the initial difference between the a-SiC valence band edge and $E^{0\prime}$ ($H^+/H_2$). On the basis of $E_{fb}$ of the p-i a-SiC (+1.17 V *versus* RHE), and the Fermi level position with respect to the valence band edge (0.1 eV), the p-i a-SiC photocathode in contact with aqueous electrolyte should ideally achieve a barrier height of 1.27 eV. This theoretical value is substantially higher than the actual barrier height of the p-i-liquid junction a-SiC which in turn results in a non-optimal value of photovoltage. The higher photovoltage of the p-i a-SiC/$TiO_2$ than the p-i a-SiC photocathode thus suggests that the $TiO_2$ is capable of improving the band-edge energetics of the p-i a-SiC and eliminating the Fermi level pinning effect caused by the high-density defect states at the a-SiC surface.

In addition to the improved energetics, the introduction of $TiO_2$ onto the p-i a-SiC forms a buried junction that physically separates the rectifying junction from liquid contact. In the p-i-liquid junction, the band edges of the i a-SiC are essentially fixed at the solid-liquid interface and the ability of the photocathode to produce photovoltage is determined by the position of the conduction and valence band edges relative to $E^{0\prime}$ ($H^+/H_2$). In contrast, the buried p-i-n structure isolates the internal electric field across the solid-state junction and enables photovoltage generation that is independent of solid-liquid interaction. Under applied bias, the buried junction allows the photocathode to float and adjust with the current density and the kinetics of the surface reaction (Fig. 5.6a and b). As a result, the onset potential of the photocurrent relative to $E^{0\prime}$ ($H^+/H_2$) does not only depend on the junction photovoltage but also on the thermodynamic and kinetic overpotentials of

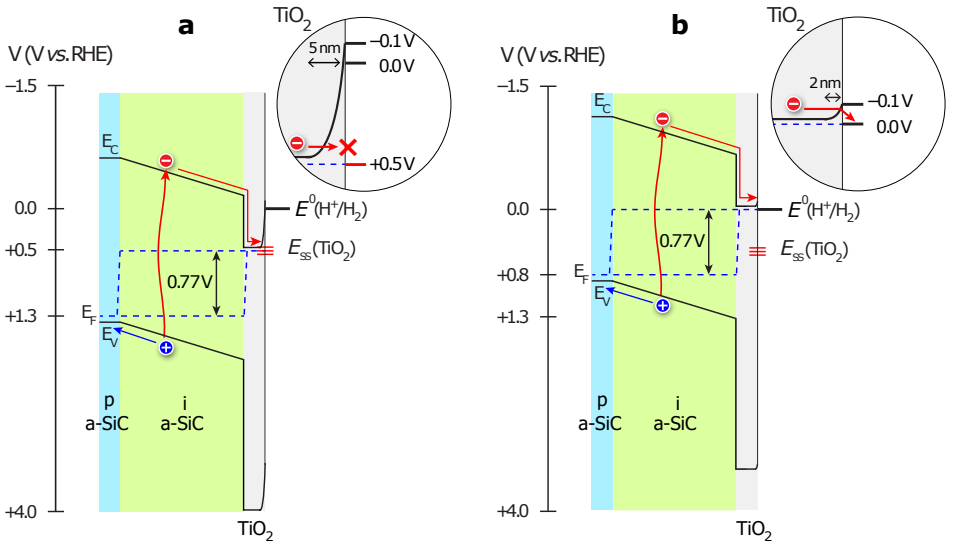



**Figure 5.6:** Energy band diagram of the p-i a-SiC/$TiO_2$ photocathode (a) at a potential of ~ +1.25 V *versus* RHE, corresponding to its open-circuit potential under illumination, and (b) under bias at ~ +0.77 V *versus* RHE, corresponding to its photocurrent onset potential. The catalyst (Ni–Mo or Pt) is not shown in the figure since $TiO_2$ is still in contact with the electrolyte, and therefore does not influence the band-edge energetics.

the surface layer to drive the electrocatalytic reaction of hydrogen evolution. Because the $TiO_2$ front surface layer is not completely covered by the catalyst, the $TiO_2$ band edges generally remain pinned at the solid-liquid interface, resulting in band bending with rectifying characteristic that creates a barrier for electron transfer to the electrolyte (inset of Fig. 5.6a). However, the high electron concentration of the $TiO_2$ front surface layer allows the band bending to occur across a narrow region adjacent to the liquid interface (inset of Fig. 5.6b). Given an electron concentration ($N_D$) of $1.62 \times 10^{20}$ $cm^{-3}$ as determined from Mott-Schottky analysis, the width of the space-charge region of the $TiO_2$ is approximately 2 nm, which is thin enough for photogenerated electrons from the a-SiC to tunnel across the barrier and transfer to the electrolyte (details of the calculation are described in Appendix C.1).

In comparison to the p-i a-SiC/$TiO_2$/Pt photocathode, the p-i a-SiC/$TiO_2$/Ni–Mo showed a distinctive s-shaped kink in the observed $j$–$V$ curve. The s-shaped $j$–$V$ characteristic of a PEC electrode is usually attributed to the increased surface recombination due to slow charge transfer kinetics on the semiconductor surface. Prior study has shown that Ni–Mo formed by electrodeposition exhibits geometric activity identical to that of Pt with almost the same overpotential to achieve a given current density.[47] In agreement with the previous results, dark electrolysis $j$–$V$ responses in Fig. 5.5 indicate that Pt and Ni–Mo have a similar fundamental electrocatalytic activity for hydrogen evolution with nearly negligible overpotential to drive the reaction, but Ni–Mo shows a slower increasing onset of cathodic current density relative to Pt. Top-view scanning electron microscopy (SEM) images of the surface morphology revealed that the resulting deposits of Ni–Mo by electrochemical deposition were generally discontinuous particles with nano-scale gaps that expose the underlying surface (Fig. 5.7). The inhomogeneous distribution of Ni–Mo particles is most likely due to the co-evolution of hydrogen bubbles that blocks the surface of the substrate from access to the precursor solution as visually observed during the electrodeposition. The incomplete coverage of electrocatalyst on the photocathode thus may result in extensive charge accumulation, particularly at the uncatalyzed region which makes the photocathode requires a more negative potential to produce a given current density. Conversely, the resulting Pt film by sputter-deposition is expected to result in an essentially uniform coverage which should allow electron transfer to occur throughout the whole surface of the electrode. This behavior is consistent with the rapid increase of cathodic current onset both for the dark Pt electrode and the illuminated p-i a-SiC/$TiO_2$/Pt

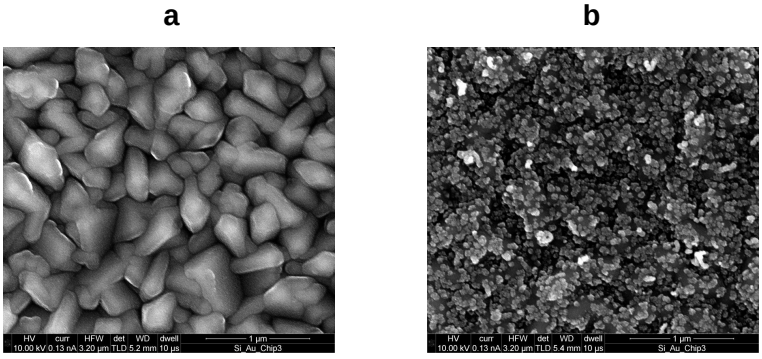



**Figure 5.7:** a) Top-view scanning electron microscopy images of the p-i a-SiC/$TiO_2$ and b) the p-i a-SiC/$TiO_2$/Ni–Mo photocathodes deposited on a textured Asahi VU-type FTO substrate.

photocathode. In the absence of hydrogen-evolving catalyst, the photocathode suffers from both negative photocurrent onset potential and low photocurrent at $E^{0\prime}$ ($H^+/H_2$) (Fig. C.5, Appendix C).

### Photoresponse characterization

The photoelectrochemical performance of the a-SiC photocathodes was further characterized by measuring the incident photon-to-current conversion efficiency (IPCE) in 0.5 M KHP electrolyte solution at pH 4, at an applied potential of 0 V *versus* RHE (Fig. 5.8). Throughout the entire spectrum, the p-i a-SiC/$TiO_2$/Ni–Mo photocathode demonstrated a significantly higher IPCE than the p-i a-SiC/Ni–Mo photocathode that did not have $TiO_2$ and yielded a quantum efficiency peak of 63% at a wavelength of 460 nm. The low IPCE in the ultraviolet (UV) region is attributed to the parasitic absorption by the

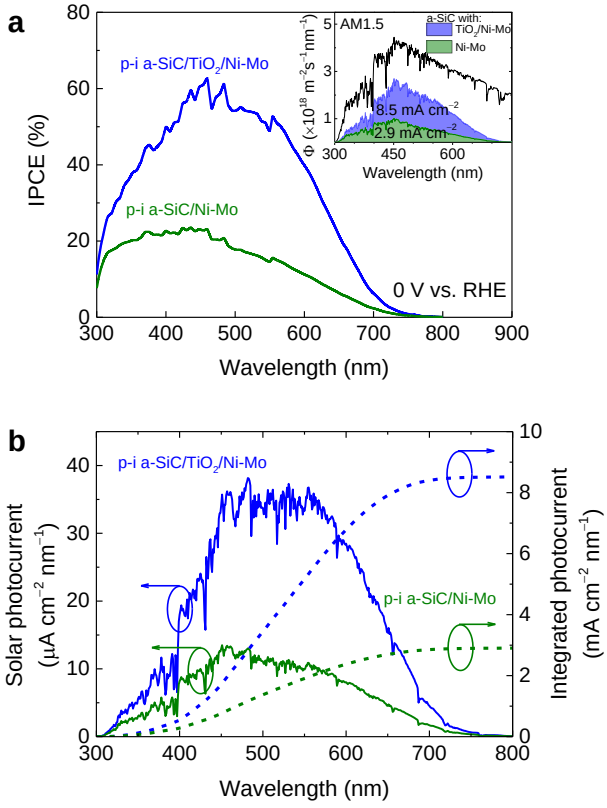



**Figure 5.8:** (a) Incident photon-to-current conversion efficiency (IPCE) of the p-i a-SiC and the p-i a-SiC/$TiO_2$ photocathodes with Ni–Mo catalysts measured in 0.5 M KHP electrolyte solution at pH 4 and held potentiostatically at 0 V *versus* RHE while illuminated by monochromatic light. The shaded areas under the curves shown in the inset are the converted photon fluxes and are derived from the multiplication of IPCE of each photocathode and the photon flux of the ASTM AM1.5G spectrum. (b) The predicted solar photocurrent as a function of wavelength, calculated by integrating the product of IPCE and the spectral irradiance of the ASTM AM1.5G over the spectrum. Details of the calculation are provided in Appendix C.4.

FTO and the p-type layer that does not contribute to photocurrent generation, while the decline of IPCE in the near-infrared (NIR) region is related to the band gap limitation of the a-SiC. It is important to note that the band gap of a-SiC used in this study was 2.0 eV as approximated using the Tauc plot (Fig. C.4, Appendix C), which corresponds to an absorption edge at 620 nm. The extended spectral response up to 700 nm in the a-SiC is ascribed to the light absorption due to transitions between band tail states whose energy distributions are increased with carbon incorporation.[48] In addition, light scattering by the rough surface of the textured FTO substrate (Asahi VU-type) may extend the optical path length and increase the light absorption of the weakly absorbed light at long wavelengths. The predicted solar photocurrent density using the American Society for Testing and Materials Air Mass 1.5 Global (ASTM AM1.5G) spectrum[49] indicated values of −2.9 mA $cm^{-2}$ and −8.5 mA $cm^{-2}$ for the p-i a-SiC/Ni–Mo and the p-i a-SiC/$TiO_2$ photocathodes, respectively (details of calculation are described in C.4) These values are slightly higher than photocurrent densities previously shown in Fig. 5.5 (*i.e.*, −2.58 mA $cm^{-2}$ for the p-i a-SiC/Ni–Mo and −7.49 mA $cm^{-2}$ for the p-i a-SiC/$TiO_2$/Ni–Mo). The discrepancy in the observed photocurrent of the same photocathode may be attributed to the mismatch of spectral irradiance between our solar simulator and the ASTM AM1.5G (Fig. C.6, Appendix C) and/or the extensive charge generation and accumulation at the photocathode surface due to high light intensities generated by the solar simulator (~100 mA $cm^{-2}$) which result in excessive surface recombination and reduced photocurrent in the observed $j$–$V$ curve.

#### Stability measurement

The stability of both Ni–Mo catalyzed p-i a-SiC and p-i a-SiC/$TiO_2$ photocathodes was evaluated by chronoamperometry measurements for 12 hours at a potentiostatic control of 0 V *versus* RHE under simulated solar illumination in 0.5 M KHP electrolyte solution (Fig. 5.9a). Without the $TiO_2$ front surface layer, the photocurrent of the p-i a-SiC photocathode drastically dropped to only 20% of its initial value. The decay of photocurrent is most likely associated with the detachment of the Ni–Mo catalyst due to its poor adhesion on the a-SiC surface that caused a decrease of photoelectrocatalytic activity of the electrode. After Ni–Mo redeposition, the photocurrent could be restored to its initial value without any change in the photocurrent onset potential (Fig. 5.9b).

The p-i a-SiC/$TiO_2$/Ni–Mo photocathode exhibited a high stability without noticeable degradation of photocurrent during the 12-hour measurement in 0.5 M KHP electrolyte solution at pH 4, at an applied potential of 0 V *versus* RHE (Fig. 5.9a). After 3 hours of chronoamperometry test, the p-i a-SiC/$TiO_2$/Ni–Mo photocathode demonstrated an improved catalytic performance, indicated by the rapid increase of cathodic current onset (Fig. 5.9c), and displayed a $j$–$V$ characteristic similar to that of the p-i a-SiC/$TiO_2$/Pt photocathode. The increase of photocurrent within the first three hours is ascribed to surface etching of the uncatalyzed region of the $TiO_2$ under cathodic condition that changes the surface composition and affects the surface trapping effects, or incidental platinization of the working electrode as a result of cross-contamination from the Pt counter electrode that is placed in the same electrochemical compartment.

Previous studies have shown that electron transfer from the bulk $TiO_2$ to the uncatalyzed surface may result in electron accumulation that can subsequently promote the proton-assisted reduction process of $Ti^{4+}$ to $Ti^{3+}$ on the surface, which is usually accompanied with an insignificant rate of hydrogen evolution.[26,50] Thus, the measured device photocurrent of $TiO_2$-coated electrodes may predominantly correspond to the reduction of titania film rather than water. However, the application of an efficient hydrogen evolving

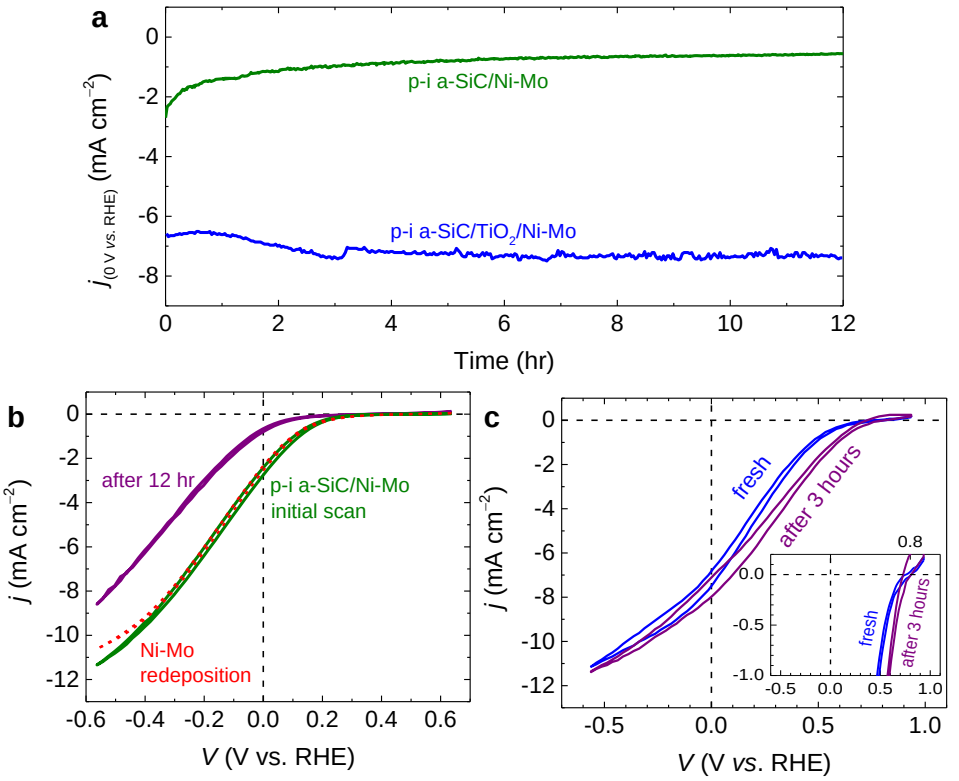



**Figure 5.9:** (a) Chronoamperometry measurement of the Ni–Mo coated p-i a-SiC and p-i a-SiC/$TiO_2$ photocathodes for 12 hours of operation under simulated AM1.5 illumination in 0.5 M potassium hydrogen phthalate (KHP) electrolyte solution at pH 4. During the measurement, the potential was held at $E^{0\prime}$ ($H^+/H_2$). (b) Cyclic voltammetry of the p-i a-SiC/Ni–Mo photocathode, recorded during the first scan, after 12 hours of chronoamperometry test and after redeposition of Ni–Mo catalyst. (c) Comparison of the cyclic voltammetry of the p-i a-SiC/$TiO_2$/Ni–Mo photocathode before and after 3 hours of chronoamperometry measurement.

catalyst such as Ni–Mo may facilitate fast electron transfer at the solid-liquid interface which can prevent the detrimental effect of electron trapping at the $TiO_2$ surface.[51] Thus, the observed constant photocurrent of our p-i a-SiC/$TiO_2$/Ni–Mo photocathode within 12 hours of measurement can be assigned to hydrogen generation with a Faradaic efficiency of nearly unity. Although the experiment was not continued further, the 12-hour stability measurement demonstrates the beneficial properties of $TiO_2$, not only as an n-type front surface field layer, but also as an adhesive layer for catalyst support on the photocathode surface. Many reports have shown that $TiO_2$ and Ni–Mo catalysts are highly stable at moderate applied cathodic bias in a wide range of pH within the course of months.[26–37]

While showing a notably high photocurrent density, a photocurrent onset potential of +760 ± 10 mV relative to $E^{0\prime}$ ($H^+/H_2$) still cannot satisfy the thermodynamic potential requirement for spontaneous water splitting. Nevertheless, the absorption edge of 700 nm and the total thickness of our p-i a-SiC/$TiO_2$/Ni–Mo photocathode which is approximately only 150 nm may allow for the use of a second (or third) solar absorber with smaller band

gaps in a tandem structure or in a dual photoelectrode configuration (*e.g.*, photocathode and photoanode in a side-by-side configuration) to provide additional photovoltages. To give an illustration, assuming there is no limitation on the photocurrent due to light shading and series connection of multi-junction structure, the integration with a micromorph (a-Si/nc-Si) PV cells will give an extra +1.2 V to the initial photocurrent onset potential.[25] Additionally, by using an efficient oxygen evolution catalyst as the counter electrode, a benchmark of 10% solar-to-hydrogen (STH) efficiency PEC water-splitting device can be achieved using all thin film Si-based photoelectrodes.

## 5.4. Conclusion

In summary we have investigated the change in the interfacial energetics of the semiconductor–liquid junction belonging to a p-i a-SiC photocathode by introducing a thin $TiO_2$ front surface field layer to form a p-i-n heterojunction. The photocurrent onset potential of the catalyzed p-i a-SiC/$TiO_2$ photocathode anodically shifted from +413 ± 9 mV to +734 ± 9 mV relative to $E^{0\prime}$ ($H^+/H_2$). The p-i a-SiC/$TiO_2$ showed a maximum photocurrent density of $-7.49$ mA cm$^{-2}$ with a Ni–Mo catalyst and $-8.64$ mA cm$^{-2}$ with a Pt catalyst during the first scan of cyclic voltammetry, which is markedly higher than the Ni–Mo-catalyzed p-i a-SiC ($-2.58$ mA cm$^{-2}$) at the standard $H^+/H_2$ reduction potential. Using Mott–Schottky analysis, energy band diagrams were constructed, which helped to verify the improved energetics and thus the photovoltage of the p-i-n structure relative to the p-i-liquid junction photocathode. The spectral response showed a dramatic increase throughout the spectrum upon the introduction of $TiO_2$ onto the p-i a-SiC, indicating a higher conversion of light to photocurrent within the same spectral range. We finally showed that the 25 nm thick ALD $TiO_2$ coupled with a Ni–Mo catalyst was stable and able to maintain a nearly constant photocurrent of the a-SiC photocathode, as suggested by the 12-hour stability measurement under PEC operating conditions. This experimental study also suggests that $TiO_2$ can be used as the n-type layer for heterojunction thin-film-Si-based photoelectrodes.

## References

[1] I. A. Digdaya, L. Han, T. W. F. Buijs, M. Zeman, B. Dam, A. H. M. Smets, and W. A. Smith, *Extracting large photovoltages from a-SiC photocathodes with an amorphous $TiO_2$ front surface field layer for solar hydrogen evolution,* Energy Environ. Sci. **8**, 1585 (2015).

[2] R. Sathre, C. D. Scown, W. R. Morrow, J. C. Stevens, I. D. Sharp, J. W. Ager, K. Walczak, F. A. Houle, and J. B. Greenblatt, *Life-cycle net energy assessment of large-scale hydrogen production via photoelectrochemical water splitting,* Energy Environ. Sci. **7**, 3264 (2014).

[3] T. J. Jacobsson, V. Fjällström, M. Edoff, and T. Edvinsson, *Sustainable solar hydrogen production: from photoelectrochemical cells to PV-electrolyzers and back again,* Energy Environ. Sci. **7**, 2056 (2014).

[4] D. V. Esposito, I. Levin, T. P. Moffat, and A. A. Talin, *$H_2$ evolution at Si-based metal–insulator–semiconductor photoelectrodes enhanced by inversion channel charge collection and H spillover,* Nature Materials **12**, 562 (2013).

[5] J. Oh, T. G. Deutsch, H.-C. Yuan, and H. M. Branz, *Nanoporous black silicon*

*photocathode for $H_2$ production by photoelectrochemical water splitting,* Energy & Environmental Science **4**, 1690 (2011).

[6] Y. Hou, B. L. Abrams, P. C. K. Vesborg, M. E. Björketun, K. Herbst, L. Bech, A. M. Setti, C. D. Damsgaard, T. Pedersen, O. Hansen, J. Rossmeisl, S. Dahl, J. K. Nørskov, and I. Chorkendorff, *Bioinspired molecular co-catalysts bonded to a silicon photocathode for solar hydrogen evolution,* Nature Materials **10**, 434 (2011).

[7] U. Sim, H.-Y. Jeong, T.-Y. Yang, and K. T. Nam, *Nanostructural dependence of hydrogen production in silicon photocathodes,* Journal of Materials Chemistry A **1**, 5414 (2013).

[8] U. Sim, T.-Y. Yang, J. Moon, J. An, J. Hwang, J.-H. Seo, J. Lee, K. Y. Kim, J. Lee, S. Han, B. H. Hong, and K. T. Nam, *N-doped monolayer graphene catalyst on silicon photocathode for hydrogen production,* Energy & Environmental Science **6**, 3658 (2013).

[9] S. W. Boettcher, J. M. Spurgeon, M. C. Putnam, E. L. Warren, D. B. Turner-Evans, M. D. Kelzenberg, J. R. Maiolo, H. a. Atwater, and N. S. Lewis, *Energy-Conversion Properties of Vapor-Liquid-Solid-Grown Silicon Wire-Array Photocathodes,* Science **327**, 185 (2010).

[10] E. L. Warren, J. R. McKone, H. a. Atwater, H. B. Gray, and N. S. Lewis, *Hydrogen-evolution characteristics of Ni–Mo-coated, radial junction, $n^+p$-silicon microwire array photocathodes,* Energy & Environmental Science **5**, 9653 (2012).

[11] J. R. McKone, E. L. Warren, M. J. Bierman, S. W. Boettcher, B. S. Brunschwig, N. S. Lewis, and H. B. Gray, *Evaluation of Pt, Ni, and Ni–Mo electrocatalysts for hydrogen evolution on crystalline Si electrodes,* Energy & Environmental Science **4**, 3573 (2011).

[12] R. van de Krol and M. Grätzel, *Photoelectrochemical Hydrogen Production*, edited by R. van de Krol and M. Grätzel, Electronic Materials: Science & Technology, Vol. 102 (Springer US, Boston, MA, 2012).

[13] M. T. Koper, *Thermodynamic theory of multi-electron transfer reactions: Implications for electrocatalysis,* Journal of Electroanalytical Chemistry **660**, 254 (2011).

[14] J. R. Bolton, S. J. Strickler, and J. S. Connolly, *Limiting and realizable efficiencies of solar photolysis of water,* Nature **316**, 495 (1985).

[15] J. Brillet, J.-H. Yum, M. Cornuz, T. Hisatomi, R. Solarska, J. Augustynski, M. Graetzel, and K. Sivula, *Highly efficient water splitting by a dual-absorber tandem cell,* Nat. Photonics **6**, 824 (2012).

[16] S. Hu, C. Xiang, S. Haussener, A. D. Berger, and N. S. Lewis, *An analysis of the optimal band gaps of light absorbers in integrated tandem photoelectrochemical water-splitting systems,* Energy & Environmental Science **6**, 2984 (2013).

[17] H. Döscher, J. F. Geisz, T. G. Deutsch, and J. A. Turner, *Sunlight absorption in water – efficiency and design implications for photoelectrochemical devices,* Energy Environ. Sci. **7**, 2951 (2014).

[18] F. Zhu, J. Hu, A. Kunrath, I. Matulionis, B. Marsen, B. Cole, E. Miller, and A. Madan, *a-SiC:H films used as photoelectrodes in a hybrid, thin-film silicon photoelectrochemical (PEC) cell for progress toward 10% solar-to hydrogen efficiency,* in *Solar Hydrogen and Nanotechnology II, Proc. of SPIE*, Vol. 6650, edited by J. Guo (2007) p. 66500S.

[19] J. Hu, F. Zhu, I. Matulionisa, K. Augusto, T. Deutsch, E. Miller, and A. Madan, *Solar-to-hydrogen photovoltaic/photoelectrochemical devices using amorphous silicon carbide as the photoelectrode,* in *23rd European Photovoltaic Solar Energy Conference and Exhibition* (2008) pp. 69–72.

[20] I. Matulionis, F. Zhu, J. Hu, T. Deutsch, A. Kunrath, E. Miller, B. Marsen, and A. Madan, *Development of a corrosion-resistant amorphous silicon carbide photoelectrode for solar-to-hydrogen photovoltaic/photoelectrochemical devices,* in *Solar Hydrogen and Nanotechnology II, Proc. of SPIE*, Vol. 7044, edited by G. Westin (2008) p. 70440D.

[21] F. Zhu, J. Hu, I. Matulionis, T. Deutsch, N. Gaillard, A. Kunrath, E. Miller, and A. Madan, *Amorphous silicon carbide photoelectrode for hydrogen production directly from water using sunlight,* Philosophical Magazine **89**, 2723 (2009).

[22] I. Matulionis, J. Hu, F. Zhu, J. Gallon, N. Gaillard, T. Deutsch, E. Miller, and A. Madan, *Surface modification of a-SiC photoelectrodes for photocurrent enhancement,* in *Solar Hydrogen and Nanotechnology II, Proc. of SPIE*, Vol. 7770, edited by H. Idriss and H. Wang (2010) p. 77700Z.

[23] F. Zhu, J. Hu, I. Matulionis, T. Deutsch, N. Gaillard, E. Miller, and A. Madan, *Solar Power*, edited by R. Rugescu, February (InTech, 2012).

[24] A. Madan and M. P. Shaw, *The physics and applications of amorphous semiconductors*, edited by A. Madan and M. P. Shaw (Academic Press, Inc., San Diego, 1988).

[25] L. Han, I. A. Digdaya, T. W. F. Buijs, F. F. Abdi, Z. Huang, R. Liu, B. Dam, M. Zeman, W. A. Smith, and A. H. M. Smets, *Gradient dopant profiling and spectral utilization of monolithic thin-film silicon photoelectrochemical tandem devices for solar water splitting,* J. Mater. Chem. A **3**, 4155 (2015).

[26] A. Paracchino, V. Laporte, K. Sivula, M. Grätzel, and E. Thimsen, *Highly active oxide photocathode for photoelectrochemical water reduction,* Nature Materials **10**, 456 (2011).

[27] B. Seger, T. Pedersen, A. B. Laursen, P. C. K. Vesborg, O. Hansen, and I. Chorkendorff, *Using $TiO_2$ as a Conductive Protective Layer for Photocathodic $H_2$ Evolution,* Journal of the American Chemical Society **135**, 1057 (2013).

[28] Y. Lin, C. Battaglia, M. Boccard, M. Hettick, Z. Yu, C. Ballif, J. W. Ager, and A. Javey, *Amorphous Si Thin Film Based Photocathodes with High Photovoltage for Efficient Hydrogen Production,* Nano Letters **13**, 5615 (2013).

[29] Y. W. Chen, J. D. Prange, S. Dühnen, Y. Park, M. Gunji, C. E. D. Chidsey, and P. C. McIntyre, *Atomic layer-deposited tunnel oxide stabilizes silicon photoanodes for water oxidation,* Nature Materials **10**, 539 (2011).

[30] S. Hu, M. R. Shaner, J. A. Beardslee, M. Lichterman, B. S. Brunschwig, and N. S. Lewis, *Amorphous $TiO_2$ coatings stabilize Si, GaAs, and GaP photoanodes for efficient water oxidation,* Science **344**, 1005 (2014).

[31] M. T. McDowell, M. F. Lichterman, J. M. Spurgeon, S. Hu, I. D. Sharp, B. S. Brunschwig, and N. S. Lewis, *Improved Stability of Polycrystalline Bismuth Vanadate Photoanodes by Use of Dual-Layer Thin $TiO_2$/Ni Coatings,* The Journal of Physical Chemistry C **118**, 19618 (2014).

[32] M. F. Lichterman, A. I. Carim, M. T. McDowell, S. Hu, H. B. Gray, B. S. Brunschwig, and N. S. Lewis, *Stabilization of n-cadmium telluride photoanodes for water oxidation to $O_2$(g) in aqueous alkaline electrolytes using amorphous TiO2 films formed by atomic-layer deposition,* Energy Environ. Sci. **7**, 3334 (2014).

[33] C. G. Morales-Guio, S. D. Tilley, H. Vrubel, M. Grätzel, and X. Hu, *Hydrogen evolution from a copper(I) oxide photocathode coated with an amorphous molybdenum sulphide catalyst,* Nature Communications **5**, 3059 (2014).

[34] Y. J. Hwang, A. Boukai, and P. Yang, *High Density n-Si/n-TiO 2 Core/Shell Nanowire Arrays with Enhanced Photoactivity,* Nano Letters **9**, 410 (2009).

[35] W. Siripala, A. Ivanovskaya, T. F. Jaramillo, S.-H. Baeck, and E. W. McFarland, *A $Cu_2O/TiO_2$ heterojunction thin film cathode for photoelectrocatalysis,* Sol. Energy Mater. Sol. Cells **77**, 229 (2003).

[36] M. Wang, L. Sun, Z. Lin, J. Cai, K. Xie, and C. Lin, *p-n Heterojunction photoelectrodes composed of $Cu_2O$-loaded $TiO_2$ nanotube arrays with enhanced photoelectrochemical and photoelectrocatalytic activities,* Energy & Environmental Science **6**, 1211 (2013).

[37] M. Malizia, B. Seger, I. Chorkendorff, and P. C. K. Vesborg, *Formation of a p-n heterojunction on GaP photocathodes for $H_2$ production providing an open-circuit voltage of 710 mV,* J. Mater. Chem. A **2**, 6847 (2014).

[38] M. Zeman, *Advanced Amorphous Silicon Solar Cell Technologies,* in *Thin Film Solar Cells Fabrication, Characterization and Applications*, edited by J. Poortmans and V. Arkhipov (John Wiley & Sons, Ltd, Chichester, 2006) Chap. Advanced A, pp. 173–236.

[39] IUPAC. Compendium of Chemical Terminology, 2nd ed. (the "Gold Book"). Compiled by A. D. McNaught and A. Wilkinson, `http://goldbook.iupac.org/html/S/S05917.html` (Blackwell Scientific Publications, Oxford, 1997), accessed: February, 2018.

[40] M. W. M. van Cleef, F. A. Rubinelli, R. Rizzoli, R. Pinghini, R. E. I. Schropp, and W. F. van der Weg, *Amorphous Silicon Carbide/Crystalline Silicon Heterojunction Solar Cells: A Comprehensive Study of the Photocarrier Collection,* Japanese Journal of Applied Physics **37**, 3926 (1998).

[41] M. I. Kabir, A. Amin, Nowshad anjd Zaharim, and K. Sopian, *Effect of Energy Bandgap of the Amorphous Silicon Carbide (a-SiC:H) Layers On a-Si Multijuntion Solar Cells from Numerical Analysis,* in *Proceedings of the 11th WSEAS International Conference on Mathematical Methods, Computational Techniques and Intelligent Systems, MAMECTIS '09, Proc. 8th WSEAS NOLASC '09, Proc. 5th WSEAS CONTROL '09* (2009) pp. 334–337.

[42] S. Dhar, O. Seitz, M. D. Halls, S. Choi, Y. J. Chabal, and L. C. Feldman, *Chemical Properties of Oxidized Silicon Carbide Surfaces upon Etching in Hydrofluoric Acid,* Journal of the American Chemical Society **131**, 16808 (2009).

[43] W. M. Ayers, *Hydrogenated amorphous silicon/electrolyte contacts: Band bending and photoresponse dependence on surface reactions,* Journal of Applied Physics **53**, 6911 (1982).

[44] Y. Chan and T. Jayadevaiah, *Amorphous silicon-electrolyte interface,* Journal of Non-Crystalline Solids **12**, 314 (1973).

[45] J. V. Chazalviel, *The silicon/electrolyte interface,* in *Porous Silicon Science Technology*, edited by J.-C. Vial and J. Derrien (1995) Chap. The silicon/electrolyte interface, pp. 17–32.

[46] S. Weisz, J. Avalos, M. Gomez, A. Many, Y. Goldstein, and E. Savir, *Surface states on amorphous silicon,* Surf. Sci. **338**, 117 (1995).

[47] C. C. L. McCrory, S. Jung, I. M. Ferrer, S. M. Chatman, J. C. Peters, and T. F. Jaramillo, *Benchmarking Hydrogen Evolving Reaction and Oxygen Evolving Reaction Electrocatalysts for Solar Water Splitting Devices,* Journal of the American Chemical Society **137**, 4347 (2015).

[48] P. A. Bayley and J. M. Marshall, *Transient photoconductivity in a-$Si_{1-x}C_x$:H thin films,* Philosophical Magazine Part B **73**, 429 (1996).

[49] American Society for Testing and Materials (ASTM), *Reference Solar Spectral Irradiance: Air Mass 1.5,* `http://rredc.nrel.gov/solar/spectra/am1.5/`, accessed: February, 2018.

[50] H. Pelouchova, P. Janda, J. Weber, and L. Kavan, *Charge transfer reductive doping of single crystal $TiO_2$ anatase,* Journal of Electroanalytical Chemistry **566**, 73 (2004).

[51] S. D. Tilley, M. Schreier, J. Azevedo, M. Stefik, and M. Graetzel, *Ruthenium Oxide Hydrogen Evolution Catalysis on Composite Cuprous Oxide Water-Splitting Photocathodes,* Advanced Functional Materials **24**, 303 (2014).

# 6

# Engineering the kinetics and interfacial energetics of Ni/Ni–Mo catalyzed amorphous silicon carbide photocathodes in alkaline media

Photoelectrochemical (PEC) water splitting is an attractive approach to converting and storing the abundant solar energy in the form of chemical bonds of hydrogen and oxygen. In order to efficiently evolve hydrogen, substantial kinetic losses on the photocathode surface and significant ohmic losses in the electrolyte should be avoided. Herein, we demonstrate amorphous silicon carbide (a-SiC) photocathodes that overcome these losses through the use of an ultrathin nickel (Ni) film coupled with a nickel molybdenum (Ni–Mo) alloy catalyst in a strongly alkaline solution (pH 14). The incorporation of a thin Ni film increases the number of catalytic active sites and improves the reaction kinetics of the hydrogen evolution on the photocathode surface. Additionally, we report the influence of the catalyst coverage on the junction behavior at the solid-liquid interface. Furthermore, we discuss the chemical stability of the a-SiC photocathode with a thin titanium dioxide ($TiO_2$) protective layer in a highly alkaline environment.

Parts of this chapter have been published in I. A. Digdaya, P. Perez Rodriguez, M. Ma, G. W. P. Adhyaksa, E. C. Garnett, A. H. M, Smets and W. A. Smith, *J. Mater. Chem. A*, 2016, **4**, 6872–6852. [1]

## 6.1. Introduction

Amorphous silicon (a-Si) is a promising semiconductor material for use in photoelectrochemical water splitting devices because of its strong light absorption (up to $10^3$ times stronger than crystalline silicon) in the ultraviolet and visible part of solar spectrum, its band gap energy that can be tuned with carbon incorporation (from 1.8 to 2.3 eV), and the low temperature device processing relative to diffused homojunction crystalline silicons that allows for large area thin film deposition on a wide variety of low-cost substrates.[2] However, the chemical instability of a-Si in aqueous solutions has impeded its direct use as a photoabsorber in solar hydrogen generating systems.[3–5] The protection of the semiconductor electrode commonly involves a thin-film coating that has multiple properties such as optical transparency, electrical conductivity and electrochemical stability. Titanium dioxide ($TiO_2$) is one of the most investigated materials that has been repeatedly shown to be effective in stabilizing a wide range of photoelectrodes, including single crystal Si, II-VI and III-V compounds, as well as metal oxide semiconductors.[6–9] $TiO_2$ protective coatings have also been implemented on a-Si photocathodes and yielded stable photocurrent densities as high as $-11.6$ mA cm$^{-2}$ at the formal potential for hydrogen evolution ($E^{0\prime}$ ($H^+/H_2$) = 0 V *versus* a reversible hydrogen electrode, RHE) and device photovoltages of up to 0.85 V.[3,10] Similarly in the previous chapter, we have shown a thin film a-Si with 10% carbon content (amorphous silicon carbide, a-SiC) protected by an amorphous $TiO_2$ capable of generating a constant photocurrent density of $-8.6$ mA cm$^{-2}$ at $E^{0\prime}$ ($H^+/H_2$) and a cathodic photocurrent onset at +0.76 V *versus* RHE in an electrolyte solution at pH 4.[11] Although the photocurrent density of the previously reported a-SiC is notably high, it is still far below the maximum value that can be obtained from a semiconductor electrode having a band gap of 2 eV. A significant part of this photocurrent loss arises from the inability of our a-SiC to rapidly rise the onset of cathodic photocurrent as a result of the poor ionic conductivity of the near-neutral electrolyte that causes a large voltage drop across the Helmholtz plane. In order to minimize substantial ohmic losses in the electrochemical environment, it is therefore imperative to examine the photoelectrochemical performance of the photocathode at an extreme pH.

In addition to the electrolyte pH, the inherent catalytic activity of the photocathode surface must be favorable to evolve hydrogen. While $TiO_2$ can effectively protect the chemically unstable photocathodes, its surface is not catalytically active for the hydrogen evolution reaction (HER), and therefore, surface modification with a hydrogen-evolving catalyst is required to facilitate the charge transfer process at the solid-liquid interface. Platinum (Pt) catalysts has been widely used for hydrogen evolution due to its ability to drive the HER close to the actual thermodynamic requirement, but the scarcity of Pt might be impractical for large-scale implementation.[12] New classes of HER catalysts composed from earth abundant elements, such as metal sulfides,[13–17] metal phosphides,[18,19] and metal carbides,[20,21] have recently emerged as cheap and efficient alternatives to substitute for Pt. However, these catalysts are mostly active and stable only in acidic media.[22] When considering the overall water splitting reaction, both hydrogen and oxygen evolution need to take place simultaneously, and in many proposed configurations, in the same (photo)electrochemical cell. Therefore, considerations of stability and performance of the catalyst materials for water oxidation at the anode and water reduction at the cathode in a given electrolyte must be taken into account. Using highly acidic electrolytes will leave noble-metal-based catalysts such as $IrO_x$ and $RuO_x$ as the only viable options for the oxygen-evolving anode. On the other hand, cheap and abundant oxygen evolution catalysts such as NiFeOOH are stable and work more efficiently in alkaline solutions.[23] Therefore, when envisioning a practical solar water splitting device that must operate in

an extreme pH and considering the cost of materials, the most promising solution may be to operate the system in an alkaline electrolyte. Fortunately, several HER catalysts made from binary and ternary mixtures of Ni-alloys have recently demonstrated high activity and stability in strongly alkaline solutions.[24–27] Nickel-molybdenum (Ni–Mo) catalysts, in particular, have been reported to require less than 40 mV of overpotential to achieve a constant current density of $-10$ mA cm$^{-2}$ in strong alkaline media for at least 24 hours.[28]

Besides the ability to enhance the kinetics of the surface reaction, the catalyst may have fundamental roles on the energetics and charge transfer processes at the solid-liquid interface. We have previously demonstrated the improved energetics of a-SiC photocathodes coupled with a $TiO_2$ front surface layer which significantly affect the photovoltage of the isolated junction photocathodes.[11] However, the effect of Ni–Mo catalyst on the interfacial electronic structure of the composite was not further clarified since the catalyst was in the form of nanoparticles, thus still exposing the semiconductor surface to the electrolyte, and therefore was assumed to have no substantial impact on the energetics at the solid-liquid interface and the resulting photocurrent onset.

Herein we report the photoelectrochemical activity of a-SiC photocathodes coated with a $TiO_2$ protective layer and hydrogen-evolving catalysts in a strongly alkaline electrolyte. The reaction kinetics on the photocathode surface is improved by the introduction of a thin Ni film in conjunction with a Ni–Mo alloy catalyst. The energetics at the $TiO_2$, the catalyst and the liquid interfaces are thoroughly investigated using electrochemical impedance spectroscopy (EIS). Finally, we demonstrate the use of Ni/Ni–Mo dual catalysts that significantly increases the photoelectrochemical performance of the $TiO_2$-protected a-SiC photocathodes under simulated solar illumination using only cheap earth abundant materials.

## 6.2. Experimental details

### Fabrication of a-SiC photocathodes

Hydrogenated amorphous silicon carbide (a-SiC) photocathodes were deposited onto textured fluorine-doped tin oxide ($SnO_2$:F, FTO) substrates (Asahi VU-type) using a radio frequency plasma enhanced chemical vapor deposited (RF-PECVD) multi-chamber tool. The substrate was kept at 170 °C during the deposition. An ultrathin (10 nm) boron doped hydrogenated amorphous silicon carbide (a-SiC(B)) was used as the p-type layer, decomposed from $SiH_4$ (20 sccm), $CH_4$ (45 sccm), and $B_2H_6$ (2 sccm) diluted gas flow under controlled pressure. The thin (100 nm) intrinsic a-SiC ($SiH_4$: 20 sccm, $CH_4$: 2.5 sccm, $H_2$: 170 sccm) was deposited in a separate chamber to avoid cross contamination. To complete the p-i-n structure, a thin (20 nm) n-type layer of phosphorus (P) doped nc-$SiO_x$ ($SiH_4$: 2.5 sccm, $CO_2$: 2 sccm, $PH_3$: 1.2 sccm, $H_2$: 100 sccm). In our previous work we used an amorphous $TiO_2$ as the n-type layer, but we obtained more consistent photovoltage when using the n-type nc-$SiO_x$. An $H_2$ treatment in a low RF power density is followed in the same chamber in order to passivate the p-i-n interface. After the deposition, the p-i-n a-SiC is complete and a stripe of 300 nm Al was coated on the pre-covered FTO substrate area as the metal back contact using a Provac electron beam evaporator in rotation mode. Electrical contact was made using a silver wire attached by graphite paste.

### Atomic layer deposition of $TiO_2$

Thin layers of amorphous $TiO_2$ (25 nm) were deposited onto the a-SiC photocathode or FTO glass substrate using a homemade thermal atomic layer deposition (ALD) system. The $TiO_2$ ALD was carried out at a substrate temperature of 200 °C using tetrakis-

(dimethylamido)-titanium (TDMAT) and $H_2O$ as the Ti and O precursors, respectively. The pulsing times are 5 s and 10 ms for Ti and O, respectively. Each precursor was purged for 30 seconds after each pulse. The thickness of ALD $TiO_2$ was measured using spectroscopic ellipsometer (J.A. Woollam Co., Inc.) by depositing $TiO_2$ onto a Si wafer covered by its native oxide. The obtained data were fitted with the dieletric $TiO_2$ model and the growth rate per cycle was found to be 0.8 Å per cycle at deposition temperature of 200 °C. All samples were post-annealed in vacuum at 300 °C.

### Catalyst depositions

Ultrathin Ni films were deposited using radio frequency (RF) magnetron sputter deposition in a Prevac sputter machine from a pure Ni target (99.95%). The Ar flow rate was 15 sccm and the power was 100 W. The Ni deposition time was 100 s, resulting in an approximately 2-nm-think Ni film. The Ni–Mo catalyst was deposited by electrodeposition technique using the recipe that has been described previously in another report,[29] except nickel sulfate was used instead of nickel sulfamate. The electrodeposition bath consisted of 1.3 M nickel(II) sulfate hexahydrate (Sigma-Aldrich, 99%), 0.5 M boric acid (Sigma-Aldrich, 99.5%) and 20 mM sodium molybdate dihydrate (Sigma-Aldrich, 99%). The pH of the solution was 5 and no pH adjustment was carried out. The Ni–Mo catalysts were potentiostatically deposited on the $TiO_2$ and the Ni coated $TiO_2$ at a fixed potential of −1.2 V *versus* Ag/AgCl using a potentiostat (PARSTAT MC, Princeton Applied Research) until 1.0 C $cm^{-2}$ of charge passed. The electrodeposition of Ni–Mo on the photocathodes was performed potentiostatically at −1.0 V *versus* Ag/AgCl. During the deposition, the photocathodes were illuminated from the back side (*i.e.*, light enters the photocathode through the FTO-coated glass substrate) with the standard AM1.5 illumination (100 mW $cm^{-2}$) using a Newport Sol3A Class AAA solar simulator (type 94023A-SR3) with 450 Watt Xenon short arc lamp. Finally, the photocathodes were rinsed with milli-Q water before the photoelectrochemical measurements.

### Photoelectrochemical measurements

The photoelectrochemical activity of a-SiC photocathodes was tested using a potentiostat (Parstat MC, Princeton Applied Research) in a three-electrode system, where the a-SiC photocathode with an exposed surface area of 0.283 $cm^{-2}$ acted as the working electrode, a Ni coil in a fritted-glass gas dispersion tube (Sigma-Aldrich) acted as the counter electrode and an Ag/AgCl electrode (in saturated KCL and AgCl, Radiometer Analytical XR300, Hach) is used as the reference electrode. The electrolyte used was 1 M potassium hydroxide (KOH) (Alfa Aesar, 85%) solution. The Ag/AgCl reference electrode was converted to the reversible hydrogen electrode (RHE) and had a potential of 1.026 V *versus* RHE in 1 M KOH solution. Cyclic voltammetries were performed at a scan rate of 50 mV $s^{-1}$ with 10 mV incremental steps. Photocurrent densities of a-SiC photocathodes were characterized under simulated AM1.5 solar irradiation (100 mW $cm^{-2}$) using a Newport Sol3A Class AAA solar simulator (type 94023A-SR3) with 450 Watt Xenon short arc lamp. Gas product measurement of the sample was performed in a gas-tight electrochemical cell with an exposed active area of 0.785 $cm^{-2}$, using a gas chromatograph (GC, Interscience). The cell was continuously purged with a constant $N_2$ flow rate (20 sccm) and vented directly into the gas-sampling loop of the GC to enable periodic quantification of the gas-phase products. A thermal conductivity detector (TCD) was utilized to quantify hydrogen concentration. The Faradaic efficiency was determined by: $2n_{H_2}F/Q$, where $n_{H_2}$ is the total amount of produced hydrogen (mol), $F$ is the Faraday constant (96485 C $mol^{-1}$) and $Q$ is the electric charge. The data were collected every 18 minutes and the current was integrated over the

data collection time to calculate the Faradaic efficiency.

#### Electrochemical impedance spectroscopy

Electrochemical Impedance spectroscopy (EIS) measurements were performed on the bare $TiO_2$ (100 nm) substrates and with the catalyst coated $TiO_2$ substrates in a 1 M KOH electrolyte solution at pH 14 using a PARSTAT 4000 (Princeton Applied Research) potentiostat. During EIS measurements, the potential was scanned in the cathodic direction from +0.8 V to 0 V *versus* RHE. The frequency range of measurement was 100 kHz to 0.1 Hz at a DC potential amplitude of 10 mV. EIS data were fitted to equivalent electronic cicuits using the ZView® software (Scribner Associates). Mott-Schottky plots were obtained from the real capacitance values obtained by fitting the semicircles in the Nyquist plot, using a constant phase element instead of a perfect capacitor to account for non-ideal capacitive behaviors of the electrodes.

#### Material characterization

The morphology of the samples were characterized using a high-resolution scanning electron microscope (SEM, FEI Verios 460) with a through the lens detector (TLD) for secondary electrons. SEM images were recorded using an accelerating voltage of 10 kV. The material composition was characterized using an X-ray photoelectron spectroscopy (XPS, Thermo Scientific K-alpha) equipped with an Al K-alpha X-ray source and a flood gun. The crystal structure of the samples were characterized using a Bruker D8 Advance X-ray diffractometer equipped with LynxEye linear detector in a Bragg-Brentano configuration, with a cobalt source (Co–K$\alpha_1$ $\lambda = 1.788965$ Å).

## 6.3. Results and discussion

#### Electrohemical activity of the deposited electrocatalysts

The resulting deposits of Ni–Mo by electrochemical synthesis were uniformly dispersed nanoparticles with a mean size of 10 nm and with an interparticle spacing distance of a few nanometers that, in some regions, formed agglomerates (shown by scanning electron microscopy (SEM) images in Fig. 6.1 and more detailed images are shown in Fig. D.1, Appendix D). Figure 6.2a shows the current–voltage ($j$–$V$) characteristics of Ni–Mo electrocatalyst in contact with 1 M KOH electrolyte. The Ni–Mo alloy catalyst demonstrated a negligible overpotential to drive the hydrogen evolution reaction but showed a slow increasing onset of cathodic current in the observed $j$–$V$ curve. This behavior is ascribed to the incomplete coverage of Ni–Mo that limits the pathways for electron transfer through only the surface region covered by the catalyst particles (illustrated in Fig. 6.2b). The low number of catalytically active sites results in an extensive electron accumulation at the $TiO_2$/Ni–Mo interface which lowers the rate of catalytic reaction of hydrogen evolution, thus reducing the cathodic current near the onset potential (defined as the potential required to achieve a cathodic current of $-10$ $\mu A/cm^{-2}$, Fig. 6.1).

Figure 6.2 also depicts the $j$–$V$ characteristic of Ni film (2 nm) on $TiO_2$-coated FTO substrate in 1 M KOH electrolyte. Ni electrocatalyst showed a relatively late current onset potential for oxygen evolution (+0.2 V), but it demonstrated a steep $j$–$V$ slope relative to Ni–Mo particles. To try to overcome the poor activity, Ni–Mo catalyst was electrodeposited onto the Ni film. SEM images showed that the electrochemical deposition of Ni–Mo onto Ni resulted in compact agglomerates with a larger spacing distance and a non-uniform distribution of larger particles over the surface (Fig. D.1, Appendix D). The Ni/Ni–Mo dual catalysts on the $TiO_2$ showed an enhanced activity for hydrogen evolution relative

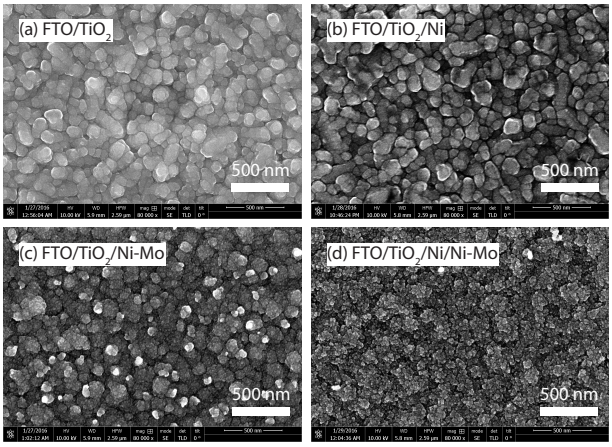



**Figure 6.1:** Top-view scanning electron microscopy (SEM) images of (a) FTO/$TiO_2$, (b) FTO/$TiO_2$/Ni, (c) FTO/$TiO_2$/Ni–Mo, (d) FTO/$TiO_2$/Ni/Ni–Mo. The thickness of the $TiO_2$ is 25 nm and the thickness of the Ni film is 2 nm.

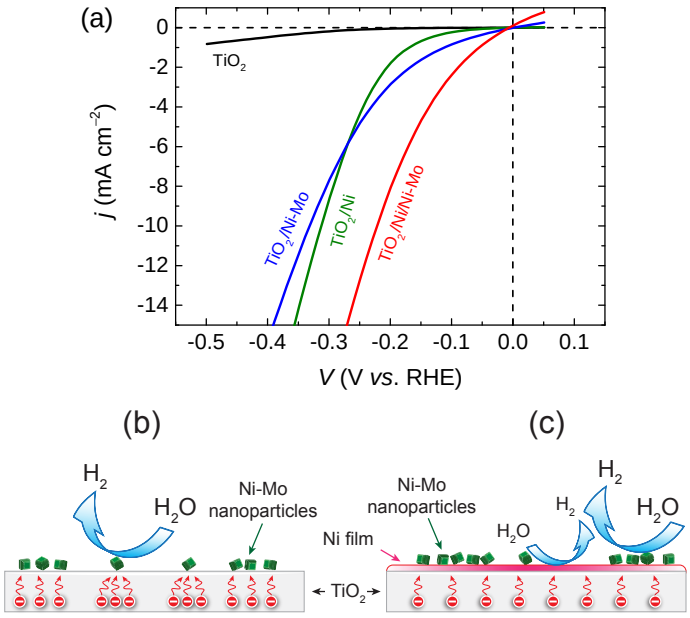



**Figure 6.2:** (a) Current–voltage ($j$–$V$) characteristics of Ni, Ni–Mo, and Ni/Ni–Mo electrocatalysts on $TiO_2$-coated FTO substrate recorded from linear sweep voltammetry in 1 M KOH electrolyte. Ni film was deposited using sputtering with an approximate thickness of 2 nm and Ni–Mo particles were deposited using electrodeposition. All samples were measured in 1 M KOH at pH 14.(b) Schematic illustration of electron pathways through the catalytically active sites of Ni–Mo particles and (c) Ni/Ni–Mo dual-catalysts.

to Ni–Mo as evidenced by its ability to rapidly increase the cathodic current near the same onset potential and produced higher currents at more negative potentials. To give an illustration, Ni–Mo required an extra potential of 130 mV to achieve the same current density of $-10$ mA cm$^{-2}$ that the Ni/Ni–Mo dual-catalyst needed. The improved activity of the electrocatalyst is attributed to the homogeneous coverage of continuous Ni film that fills the interparticle gap of Ni–Mo particles and subsequently increases the number of active sites, and therefore allow electrons to transfer across the entire surface (illustrated in Fig. 6.2c). Additionally, the Ni/Ni–Mo composite indirectly creates a synergistic effect that drives the reaction at a low overpotential while still maintaining the fast rate of the reaction.

**Band-edge energetics of the interfacial layers**

To understand the interfacial energetics between the $TiO_2$ layer, the catalyst and/or the electrolyte, electrochemical impedance spectroscopy (EIS) was performed in the dark in 1 M KOH electrolyte at pH 14. Representative Nyquist plots of each configuration are shown in Fig. 6.3a. Although EIS measurement of the bare $TiO_2$ was recorded over a frequency range between 100 kHz and 0.1 Hz, the analysis was only performed in the high-frequency region (*i.e.*, between 100 kHz and 50 Hz) where capacitive response in this region was prominent. Therefore impedance data can be modeled using a simple Randles circuit consisting of a series resistance of the electrolyte and electrical back contact ($R_{\text{series}}$), and a bulk resistance of $TiO_2$ that is related to exchange of electrons between the conduction band and electronic states on the surface (in this case the surface states) ($R_{\text{bulk}}$)[30,31] in parallel with a space-charge capacitance of $TiO_2$ ($C_{\text{sc}}$), as shown in Fig. 6.3b. The complete data scan can be found in Fig. D.2, Appendix D. Adding extra components and using a more complex electronic circuit would allow for more accurate fitting of the impedance data, particularly in the low frequency region to account for processes occurring at the semiconductor-electrolyte interface, arising from the Helmholtz layer. However, we noticed that the high-frequency response was somewhat overlapping with the low-frequency response in the Nyquist plot, corresponding to the space-charge layer and Helmholtz layer, respectively. Consequently, no distinct semicircles could be observed to discriminate each contribution. Taking all these individual processes into account in the equivalent circuit would inevitably lead to ambiguous interpretation, and therefore separating non-relevant contributions from the space-charge layer becomes even more complicated. To avoid this complexity, fitting impedance data was restricted to only region dominated by the space-charge layer (*i.e.*, typically between 100 kHz and 100 Hz) using a simple Randles circuit, thus allowing identification and determination of solely $C_{\text{sc}}$ of the $TiO_2$.

Besides the Nyquist plot, additional valuable information of the EIS results can be obtained from the Bode phase plot shown in Fig. 6.4b. In the Bode phase plot, the $TiO_2$/electrolyte system exhibits phase angles lower than $-90°$, which is typically ascribed to a non-ideal capacitive behavior. Therefore, a constant phase element of the space-charge layer ($\text{CPE}_{\text{sc}}$) is used instead of the perfect $C_{\text{sc}}$ element in the equivalent electronic circuit to fit the impedance data. The equivalent capacitance of a CPE is given by[32]

$$C = \text{CPE}(\omega_{\max})^{n-1} \tag{6.1}$$

where $\omega_{\max}$ is the frequency at which the imaginary value of the impedance has the maximum, and $n$ is the empirical constant that describes the electrical behavior of CPE, and can range between 0 (purely resistive) and 1 (purely capacitive). In a circuit model where the CPE is in parallel with $R$, the true capacitance can be estimated using the following relationship:[33]

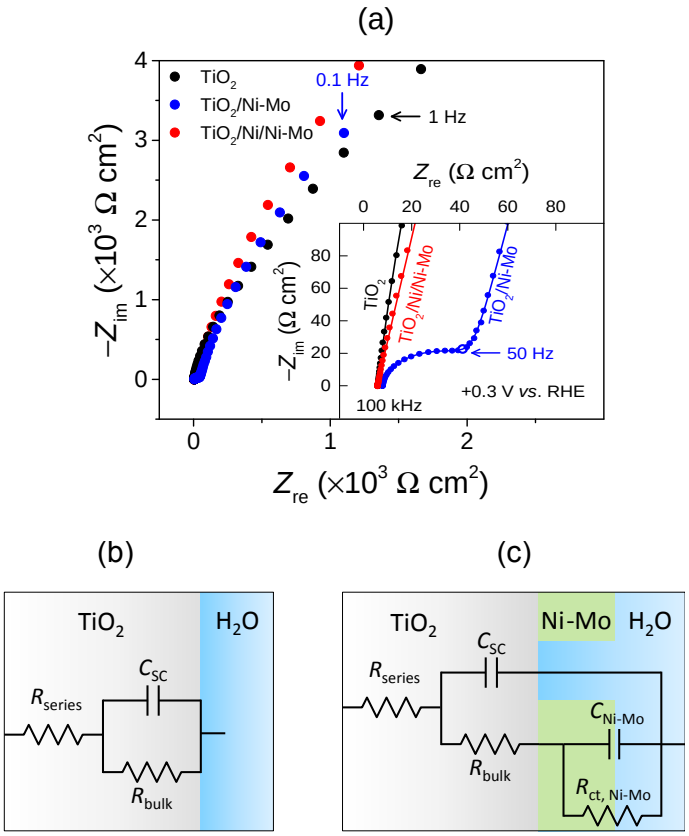



**Figure 6.3:** (a) Nyquist plots of $TiO_2$ with and without the catalysts at +0.3 V *versus* RHE. The horizontal axis is the real part of impedance ($Z_{re}$) and the vertical axis is the imaginary part of impedance ($Z_{im}$). The inset shows the magnification of the impedance response in the high-frequency region. The symbols represent the impedance data points from the EIS measurements and the solid lines represent the fit results using the equivalent electronic circuits. (b) Randles circuit used when one semicircle in the Nyquist plot is observed. (c) Equivalent circuit used when two semicircles are apparent, involving the contribution from the Ni–Mo catalyst.

$$C = R^{(1-n/n)}\mathrm{CPE}^{(1/n)} \tag{6.2}$$

The origin of this CPE behavior is most likely due to the presence of multiple surface states and/or deep impurity states with energy levels distributed within the band gap.[34]

In the presence of the Ni–Mo catalyst on the $TiO_2$, two semicircles were apparent in the Nyquist plot. The first semicircle (shown in the inset of Fig. 6.3a) in the high-frequency region is related to the contribution from the space-charge layer of $TiO_2$ and the low-frequency semicircle is associated with the contribution from the Ni–Mo catalyst. To assign both features, extra components such as the constant phase element of Ni–Mo ($\mathrm{CPE}_{\mathrm{Ni–Mo}}$) and the charge transfer resistance of Ni–Mo ($R_{\mathrm{ct,\ Ni–Mo}}$) were added to the equivalent circuit to interpret the impedance data, as shown in Fig 6.3c. The validity of this circuit was verified by independent investigation of the high-frequency response of the impedance

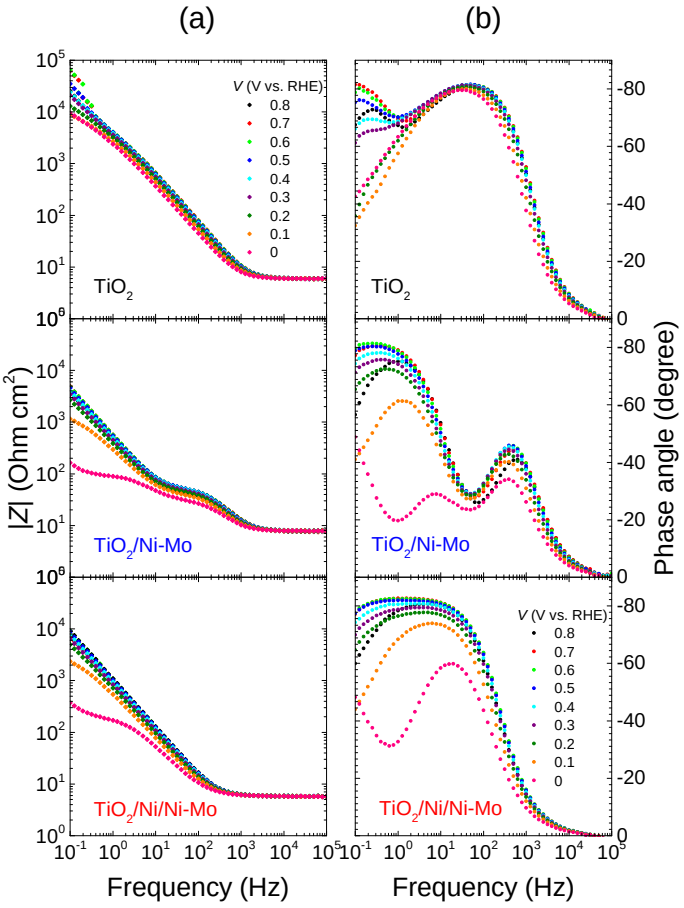



**Figure 6.4:** Bode plots of (a) total impedance ($|Z|$) and (b) phase angle of $TiO_2$ with and without and the catalysts collected during EIS measurements at different applied potentials.

data (*i.e.*, low semicircle); the obtained capacitances of the $TiO_2$/Ni–Mo from the fitted high-frequency impedance revealed identical values (in the same order of magnitude) as that of the bare $TiO_2$ throughout the whole potential range of measurement, as shown in Fig. 6.5a. Since the high-frequency impedance of a semiconductor is generally attributed to the contribution of $C_{sc}$, this implies that the space-charge layer of the $TiO_2$ is not affected by the presence of Ni–Mo particles, and therefore the $TiO_2$ still forms a solid-liquid junction with the electrolyte. The existence of $C_{sc}$ of the $TiO_2$ is also evidenced by the distinguishable peaks of phase angle in the high-frequency region (*i.e.*, 1 kHz) in the Bode phase plot (Fig. 6.4b), in addition to the broad phase-angle peaks in the low-frequency regime (10 Hz to 0.1 Hz). Another reason that allowed us to use this equivalent circuit was the fitting results of $R_{bulk}$ of the $TiO_2$/Ni–Mo having lower values than that of the bare $TiO_2$ (Fig. 6.5b). This means that the exchange of electrons occurs predominantly between the $TiO_2$ conduction band and the metallic Ni–Mo that have higher electron density than the $TiO_2$ surface state, and therefore lowering the resistance. To account for this process,

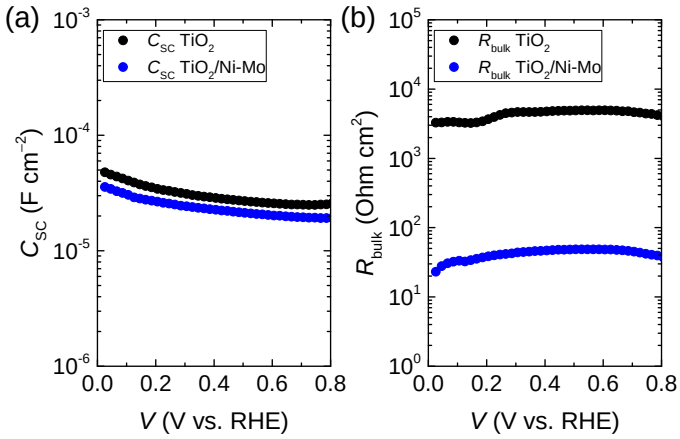



**Figure 6.5:** (a) Space-charge capacitance ($C_{sc}$) and (b) bulk resistance ($R_{bulk}$) of the $TiO_2$ in the bare $TiO_2$ and in the $TiO_2$/Ni–Mo. Values are obtained by fitting the impedance data with the equivalent circuits.

the $R_{bulk}$ element was used in parallel association with $CPE_{Ni–Mo}$ and $R_{ct,\ Ni–Mo}$. This equivalent circuit allowed us to accurately fit the impedance data throughout the whole frequency range of measurement (Fig. D.3, Appendix D).

When a thin Ni film (2 nm) is introduced between the $TiO_2$ and Ni–Mo nanoparticles, the EIS data reveal only one semicircle in the Nyquist plot (Fig. 6.3a). Although the $TiO_2$/Ni/Ni–Mo exhibits a seemingly identical semicircle as that of the bare $TiO_2$, a careful examination in the Bode plot shows a clear shift of the onset of the total impedance ($|Z|$) from 2 kHz in for the bare $TiO_2$ to 200 Hz for the $TiO_2$/Ni/Ni–Mo (Fig. 6.4a). This means that the $TiO_2$/Ni/Ni–Mo has a nearly constant impedance in the high-frequency region (100 kHz to 200 Hz). In this frequency range, the $|Z|$ is almost equal to the real impedance ($Z_{re}$, *i.e.*, resistance, $R$) because the imaginary impedance ($Z_{im}$, *i.e.*, $-1/\omega C$) is too insignificant such that its contribution to the $|Z|$ is negligible (Fig. D.4, Appendix D). This is also consistent with the zero or small phase angle observed from the $TiO_2$/Ni/Ni–Mo within the frequency range between 100 kHz and 200 Hz, contrary to the bare $TiO_2$ of which the phase angle peak is already observed at 100 Hz (Fig. 6.4b). This implies that the capacitive behavior of the $TiO_2$/Ni/Ni–Mo in the high frequency region is not present. Since the high-frequency impedance is generally attributed to the contribution from the electrical characteristic of the space-charge layer of the semiconductor, the constant response of impedance in the high-frequency region, thus the absence of $C_{sc}$, explicitly suggests that the electrical junction between $TiO_2$ and Ni is entirely dominated by the resistive behavior. Previous investigation using operando X-ray photoelectron spectroscopy (XPS) in an electrochemical cell has also revealed that an ultrathin film of Ni is sufficient to effectively maintain a constant electronic band structure of the $TiO_2$ closer to the flat-band potential across a wide potential range, thus providing an ohmic behavior instead of a rectifying junction.[35] The ohmic contact across the whole surface of the $TiO_2$ can be evidently true as confirmed by the nearly uniform coverage of Ni (Fig. D.5, Appendix D). In a strongly alkaline electrolyte, the thin Ni will oxidize to form nickel hydroxide, but will transform back to Ni at reductive potentials and is stable in the metallic form under cathodic conditions (Fig. D.7, Appendix D). These electrochemical processes where the $TiO_2$ exhibits an ohmic be-

havior with the catalyst can be modeled using a Randles circuit consisting of a $R_{series}$ that also includes the resistance of the bulk $TiO_2$ (*i.e.*, $R_{series} = R_{contact} + R_{electrolyte} + R_{bulk}$), the charge transfer from Ni/Ni–Mo ($R_{ct,\ Ni/Ni–Mo}$) and the capacitance or CPE of Ni/Ni–Mo ($CPE_{Ni/Ni–Mo}$). The fit results of the impedance data using this equivalent circuit can be found in Fig. D.6, Appendix D.

The fit results of $C_{sc}$ of the $TiO_2$ from the EIS data were used to construct Mott-Schottky plots in order to analyze the influence of the HER catalysts on the flat-band potential of $TiO_2$ (shown in Fig. 6.6). The intercept between the extrapolated inverse square of the capacitance of the $TiO_2$ space-charge layer with the $x$-axis indicates the flat-band potential of the $TiO_2$. The $TiO_2$ electrodes with and without Ni–Mo particles exhibited nearly the same flat-band potential as the bare $TiO_2$ (−0.2 V *versus* RHE) with a slight deviation which is still in the acceptable margin of error. This band pinning is expected as Ni–Mo particles did not completely cover the $TiO_2$ film, thus still allowing the underlying $TiO_2$ to be in contact with the electrolyte, and forming a rectifying solid-liquid junction. In the case of the $TiO_2$ coated with Ni/Ni–Mo, the high-frequency impedance was not present, and therefore the flat-band potential could not be determined. Fitting the low-frequency impedance with a Randles circuit resulted in a very distinct slope of the Mott-Schottky plot compared to the other two configurations. Since the low-frequency impedance is mainly attributed to the capacitance of the catalyst, the Mott-Schottky result obtained by fitting the impedance data with the equivalent circuit does not reflect the flat-band potential of the $TiO_2$.

Following the electrochemical characterization of the different catalyst layers on the $TiO_2$, the composite layers were deposited in the same conditions on the $TiO_2$-coated a-SiC photocathodes to observe their ability to transfer photogenerated charges to drive the HER. The influence of the catalysts on the interfacial energetics of a-SiC/$TiO_2$ photocathodes at the solid-liquid interface was investigated by performing electrochemical open-circuit potential (OCP) measurements in 1 M KOH electrolyte solution, in the dark and under illumination, (Fig. 6.7). The presence of the $TiO_2$ front layer was important to maintain the stability of the a-SiC photocathode during OCP measurements, since

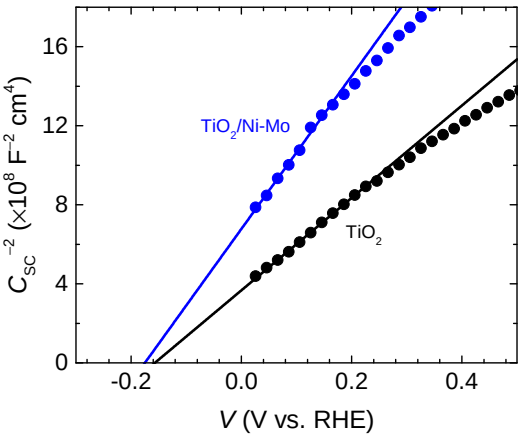



**Figure 6.6:** Mott-Schottky plots ($C_{sc}^{-2}$–$V$) of $TiO_2$ with and without Ni–Mo. The intercept between the extrapolated linear line with the $x$-axis indicate the flat-band potential. The thickness of the $TiO_2$ is 100 nm. All measurements were performed in 1 M KOH pH 14.

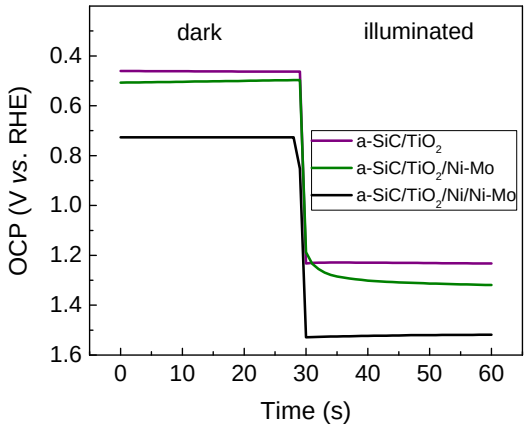



**Figure 6.7:** Electrochemical open-circuit potential (OCP) measurements of the a-SiC/$TiO_2$ photocathode with and without the catalyst layers. The change in the open-circuit voltage in the dark and under illumination represents the photovoltage of the composite systems.

without $TiO_2$ the a-SiC photocathode underwent rapid corrosion even under open-circuit conditions. The OCP in the dark represents the pinning of the Fermi level of the photocathode with electronic states of the front layer and the change in OCP under illumination represents the quasi-Fermi level splitting that translates into the built-in photovoltage of the photocathode. In the dark condition, the Fermi level of the uncatalyzed a-SiC photocathode equilibrates with the surface electronic states of the $TiO_2$ at +0.46 V *versus* RHE. The dark OCP value measured at pH 14 turns out to be close to the previously reported OCP measurement of a-SiC/$TiO_2$ measured at pH 4 (+0.48 V *versus* RHE),[11] implying that the energy level of the amorphous $TiO_2$ surface states with respect to water redox potentials is almost independent of the electrolyte pH. The introduction of the Ni–Mo catalyst onto the a-SiC/$TiO_2$ did not lead to a noticeable change of the dark OCP. This is mainly due to the fact that the $TiO_2$ interfacial layer still forms a solid-liquid junction with the electrolyte and therefore the equilibration of the Fermi level is not substantially affected by Ni–Mo particles on the surface. In the case of Ni/Ni–Mo dual catalysts on the a-SiC/$TiO_2$ photocathode, a new thermal equilibrium is established and the Fermi level of the photocathode is pinned to the new equilibrium surface potential of the outermost layer (*i.e.*, Ni) at +0.7 V *versus* RHE in the dark. Under dark open-circuit condition, no solid-liquid junction is expected because the electrical behavior between $TiO_2$ and Ni is dictated by an ohmic contact. During the dark and illuminated OCP measurements, all the photocathodes showed a photovoltage of 0.8 V, confirming that the addition of the catalysts does not affect the electronic equilibration of the (p-i-n) structure of the a-SiC with the $TiO_2$, *i.e.*, that the buried junction photovoltage is maintained.

### Photoelectrochemical activities of a-SiC photocathodes

The catalytic activity of Ni–Mo and Ni/Ni–Mo catalysts on the a-SiC photocathodes was further evaluated by cyclic voltammetry under simulated solar illumination in 1 M KOH electrolyte solution (Fig. 6.8). Without the catalyst, the $TiO_2$ protected a-SiC showed a late photocurrent onset potential (+0.2 V *versus* RHE), mainly due to the poor reaction kinetics on the uncatalyzed $TiO_2$ surface. The introduction of Ni–Mo catalyst on the

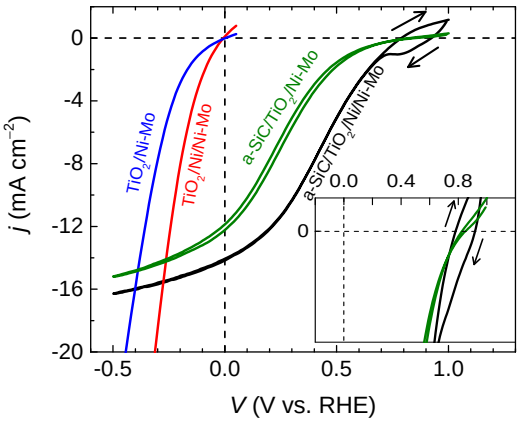



**Figure 6.8:** Current–voltage characteristics ($j$–$V$) of a-SiC/$TiO_2$ with Ni–Mo and Ni/Ni–Mo catalysts under simulated solar illumination. The inset shows the photocurrent onset potential of the photocathodes at +0.8 V *versus* RHE. The measurements were performed in 1 M KOH at pH 14.

photocathode significantly shifted the onset potential, which can be closely seen from the intercept between the anodic and cathodic photocurrent at +0.8 V *versus* RHE, shown in the inset of Fig. 6.8. This result is expected since at this onset potential, the photovoltage of 0.8 V of a buried junction a-SiC photocathode should allow the potential at the surface/electrolyte interface to be positioned at $E^{0\prime}$ ($H^+/H_2$), as illustrated in Fig. 6.9a. However, the photocurrent did not rise steeply at the onset potential due to the low number of active sites for hydrogen evolution of Ni–Mo on the photocathode surface.

Cyclic voltammetry data (Fig. 6.8) also indicated that the photoelectrochemical activity of the a-SiC photocathode with Ni/Ni–Mo dual-catalyst was noticeably higher than that with only the Ni–Mo catalyst. A closer inspection in the inset of Fig. 6.8 reveals that both a-SiC photocathodes with Ni–Mo and Ni/Ni–Mo catalysts had the same onset potential of +0.8 V *versus* RHE. However, the instantaneous increase of photocurrent onset by the more efficient Ni/Ni–Mo improved the photocurrent significantly throughout the whole potential range of measurement. Despite the increase of cathodic photocurrent, the anodic current of the a-SiC with Ni/Ni–Mo was also profound at potentials more positive than +0.8 V *versus* RHE. The apparent anodic current is related to the oxidation of the exposed Ni catalyst to $Ni(OH)_3^-$ and the cathodic current at +0.9 V *versus* RHE is associated with its reduction back to Ni. It is generally known from the Pourbaix diagram that the redox-phase transformation between Ni and $Ni(OH)_3^-$ in an extremely alkaline environment occurs near the hydrogen evolution potential (Fig. D.7, Appendix D). The reduction and oxidation of Ni near the photocurrent onset potential at +0.8 V *versus* RHE is also consistent with the constant photovoltage of a-SiC (0.8 V) that brings the Ni surface potential to a position near the formal potential for hydrogen evolution, thus allowing Ni to oxidize or reduce itself depending on the direction of the potential scan during cyclic voltammetry, as illustrated in Fig. 6.9b. At surface potentials more negative than 0 V *versus* RHE in an alkaline solution at ph 14, Ni is stable in the metallic form (Fig. D.7, Appendix D) and is able to drive the catalytic reaction of hydrogen evolution (Fig. 6.9c).

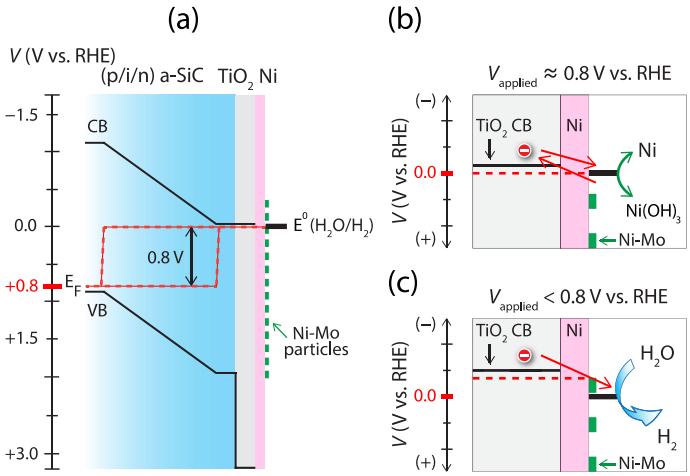



**Figure 6.9:** (a) Energy band diagram at applied potential +0.8 V *versus* RHE. Schematic illustration of (b) Ni oxidation and reduction at an applied potential on a-SiC of ≈ +0.8 V *versus* RHE and (c) the position of surface potential at applied potentials on a-SiC of < +0.8 V *versus* RHE.

### Stability of a-SiC photocathodes

The stability of the a-SiC photocathode in 1 M KOH solution under photoelectrocatalytic condition was evaluated by chronoamperometry test at a constant applied potential of 0 V *versus* RHE (Fig. 6.10). The a-SiC photocathode only showed a stable photocurrent for 40 minutes, followed by a rapid deactivation and a sharp decrease of photocurrent, which left only 35% of the initial value after 1 hour. To confirm that the photocurrent was related to the hydrogen evolution, the hydrogen was measured during the illuminated chronoamperometry experiment using a gas chromatography (GC). The time resolution of data collection of our GC was 18 minutes (the lowest time limit for our particular device). In order to accurately calculate the Faradaic efficiency, the current was integrated every 18 minutes to determine the total number of charge generated over the data collection time. This measurement allowed for quantification of evolved hydrogen gas and the rate of corrosion of the photocathode by chemical and/or electrochemical reaction with the electrolyte solution. During the measurement, the Faradaic efficiency remained nearly 100% in the first 40 minutes, and exceeded unity (117%) as the photocurrent dropped steeply. The overestimated Faradaic efficiency is probably due to the dissolution of the hydrogenated a-SiC during the chronoamperometry test that released hydrogen, and was detected by the GC. The origin of the decay of photocurrent may be caused by the ineffective protection by the $TiO_2$ presumably due to the presence of pinholes in the film that exposes the underlying a-SiC to the highly corrosive electrolyte (1 M KOH), and subsequently etches the a-SiC. As the thickness of the photocathode is reduced, the number of photogenerated electron decreases, causing the photocurrent to drop. Without the $TiO_2$ layer, the a-SiC dissolved faster even in the dark, in the same electrolyte solution, under open-circuit condition (no net current flow), leaving only the FTO after 1 hour (Fig. D.8, Appendix D). This confirms that a-SiC is intrinsically unstable when exposed to a strongly alkaline environment.

In order to evaluate the protection ability of the $TiO_2$, a separate stability experiment was performed using only $TiO_2$ on FTO (without the a-SiC photocathode) with different catalysts in the same 1 M KOH electrolyte solution. From the results of chronopotentiom-

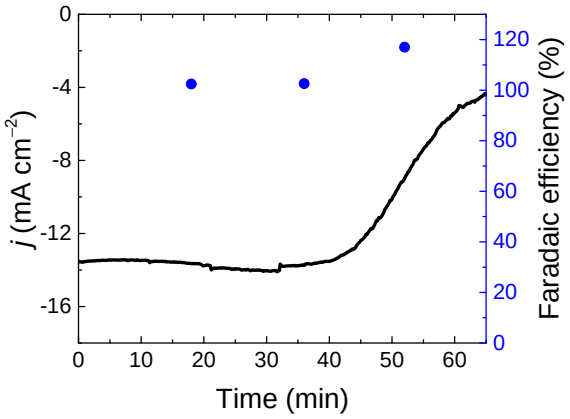



**Figure 6.10:** Chronoamperometry measurement of $TiO_2$ coated a-SiC photocathodes with Ni/Ni–Mo catalyst at a fixed potential of 0 V *versus* RHE.

etry measurement in the dark at a fixed current of −10 mA $cm^{-2}$, it is evident that all catalyzed FTO/$TiO_2$ electrodes demonstrated a good stability for 24 hours and were able to maintain a potential more positive than −0.5 V *versus* RHE (Fig. D.9, Appendix D). To confirm the stability of the $TiO_2$, XPS analyses were performed on the Ni-catalyzed $TiO_2$ before and after the stability test. The FTO/$TiO_2$ electrode with a thin Ni film was chosen over the FTO/$TiO_2$/Ni/Ni–Mo electrode because a thin Ni surface film with a thickness of 2 nm should allow the photoelectron from the $TiO_2$ to escape and be detected by the XPS, since the escape depth is typically in the range of 3–4 nm. Before the stability test, the Ti 2*p* signal from the $TiO_2$ was weak because it was covered by the Ni film (Fig. D.10, Appendix D). XPS data revealed that the Ti 2*p* signal was still detectable after 24 hours, indicating that the $TiO_2$ was not dissolved, and remained present after the test. Interestingly, the Ti 2*p* signal became stronger after 24-hour measurement. This is probably because of the detachment of Ni from $TiO_2$ during the long chronoamperometry test. The removal of Ni was also observed from the reduced intensity of Ni 2*p* signals in the XPS data and the increased intensity of Ti 2*p* signal after prolonged testing, suggesting that the $TiO_2$ became uncovered and more detectable due to the disappearance of the Ni surface film Fig. D.11, Appendix D).

In the case of $TiO_2$-protected a-SiC photocathode, degradation of the photocurrent still occurred even at a lower applied potential (+0.3 V *versus* RHE, Fig. D.12, Appendix D) and at photocurrents below −10 mA $cm^{-2}$. Visual inspection after the experiment revealed that the rapid decay of photocurrent was related to chemical dissolution of a-SiC in 1 M KOH solution. Since the catalyzed $TiO_2$ alone was stable under moderate potential bias (more positive than −0.5 V *versus* RHE, shown in Fig. D.9, Appendix D), we therefore speculate that the corrosion of a-SiC occurs because of the permeation of the highly concentrated KOH through pinholes in the thin amorphous $TiO_2$ produced by low-temperature ALD.[36] KOH permeation could also occur through the amorphous $TiO_2$ on the FTO sample, but since the underlying FTO substrate is more chemically stable than the a-SiC, the composite system remained stable without substantial potential degradation during the chronopotentiometry measurement (Fig. D.9, Appendix D).

Prior efforts have attempted to use amorphous $TiO_2$ coatings for protection of photocathodes in a strongly alkaline environment, yet similar failures were obtained after a

few hours.[10,37] These observations likely imply that although amorphous $TiO_2$ may be an excellent passivation material in a near neutral environment,[38] it may be unsuitable as a protection layer for photocathodes in a strongly alkaline electrolyte. Numerous studies have suggested that $TiO_2$ is electrochemically stable in the compact crystalline form.[6,36,39] Transforming the amorphous structure of $TiO_2$ to a crystalline phase may require in-situ or post-annealing at a temperature of at least 400 °C. However our a-SiC could not survive at this extreme temperature (Fig. D.13, Appendix D), and therefore the post-annealing treatment was carried out at a temperature of only 300 °C. This annealing condition was evidently insufficient to improve the amorphous $TiO_2$ to its crystalline form, as suggested by the absence of $TiO_2$ peaks in the X-ray diffraction pattern (Fig. D.14, Appendix D). Previous reports have demonstrated that the deposition of crystalline $TiO_2$ by low-temperature ALD is indeed possible even without annealing treatment.[40,41] In our future work, a similar approach will be attempted to maintain the high performance and stability of the a-SiC photocathodes in an alkaline solution.

## 6.4. Conclusion

In summary, we have demonstrated a significant photoelectrochemical improvement of a $TiO_2$-protected a-SiC photocathode by use of a dual-layer Ni/Ni–Mo coating, which shows a rapidly increasing onset of photocurrent relative to the photocathode that only have Ni–Mo catalyst. The enhancement of the observed photocurrent is a result of the increased number of surface catalytic active sites for hydrogen evolution on the photocathode upon the incorporation of a thin Ni film that allows electron to transfer through a large area and prevents charge accumulation on the surface. Additionally, using EIS and Mott-Schottky analysis, we have investigated the solid-liquid rectifying characteristic when only Ni–Mo is used, and the ohmic behavior when a thin Ni film is added before the deposition of Ni–Mo. This work clearly shows the potential of the dual-layer Ni/Ni–Mo coating as an efficient electrocatalyst for hydrogen-evolving photocathodes, and demonstrates the importance of the high surface catalyst coverage for improving the photoelectrochemical performance of the photocathodes. The high electrocatalytic activity of the Ni/Ni–Mo should motivate the utilization of dual-layer catalysts to maximize the photocurrent output of the photocathodes for efficient solar hydrogen evolution.

## References

[1] I. A. Digdaya, P. P. Rodriguez, M. Ma, G. W. P. Adhyaksa, E. C. Garnett, A. H. M. Smets, and W. A. Smith, *Engineering the kinetics and interfacial energetics of ni/ni–mo catalyzed amorphous silicon carbide photocathodes in alkaline media,* J. Mater. Chem. A **4**, 6842 (2016).

[2] M. Zeman, *Thin Film Solar Cells Fabrication, Characterization and Applications*, edited by J. Poortmans and V. Arkhipov (John Wiley & Sons, Ltd, Chichester, 2006) Chap. Advanced A, pp. 173–236.

[3] Y. Lin, C. Battaglia, M. Boccard, M. Hettick, Z. Yu, C. Ballif, J. W. Ager, and A. Javey, *Amorphous Si thin film based photocathodes with high photovoltage for efficient hydrogen production.* Nano lett. **13**, 5615 (2013).

[4] S. K. Kang, G. Park, K. Kim, S. W. Hwang, H. Cheng, J. Shin, S. Chung, M. Kim, L. Yin, J. C. Lee, K. M. Lee, and J. A. Rogers, *Dissolution chemistry and biocompat-*

*ibility of silicon- and germanium-based semiconductors for transient electronics,* ACS Applied Materials & Interfaces **7**, 9297 (2015).

[5] W. Qin, N. Wang, T. Yao, S. Wang, H. Wang, Y. Cao, S. Liu, and C. Li, *Enhancing the Performance of Amorphous-Silicon Photoanodes for Photoelectrocatalytic Water Oxidation,* ChemSusChem **8**, 3987 (2015).

[6] B. Seger, T. Pedersen, A. B. Laursen, P. C. K. Vesborg, O. Hansen, and I. Chorkendorff, *Using $TiO_2$ as a conductive protective layer for photocathodic $H_2$ evolution.* J. Am. Chem. Soc. **135**, 1057 (2013).

[7] Y. W. Chen, J. D. Prange, S. Dühnen, Y. Park, M. Gunji, C. E. D. Chidsey, and P. C. McIntyre, *Atomic layer-deposited tunnel oxide stabilizes silicon photoanodes for water oxidation.* Nat. Mater. **10**, 539 (2011).

[8] S. Hu, M. R. Shaner, J. A. Beardslee, M. Lichterman, B. S. Brunschwig, and N. S. Lewis, *Amorphous $TiO_2$ coatings stabilize Si, GaAs, and GaP photoanodes for efficient water oxidation.* Science **344**, 1005 (2014).

[9] S. Hu, N. S. Lewis, J. W. Ager, J. Yang, J. R. McKone, and N. C. Strandwitz, *Thin-Film Materials for the Protection of Semiconducting Photoelectrodes in Solar-Fuel Generators,* The Journal of Physical Chemistry C **119**, 24201 (2015).

[10] C. G. Morales-Guio, K. Thorwarth, B. Niesen, L. Liardet, J. Patscheider, C. Ballif, and X. Hu, *Solar Hydrogen Production by Amorphous Silicon Photocathodes Coated with a Magnetron Sputter Deposited $Mo_2C$ Catalyst.* J. Am. Chem. Soc. **137**, 7035 (2015).

[11] I. A. Digdaya, L. Han, T. W. F. Buijs, M. Zeman, B. Dam, A. H. M. Smets, and W. A. Smith, *Extracting large photovoltages from a-SiC photocathodes with an amorphous $TiO_2$ front surface field layer for solar hydrogen evolution,* Energy Environ. Sci. **8**, 1585 (2015).

[12] E. Kemppainen, A. Bodin, B. Sebok, T. Pedersen, B. Seger, B. Mei, D. Bae, P. C. K. Vesborg, J. Halme, O. Hansen, P. D. Lund, and I. Chorkendorff, *Scalability and feasibility of photoelectrochemical $H_2$ evolution: the ultimate limit of Pt nanoparticle as an HER catalyst,* Energy Environ. Sci. **8**, 2991 (2015).

[13] D. Merki, S. Fierro, H. Vrubel, and X. Hu, *Amorphous molybdenum sulfide films as catalysts for electrochemical hydrogen production in water,* Chem. Sci. **2**, 1262 (2011).

[14] D. Merki, H. Vrubel, L. Rovelli, S. Fierro, and X. Hu, *Fe, Co, and Ni ions promote the catalytic activity of amorphous molybdenum sulfide films for hydrogen evolution,* Chem. Sci. **3**, 2515 (2012).

[15] P. D. Tran, S. S. Pramana, V. S. Kale, M. Nguyen, S. Y. Chiam, S. K. Batabyal, L. H. Wong, J. Barber, and J. Loo, *Novel assembly of an $MoS_2$ electrocatalyst onto a silicon nanowire array electrode to construct a photocathode composed of elements abundant on the earth for hydrogen generation.* Chem. Eur. J. **18**, 13994 (2012).

[16] P. D. Tran, S. Y. Chiam, P. P. Boix, Y. Ren, S. S. Pramana, J. Fize, V. Artero, and J. Barber, *Novel cobalt/nickel–tungsten-sulfide catalysts for electrocatalytic hydrogen generation from water,* Energy Environ. Sci. **6**, 2452 (2013).

[17] D. Voiry, H. Yamaguchi, J. Li, R. Silva, D. C. B. Alves, T. Fujita, M. Chen, T. Asefa, V. B. Shenoy, G. Eda, and M. Chhowalla, *Enhanced catalytic activity in strained chemically exfoliated $WS_2$ nanosheets for hydrogen evolution,* Nat. Mater. **12**, 850 (2013).

[18] E. J. Popczun, J. R. McKone, C. G. Read, A. J. Biacchi, A. M. Wiltrout, N. S. Lewis, and R. E. Schaak, *Nanostructured nickel phosphide as an electrocatalyst for the hydrogen evolution reaction.* J. Am. Chem. Soc. **135**, 9267 (2013).

[19] L. Feng, H. Vrubel, M. Bensimon, and X. Hu, *Easily-prepared dinickel phosphide ($Ni_2P$) nanoparticles as an efficient and robust electrocatalyst for hydrogen evolution.* Phys. Chem. Chem. Phys. **16**, 5917 (2014).

[20] M. D. Scanlon, X. Bian, H. Vrubel, V. Amstutz, K. Schenk, X. Hu, B. Liu, and H. H. Girault, *Low-cost industrially available molybdenum boride and carbide as "platinum-like" catalysts for the hydrogen evolution reaction in biphasic liquid systems.* Phys. Chem. Chem. Phys. **15**, 2847 (2013).

[21] W.-F. Chen, C.-H. Wang, K. Sasaki, N. Marinkovic, W. Xu, J. T. Muckerman, Y. Zhu, and R. R. Adzic, *Highly active and durable nanostructured molybdenum carbide electrocatalysts for hydrogen production,* Energy Environ. Sci. **6**, 943 (2013).

[22] P. C. K. Vesborg, B. Seger, and I. Chorkendorff, *Recent Development in Hydrogen Evolution Reaction Catalysts and Their Practical Implementation,* J. Phys. Chem. C **6**, 951 (2015).

[23] C. C. L. McCrory, S. Jung, J. C. Peters, and T. F. Jaramillo, *Benchmarking heterogeneous electrocatalysts for the oxygen evolution reaction,* J. Am. Chem. Soc. **135**, 16977 (2013), pMID: 24171402.

[24] I. A. Raj and K. I. Vasu, *Transition metal-based cathodes for hydrogen evolution in alkaline solution: Electrocatalysis on nickel-based ternary electrolytic codeposits,* J. Appl. Electrochem. **22**, 471 (1992).

[25] C. Fan, D. L. Piron, A. Sleb, and P. Paradis, *Study of electrodeposited nickel-molybdenum, nickel-tungsten, cobalt-molybdenum, and cobalt-tungsten as hydrogen electrodes in alkaline water electrolysis,* J. Electrochem. Soc. **141**, 850 (1994).

[26] W.-F. Chen, K. Sasaki, C. Ma, A. I. Frenkel, N. Marinkovic, J. T. Muckerman, Y. Zhu, and R. R. Adzic, *Hydrogen-evolution catalysts based on non-noble metal nickel-molybdenum nitride nanosheets.* Angew. Chem. Int. Ed. **51**, 6131 (2012).

[27] Y. Wang, G. Zhang, W. Xu, P. Wan, Z. Lu, Y. Li, and X. Sun, *A 3D Nanoporous Ni-Mo Electrocatalyst with Negligible Overpotential for Alkaline Hydrogen Evolution,* ChemElectroChem **1**, 1138 (2014).

[28] C. C. L. McCrory, S. Jung, I. M. Ferrer, S. Chatman, J. C. Peters, and T. F. Jaramillo, *Benchmarking HER and OER Electrocatalysts for Solar Water Splitting Devices,* J. Am. Chem. Soc. **137**, 4347 (2015).

[29] J. R. McKone, E. L. Warren, M. J. Bierman, S. W. Boettcher, B. S. Brunschwig, N. S. Lewis, and H. B. Gray, *Evaluation of Pt, Ni, and Ni–Mo electrocatalysts for hydrogen evolution on crystalline Si electrodes,* Energy Environ. Sci. **4**, 3573 (2011).

[30] Z. Hens, *The electrochemical impedance of one-equivalent electrode processes at dark semiconductor/redox electrodes involving charge transfer through surface states. 1. theory,* J. Phys. Chem. B **103**, 122 (1999).

[31] L. Bertoluzzi and J. Bisquert, *Equivalent circuit of electrons and holes in thin semiconductor films for photoelectrochemical water splitting applications,* J. Phys. Chem. Lett. **3**, 2517 (2012).

[32] C. H. Hsu and F. Mansfeld, *Technical Note: Concerning the Conversion of the Constant Phase Element Parameter $Y_0$ into a Capacitance,* Corrosion **57**, 747 (2001).

[33] M. E. Orazem, P. Shukla, and M. A. Membrino, *Extension of the measurement model approach for deconvolution of underlying distributions for impedance measurements,* Electrochim. Acta **47**, 2027 (2002).

[34] R. van de Krol and M. Grätzel, *Photoelectrochemical Hydrogen Production*, edited by R. van de Krol and M. Grätzel, Electronic Materials: Science & Technology, Vol. 102 (Springer US, Boston, MA, 2012).

[35] M. F. Lichterman, S. Hu, M. H. Richter, E. J. Crumlin, S. Axnanda, M. Favaro, W. Drisdell, Z. Hussain, T. Mayer, B. S. Brunschwig, N. S. Lewis, Z. Liu, and H.-J. Lewerenz, *Direct observation of the energetics at a semiconductor/liquid junction by operando X-ray photoelectron spectroscopy,* Energy Environ. Sci. **8**, 2409 (2015).

[36] D. Bae, S. Shayestehaminzadeh, E. B. Thorsteinsson, T. Pedersen, O. Hansen, B. Seger, P. C. K. Vesborg, S. Ólafsson, and I. Chorkendorff, *Protection of Si photocathode using $TiO_2$ deposited by high power impulse magnetron sputtering for $H_2$ evolution in alkaline media,* Sol. Energy Mater. Sol. Cells **144**, 758 (2016).

[37] C. G. Morales-Guio, L. Liardet, M. T. Mayer, S. D. Tilley, M. Grätzel, and X. Hu, *Photoelectrochemical Hydrogen Production in Alkaline Solutions Using $Cu_2O$ Coated with Earth-Abundant Hydrogen Evolution Catalysts.* Angew. Chem. Int. Ed. , 664 (2014).

[38] J. Azevedo, L. Steier, P. Dias, M. Stefik, C. T. Sousa, J. P. Araújo, A. Mendes, M. Graetzel, and S. D. Tilley, *On the stability enhancement of cuprous oxide water splitting photocathodes by low temperature steam annealing,* Energy Environ. Sci. **7**, 4044 (2014).

[39] B. Seger, D. S. Tilley, T. Pedersen, P. C. K. Vesborg, O. Hansen, M. Grätzel, and I. Chorkendorff, *Silicon protected with atomic layer deposited $TiO_2$: durability studies of photocathodic $H_2$ evolution,* RSC Adv. **3**, 25902 (2013).

[40] A. K. Chandiran, A. Yella, M. Stefik, L.-P. Heiniger, P. Comte, M. K. Nazeeruddin, and M. Grätzel, *Low-temperature crystalline titanium dioxide by atomic layer deposition for dye-sensitized solar cells.* ACS Appl. Mater. Interfaces **5**, 3487 (2013).

[41] M. Reiners, K. Xu, N. Aslam, A. Devi, R. Waser, and S. Hoffmann-Eifert, *Growth and Crystallization of $TiO_2$ Thin Films by Atomic Layer Deposition Using a Novel Amido Guanidinate Titanium Source and Tetrakis-dimethylamido-titanium,* Chem. Mater. **25**, 2934 (2013).

# A

# Appendix A

## A.1. Corrected current-potential curve

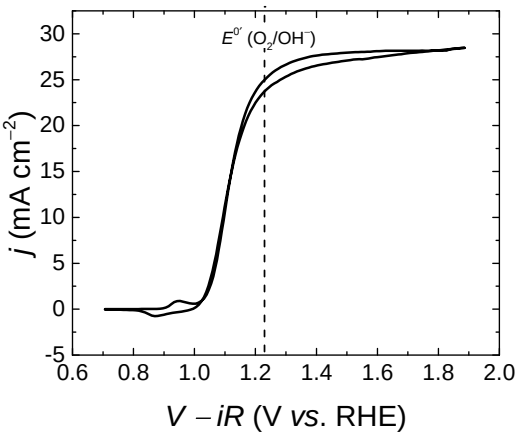



**Figure A.1:** Corrected cyclic voltammetry of n-Si/$SiO_{x,RCA}$/$Al_2O_3$/Pt/Ni photoanode after 18 of aging with compensation for the series resistance. The series resistance of the system was 4.24 $\Omega$ cm$^{-2}$ as measured by EIS, and is consistent with the resistance of 1 M KOH solution.[1]

## A.2. UV-Vis measurement

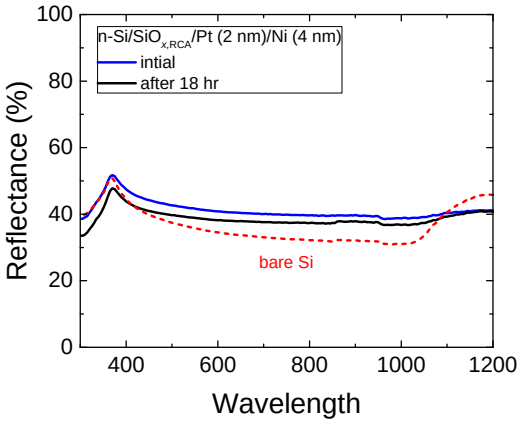



**Figure A.2:** Reflectance of the fresh and the aged n-Si/SiO$_{x,\mathrm{RCA}}$/Al$_2$O$_3$/Pt/Ni, showing a decrease in reflectance in the UV, visible, and near infrared region. For a reference, the reflectance of the bare n-Si/SiO$_{x,\mathrm{RCA}}$ (no metal layers on top) is also shown. UV-Vis measurement was performed using a Perkin-Elmer Lambda 950 spectrometer, equipped with a deuterium and a tungsten lamp to measure the reflectance of the sample in a broad spectral range.

## A.3. Equivalent photovoltaic response and open-circuit voltage

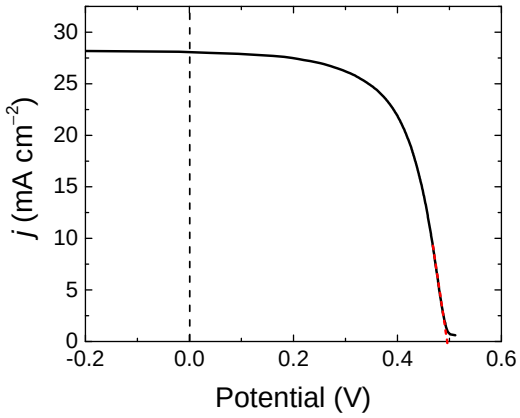



**Figure A.3:** Equivalent photovoltaic (PV) response of the n-Si/SiO$_{x,\mathrm{RCA}}$/Al$_2$O$_3$/Pt/Ni photoanode after 18 hours of aging relatove to the non-photoactive the non-photoactive p$^+$-Si/SiO$_{x,\mathrm{RCA}}$/Al$_2$O$_3$/Pt/Ni electrode, showing an equivalent open-circuit voltage ($V_{\mathrm{oc}}$) of 496 mV, a short-circuit current density ($j_{\mathrm{sc}}$) of 28.06 mA cm$^{-2}$, a fill factor ($ff$) of 0.64 and an energy-conversion-efficiency of 8.87%.

The equivalent photovoltaic response of the photoanode under illumination relative to

the non-photoactive electrode in the dark was determined by treating the photoanode performance in a simplified equivalent circuit where a PV cell is electrically connected in series with a dark electrolysis cell.The equivalent open-circuit voltage ($V_{oc}$) is defined as the voltage at zero current and the equivalent short-circuit density ($j_{sc}$) is defined as the current at zero voltage.

## A.4. Electrochemical impedance spectroscopy and Mott-Schottky analysis

The electrochemical impedance spectroscopy (EIS) data were fit with a model that consisted of a series resistance ($R_{series}$) in series connection with a parallel resistor ($R_p$) and a parallel capacitor ($C_p$) to account for the capacitance of the space-charge region, as shown in Fig. A.4.

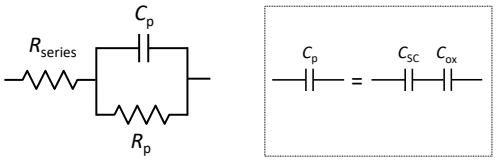



**Figure A.4:** Equivalent circuit used to fit the EIS data.

The $C_p$ is a combination of series contributions that consist of the space-charge capacitance ($C_{sc}$) and the oxide capacitance ($C_{ox}$).

$$\frac{1}{C_p} = \frac{1}{C_{sc}} + \frac{1}{C_{ox}} \tag{A.1}$$

The $C_{ox}$ equals to the series capacitance of the $SiO_x$ and $Al_2O_3$.

$$\frac{1}{C_{ox}} = \frac{1}{C_{SiO_x}} + \frac{1}{C_{Al_2O_3}} \tag{A.2}$$

The capacitance of the $SiO_x$ ($C_{SiO_x}$) and the $Al_2O_3$ ($C_{Al_2O_3}$) can be estimated by the following relationships:

$$C_{SiO_x} = \frac{\epsilon_0 \epsilon_{SiO_x}}{t_{SiO_x}} \tag{A.3}$$

$$C_{Al_2O_3} = \frac{\epsilon_0 \epsilon_{Al_2O_3}}{t_{Al_2O_3}} \tag{A.4}$$

where the $\epsilon_0$ is the vacuum permittivity ($8.85 \times 10^{-14}$ F cm$^{-1}$), $\epsilon_{SiO_x}$ is the dielectric permittivity of $SiO_x$ and is assumed to be the same as $SiO_2$ (3.9), $\epsilon_{Al_2O_3}$ is the dielectric permittivity of $Al_2O_3$ (8)[4,5] $t_{SiO_x}$ is the thickness of the $SiO_x$ (1.8 nm) and $t_{Al_2O_3}$ is the thickness of the $Al_2O_3$ (1 nm), as measured using the ellipsometer.

Assuming only the space-charge capacitance that varies with the changing electrode potential, the reverse-bias dependence of the inverse square capacitance of the space-charge region in the semiconductor is given by the Mott-Schottky relation:[6]

$$C_{sc}^{-2} = \frac{2}{\epsilon_0 \epsilon_{Si} q N_D} \left( V - E_{fb} - \frac{kT}{q} \right) \tag{A.5}$$

where $\epsilon_{Si}$ the permittivity of Si (11.7), $q$ is the elementary charge ($1.6 \times 10^{-19}$ C), $N_D$ is the donor concentration in the semiconductor, $V$ is the potential difference between the semiconductor and the redox potential of the solution, $E_{fb}$ is the flat band potential, $k$ is the Boltzmann's constant ($1.38 \times 10^{-27}$ cm$^2$ kg s$^{-2}$ K$^{-1}$) and $T$ is temperature (298 K). The $E_{fb}$ is determined by taking the value of the intercept between the extrapolated linear region of the $C_{sc}^{-2}$ with the $x$-axis in the Mott-Schottky plot.

The barrier height ($\phi_b$) was calculated using the Schottky's relation:

$$\phi_b = E_{fb} + V_n \tag{A.6}$$

Where $V_n$ is the difference between the potential of the conduction band edge and the Fermi level, and was obtained by using the following relationship:

$$V_n = kT \ln \frac{N_c}{N_D} \tag{A.7}$$

The density of conduction band states ($N_c$) was calculated by:

$$N_c = 2\left(\frac{2\pi m_e^* kT}{h^2}\right)^{3/2} \tag{A.8}$$

where $m_e^*$ is the effective mass of electron in c-Si ($1.08m_0$) and $h$ is the Planck's constant (6.63 J s). Using the slope of Mott-Schottky plot in the main text ($3.35 \times 10^{14}$ F$^{-2}$ cm$^4$ V$^{-1}$) and the above equations, the $N_D$ was calculated to be $3.54 \times 10^{16}$ cm$^{-3}$ and the $V_n$ was calculated to be 0.17 eV. From the calculated $N_d$ the resistivity of the n-type Si wafer was obtained to be 0.185 Ω cm, consistent with the range specified by the Si wafer supplier 0.1-0.3 Ω cm.

The $E_{fb}$ of the fresh and the aged n-Si/$SiO_{x,RCA}$/$Al_2O_3$/Pt/Ni photoanode were −0.6 and −0.73 V *versus* $Fe(CN)_6^{3-/4-}$, respectively. Using the Schottky relation above, the calculated $\phi_b$ were 0.77 and 0.9 eV for the fresh and the aged n-Si/$SiO_{x,RCA}$/$Al_2O_3$/Pt/Ni, respectively.

## A.5. X-ray photoelectron spectroscopy (XPS) analysis

### MIS photoanode

The nickel oxide surface can generally be reduced to its lower oxidation states when high energy beam was used during the etching process, and thus may result in an inaccurate interpretation and analysis of the XPS data. Therefore, the ion etching step should be performed using the lowest energy possible. The average etching rate was approximately 3 Å step$^{-1}$ and a total 36 steps of etching were performed on the investigated sample. In the depth profiling analysis, some signals corresponding to different elements overlapped and this is mainly due to the fact that the escape depth of photoelectron is typically 4 nm. Our samples consisted of multilayer stack, and apart from the Ni layer (thickness of 4 nm) and the Si wafer (thickness of 525  m), the rest of each layer had a thickness of less than 4 nm. For example, in our n-Si/$SiO_{x,RCA}$/$Al_2O_3$/Pt/Ni sample, the thickness of Pt film was 2 nm and the thickness of the $Al_2O_3$ was only 1 nm. This means when the ion beam has etched all the Ni away and has reached Pt, the XPS will detect signals not only from Pt but also from $Al_2O_3$ underneath. The binding energy range for Pt 4$f$ is between 70 and 75 eV, the same range as for Al 2$p$. This can possibly obscure the Al 2$p$ signals. To avoid this issue, the Al 2$s$ was therefore chosen to assign for the $Al_2O_3$ detection in the depth profiling analysis.

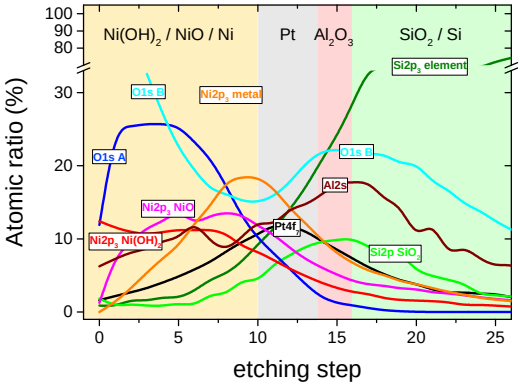



**Figure A.5:** XPS depth profiling with complete elemental scans of n-Si/$SiO_{x,RCA}$/$Al_2O_3$/Pt/Ni after 18 hours in contact with KOH solution.

### Si and $Al_2O_3$

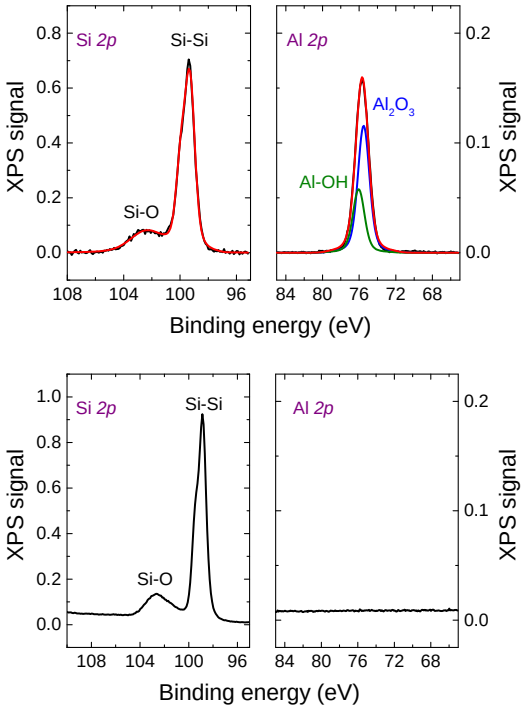



**Figure A.6:** The XPS spectra of n-Si/$SiO_{x,RCA}$/$Al_2O_3$ (1 nm) without Pt and Ni before (top graphs) and after (bottom graphs) immersion in KOH solution for 1 hour. The Al 2*p* signal was completely gone upon contact with KOH, indicating that $Al_2O_3$ was completely unstable when in a KOH solution.

## A.6. Pourbaix diagram

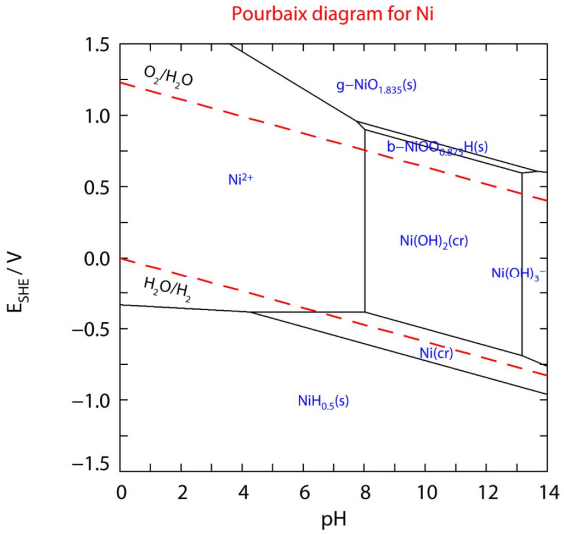



**Figure A.7:** Pourbaix diagram for Ni, generated using Medusa (http://www.kth.se/che/medusa/).

## A.7. Cyclic voltammtery and Mott-Schottky plot

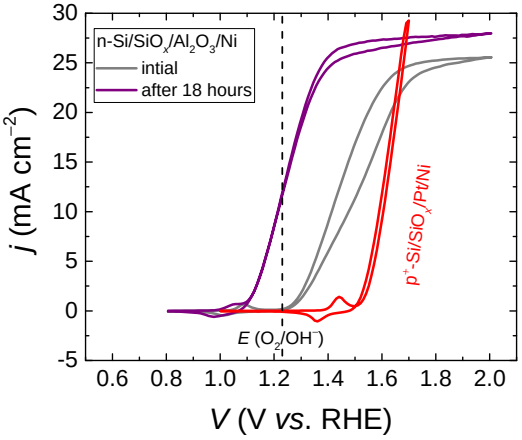



**Figure A.8:** Current–potential ($j$–$V$) curves of the illuminated n-Si/$SiO_{x,RCA}$/$Al_2O_3$/Ni photoanode recorded during the first cyclic voltammetry scan and after 18 hours of aging in 1 M KOH electrolyte. The thickness of the Ni was 6 nm.

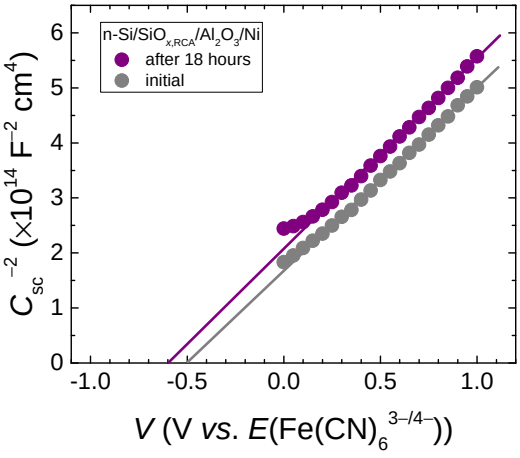



**Figure A.9:** Mott-Schottky plots of the fresh n-Si/$SiO_{x,RCA}$/$Al_2O_3$/Ni and 18 hours of aging treatment in 1 M KOH.

# References

[1] R. van de Krol and M. Grätzel, *Photoelectrochemical Hydrogen Production* (Springer US, Boston, MA, 2012) p. 79.

[2] J. C. Hill, A. T. Landers, and J. A. Switzer, *An electrodeposited inhomogeneous metal–insulator–semiconductor junction for efficient photoelectrochemical water oxidation,* Nature Materials **14**, 1150 (2015).

[3] R. H. Coridan, A. C. Nielander, S. A. Francis, M. T. McDowell, V. Dix, S. M. Chatman, and N. S. Lewis, *Methods for comparing the performance of energy-conversion systems for use in solar fuels and solar electricity generation,* Energy & Environmental Science **8**, 2886 (2015).

[4] M. D. Groner, F. H. Fabreguette, J. W. Elam, and S. M. George, *Low-Temperature $Al_2O_3$ Atomic Layer Deposition,* Chemistry of Materials **16**, 639 (2004).

[5] J. L. van Hemmen, S. B. S. Heil, J. H. Klootwijk, F. Roozeboom, C. J. Hodson, M. C. M. van de Sanden, and W. M. M. Kessels, *Plasma and Thermal ALD of $Al_2O_3$ in a Commercial 200 mm ALD Reactor,* Journal of The Electrochemical Society **154**, 639 (2007).

[6] K. Gelderman, L. Lee, and S. W. Donne, *Flat-Band Potential of a Semiconductor: Using the Mott-Schottky Equation,* Journal of Chemical Education **84**, 685 (2007).

# B

# Appendix B

## B.1. Single- and double-diode models

The current-voltage characteristic of an ideal rectifying junction can be described by a simple equivalent circuit comprising a single diode (Fig. B.1a). The single-diode model assumes that the ideality factor is constant throughout the whole potential range. At high forward voltages when the recombination in the neutral region and on the surface dominate, the ideality factor ($n$) is close to 1. At lower forward voltages, the recombination is dominated by the space-charge layer and $n$ is typically 2. The recombination in the space-charge region can be modeled by adding a second diode in parallel with the first in the equivalent circuit (Fig. B.1b). Two diodes are connected in parallel in the equivalent circuit because the electronic transport in a rectifying junction is a superposition of two processes, namely diffusion/thermionic emission and recombination occurring simultaneously under forward bias.

The transport processes in a rectifying junction can be identified by examining the diode properties through the dark measurement of current-voltage ($j$–$V$). Each region in the dark $j$–$V$ curve (Fig. B.1c and d) represents the dominant current mechanism under a certain range of applied bias: (i) generation-recombination in the space-charge region, (ii) thermionic emission, (iii) series resistance effect, and (iv) reverse leakage current due to generation and recombination and parallel resistance. Ideally, a straight line in the forward bias region is indicative of an exponential voltage dependence of current, and for a metal-insulator-semiconductor junction (analogous to Schottky junction) the forward current is limited by the thermionic emission process (process (ii), Fig. B.1c and d). If recombination exists in the space-charge layer, the curve in the low forward bias region will deviate from linear, and the current in this low forward bias region will be appreciably higher than the thermionic emission current.

The current flow due to carrier recombination in the space-charge layer (process (i), Fig. B.1d) is usually more important in devices with high barriers and can be observed in the low forward bias region of the dark $j$–$V$ curve. Under high forward bias operation, the recombination current in the space-charge layer is negligible compared to the thermionic emission current. The recombination in the space-charge region is assumed to take place at the trap centers near the middle of the energy gap through capture processes, and is called the Shockley-Read-Hall recombination.[1–3] In the reverse bias region, the generation current is more dominant than the recombination current because all the excited carriers

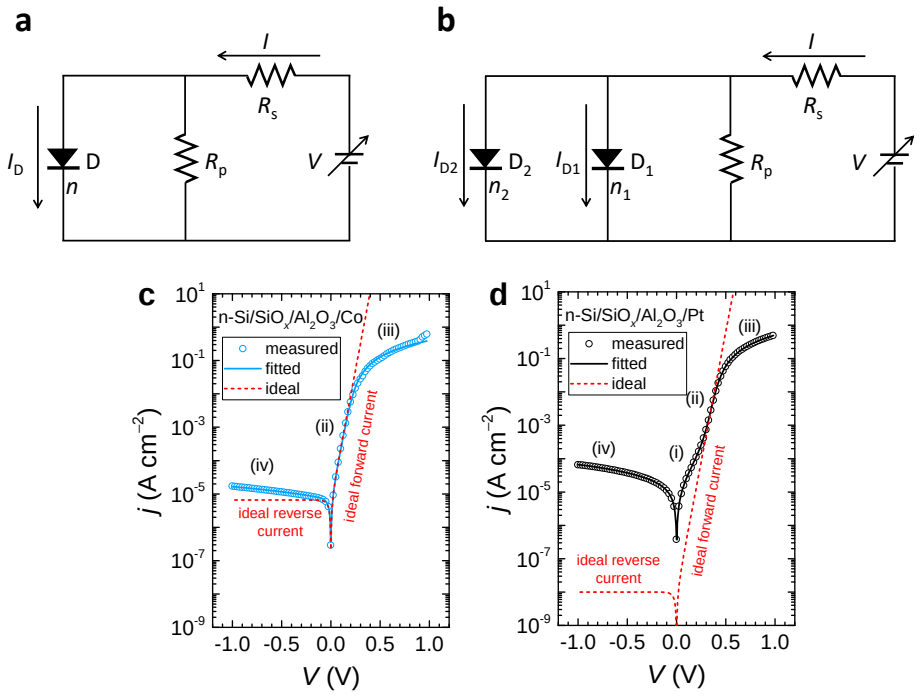



**Figure B.1:** Equivalent circuits of (a) single-diode model and (b) double-diode model in the dark. $R_p$ is the parallel resistance, $R_s$ is the series resistance, $D_1$ is the first diode, $D_2$ is the second diode and $I$ is the current. Current-voltage characteristics of n-Si/$SiO_x$/$Al_2O_3$/'*metal*'; (c) with Co, and (b) with Pt metal contacts. The ideal current-potential curves that exclude the generation-recombination in the space-charge region with no series and parallel resistance effects are shown as the dashed red lines.

are swept out of the space-charge layer by a strong electric field (process (iv), Fig. B.1c and d).

For a system showing a nonlinearity in the forward bias region such as in Fig. B.1d, the dark $j$–$V$ curve can be more accurately fitted using the double-diode model (Eq. 2 in the main paper). For a rectifying junction with a small barrier height such as the system using Co contact (Fig. B.1c), the current due to generation and recombination in the space-charge layer is extremely small in comparison to the current due to thermionic emission, and therefore these processes cannot be distinguished from the thermionic emission current in the dark $j$–$V$ curve. To avoid ambiguity, a system showing only a linear line in the forward bias region should be fitted with the single-diode model that accounts for contribution from the thermionic emission current only.

# B.2. Fit results of dark *j–V* curves

Table B.1 and B.2 summarize the fit results of the dark *j–V* curves of the n-Si/$SiO_x$/$Al_2O_3$/'*metal*' and n-Si/$SiO_x$/'*metal*' systems, respectively.

**Table B.1:** Fit results of dark *j–V* curves of n-Si/$SiO_x$/$Al_2O_3$/'*metal*' systems. The thickness of each metal is 60 nm

| n-Si/$SiO_x$/$Al_2O_3$/'*metal*' (60 nm) | | | | | | |
|---|---|---|---|---|---|---|
| metal | $j_{01}$ (A cm$^{-2}$) | $n_1$ | $j_{02}$ (A cm$^{-2}$) | $n_2$ | $R_s$ (Ω cm$^2$) | $R_p$ (Ω cm$^2$) |
| Pt | $1.0\times10^{-8}$ | 1.1 | $7.3\times10^{-6}$ | 3 | 1.0 | $1.6\times10^{5}$ |
| Ni | $1.0\times10^{-7}$ | 1.1 | $1.3\times10^{-6}$ | 2 | 3.6 | $3.4\times10^{5}$ |
| Co | $6.6\times10^{-6}$ | 1.1 | – | – | 1.7 | $3.0\times10^{5}$ |
| Ti | $6.5\times10^{-3}$ | 3.2 | – | – | 1.4 | $2.5\times10^{2}$ |

**Table B.2:** Fit results of dark *j–V* curves of n-Si/$SiO_x$/'*metal*' systems. The thickness of each metal is 60 nm

| n-Si/$SiO_x$/'*metal*' (60 nm) | | | | |
|---|---|---|---|---|
| metal | $j_0$ (A cm$^{-2}$) | $n$ | $R_s$ (Ω cm$^2$) | $R_p$ (Ω cm$^2$) |
| Pt | $1.3\times10^{-7}$ | 1.0 | 33.8 | $5.0\times10^{5}$ |
| Ni | $1.6\times10^{-3}$ | 1.07 | 0.62 | $7.9\times10^{2}$ |
| Co | $1.1\times10^{-4}$ | 1.0 | 1.0 | $8.9\times10^{3}$ |
| Ti | $8.1\times10^{-1}$ | 0.76 | 2.6 | $2.1\times10^{1}$ |

All variables in Table B.1 and Table B.2 were extracted from the dark *j–V* curves using either a single-diode model or a double-diode model, except for the n-Si/$SiO_x$/Ti. Because of the extremely high leakage current and the *j–V* curve of the the n-Si/$SiO_x$/Ti that resembles ohmic behavior, the contributions from $n$ and $R_p$ to the resulting current are hardly distinguishable. Any $n$ values can lead to an accurate fitting in exchange for lower or higher $R_p$, but still results in the same $j_0$.

In an attempt to obtain an accurate $n$ for the n-Si/$SiO_x$/Ti, we used an alternative approach described by Cheung and Cheung.[4] The method is based on the following equation:

$$V = R_s j + n\phi_b + \frac{nkT}{q}\ln\left(\frac{j}{A^* T^2}\right) \tag{B.1}$$

where $j$ is the current density in the dark, $V$ is the voltage, $R_s$ is the series resistance, $\phi_b$ is the barrier height, $k$ is the Boltzmann's constant ($1.38\times10^{-23}$ m$^2$ kg s$^{-2}$ K$^{-1}$) and $T$ is the temperature (293 K), $q$ is the elementary charge ($1.6\times10^{-19}$ C) and $A^*$ is the Richardson's constant (120 A cm$^{-2}$ K$^{-2}$ for Si). Differentiating Eq. B.1 with respect to $j$, and arranging terms lead to:

$$\frac{dV}{d(\ln j)} = R_s j + \frac{nkT}{q} \tag{B.2}$$

Equation B.2 should produce a straight line, thus a plot of $dV/d(\ln j)$ *versus* $j$ will give rise to $R_s$ as the slope and $nkT/q$ as the $y$-axis intercept. From the intercept between

$dV/d(\ln j)$ and $y$-axis in Fig. B.2, $n$ was obtained to be approximately 0.76 and from the linear fit of the slope, $R_s$ was found to be 2.42 Ω cm$^2$, close to the value obtained from the fit result of the dark $j$–$V$ curve in Table B.2. This method is also valid for other samples, and achieved identical values as those obtained from fitting the dark $j$–$V$.

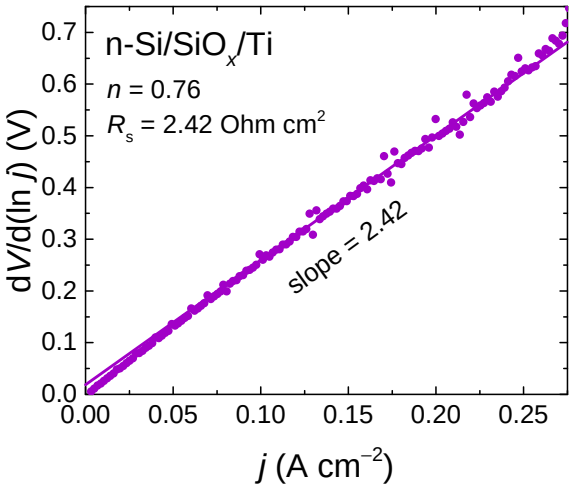



**Figure B.2:** A plot of d$V$/d(ln $j$) *versus* $j$ of the n-Si/SiO$_x$/Ti.

## B.3. Derivation of the thermionic emission equation corrected for tunneling current

The equation of the thermionic emission corrected for tunneling is based on the derivation of one-dimensional tunnel current through a rectangular barrier described by Card and Rhoderick.[5] The tunneling current is expressed by the following equation:

$$j = \frac{4\pi m_e q}{h^3} \int_0^\infty \int_0^\infty TC \cdot N \; dE_x dE_t \tag{B.3}$$

where $m_e$ is the electron mass, $q$ is the elementary charge, $h$ is the Planck's constant, $TC$ is the transmission coefficient and $N$ is the supply function. $E_x$ and $E_t$ are the component of energy for conduction electrons with momentum perpendicular and transverse to the barrier, respectively.

Within the Wentzel-Kramers-Brillouin (WKB) approximation, the transmission coefficient can be written as:

$$TC = \exp\left(-2 \int_{x_\mathrm{s}}^{x_\mathrm{m}} k_x dx\right) \tag{B.4}$$

where $x_\mathrm{m} - x_\mathrm{s} = \delta$ is the thickness of the insulator and $k_x$ is the component of the momentum in the $x$ direction.

$$k_x = \left(\frac{2m_e}{\hbar}(W - E_x)\right)^{1/2} \tag{B.5}$$

where $\hbar$ is the reduced Planck's constant ($\hbar = h/2\pi$). For a rectangular barrier, the height $W$ is independent of $x$, and $(W - E_x) = \chi$ is the distance between the conduction band edge of the semiconductor and the insulator. Thus the expression for transmission coefficient becomes:

$$\begin{aligned} TC &= \exp\left(-\frac{4\pi}{h}(2m_e\chi)^{1/2}\delta\right) \\ &= \exp\left(-1.01 \text{ eV}^{-1/2}\text{Å}^{-1} \times \chi^{1/2}\delta\right) \simeq \exp\left(-\chi^{1/2}\delta\right) \end{aligned} \tag{B.6}$$

where $\chi$ is in electronvolt (eV) and $\delta$ is in angstrom (Å). Since the unit of $\chi^{1/2}\delta$ is $\text{eV}^{1/2}$ Å, the exponent becomes dimensionless.

The supply function ($N$) describes the difference in carrier supply at the interface of the insulator, and is given by:

$$N = \int_0^\infty (f_\mathrm{s} - f_\mathrm{m})\, dE \tag{B.7}$$

where $f_\mathrm{s}$ and $f_\mathrm{m}$ are the Fermi functions. At forward bias, $f_\mathrm{m} \simeq 0$. For non-degenerate semiconductors, the Fermi-Dirac distribution can be approximated using Maxwell-Boltzmann distribution:

$$f_\mathrm{s} \simeq \exp\left(-\frac{E_x + E_t - (E_{\mathrm{F},n} - E_\mathrm{C})}{kT}\right) \tag{B.8}$$

where $k$ is the Boltzmann's constant, $T$ is the temperature, $E_{\mathrm{F},n}$ is the semiconductor Fermi level and $E_\mathrm{C}$ is the conduction band edge at the surface.

Substituting Eq. B.6, Eq. B.7 and Eq. B.8 with Eq. B.3, the current density of thermionic emission and tunneling is given by:

$$\begin{aligned} j &= \frac{4\pi m_e q}{h^3} \int_0^\infty \int_0^\infty \exp\left(-\chi^{1/2}\delta\right) \exp\left(-\frac{E_x + E_t - \left(E_{\mathrm{F},n} - E_{\mathrm{C}}\right)}{kT}\right) dE_x dE_t \\ &= \frac{4\pi m_e q}{h^3} \exp\left(-\chi^{1/2}\delta\right) \exp\left(\frac{E_{\mathrm{F},n} - E_{\mathrm{C}}}{kT}\right) \int_0^\infty \int_0^\infty \exp\left(-\frac{E_x}{kT}\right) \exp\left(-\frac{E_t}{kT}\right) dE_x dE_t \\ &= \frac{4\pi m_e q}{h^3} (kT)^2 \exp\left(-\chi^{1/2}\delta\right) \exp\left(\frac{E_{\mathrm{F},n} - E_{\mathrm{C}}}{kT}\right) \end{aligned} \tag{B.9}$$

The difference in potential between the semiconductor Fermi level and the conduction band edge at the surface ($E_{\mathrm{F},n} - E_{\mathrm{C}}$) is a function of applied voltage ($V$) and is negative because the Fermi level is positioned below the conduction band edge:

$$E_{\mathrm{F},n} - E_{\mathrm{C}} = -q(\phi_{\mathrm{b}} - V) \tag{B.10}$$

where $\phi_{\mathrm{b}}$ is the barrier height.

Substituting Eq. B.9 with Eq. B.10, the complete equation of thermionic emission corrected for tunneling becomes:

$$\begin{aligned} j &= \frac{4\pi m_e q}{h^3} (kT)^2 \exp\left(-\chi^{1/2}\delta\right) \exp\left(\frac{-q\phi_{\mathrm{b}}}{kT}\right) \exp\left(\frac{qV}{kT}\right) \\ &= A^* T^2 \exp\left(-\chi^{1/2}\delta\right) \exp\left(\frac{-q\phi_{\mathrm{b}}}{kT}\right) \exp\left(\frac{qV}{kT}\right) \end{aligned} \tag{B.11}$$

where $A^*$ is the Richardson's constant.

Recalling the ideal diode equation:

$$j = j_0 \left(\exp\left(\frac{qV}{kT}\right)\right) \tag{B.12}$$

where $j_0$ is the dark saturation current density. Thus, $j_0$ can be expressed as:

$$j_0 = A^* T^2 \exp\left(-\chi^{1/2}\delta\right) \exp\left(\frac{-q\phi_{\mathrm{b}}}{kT}\right) \tag{B.13}$$

## B.4. Flat band potentials and barrier heights obtained from Mott-Schottky relationships

The barrier heights were independently determined by measuring the capacitance of the electrode using impedance spectroscopy. Impedance measurements were performed in a solid-state configuration by connecting the front metal contact to the back metal contact. The space-charge capacitance ($C_{sc}$) of the semiconductor was extracted by fitting the impedance with an equivalent electronic circuit consisting of a resistor ($R_{series}$) in a series connection with a parallel resistor ($R_{par}$, to account for electron exchange between the semiconductor, insulator and metal), and a parallel capacitor ($C_{par}$), as shown in Fig. B.3.

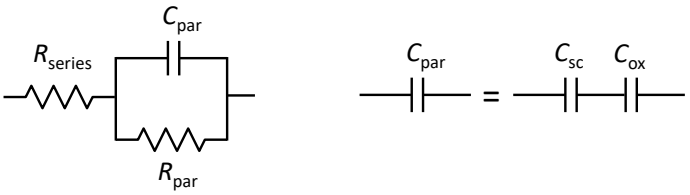



**Figure B.3:** Equivalent circuits to fit the impedance data.

$C_{par}$ is a combination of series contributions that consist of the space-charge capacitance ($C_{sc}$) and the oxide capacitance ($C_{ox}$).[6]

$$\frac{1}{C_{par}} = \frac{1}{C_{sc}} + \frac{1}{C_{ox}} \tag{B.14}$$

For interfacial oxide layers consisting of $SiO_x$ and $Al_2O_3$, $C_{ox}$ equals to the series capacitance of both oxides.

$$\frac{1}{C_{ox}} = \frac{1}{C_{SiO_x}} + \frac{1}{C_{Al_2O_3}} \tag{B.15}$$

The capacitances of $SiO_x$ and $Al_2O_3$ were estimated by the following relationships:

$$C_{SiO_x} = \frac{\varepsilon_0 \varepsilon_{SiO_x}}{t_{SiO_x}} \tag{B.16}$$

$$C_{Al_2O_3} = \frac{\varepsilon_0 \varepsilon_{Al_2O_3}}{t_{Al_2O_3}} \tag{B.17}$$

where $\varepsilon_0$ is the vacuum permittivity ($8.85 \times 10^{-14}$ F cm$^{-1}$), $\varepsilon_{SiO_x}$ is the relative permittivity of $SiO_x$ and is assumed to be the same as $SiO_2$ (3.9), $\varepsilon_{Al_2O_3}$ is the relative permittivity of $Al_2O_3$ (8),[7,8] $t_{SiO_x}$ is the thickness of the $SiO_x$ (1.8 nm) and $t_{Al_2O_3}$ is the thickness of the $Al_2O_3$ (1 nm), as measured using ellipsometer.

Assuming only the space-charge capacitance that varies with the changing potential, the reverse-bias dependence of the inverse square of the space-charge capacitance in the semiconductor ($C_{sc}^{-2}$) is given by the Mott-Schottky relationship:

$$C_{sc}^{-2} = \frac{2}{\varepsilon_0 \varepsilon_{Si} q N_d} \left( V - E_{fb} - \frac{kT}{q} \right) \tag{B.18}$$

where $\varepsilon_{Si}$ is the relative permittivity of Si (11.7), $q$ is the elementary charge ($1.6 \times 10^{-19}$ C), $N_d$ is the donor concentration in the semiconductor, $V$ is the applied voltage, $E_{fb}$ is the

flat band potential, $k$ is the Boltzmann's constant ($1.38 \times 10^{-23}$ m$^2$ kg s$^{-2}$ K$^{-1}$) and $T$ is the temperature (293 K). $E_{fb}$ was determined by taking the value of the intercept between the extrapolated linear region of the $C_{sc}^{-2}$ with the $x$-axis in the Mott-Schottky ($C_{sc}^{-2}$–$V$) plot.

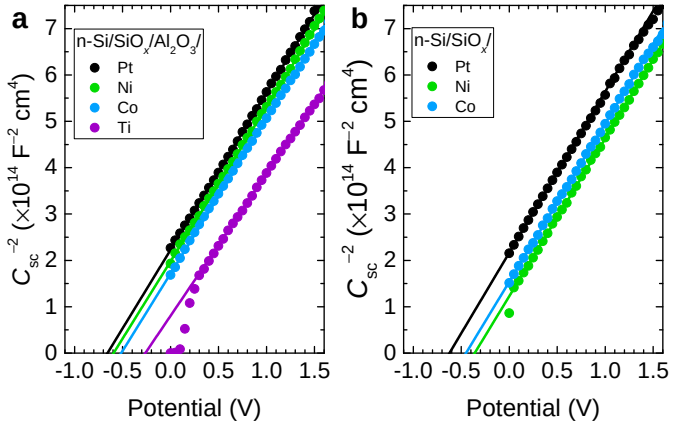



**Figure B.4:** Mott-Schottky plots of the inverse square of the space-charge capacitance–voltage ($C_{sc}^{-2}$–$V$) of (a) n-Si/SiO$_x$/Al$_2$O$_3$/'*metal*' and (b) n-Si/SiO$_x$/'*metal*' systems. The thickness of each metal is 60 nm. The intercept of the extrapolated linear line indicates the $E_{fb}$.

The barrier heights were calculated using the following equation:

$$\phi_b = E_{fb} + V_n \tag{B.19}$$

where $V_n$ is the difference between the potential of the conduction band edge and the Fermi level, and was obtained by using the following relationship:

$$V_n = \frac{kT}{q} \ln\left(\frac{N_c}{N_d}\right) \tag{B.20}$$

The density of conduction band states ($N_c$) is given by:

$$N_c = 2\left(\frac{2\pi m_e^* kT}{h^2}\right)^{3/2} \tag{B.21}$$

where $m_e^*$ is the effective mass of electron in c-Si (1.08 $m_0$) and $h$ is the Planck's constant ($6.63 \times 10^{-34}$ J s). Using the slope in the linear region of the Mott-Schottky plot ($3.4 \pm 0.1 \times 10^{14}$ F$^{-2}$ cm$^4$ V$^{-1}$) and the Eq. B.20 and Eq. B.21, the $N_d$ was calculated to be $3.5 \pm 0.1 \times 10^{16}$ cm$^{-3}$ and the $V_n$ was calculated to be 0.17 eV. From the calculated $N_d$, the resistivity of the n-type Si wafer was obtained to be 0.185 Ωcm, consistent with the range specified by the Si wafer supplier 0.1–0.3 Ω cm.

Table B.3 and B.4 summarize the calculated flat band potentials and barrier heights of the n-Si/SiO$_x$/Al$_2$O$_3$/'*metal*' and n-Si/SiO$_x$/'*metal*' systems, respectively.

**Table B.3:** Flat band potentials and calculated barrier heights of n-Si/$SiO_x$/$Al_2O_3$/'*metal*' systems. The thickness of each metal is 60 nm

| **n-Si/$SiO_x$/$Al_2O_3$/'*metal*' (60 nm)** | | |
|---|---|---|
| metal | $E_{\mathrm{fb}}$ (V) | $\phi_{\mathrm{b}}$ (eV) |
| Pt | 0.66 | 0.83 |
| Ni | 0.59 | 0.76 |
| Co | 0.51 | 0.68 |
| Ti | 0.26 | 0.43 |

**Table B.4:** Flat band potentials and calculated barrier heights of n-Si/$SiO_x$/'*metal*' devices. The thickness of each metal is 60 nm

| **n-Si/$SiO_x$/'*metal*' (60 nm)** | | |
|---|---|---|
| metal | $E_{\mathrm{fb}}$ (V) | $\phi_{\mathrm{b}}$ (eV) |
| Pt | 0.62 | 0.79 |
| Ni | 0.36 | 0.53 |
| Co | 0.45 | 0.62 |
| Ti | – | – |

## B.5. Flat band potentials and barrier heights of MIS photoanodes

Impedance measurements of MIS photoanodes with thin bimetal contacts were performed electrochemically in an electrolyte solution containing electrochemically reversible, one-electron $Fe(CN)_6^{3-/4-}$ redox couple. Afterwards, all photoanodes were subjected to contact with 1 M of potassium hydroxide (KOH) solution for at least 24 hours (*i.e.*, aging process). Impedance measurements were then repeated to estimate the barrier heights of all photoanodes. The $C_{sc}$, $E_{fb}$ and barrier heights were calculated using Eq. B.14–B.21. Figure B.5a–c show the $C_{sc}^{-2}$–$V$ plots of n-Si/$SiO_x$/$Al_2O_3$/'*metal*' (2 nm)/Ni (4 nm) and n-Si/$SiO_x$/'*metal*' (2 nm)/Ni (4 nm) photoanodes, before and after aging process.

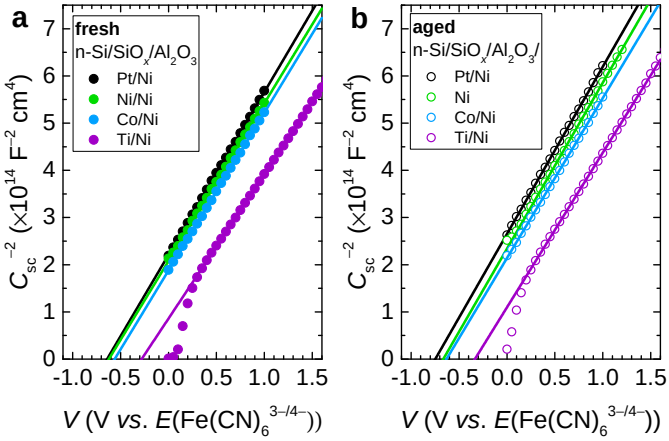



**Figure B.5:** Mott-Schottky plots of the inverse square of the space-charge capacitance–voltage ($C_{sc}^{-2}$–$V$) of the n-Si/$SiO_x$/$Al_2O_3$/'*inner metal*' (2 bn)/Ni (4nm) photoanodes (a) before and (b) after aging process, and (c) the n-Si/$SiO_x$/'*inner metal*' (2 nm)/Ni (4 nm). No notable differences observed between the fresh and the aged samples.

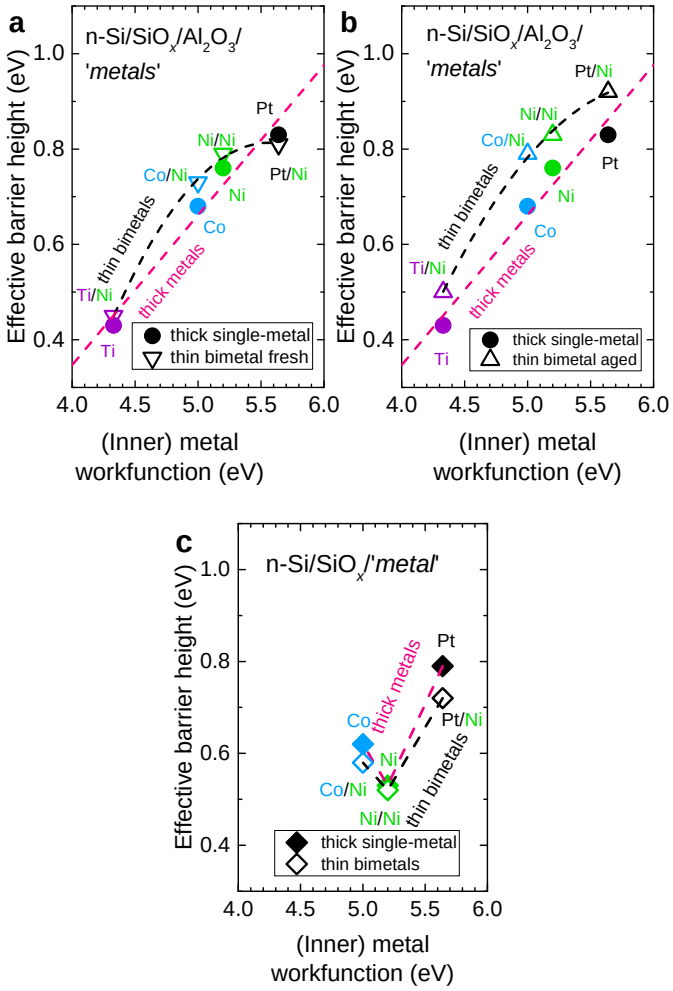



**Figure B.6:** (a) Comparison of effective barrier heights between the n-Si/$SiO_x$/$Al_2O_3$/'*metal*' (60 nm) (solid circles) and (a) the fresh n-Si/$SiO_x$/$Al_2O_3$/'*inner metal*' (2 nm)/Ni (4 nm) (hollow downward triangles), and (b) the aged n-Si/$SiO_x$/$Al_2O_3$/'*inner metal*' (2 nm)/Ni (4 nm) (hollow upward triangles). (c) Barrier height comparison between n-Si/$SiO_x$/'*metal*' (60 nm) (solid diamonds) and n-Si/$SiO_x$/'*inner metal*' (2 nm)/Ni (4 nm) (hollow diamonds) devices.

**Table B.5:** Flat band potentials and calculated barrier heights of n-Si/$SiO_x$/$Al_2O_3$/'*inner metal*' (2 nm)/Ni (4 nm) photoanodes.

**n-Si/$SiO_x$/$Al_2O_3$/'*inner metal*' (2 nm)/Ni (4 nm)**

| inner metal | $E_{fb}$ (V) | | $\phi_b$ (eV) | |
|---|---|---|---|---|
| | fresh | aged | fresh | aged |
| Pt | 0.64 | 0.75 | 0.81 | 0.92 |
| Ni | 0.62 | 0.66 | 0.79 | 0.83 |
| Co | 0.56 | 0.62 | 0.73 | 0.79 |
| Ti | 0.28 | 0.33 | 0.45 | 0.50 |

**Table B.6:** Flat band potentials and calculated barrier heights of n-Si/$SiO_x$/'*inner metal*' (2 nm)/Ni (4 nm) photoanodes.

**n-Si/$SiO_x$/'*inner metal*' (2 nm)/Ni (4 nm)**

| metal | $E_{fb}$ (V) | $\phi_b$ (eV) |
|---|---|---|
| Pt | 0.55 | 0.72 |
| Ni | 0.35 | 0.52 |
| Co | 0.41 | 0.58 |
| Ti | – | – |

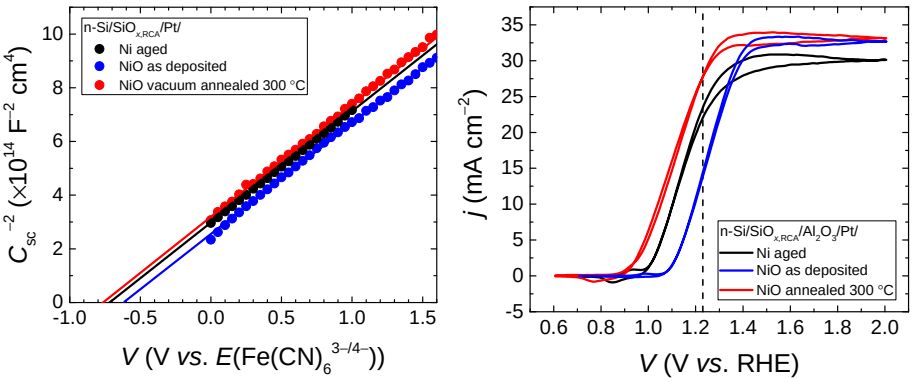



**Figure B.7:** Mott-Schottky plots of the inverse square of the space-charge capacitance–voltage ($C_{sc}^{-2}$–$V$) of the aged n-Si/$SiO_x$/$Al_2O_3$/Pt/Ni, the as-deposited n-Si/$SiO_x$/$Al_2O_3$/Pt/NiO and the vacuum annealed n-Si/$SiO_x$/$Al_2O_3$/Pt/NiO in contact with a solution containing elecetrochemically reversible, one-electron $Fe(CN)_6^{3-/4-}$ redox couple. (b) Current–potential ($j$–$V$) characteristics of the aged n-Si/$SiO_x$/$Al_2O_3$/Pt/Ni, the as-deposited n-Si/$SiO_x$/$Al_2O_3$/Pt/NiO and the vacuum annealed n-Si/$SiO_x$/$Al_2O_3$/Pt/NiO photoanodes in contact with 1 M KOH electrolyte and under simulated solar illumination. The NiO film was deposited using sputtering from a NiO target (Mateck) and the thickness of the NiO film was 20 nm.

## B.6. Photovoltages of MIS photoandoes

The photovoltages of all the investigated photoanodes were confirmed by measuring the electrochemical open-circuit voltages (OCP) in a 1 M KOH solution, in the dark and under illumination. The shift of OCP from the dark value to the illuminated value indicates the photovoltage.

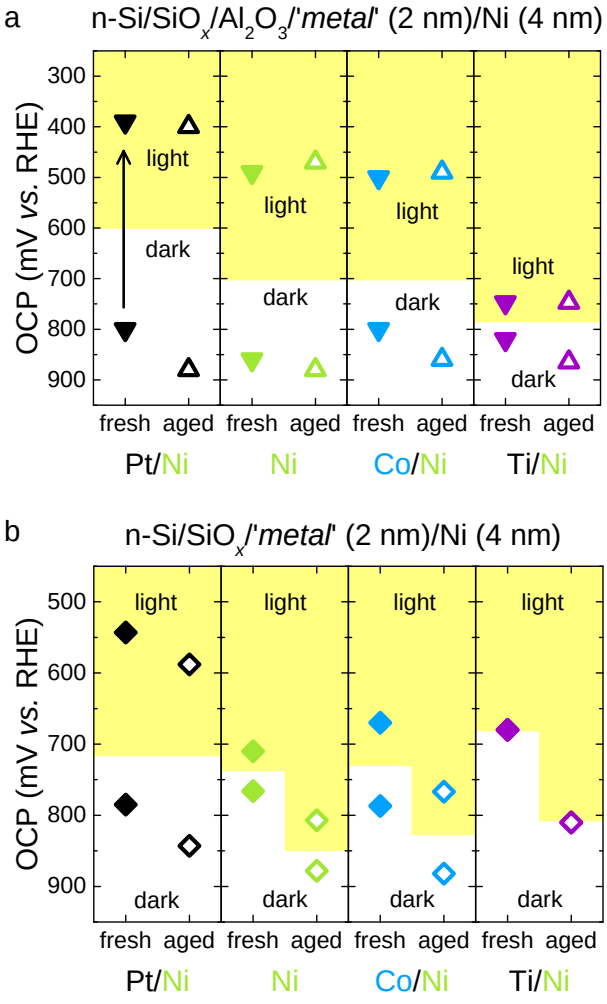



**Figure B.8:** Electrochemical open-circuit potential (OCP) of (a) n-Si/SiO$_x$/Al$_2$O$_3$/'*inner metal*' (2 nm)/Ni (4 nm) and (b) n-Si/SiO$_x$/'*inner metal*' (2 nm)/Ni (4 nm) photoanodes, measured in the dark and under illumination.

Table B.7 and B.8 summarize the photovoltages of the photoanodes obtained both from the current onset potential difference between the photoanode and the non-photoactive electrode (*i.e.*, $p^+$-Si/$SiO_x$/Ni), and from the electrochemical OCP measurements in the dark and under illumination.

**Table B.7:** Photovoltages of n-Si/$SiO_x$/$Al_2O_3$/'*inner metal*' (2 nm)/Ni (4 nm) photoanodes.

| **n-Si/$SiO_x$/$Al_2O_3$/'*inner metal*' (2 nm)/Ni (4 nm)** | | | | |
|---|---|---|---|---|
| inner metal | photovoltage (mV) obtained from: | | | |
| | *j*–*V* | | OCP | |
| | fresh | aged | fresh | aged |
| Pt | 420 | 520 | 390 | 480 |
| Ni | 364 | 424 | 370 | 410 |
| Co | 294 | 384 | 300 | 370 |
| Ti | 54 | 108 | 73 | 118 |

**Table B.8:** Photovoltages of n-Si/$SiO_x$/'*inner metal*' (2 nm)/Ni (4 nm) photoanodes.

| **n-Si/$SiO_x$/'*inner metal*' (2 nm)/Ni (4 nm)** | | | | |
|---|---|---|---|---|
| inner metal | photovoltage (mV) obtained from: | | | |
| | *j*–*V* | | OCP | |
| | fresh | aged | fresh | aged |
| Pt | 274 | 298 | 242 | 255 |
| Ni | 60 | 72 | 56 | 74 |
| Co | 114 | 112 | 115 | 117 |
| Ti | 0 | 0 | 0 | 0 |

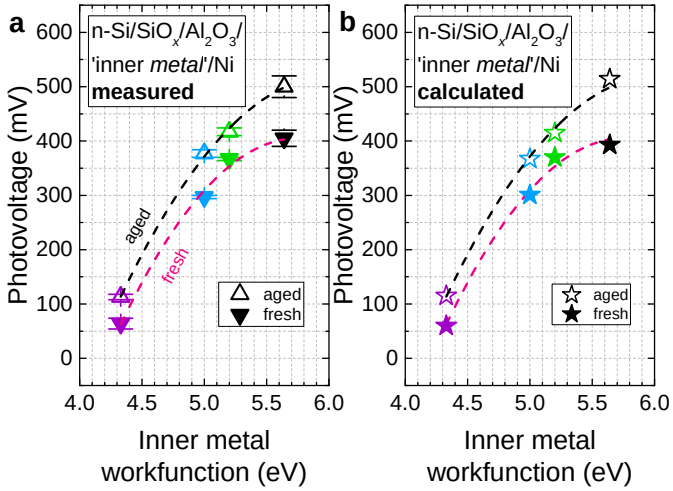



**Figure B.9:** Photovoltages of the n-Si/$SiO_x$/$Al_2O_3$/'*inner metal*'/Ni photoanodes obtained from (a) experimental measurement (a), and (b) theoretical calculation. The effective tunnel exponent $(\sqrt{\chi}\delta)_{\text{eff}}$ used for the calculation is 1.6, except for the n-Si/$SiO_x$/$Al_2O_3$/Ti/Ni: $(\sqrt{\chi}\delta)_{\text{eff}} = 4$.

## B.7. Barrier heights and flat band potentials of MIS photoandoes with various $Al_2O_3$ thicknesses

Figure B.10a indicates that the barrier height decreases with increasing $Al_2O_3$ thickness. In particular, increasing the oxide thickness will reduce the oxide capacitance. For a system comprising multiple oxides, it is more convenient to use the equivalent oxide thickness (EOT) to represent the total oxide thickness. The introduction of EOT is particularly important because two different oxides with different dielectric permittivities are combined. The EOT of a high-$k$ dielectric can be calculated by the following relationship:[9]

$$\mathrm{EOT} = t_{\text{high-}k}\frac{\epsilon_{SiO_2}}{\epsilon_{\text{high-}k}} \tag{B.22}$$

So the total EOT of $SiO_x/Al_2O_3$ layers is equal to the sum of the $SiO_x$ thickness and the $EOT_{Al_2O_3}$.

Recalling Eq. B.19, the barrier height is proportional to the flat band potential ($E_{fb}$). The correlation between the flat band potential, EOT and the oxide capacitance $C_{ox}$ is given by:[10–12]

$$\begin{aligned} E_{fb} &= \Phi_{ms} - q\frac{Q_{interface}}{C_{ox}} - q\frac{Q_{bulk}\,t_{ox}}{2C_{ox}} \\ &= \Phi_{ms} - q\frac{Q_{interface}\mathrm{EOT}}{\epsilon_0\epsilon_{SiO_2}} - q\frac{Q_{bulk}\mathrm{EOT}^2}{2\epsilon_0\epsilon_{SiO_2}} \end{aligned} \tag{B.23}$$

where $\Phi_{ms}$ is the workfunction difference between the metal and the semiconductor, $Q_{interface}$ is the areal charge density at the Si/oxide interface (in $cm^{-2}$) and $Q_{bulk}$ is the volumetric charge density in the high-$k$ layer (in $cm^{-3}$). The areal charge density at the Si interface is usually described as the fixed charge. Neglecting charges in the ultrathin $SiO_x$ layer,[13,14] the $Q_{interface}$ is equal to the fixed charge of the high-$k$, and in this particular case is the fixed charge of the $Al_2O_3$ ($Q_{f,\,Al_2O_3}$).

Figure B.10b shows the $E_{fb}$ as a function of the EOT. According to Eq. B.23, the presence of $Q_{bulk}$ will give parabolic dependence between the $E_{fb}$ and the EOT. From the fit results of the parabolic curves in Figure B.10b, the $Al_2O_3$ has a negative fixed charge of $-2.7 \pm 0.1 \times 10^{12}$ $cm^{-2}$, consistent with the value reported by literatures.[15–17] The calculated $Q_{bulk}$ is $4.5 \pm 0.3 \times 10^{18}$ $cm^{-3}$. The opposite charges between the $Q_{f,\,Al_2O_3}$ and the $Q_{bulk,\,Al_2O_3}$ has also been experimentally observed by other works,[11] and has been attributed to the dominant nature of tetrahedral $AlO_{4/2}^-$ at the surface and the octahedral coordination of $Al^{3+}$ in the bulk.[18,19]

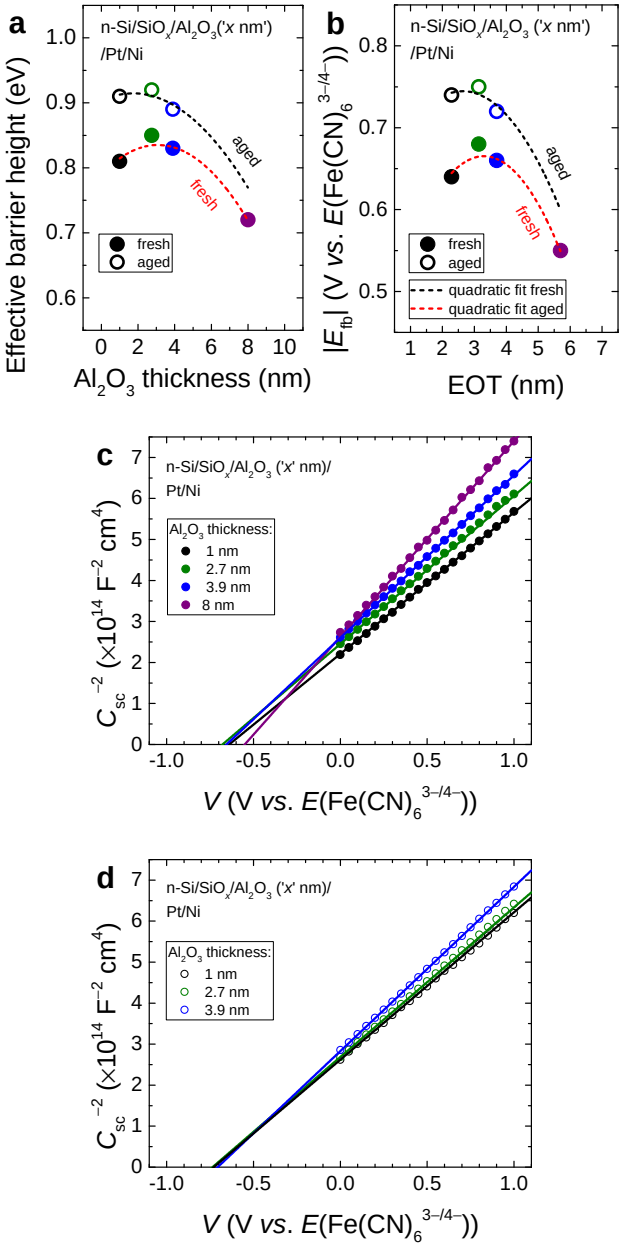



**Figure B.10:** (a) Barrier heights of MIS photoanodes as functions of the $Al_2O_3$ thickness. (b) Flat band potentials of MIS photoanodes as functions of the equivalent oxide thickness (EOT). (c) Mott-Schottky plot of the fresh n-Si/$SiO_x$/$Al_2O_3$/Ti/Ni with various $Al_2O_3$ thicknesses. (d) Mott-Schottky plots of the same samples as in (c) but after aging in KOH.

# References


[1] W. Shockley and W. T. Read, *Statistics of the Recombination of Holes and Electrons,* Physical Review **87**, 835 (1952).

[2] R. N. Hall, *Electron-Hole Recombination in Germanium,* Physical Review **87**, 387 (1952).

[3] C.-T. Sah, R. Noyce, and W. Shockley, *Carrier generation and recombination in p-n junctions and p-n junction characteristics,* Proceedings of the IRE **45**, 1228 (1957).

[4] S. K. Cheung and N. W. Cheung, *Extraction of schottky diode parameters from forward current-voltage characteristics,* Appl. Phys. Lett. **49**, 85 (1986).

[5] H. C. Card and E. H. Rhoderick, *Studies of tunnel MOS diodes I. Interface effects in silicon Schottky diodes,* Journal of Physics D: Applied Physics **4**, 319 (1971).

[6] E. Mahé, F. Rouelle, I. Darolles, and D. Devilliers, *Electrochemical characterization of silicon electrodes: Part 1: Capacitance-voltage method,* J. New Mater. Electrochem. Syst. **9**, 257 (2006).

[7] M. D. Groner, F. H. Fabreguette, J. W. Elam, and S. M. George, *Low-temperature al2o3 atomic layer deposition,* Chem. Mater. **16**, 639 (2004), http://dx.doi.org/10.1021/cm0304546 .

[8] J. L. van Hemmen, S. B. S. Heila, J. H. Klootwijk, F. Roozeboom, C. J. Hodson, M. C. M. van de Sanden, and W. M. M. Kessels, *Plasma and thermal ald of al2o3 in a commercial 200 mm ald reactor,* J. Electrochem. Soc. **154**, G165 (2007).

[9] S. M. Sze and K. K. Ng, *Physics of Semiconductor Devices* (Wiley-Interscience, 2007).

[10] R. S. Johnson, G. Lucovsky, and I. Baumvol, *Physical and electrical properties of noncrystalline $Al_2O_3$ prepared by remote plasma enhanced chemical vapor deposition,* Journal of Vacuum Science & Technology A: Vacuum, Surfaces, and Films **19**, 1353 (2001).

[11] Y. Ahn, S. H. Choudhury, D. Lee, S. M. Sadaf, M. Siddik, M. Jo, S. Park, Y. Kim, D. H. Kim, and H. Hwang, *Estimation of interfacial fixed charge at $Al_2O_3/SiO_2$ using slant-etched wafer for solar cell application,* Jpn. J. Appl. Phys. **50**, 071503 (2011).

[12] Y. Yamamoto, K. Kita, K. Kyuno, and A. Toriumi, *Study of La-induced flat band voltage shift in metal/$HfLaO_x/SiO_2/Si$ capacitors,* Jpn. J. Appl. Phys. **46**, 7251 (2007).

[13] S. Y. No, D. Eom, C. S. Hwang, and H. J. Kim, *Property changes of aluminum oxide thin films deposited by atomic layer deposition under photon radiation,* J. Electrochem. Soc. **153**, F87 (2006).

[14] A. Rothschild, B. Vermang, X. Loozen, B. J. O'Sullivan, J. John, J. Poortmans, G. F. De Santi, H. Ossenbrink, and P. Helm, *ALD-$AL_2O_3$ passivation for solar cells,* EU PVSEC Proc. , 1382 (2010).

[15] G. Dingemans and W. M. M. Kessels, *Status and prospects of $Al_2O_3$-based surface passivation schemes for silicon solar cells,* Journal of Vacuum Science & Technology A: Vacuum, Surfaces, and Films **30**, 040802 (2012).

[16] F. Werner, B. Veith, D. Zielke, L. Kühnemund, C. Tegenkamp, M. Seibt, R. Brendel, and J. Schmidt, *Electronic and chemical properties of the c-Si/$Al_2O_3$ interface,* Journal of Applied Physics **109**, 113701 (2011).

[17] D. K. Simon, P. M. Jordan, T. Mikolajick, and I. Dirnstorfer, *On the control of the fixed charge densities in $Al_2O_3$-based silicon surface passivation schemes,* Journal of Applied Physics **109**, 113701 (2011).

[18] G. Lucovsky, *A chemical bonding model for the native oxides of the III–V compound semiconductors,* Journal of Vacuum Science and Technology **19**, 456 (1981).

[19] K. Kimoto, Y. Matsui, T. Nabatame, T. Yasuda, T. Mizoguchi, I. Tanaka, and A. Toriumi, *Coordination and interface analysis of atomic-layer-deposition $Al_2O_3$ on Si(001) using energy-loss near-edge structures,* Applied Physics Letters **83**, 4306 (2003).

# C

# Appendix C

## C.1. Energy band diagram analysis

**p-i amorphous silicon carbide (a-SiC)**

The band-edge energetics of the p-i amorphous silicon carbide (a-SiC) electrode with an active area of 0.283 $cm^{-2}$ were characterized by electrochemical impedance spectroscopy (EIS) and were analyzed using the Mott-Schottky relationship.[1] In order to obtain an accurate Mott-Schottky analysis, the scanning frequency was chosen in the range where the real part of the impedance ($Z_{re}$) is constant and only the imaginary part of the impedance ($Z_{im}$) is varied and the ($\log(-Z_{im})$ *versus* $\log(f)$) has a slope of −1 in the complex Bode plot.[2] Thereby, the imaginary impedance can be fully interpreted as the contribution from the space-charge layer capacitance. From the complex bode plot ($\log(Z_{re})$, $\log(-Z_{im})$ *versus* $\log(f)$), the frequency range at which $Z_{re}$ is constant and $\log(-Z_{im})$ *versus* $\log(f)$ has a slope of −1 is between 5 kHz and 100 kHz (Fig. C.1).

The acceptor concentration ($N_A$) in the p-type a-SiC was calculated by the Mott-Schottky relationship:

$$C_{sc}^{-2} = \frac{2}{\epsilon_0 \epsilon_r q N_A}\left(V - E_{fb} - \frac{kT}{q}\right) \tag{C.1}$$

where $C_{sc}$ is the space charge capacitance density, $\epsilon_0$ is the vacuum permittivity (8.85 × $10^{-12}$ F $m^{-1}$), $\epsilon_r$ is the relative permittivity of the semiconductor ($\epsilon_r$ = 14 for a-SiC),[3] $q$ is the electron charge (1.60 × $10^{-19}$ C), $k$ is the Boltzmann's constant (1.38 × $10^{-23}$ $m^2$ kg $s^{-2}$ $K^{-1}$), $T$ is the temperature (298 K) and $V$ is the applied voltage. From the intercept between the extrapolated inverse space-charge capacitance ($C_{sc}^{-2}$) and the $x$-axis in Fig. 5.2a, the flat band potential ($E_{fb}$) of the p-i a-SiC was approximated to be 1.17 V *versus* the reversible hydrogen electrode (RHE). Using the slope in the linear region of the $C_{sc}^{-2}$–$V$ plot in Fig. 5.2a, $N_A$ was calculated to be 1.46 × $10^{17}$ $cm^{-3}$.

The position of Fermi level ($E_F$) relative to the valence band edge ($E_V$) of the a-SiC was determined by the following relationship:

$$E_F - E_V = V_p = kT \ln \frac{N_V}{N_A} \tag{C.2}$$

The density of valance band states ($N_v$) can be obtained using the following equation:

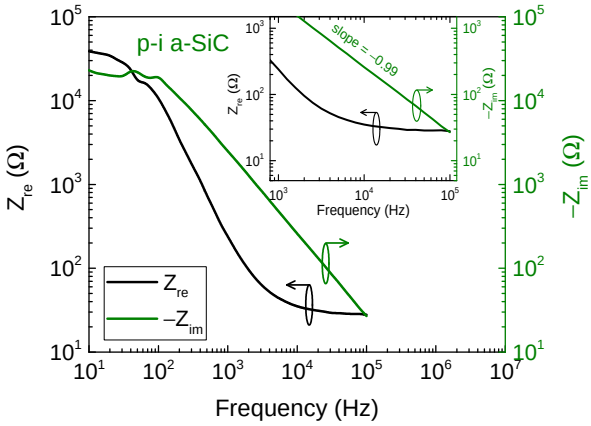



**Figure C.1:** Complex Bode plots of real ($Z_{re}$) and imaginary impedance ($-Z_{im}$) as functions of a frequency ($f$) plot in logarithmic scales of the p-i a-SiC electrode in contact with 0.5 M KHP electrolyte solution (p-i-liquuid junction). The inset shows the magnification in a frequency range between 100 Hz and 10 kHz where $Z_{re}$ is constant and the slope of $\log(-Z_{im})$ *versus* $\log(f)$ is close to −1.

$$N_V = 2\left(\frac{2\pi m_h^* kT}{h^2}\right)^{3/2} \tag{C.3}$$

where $m_h^*$ is the effective mass of hole, and is assumed to be the same as that of amorphous silicon ($0.5m_0$).[4] The calculated $N_V$ was $8.78 \times 10^{18}$ cm$^{-3}$, and using Eq. C.2, the Fermi level was estimated to be positioned at 105.26 meV above the valence band edge.

Assuming the band edges are pinned at the solid/liquid interface, the position of the valence band edge ($E_V$) at the interface is given by:

$$E_V = E_{fb} + V_p \tag{C.4}$$

The calculated $E_V$ was 1.27 V *versus* RHE. Using a value of 4.44 eV for the redox energy of $H^+/H_2$ relative to the vacuum level[5], a value of +1.17 V *versus* RHE for $E_{fb}$ and a value of 105.26 meV for $V_p$, the position of the valence band edge with respect to the vacuum level or the ionization energy ($IE$) was approximated to be 5.71 eV. Using a band gap ($E_g$) of 2 eV for the a-SiC, the position of the conduction band ($E_C$) was determined to be −0.72 V *versus* RHE and the electron affinity of the a-SiC ($\chi_{a\text{-SiC}}$) was approximated to be 3.71 eV.

The built-in voltage ($V_{bi}$) of the p-i-liquid junction a-SiC electrode was calculated from the difference between $E_{fb}$ of the a-SiC and the redox energy level of the surface states ($E_{ss}$). The $E_{ss}$ is assumed to be equal to the position of the Fermi level after equilibrium ($E_F$), which is represented by the dark open-circuit potential of the p-i a-SiC electrode (OCP $\approx E_F \approx \Phi_{ss} =$ ~0.48 V *versus* RHE):

$$V_{bi} = E_{fb} - E_F \tag{C.5}$$

The barrier height ($\phi_b$) of the p-i-liquid junction a-SiC electrode was determined by subtracting $E_V$ with the dark OCP (~0.48 V *versus* RHE):

$$\phi_b = E_V - E_F \tag{C.6}$$

Thus, the barrier height of the p-i-liquid junction a-SiC electrode was estimated to be 0.79 eV.

The width of the space-charge region ($W$) of the p-i a-SiC in contact with the electrolyte is given by the following relationship:

$$W = \left[\frac{2\epsilon_0\epsilon_r}{qN_A}\left(E_{fb} - E_F - \frac{kT}{q}\right)\right]^{1/2} \tag{C.7}$$

Under open-circuit condition, the Fermi level of the p-i a-SiC equilibrates at ~ +0.48 *versus* RHE, and the calculated $W$ was 88.90 nm. This value is close to the approximate thickness of the intrinsic layer of the a-SiC (100 nm), thus confirming the validity of our measurement and calculations. The extracted parameters from Mott-Schottky analysis are summarized in Table C.1.

**Titanium dioxide ($TiO_2$)**

EIS measurement of the titanium dioxide ($TiO_2$) was performed at a frequency of 1 kHz based on the range where $Z_{re}$ is constant and $\log(-Z_{im})$ *versus* $\log(f)$ has a slope of close to −1 in the complex Bode plots (Fig. C.2).

The electron density ($N_D$) in the $TiO_2$ was estimated using the Mott-Schottky relationship for n-type semiconductors:

$$C_{sc}^{-2} = \frac{2}{\epsilon_0\epsilon_r qN_D}\left(V - E_{fb} - \frac{kT}{q}\right) \tag{C.8}$$

where $\epsilon_r = 75$ for amorphous $TiO_2$ is assumed to be the same as crystalline anatase $TiO_2$.[6] From the intercept between the extrapolated $C_{sc}^{-2}$ and the $x$-axis in Fig. 5.2b, $E_{fb}$ of the $TiO_2$ was approximated to be −0.11 V *versus* RHE. Using the slope in the linear region of the $C_{sc}^{-2}$–$V$ plot in Fig. 5.2b, $N_D$ was calculated to be $1.62 \times 10^{20}$ $cm^{-3}$.

The position of Fermi level ($E_F$) relative to the conduction band edge ($E_C$) of the $TiO_2$ was determined by the following relationship:

$$E_C - E_F = V_n = kT\ln\frac{N_C}{N_D} \tag{C.9}$$

The density of conduction band states ($N_C$) can be obtained using the following equation:

$$N_C = 2\left(\frac{2\pi m_e^* kT}{h^2}\right)^{3/2} \tag{C.10}$$

where $m_e^*$ is the effective mass of electron of the amorphous $TiO_2$, and is assumed to be the same as that of anatase $TiO_2$ ($10m_0$).[7] The calculated $N_D$ was $1.62 \times 10^{20}$, and using Eq. C.9, the Fermi level of the $TiO_2$ was estimated to be positioned at 40.54 meV below the conduction band edge.

Assuming the band edges are pinned at the solid/liquid interface, the position of the conduction band edge ($E_C$) at the interface is given by:

$$E_C = E_{fb} - V_n \tag{C.11}$$

The position of the conduction band edge was estimated to be −0.15 V *versus* RHE. Using a value of 4.44 eV for the redox energy of $H^+/H_2$ relative to the vacuum level,[5] the position

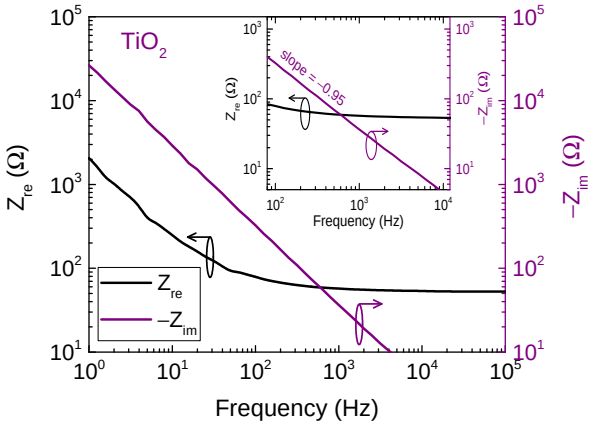



**Figure C.2:** Complex Bode plots of real ($Z_{re}$) and imaginary impedance ($-Z_{im}$) as functions of a frequency ($f$) plot in logarithmic scales of the $TiO_2$ electrode in contact with 0.5 M KHP electrolyte solution (p-i-liquuid junction). The inset shows the magnification in a frequency range between 100 Hz and 10 kHz where $Z_{re}$ is constant and the slope of $\log(-Z_{im})$ *versus* $\log(f)$ is close to −1.

of the conduction band edge relative to vacuum, and thus the electron affinity of the $TiO_2$ ($\chi_{TiO_2}$) was approximated to be 4.29 eV below the the vacuum level.

The width of the space-charge region ($W$) of the $TiO_2$ in contact with the electrolyte is given by the following relationship:

$$W = \left[\frac{2\epsilon_0\epsilon_r}{qN_D}\left(E_F - E_{fb} - \frac{kT}{q}\right)\right]^{1/2} \tag{C.12}$$

Under open-circuit condition, the Fermi level of the $TiO_2$ equilibrates at ~ +0.48 *versus* RHE, and the calculated $W$ was 5.47 nm. At an applied bias equal to the formal potential for hydrogen evolution ($E^{0\prime}$ ($H^+/H_2$) = 0 V *versus* RHE), $W$ was determined to be 2.08 nm. Table C.1 summarizes the extracted parameters from the Mott-Schottky analysis.

### p-i a-SiC/$TiO_2$

The energy band diagram of the p-i a-SiC/$TiO_2$ heterojunction electrode was constructed using the parameters extracted from independent EIS measurements and Mott-Schottky analysis for the a-SiC and the $TiO_2$, and using an assumption that the density of interface states between the a-SiC and the $TiO_2$ is significantly low so that no Fermi level pinning occurs at the a-SiC/$TiO_2$ interface. The conduction band offset ($\Delta E_C$) was calculated by subtracting the electron affinity of the $TiO_2$ ($\chi_{TiO_2}$) and the electron affinity of the a-SiC ($\chi_{a\text{-}SiC}$):

$$\Delta E_C = \chi_{TiO_2} - \chi_{a\text{-}SiC} \tag{C.13}$$

The valence band offset ($\Delta E_V$) at the heterointerface between the a-SiC and the $TiO_2$ was determined by:

$$\Delta E_V = \left(\chi_{TiO_2} + E_{g,TiO_2}\right) - \left(\chi_{a\text{-}SiC} + E_{g,a\text{-}SiC}\right) \tag{C.14}$$

The built-in voltage ($V_{bi}$) of the p-i a-SiC/$TiO_2$ heterojunction was calculated from the workfunction ($\Phi$) difference between the p-type a-SiC and the $TiO_2$:

**Table C.1:** Extracted parameters obtained from the Mott-Schottky analysis.

| | p-i a-SiC | $TiO_2$ |
|---|---|---|
| Band gap, $E_g$ (eV) | 2.0 | 3.2 |
| Flat band potential, $E_{fb}$ (V *versus* RHE) | +1.17 | −0.11 |
| Fermi level above valence band edge, $E_F - E_V$ (meV) | 105.26 | – |
| Fermi level below conduction band edge, $E_C - E_F$ (meV) | – | 40.54 |
| Conduction band edge position, $E_C$ (V *versus* RHE) | −0.73 | −0.15 |
| Valence band edge position, $E_V$ (V *versus* RHE) | +1.27 | +3.05 |
| Electron affinity, $\chi$ (eV) | 3.71 | 4.29 |
| Ionization energy, *IE* (eV) | 5.71 | 7.49 |
| Workfunction, $\Phi$ (eV) | 5.61 | 4.33 |
| Barrier height, $\phi_b$ (eV) | 0.79 | 0.63 |
| Space-charge width, $W$ (nm) | 88.90 | 5.47 |

$$V_{bi} = \Phi_{\text{a-SiC}} - \Phi_{TiO_2} = \left(\chi_{\text{a-SiC}} + E_{g,\text{a-SiC}} - V_{p,\text{a-SiC}}\right) - \left(\chi_{TiO_2} + V_{n,TiO_2}\right) \tag{C.15}$$

The barrier height of the p-i a-SiC/$TiO_2$ electrode was determined from the following relationship:

$$\phi_b = V_{bi} + V_{p,\text{a-SiC}} \tag{C.16}$$

**Table C.2:** Calculated parameters to construct the energy band diagram of the p-i a-SiC and the p-i a-SiC/$TiO_2$ electrodes.

| | p-i a-SiC | p-i a-SiC/$TiO_2$ |
|---|---|---|
| Conduction band offset, $\Delta E_C$ (eV) | – | 0.57 |
| Valence band offset, $\Delta E_V$ (eV) | – | 1.77 |
| Built-in voltage, $V_{bi}$ (eV) | 0.69 | 1.28 |
| Barrier height, $\phi_b$ (eV) | 0.79 | 1.38 |

Figure C.3 shows the energy band diagrams of the p-i a-SiC and the p-i a-SiC/$TiO_2$ electrodes generated using AFORS-HET.[8,9]

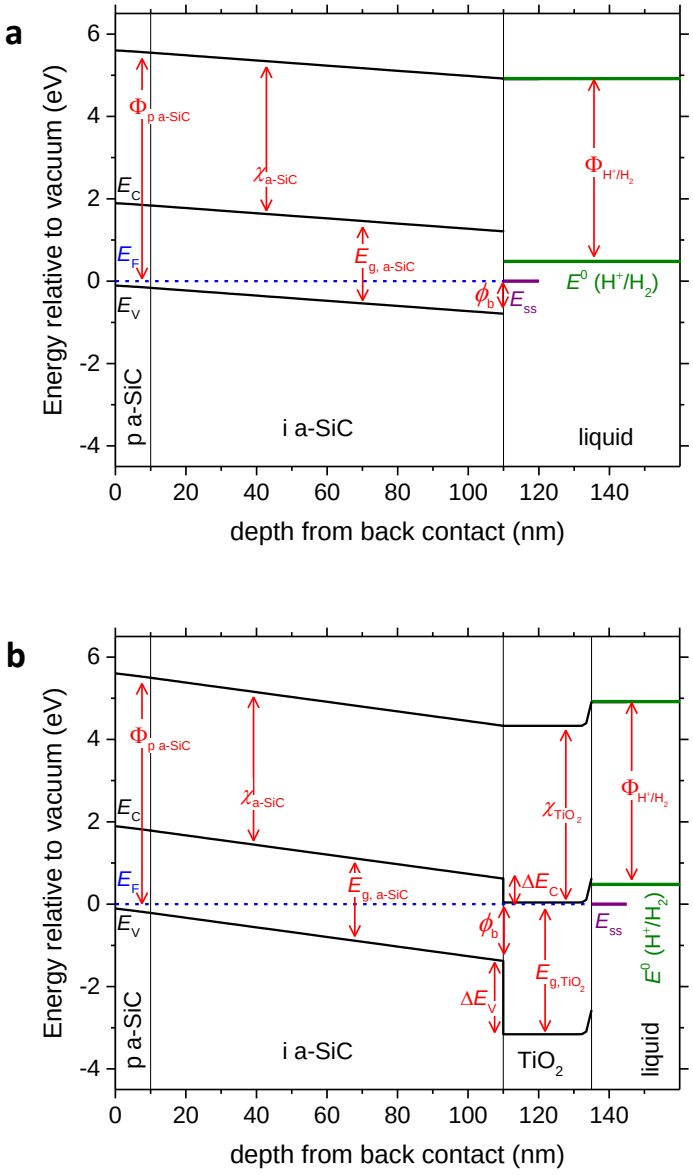



**Figure C.3:** Energy band diagrams of (a) the p-i-liquid junction a-SiC and (b) p-i a-SiC/$TiO_2$ heterojunction electrodes under equilibrium in an electrolyte solution, generated using AFORS-HET.[8,9] The thickness of the surface states and the liquid are not drawn to scale.

## C.2. Optical band gap

The absorption coefficient ($\alpha$) is calculated using the extinction coefficient ($\kappa$) from the measured complex refractive index by spectroscopic ellipsometry and the light wavelength ($\lambda$):

$$\alpha = \frac{4\pi\kappa}{\lambda} \tag{C.17}$$

The photon energy is calculated using the following equation:

$$\text{photon energy} = \frac{h\nu}{\lambda} \tag{C.18}$$

where $h$ is the Planck's constant ($6.626 \times 10^{-34}$ J s) and $\nu$ is the speed of light ($2.99 \times 10^{8}$ m $s^{-1}$). Figure C.4 shows the Tauc plots ($(\alpha h\nu)^{1/2}$–photon energy) of the a-SiC and the $TiO_2$. The intercept of the extrapolated linear region of $(\alpha h\nu)^{1/2}$ with the $x$-axis indicates the band gap of the semiconductor. The estimated band gap of a-SiC is 2.0 eV and the approximated band gap of $TiO_2$ is 3.2 eV.

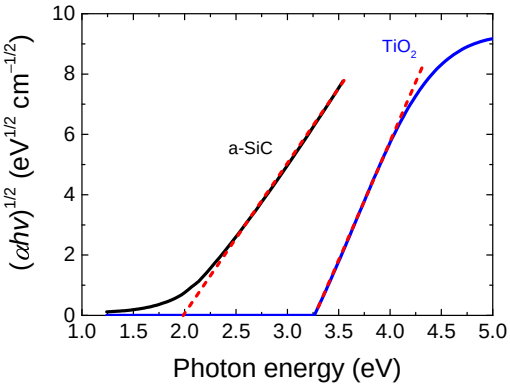



**Figure C.4:** Tauc plots of the a-SiC and $TiO_2$ based on the refractive indices ($n$ & $k$) measured using ellipsometry. The interception between the extrapolated linear line and the $x$-axis represents the direct optical band gap. The band gap of a-SiC and $TiO_2$ are 2 eV and 3.2 eV, respectively.

## C.3. Current-potential characteristics of uncatalyzed photocathodes

Figure C.5 shows the current–potential ($j$–$V$) behavior of the uncatalyzed p-i a-SiC and p-i a-SiC/$TiO_2$, recorded during the first scan of cyclic voltammetry in 0.5 M potassium hydrogen phthalate (KHP) electrolyte solution at pH 4 under simulated solar irradiation.

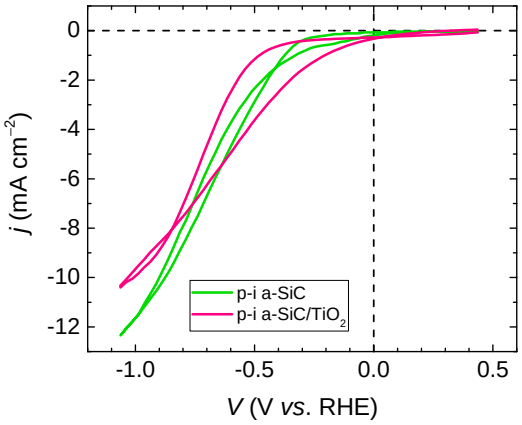



**Figure C.5:** Current–potential ($j$–$V$) characteristics of the p-i a-SiC and the p-i a-SiC/$TiO_2$ photocathodes without catalyst, measured during the first scan of cyclic voltammetry in 0.5 M potassium hydrogen phthalate (KHP) electrolyte solution at pH 4 under simulated solar irradiation.

## C.4. Solar photocurrent and irradiance spectra

The solar photocurrent as a function of photon wavelength is obtained by the multiplication of the (incident-photon-to-current efficiency (IPCE) spectrum with the the Air Mas 1.5 Global (AM1.5G = 100 mW $cm^{-2}$) irradiance spectrum from the American Society for Testing and Materials (ASTM):[10]

$$I(\lambda) = \mathrm{IPCE} \times F(\lambda) \times \frac{q}{h\nu} \tag{C.19}$$

where $I(\lambda)$ is the spectral photocurrent and $F(\lambda)$ is the spectral irradiance of the ASTM AM1.5G. The total photocurrent density of the photocathode under ASTM AM1.5G illumination ($j_{\mathrm{AM1.5G}}$) is obtained by integrating the spectral photocurrent over the spectrum:

$$j_{\mathrm{AM1.5G}} = \int I(\lambda) d(\lambda) \tag{C.20}$$

Using the IPCE spectrum in Fig. 5.8 and putting it into Eq. C.19 and Eq. C.20, the integrated solar photocurrent of the p-i a-SiC/Ni–Mo and the p-i a-SiC/$TiO_2$/Ni–Mo photocathodes are calculated to be −2.9 mA $cm^{-2}$ and −8.5 mA $cm^{-2}$, respectively.

Figure C.6 shows the comparison between the spectral irradiance of our solar simulator with xenon (Xe) lamp and the spectral irradiance of the ASTM AM1.5.

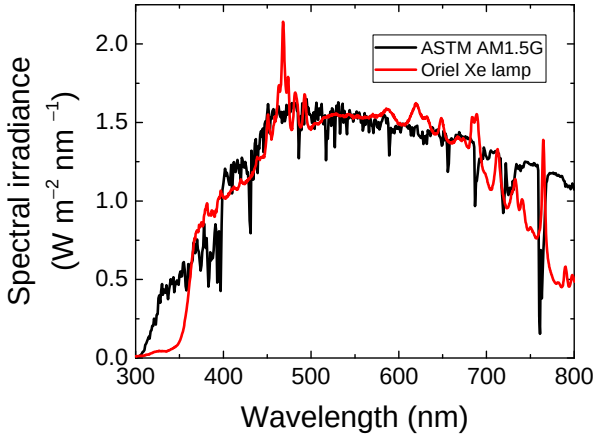



**Figure C.6:** Irradiance spectra of the solar simulator Xe lamp used for *j–V* measurements (red line) and the ASTM AM1.5G (black line).

# References

[1] K. Gelderman, L. Lee, and S. W. Donne, *Flat-Band Potential of a Semiconductor: Using the Mott-Schottky Equation,* Journal of Chemical Education **84**, 685 (2007).

[2] R. van de Krol and M. Grätzel, *Photoelectrochemical Hydrogen Production* (Springer US, Boston, MA, 2012) p. 79.

[3] D. Brassard and M. A. El Khakani, *Flat-Band Potential of a Semiconductor: Using theMott-Schottky Equation,* Journal of Applied Physics **93**, 4066 (2003).

[4] M. Brodsky, *Quantum well model of hydrogenated amorphous silicon,* Solid State Communications **36**, 55 (1980).

[5] IUPAC. Compendium of Chemical Terminology, 2nd ed. (the "Gold Book"). Compiled by A. D. McNaught and A. Wilkinson, `http://goldbook.iupac.org/html/S/S05917.html` (Blackwell Scientific Publications, Oxford, 1997), accessed: February, 2018.

[6] D. M. King, X. Du, A. S. Cavanagh, and A. W. Weimer, *Quantum confinement in amorphous $TiO_2$ films studied via atomic layer deposition,* Nanotechnology **19**, 445401 (2008).

[7] B. Enright and D. Fitzmaurice, *Spectroscopic Determination of Electron and Hole Effective Masses in a Nanocrystalline Semiconductor Film,* The Journal of Physical Chemistry **100**, 1027 (1996).

[8] R. Varache, C. Leendertz, M. E. Gueunier-Farret, J. Haschke, D. Muñoz, and L. Korte, *Investigation of Selective Junctions Using a Newly Developed Tunnel Current Model for Solar Cell Applications,* Solar Energy Materials and Solar Cells **141**, 14 (2015).

[9] AFORS-HET: numerical simulation of Solar Cells and Measurements, `https://www.helmholtz-berlin.de/forschung/oe/ee/si-pv/projekte/asicsi/afors-het/index_en.html`.

[10] American Society for Testing and Materials (ASTM), *Reference Solar Spectral Irradiance: Air Mass 1.5,* http://rredc.nrel.gov/solar/spectra/am1.5/, accessed: February, 2018.

# D

# Appendix D

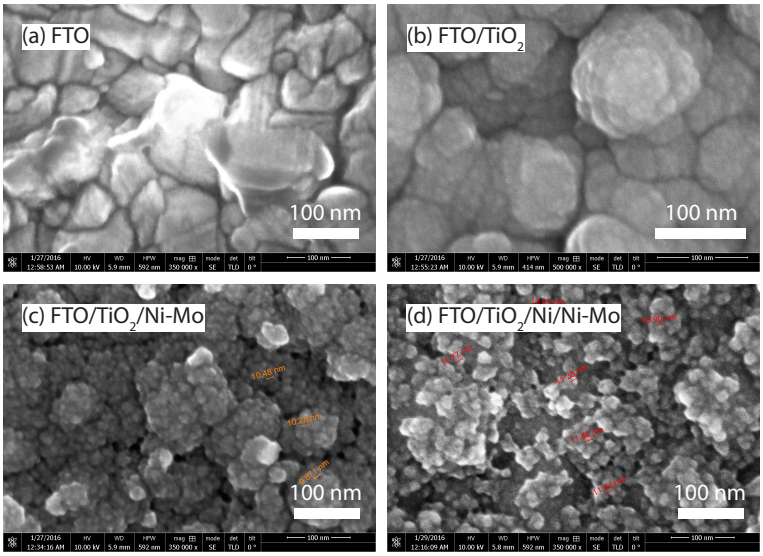



**Figure D.1:** Scanning electron microscopy (SEM) images of FTO, FTO/$TiO_2$, FTO/$TiO_2$/Ni–Mo, FTO/$TiO_2$/Ni/Ni–Mo.

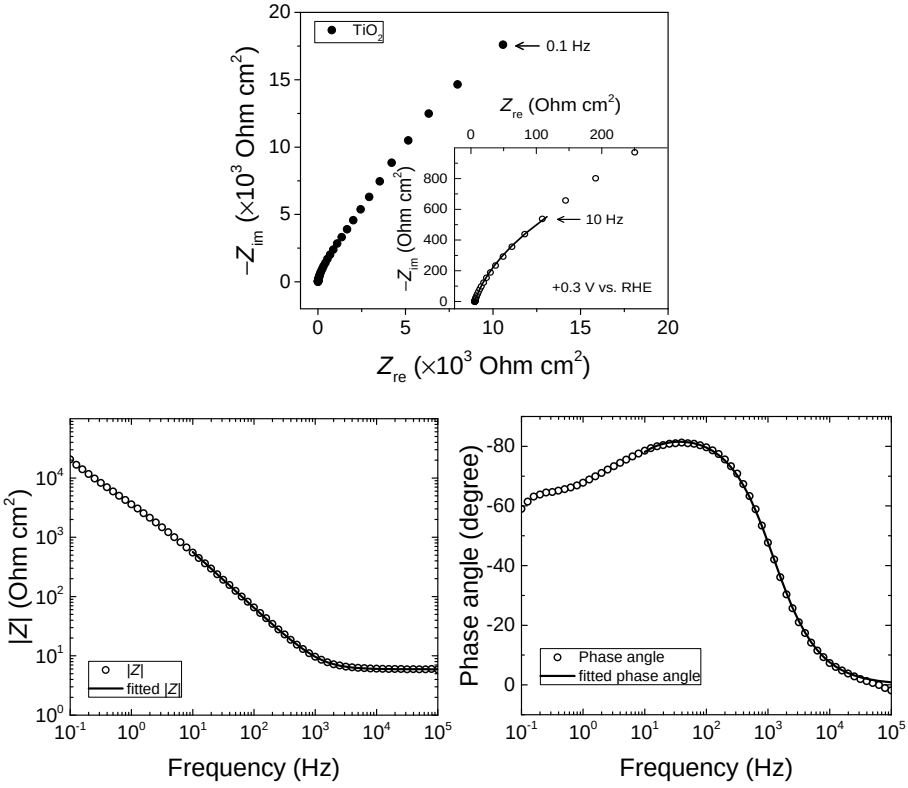



**Figure D.2:** (top) Nyquist plot, (bottom left) bode plots of total impedance and (bottom right) phase angle of $TiO_2$ at an applied potential of +0.3 V vs. RHE.

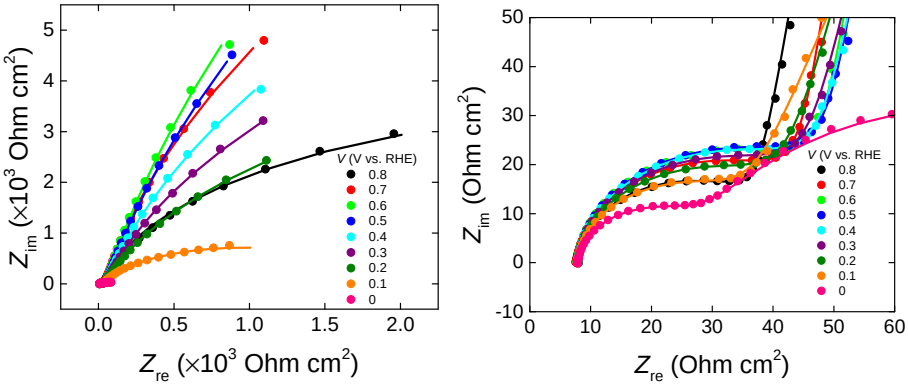



**Figure D.3:** (left) Nyquist plots of $TiO_2$/Ni–Mo at various applied potentials. The solid lines represents the fitted impedance data using the equivalent circuit in Fig. 4c. (right) The magnification of figure in the left, showing the fitted high-frequency impedance (*i.e.*, the low semicircles)

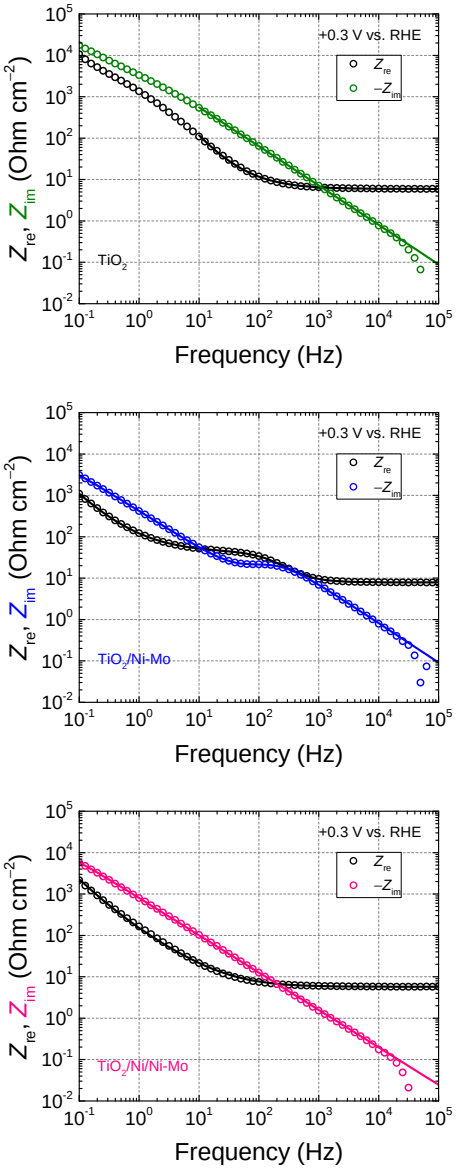



**Figure D.4:** The real part ($Z_{re}$) and the imaginary part ($Z_{im}$) of impedance spectra of $TiO_2$ with and without the catalysts at an applied potential of +0.3 V vs. RHE. The solid lines represent the fitted data using the equivalent electronic circuits

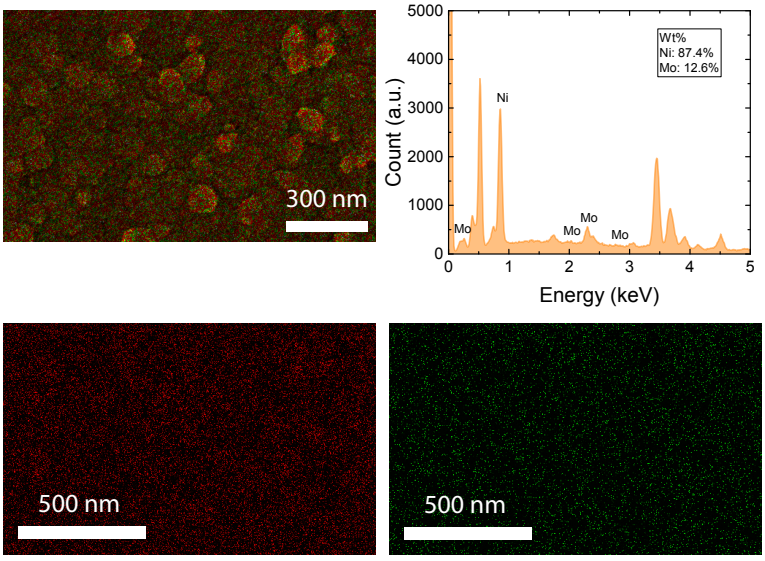



**Figure D.5:** Energy dispersive X-ray sperctroscopy (EDS) elemental mapping of Ni distribution (red) and Mo distribution (green) in a $TiO_2$/Ni/Ni-Mo sample.

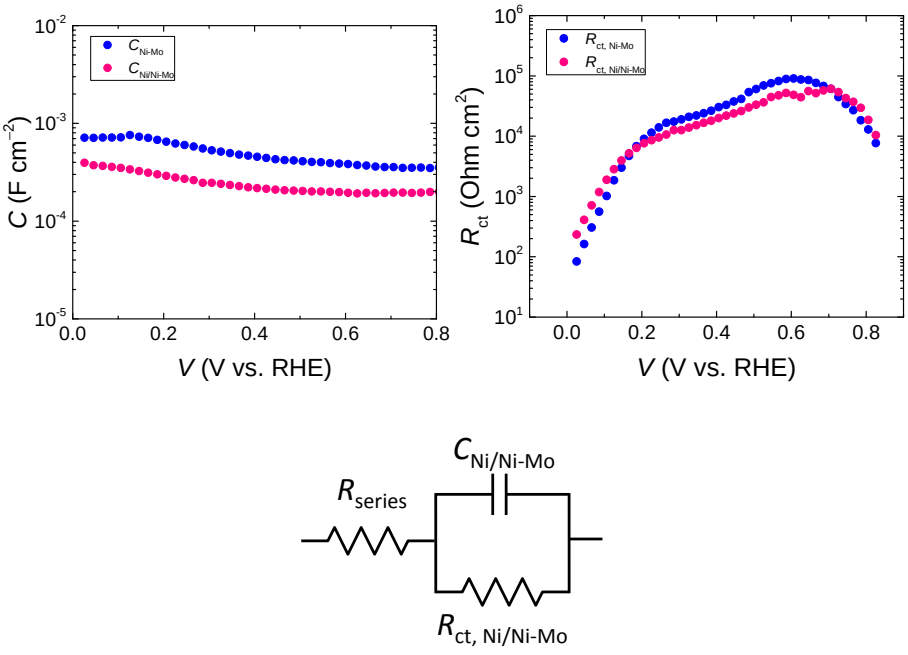



**Figure D.6:** (top left) Capacitance and (top right) charge transfer resistance of the Ni–Mo and Ni/Ni–Mo. The values are obtained from the fitted impedance data. (bottom) Equivalent circuit to fit the impedance data of $TiO_2$/Ni/Ni–Mo.

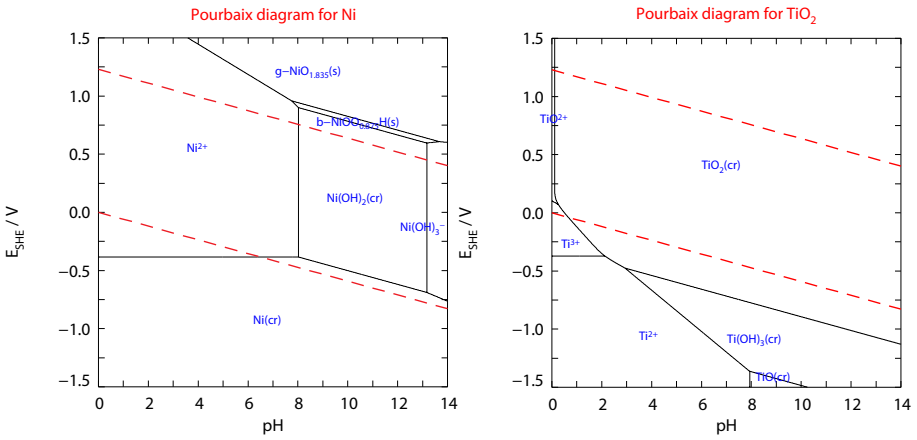



**Figure D.7:** Pourbaix diagram for Ni (left) and $TiO_2$ (right) at T = 25 °C, for $[Ni^{2+}]$ = 10 μM, generated using Medusa (`http://www.kth.se/che/medusa/`).

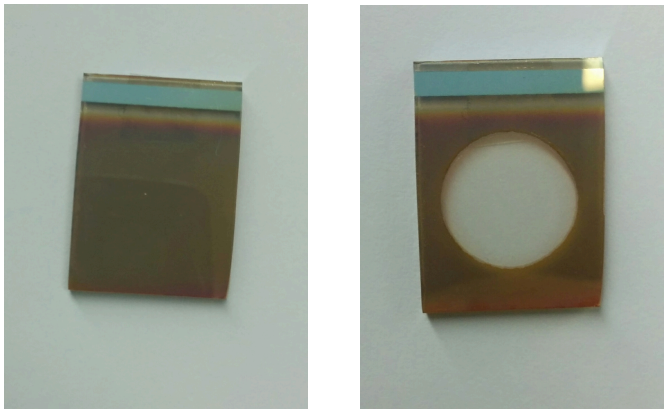


**Figure D.8:** Photographs of (left) a-SiC without $TiO_2$ layer and (right) a-SiC after being soaked in 1 M KOH in the dark (no applied bias) for 1 hour. The transparent circular area is the active area that was exposed area to the electrolyte, indicating that a-SiC was completely dissolved after 1 hour.

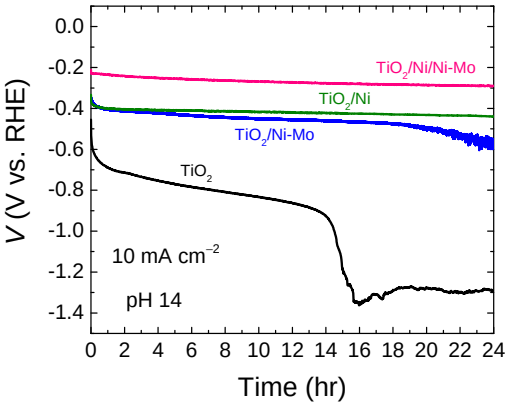



**Figure D.9:** Chronopotentiomtery test of $TiO_2$-coated FTO substrate with catalysts at a fixed applied current of $-10$ mA cm$^2$, measured in 1 M KOH at pH 14.

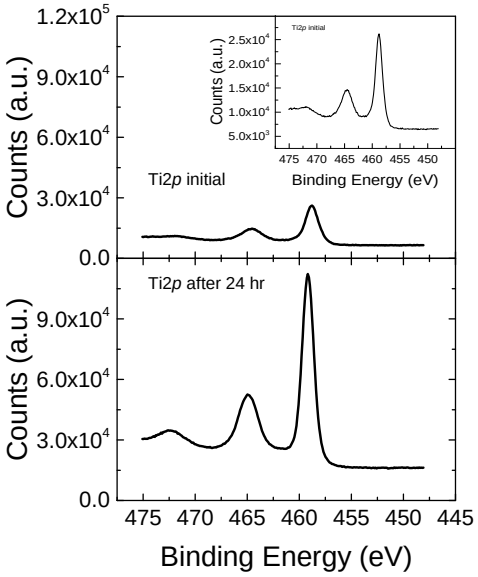



**Figure D.10:** Ti 2*p* signal from XPS spectra of $TiO_2$ coated with Ni before (top graph) and after chronopotentiometry test (bottom graph) at a fixed current of $-10$ mA cm$^{-2}$ for 24 hours. The XPS spectra shows a weaker Ti 2*p* signal before the chronopotentiometry measurement because the $TiO_2$ is still covered by Ni.

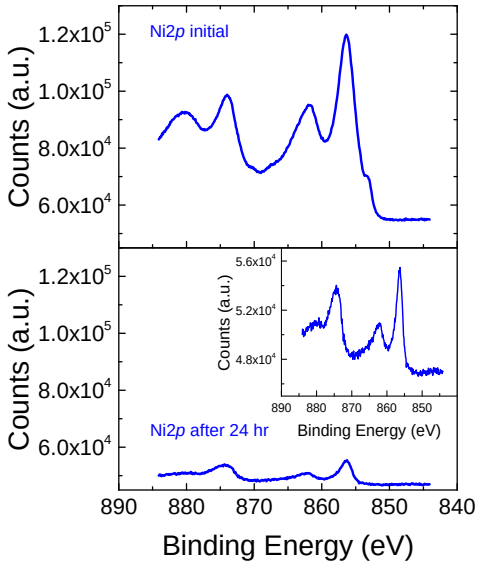



**Figure D.11:** Ni 2*p* signal from XPS spectra of $TiO_2$ coated with Ni before (top graph) and after chronopotentiometry test (bottom graph) at a fixed current of $-10$ mA cm$^{-2}$ for 24 hours. The Ni 2*p* signal is weaker after the 24-hour measurement because the Ni was detached from $TiO_2$ during the test.

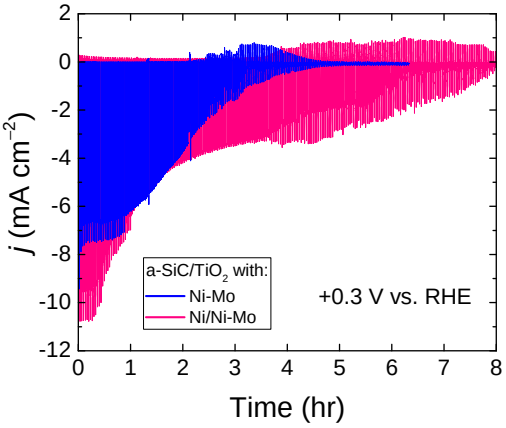



**Figure D.12:** Chronoamperometry test of a-SiC/$TiO_2$ with Ni-Mo and Ni/Ni-Mo catalysts at an applied potential of +0.3 V vs. RHE, measured under chopped illumination in 1 M KOH electrolyte at pH 14.

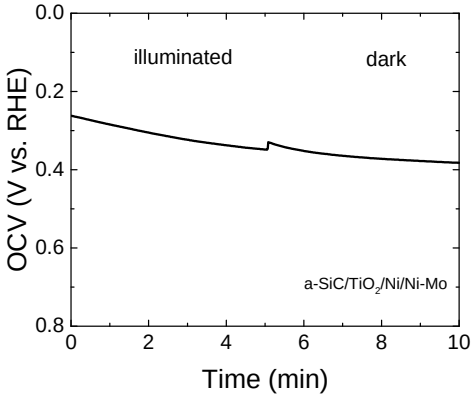



**Figure D.13:** Open circuit voltage of a-SiC/$TiO_2$ annealed at 400 °C in vacuum, measured in the dark and under illumination, showing no photovoltage.

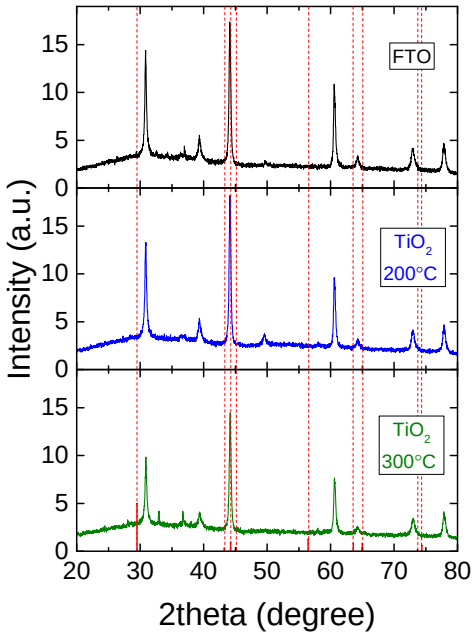



**Figure D.14:** X-ray diffractogram (XRD) of ALD $TiO_2$ deposited on FTO substrate at 200 °C and 300 °C. For comparison, the XRD of the FTO is shown. The red dash lines indicate the peak locations of crystalline anatase $TiO_2$.

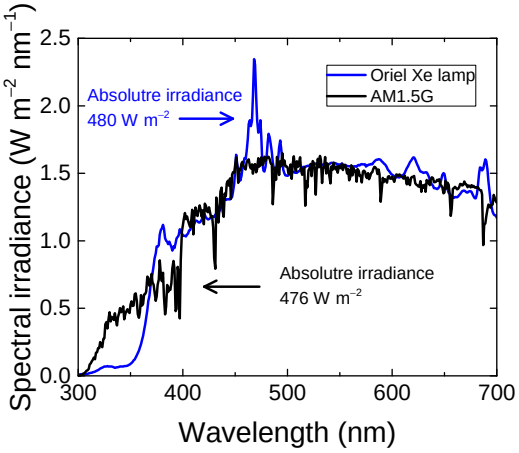



**Figure D.15:** Irradiance spectra provided the solar simulator with a Xe lamp (blue) and the ASTM AM1.5G (black).

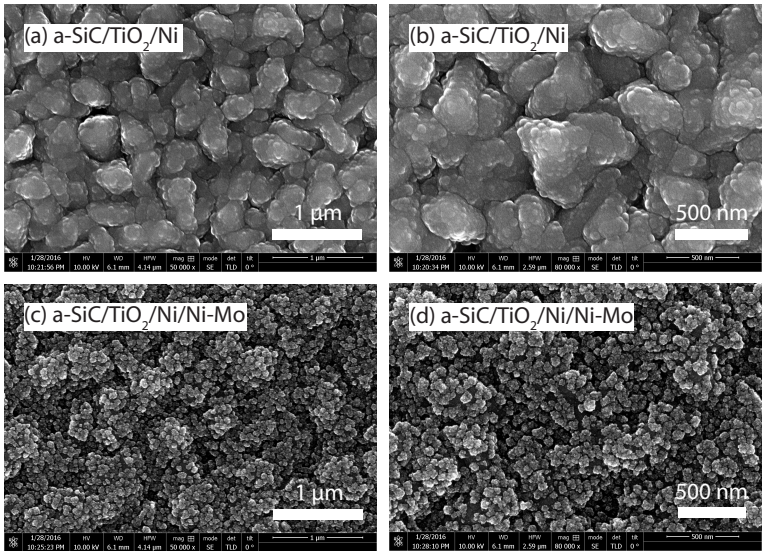



**Figure D.16:** SEM images of (a) a-SiC/$TiO_2$/Ni and (b) its magnification, (c) a-SiC/$TiO_2$/Ni/Ni–Mo and (d) its magnification.

# Summary

The global transition from fossil-based resources to renewable energy is critically important to address the sharply increasing threat of global climate change and to ensure long-term energy security. One attractive candidate to substitute for conventional fossil fuels is hydrogen. Hydrogen is an excellent energy carrier that can be directly converted into electricity *via* fuel cells, or be combined with carbon dioxide ($CO_2$) or carbon monoxide (CO) to form high energy density synthetic fuels. Most of the current industrial methods for hydrogen production, however, is by steam reforming of natural gas, which releases $CO_2$ as a by-product, making it environmentally unsustainable. Photoelectrochemical (PEC) water splitting, on the other hand, is a carbon-neutral approach that enables the conversion and storage of the abundant solar energy into hydrogen using only renewable and clean resources. This process uses semiconductors to capture and convert sunlight into photogenerated charge carriers (*i.e.*, electrons and holes), and electrocatalysts to facilitate the multi-charge transfer process for the oxidation and reduction of water to oxygen and hydrogen, respectively.

At the beginning of this thesis, we fabricated metal-insulator-semiconductor (MIS) junction silicon (Si) photoanodes and investigated their PEC performance for solar-driven water oxidation. A high photovoltage and an early photocurrent onset relative to the water oxidation potential were achieved by engineering the MIS junction using a chemically-grown silicon oxide ($SiO_x$) in conjunction with a thin aluminum oxide ($Al_2O_3$) as the interfacial layers, and using platinum (Pt) and nickel (Ni) as the front metal contacts. Bilayer metal structure was used in the MIS photoanode to decouple its function as a Schottky contact from its function as an electrocatalyst. The Pt and Ni metal contacts were designed sufficiently thin to provide optical transparency without compromising the electrical conductivity, electrocatalytic activity and chemical stability for the underlying Si. The incorporation of $Al_2O_3$ in the MIS structure alleviated the pinning of Fermi level and subsequently improved the barrier height and cathodically shifted the photocurrent onset potential for water oxidation. The incidental oxidation of Ni surface layer in 1 M potassium hydroxide (KOH) electrolyte further increased the barrier height and yielded a higher MIS photovoltage with a value close to that obtainable from diffused Si p-n junction electrodes. The protection ability of Ni surface layer was proven to be effective in sustaining a PEC operation of MIS junction Si photoanode in a strongly alkaline electrolyte.

We further analyzed the role of interfacial oxides and explored the use of less-precious metal contacts in MIS junction Si photoanodes. We discovered that the improvement of photovoltage was not only a result of the increased effective barrier height upon the introduction of $Al_2O_3$ but also the reduced dark reverse saturation current of the MIS junction with increasing thickness of interfacial oxides. With an optimum thickness, the interfacial oxides reduce the majority carrier thermionic emission without significantly affecting the minority carrier injection, thus decreasing the rate of interfacial recombination and improving the junction photovoltage. Adding a complimentary oxide such as $Al_2O_3$ to the chemically-grown $SiO_x$ could also eliminate the development of extrinsic defect states arising from interfacial chemical reaction between the metal and the $SiO_x$ or the underlying Si which could pin the metal Fermi level and reduce its effective workfunction. The effective barrier height and the photovoltage of MIS electrodes containing wet-chemical

$SiO_x$ and $Al_2O_3$ interface layers showed a strong linear dependence with increasing metal workfunction. These behaviors suggest that having passivating interfacial oxides and high workfunction metal contacts are critically important to achieving a highly efficient MIS photoanode.

In addition to studying photoanodes, we fabricated a photocathode comprising a p-type (p) and an intrinsic-type (i) amorphous silicon carbide (a-SiC) for solar hydrogen evolution. When in contact with electrolyte, the p-i a-SiC showed a rectifying behavior that is similar to that of a semiconductor-liquid junction. The energetics of the p-i-liquid junction a-SiC is limited by the solid-liquid interaction at the interface that in turn results in a non-ideal alignment of the conduction and valence band edge positions relative to the formal potential for hydrogen evolution ($E^{0\prime}$ ($H^+/H_2$)). The photovoltage produced by such a p-i-liquid junction photocathode was far below the optimal values with an onset potential that was unfavorable to generate a sufficiently high photocurrent at $E^{0\prime}$ ($H^+/H_2$). The introduction of an amorphous titanium dioxide ($TiO_2$) front surface field layer with a natural n-type conductivity onto the p-i a-SiC solved this problem by physically separating the rectifying junction from liquid contact and isolating the electric field across the solid-state p-i-n junction. The improved energetics of the buried p-i-n junction photocathode increased the barrier height and enabled a large generation of photovoltage with a value of almost two times higher than that produced by the p-i-liquid junction a-SiC photocathode. The reaction kinetics on the photocathode surface was enhanced by the application of Pt and nickel–molybdenum (Ni–Mo) electrocatalysts. Ni–Mo alloy displayed fundamental electrocatalytic activity comparable to that obtained from Pt electrocatalyst, but exhibited a slow increase of cathodic current onset, so the photocurrent generated by the Ni–Mo-catalyzed photocathode was not optimal at $E^{0\prime}$ ($H^+/H_2$). Thus, if the deposition method of Ni–Mo can be optimized in order to further increase the rate of surface catalytic reaction, it may provide a promising alternative to noble metal electrocatalysts for hydrogen-evolving photocathodes. In near-neutral electrolyte, the a-SiC photocathode coated with a $TiO_2$ front surface layer and decorated with Ni–Mo catalyst demonstrated a high photoelectrochemical stability with a nearly constant photocurrent under continuous PEC operation under simulated solar irradiation.

The activity of Ni–Mo electrocatalyst on $TiO_2$-coated conductive substrates and on a-SiC/$TiO_2$ photocathodes was further evaluated in a strongly alkaline electrolyte. The electrochemical deposition of Ni–Mo did not result in a continuous layer, but instead formed a nanoparticulate network with nano-scale interparticle gaps that exposed the underlying substrate. The incomplete coverage of Ni–Mo gives rise to a limited number of pathways for electron transfer to the electrolyte which subsequently causes a slow increasing onset of cathodic current in the observed current–potential ($j$–$V$) curve. The introduction of Ni film prior to the electrodeposition of Ni–Mo improved the apparent activity of the electrode for hydrogen evolution. The interfacial Ni increases the number of active sites and allows the electrons to transfer through a larger area, preventing charge accumulation on the electrode surface. Ni/Ni–Mo composite on the a-SiC photocathode showed a high PEC activity with a rapid increase of photocurrent onset, making it promising alternative to substitute for the noble Pt. Despite being chemically stable, the amorphous $TiO_2$ failed to prevent corrosion of the underlying a-SiC in a corrosive electrolyte. This suggests that amorphous $TiO_2$ coating may be unsuitable for photocathode stabilization in harsh environmental conditions.

Overall, this thesis has demonstrated various strategies to improve the device performance of single-absorber PEC systems and highlighted the importance of band-edge energetics control to achieve meaningful photovoltages from Si-based photoelectrodes for

solar water-splitting half reactions. Although the photovoltage generated by such single-absorber PEC systems is not sufficient to satisfy the necessary potential requirement to spontaneously split water, the high photovoltage produced by each photoelectrode shown in this thesis should relax the demand for extra voltage provided by the second (or the third) absorber in an integrated system of multijunction electrodes. Considering the various band gaps and thicknesses of Si materials studied in this thesis, which should be able to capture various portions of the solar spectrum, a solar water splitting device with a high solar-to-hydrogen efficiency can be achieved using all Si-based semiconductor electrodes.

# Samenvatting

De transitie van fossiele brandstoffen naar duurzame energie is cruciaal om klimaatverandering tegen te gaan en om lange termijn energiezekerheid te bewerkstelligen. Een aantrekkelijke kandidaat ter substitutie voor fossiele brandstoffen is waterstof. Waterstof is een uitstekende energiedrager die direct omgezet kan worden in elektriciteit door middel van brandstofcellen, en indien gecombineerd met koolstofdioxide ($CO_2$) of koolstofmonoxide (CO), kunnen er synthetische brandstoffen worden gemaakt met een hoge energiedichtheid. Echter, het gros van de industriële productie van waterstof is niet duurzaam. Het wordt verkregen door stoomreforming, met als bijproduct $CO_2$. Foto-elektrochemische (FEC) watersplitsing is een $CO_2$-neutraal alternatief, dat geschikt is voor het omzetten en opslaan van een surplus van zonne-energie in waterstof, waarbij slechts gebruikt gemaakt wordt van duurzame bronnen. Dit proces gebruikt halfgeleiders voor het opvangen en omzetten van zonlicht in foto-gegenereerde lading dragers (zoals elektronen en gaten) en elektrokatalysatoren om het multi-ladings omzettingsproces te faciliteren voor het oxideren en reduceren van respectievelijk water naar zuurstof en waterstof.

Aan het begin van deze thesis, hebben wij een metaal-isolator-halfgeleider (MIH) overgang silicium (Si) fotoanode geconstrueerd en zijn FEC prestatie voor zonne-energie gedreven wateroxidatie onderzocht. Een hoog fotovoltage en een vroege fotostroom relatief tot het wateroxidatiepotentiaal werd bereikt door het bouwen van de MIH overgang met behulp van chemisch gegroeide siliciumoxide ($SiO_x$) tegelijk met aluminiumoxide ($Al_2O_3$) grensvlaklagen en het gebruik van platinum (Pt) en nikkel (Ni) metaalcontacten. Een tweelaags metaalstructuur werd gebruikt om de MIH fotoanode te ontkoppelen van zijn functie als Schottky contact als elektrokatalyst. De Pt en Ni metaalcontacten was voldoende dun geconstrueerd ter bevordering van optische transparantie zonder dat het ten koste gaat van de elektrische geleidingseigenschappen, elektrokatalysator activiteit en chemische stabiliteit van het onderliggende Si. Het incorporeren van $Al_2O_3$ in de MIH structuur verhielp het pinnen van de Fermi level en verbeterde de barrièrehoogte en mede het schuiven van de fotostroom potentiaal voor wateroxidatie via de kathode. Incidentele oxidatie van de Ni oppervlakte laag in 1 M kaliumhydroxide (KOH) elektrolyt verhoogde de barrièrehoogte en gaf een hogere MIH fotovoltage met een waarde dichtbij dat verkregen kan worden van een diffuse p-n gesplitste elektrode. De beschermende eigenschap van de Ni oppervlaktelaag bleek effectief in het behouden van de FEC operatie van de MIH overgang Si fotoanode in een sterke alkaline elektrolyt.

Verder hebben we de rol van grensvlak oxides geanalyseerd en hebben we het gebruik van minder waardevolle metaalcontacten in de MIH overgang Si fotoanode onderzocht. We vonden dat een verbetering van het fotovoltage niet alleen het resultaat was van de verbeterde effectieve barrièrehoogte bij de introductie van $Al_2O_3$, maar ook van gereduceerde donkere tegengestelde verzadigingsstroom van de MIH overgang met een verdikking van de grensvlak oxides. Bij een optimale dikte, zullen de grensvlak oxides een vermindering van de meerderheidsdrager thermionische emissie tot gevolg hebben zonder significant effect te hebben op de minderheidsdrager injectie, wat dus leidt tot een vermindering van de rate van grensvlak recombinatie en een verbetering van de overgang fotovoltage. Door het toevoegen van een complementaire oxide zoals $Al_2O_3$ bij de chemisch gegroeide $SiO_x$ kan ook leiden tot het elimineren van de ontwikkeling van extrinsieke defecte staten die

tot stand zouden komen door een chemische reactie bij het grensvlak tussen het metaal en $SiO_x$ of het onderliggende Si dat het metaal Fermi level kan vastpinnen en zo leidt tot een vermindering van de werkfunctie. De effectieve barrièrehoogte en de fotovoltage van de MIH elektroden bevat natchemisch $SiO_x$ en $Al_2O_3$ grensvlak lagen die een sterke lineaire afhankelijkheid laten zien bij een verhoging van de werkfunctie. Dit gedrag suggereert dat het hebben van grensvlak oxides die passiviseert en metaalcontacten met een hoge werkfunctie cruciaal zijn in het verkrijgen van zeer efficiënte MIH fotoanodes.

Naast het bestuderen van fotoanodes, hebben we een fotokathode gebouwd waaronder het p-gedoteerd (p) en het intrinsieke (i) amorph siliciumcarbide (a-SiC) voor zonne-waterstof evolutie. Wanneer het in contact komt met een elektrolyt, zal p-i a-SiC rectificerend gedrag vertonen dat vergelijkbaar is met halfgeleider-vloeibaar overgang. De energetics van de p-i-vloeistof overgang a-SiC wordt beperkt door de vast-vloeibaar interactie op het oppervlak dat voor een non-ideale uitlijning van de geleiding en valentieband op de randposities zorgt relatief tot de formele potentiaal voor waterstof evolutie ($E^{0\prime}$ ($H^+/H_2$)). De fotovoltage geproduceerd bij zo'n p-i-vloeistof overgang fotokathode was ver onder de optimale waarde van het beginpotentiaal en was dus niet capabel om een voldoende hoog fotostroom op $E^{0\prime}$ ($H^+/H_2$) te genereren. De introductie van een amorph titaandioxide ($TiO_2$) voorkantoppervlaklaag met een natuurlijk n-gedoteerd geleiderschap op het p-i a-SiC loste dit probleem op door het fysiek ontkoppelen van de rectificerende overgang van het vloeibaar contact en het isoleren van het elektrisch veld over de vaste-staat p-i-n overgang. De verbeterde energetics van de begraven p-i-n overgang fotokathode verhoogde de barrièrehoogte en maakte het mogelijk om een grote hoeveelheid fotovoltage te genereren met een waarde van bijna twee keer de hoeveelheid van een p-i-vloeibaar overgang a-SiC fotokathode. De kinetische reacties op de fotokathode oppervlak werd verbeterd door het gebruik van Pt en nikkel-molybdenum (Ni-Mo) elektrokatalysatoren. De Ni-Mo legering vertoonde fundamentele elektrokatalistische activiteit vergelijkbaar met een verkregen van een Pt elektrokatalysator, maar vertoonde ook een trage toename van kathodisch stroom aan het begin. Dus de fotostroom gegenereerd door een Ni-Mo gekatalyseerde fotokathode was niet optimaal op ($E^{0\prime}$ ($H^+/H_2$)). Dus, als de depositie methode van Ni-Mo kan worden geoptimaliseerd zodat een hogere waarde van oppervlakte katalystische reactie kan worden bereikt, kan dit een hoopvolle alternatief bieden voor edelmetaal elektrokatalysatoren voor waterstof-evoluerende fotokathodes. In bijna neutraal elektrolyt vertoonde de a-SiC fotokathode gecoat met $TiO_2$ voorkantoppervlaktelaag en gedecoreerd met Ni-Mo katalysator, een hoog fotoelektrochemische stabiliteit met een bijna constante fotostroom onder een continue werking van gesimuleerde zonne-irradiatie.

De activiteit van de Ni-Mo elektrokatalystor op $TiO_2$ gecoate geleidersubstraten en a-SiC fotokathodes werd verder geëvalueerd in een sterk alkaline elektrolyt. Het elektrochemische depositie van Ni-Mo resulteerde niet in een gelijkmatige laag, maar vormde een nanopartikel netwerk met nano-schaal interpartikel gaten dat de onderliggende substraat blootlegde. De incomplete dekking van Ni-Mo beperkt het aantal wegen voor elektronen transfer naar de elektrolyt, wat tot gevolg heeft een trage toename van het begin van de kathodestroom in de geobserveerde stroom-potentiaal ($j$–$V$) curve. De introductie van Ni film alvorens de elektrodepositie van Ni-Mo, verbeterde de geobserveerde activiteit van de elektrode voor waterstof evolutie. De grensoppervlak Ni vergroot het aantal actieve plekken en zorgt ervoor dat de elektronen kunnen bewegen naar een groter gebied. Dit voorkomt lading accumulatie op de elektrode oppervlak. De a-SiC fotokathode gekatalyseerd met Ni/NiMo composiet liet een hoge FEC activiteit zien met een snelle toename van fotostroom aan het begin. Daardoor is het een hoopvolle alternatief ter substitutie van het edele Pt. Ondanks dat het chemisch stabiel is, faalde het amorph $TiO_2$ om roest

te voorkomen op het onderliggende a-SiC in een corrosieve elektrolyt. Dit suggereert dat amorph $TiO_2$ coating ongeschikt is voor fotokathode stabilisatie in een ongunstige milieu.

Concluderend, heeft deze thesis verschillende strategieën laten zien ter verbetering van apparaat prestatie van enkel-absorberend FEC systemen. Ook heeft deze thesis het belang aangetoond van band-edge energetische controle om zinvolle fotovoltages te bereiken van Si-gebaseerde fotoelektrodes voor zonne-watersplitsing halfreacties. Ofschoon het fotovoltage dat gegenereerd wordt door zo'n enkel-absorberend FEC systeem niet voldoende is om te voldoen aan het vereiste potentiaal voor het spontaan splitsen van water, zal het hoge fotovoltage bij elk van de fotoelektrodes die in deze thesis voorbijkomen, gemakkelijker aan de vraag voldoen voor extra voltage gegeven door de tweede of derde absorber in een geïntegreerde systeem van multiovergang elektrodes. Met inachtneming van de verschillende bandgaten en de dikte van Si materialen bestudeerd in deze thesis, die het mogelijk maakt om verschillende gedeelten van de zonnespectrum op te vangen, een zonne-watersplitsend apparaat met een hoog zon-tot-waterstof efficiëntie kan worden bereikt met een puur Si gebaseerde halfgeleider elektrode.

# Acknowledgements

The completion of this thesis would have never been possible without the contribution of many people. Here, I would like to take this opportunity to express my gratitude to those who have helped me during my PhD period at TU Delft.

First and foremost, I would like to thank my promotor and supervisor, Wilson, who has given me the opportunity to join the team. It's an honor to be the first member of the group you personally hired. Thanks for introducing me this exciting photoelectrochemistry field and guiding me to be a better scientist and a better person. Most of all, thanks for your constant support, and for always placing your trust and confidence in me. I hope you enjoyed working with me as much as I did. I would also like to thank Bernard who has shown me the real meaning of being a scientist. Thanks for being critical on my works, questioning my scientific ideas and for always challenging me to do meaningful science. All my experiments would have never been possible without the help of Herman and Joost. Thanks for always providing technical support and for always being patience with my constant annoyance. To Heleen, thanks for your great help with the administration affairs. I would also like to thank Wil for the administration assistance in case of emergency. I am grateful to be surrounded with inspiring scientists: Hans, Wim, Andreas, Fokko, George. Thanks for all the discussions we had during the meetings, coffee breaks, group dinners and for making a comfortable atmosphere in the group. I would also like to thank the rest of technical support staff at ChemE: Ruben, Ben, Bart, Marcel, Edwin, Jon and Nayyar.

A big and heartfelt thank goes to the luò tuo team: Bartek, Moreno and Ma Ming. Words will never be enough to describe how grateful I am to have all of you in the group. I enjoyed every single moment we shared together, all the silly jokes and laughters, as well as our deep conversation after office hours. I owe my sincere thanks to the smartest yet the most humble person I've ever met; Fatwa. You are my source of personal and professional inspiration. Thank you for everything you've done to help me. The most awesomest neighbor during my first 8 months and my last 4 months at MECS, Divya, it's been a great time to have you in the group (again)! Thanks for being awesome! I would like to thank all the former and the current members of the MECS group: Petra, Peter, Ruud, Lennard, Arjen, Kohta, Diana, Christian, Sarmila, David, Marco, Nienke, Fahimeh, Steffen, Kai, Nathan, Anirudh, Recep, Tobias, Jicheng, Kostis, Aaike, Bernhard, Yaolin, Yingying, Jenny, Isaac, Mercedes and everyone whom I can't seem to recall. And of course I would like to acknowledge all the students I have worked with: Kelbij, Ellis, Vivian, Jessica, Lucas, Machiel, Winok. Thanks for all your contributions either directly or indirectly in some of the work in this thesis. It was great working with you!

I would like to thank my collaborators at the PVMD group: Lihao, Paula, Tom, Andrea, Arno and Miro and some other people who have indirectly contributed to my research: Stefaan, Martijn and Rudi. A special recognition goes to my former supervisors, René and Dong who have shown me the joy of research. The insights and guidance that you gave have taught me to be a responsible scientist and motivated me to pursue a PhD. I would like to acknowledge several people at AMOLF who have helped with my experiments: Laihung and Jenny. I would also like to thank Erik at AMOLF. Thanks for the great collaboration and fruitful discussion. Especially to my friend, Gede, I can't thank you enough for the assistance that you provided along the way. Most of my experiments, and therefore the

completion of this thesis, would have never been possible without your help. I'm truly grateful to you.

I am very fortunate to meet the Popta family: Durgesh and Joan. You have been a big part of my life in the Netherlands, and I am glad to have both of you in our Popta house. I hope our friendship lasts a lifetime. I am happy to come across my Indonesian friends in the Netherlands: Pram, Azzam, Ficky, Ryvo, Yuwardi, Cordova, Rihan, Yusuf, Pak Eddi. I will always remember the moments we shared together. Thanks to Azzam who helped me with the Dutch translation in this thesis.

My warmest thanks goes to my parents. Dear Mom and Dad, without your never-ending prayers and constant support, I might never be the person I am today. Thank you for being supportive to whatever I choose to do in life.

I dedicated this thesis to my little Family, Namira and Zachary. My dear Namira, thank you for all your support and encouragement, for your faith and your confidence, and for your never-ending supply of love and affection. You are my lifeline, my happiness and my source of strength. My dear Zach, you are the best gift destiny has given to me. Thanks for coming into my life. Most of all to both of you, thank you for loving me the way that you do!

# Curriculum Vitæ

## Ibadillah Ardhi DIGDAYA



Ibadillah Ardhi Digdaya was born on December 29, 1986 in Medan, Indonesia. In 2009 he graduated from Bandung Institute of Technology (ITB), Indonesia, with a degree of Bachelor of Engineering in Engineering Physics. In September 2010, he continued his study in sustainable energy technology master program at Delft University of Technology (TU Delft) in the Netherlands. During his master project, he was supervised by Dr. René van Swaaij at the Photovoltaic Materials and Devices (PVMD) group with a research focus in optical improvement for heterojunction silicon solar cells. In February 2013, he joined Dr. Wilson Smith's research group as a PhD student at the Materials for Energy Conversion and Storage (MECS) section at the Department of Chemical Engineering of TU Delft. His research interests include device fabrication, design optimization and chemical stabilization of technologically important, industrially well-developed, highly efficient yet chemically unstable semiconductors for solar fuel production.

# List of Publications

1. **I. A. Digdaya**, B. J. Trześniewski, G. W. P. Adhyaksa, E. C. Garnett, and W. A. Smith, *General Considerations for improving photovoltage of metal-insulator-semiconductor photoanodes.* The Journal of Physical Chemistry C., **122**, 5462 (2018).

2. **I. A. Digdaya**, G. W. P. Adhyaksa, B. J. Trzesniewski, E. C. Garnett, and W. A. Smith, *Interfacial engineering of metal-insulator-semiconductor junctions for efficient and stable photoelectrochemical water oxidation*, Nature Communications, **8**, 15968 (2017).

3. **I. A. Digdaya**, P. Perez-Rodriguez, M. Ma, G. W. P. Adhyaksa, E. C. Garnett, A. H. M. Smets and W. A. Smith, *Engineering the kinetics and interfacial energetics of Ni/Ni–Mo catalyzed amorphous silicon carbide photocathodes in alkaline media.* Journal of Materials Chemistry A, **4**, 6842 (2016).

4. **I. A. Digdaya**, L. Han, T. W. F. Buijs, M. Zeman, B. Dam, A. H. M. Smets and W. A. Smith, *Extracting large photovoltages from a-SiC photocathodes with an amorphous $TiO_2$ front surface field layer for solar hydrogen evolution.* Energy & Environmental Science, **8**, 1585 (2015).

5. B. J. Trześniewski, **I. A. Digdaya**, T. Nagaki, S. Ravishankar, I. Herraiz-Cardona, D. A. Vermaas, A. longo, S. Gimenez and W. A. Smith, *Near-complete suppression of surface losses and total internal quantum efficiency in $BiVO_4$ photoanodes.* Energy & Environmental Science, **10**, 1517 (2017).

6. P. Perez-Rodriguez, **I. A. Digdaya**, A. M. Raventos, M. Falkenberg, R. Vasudevan, M. Zeman, W. A. Smith and A. H. M. Smets, *Solar Fuel Production by Using PV/PEC Junctions Based on Earth-abundant Materials.* 2016 IEEE 43$^{\text{rd}}$ Photovoltaic Specialists Conference (PVSC), 3620 (2016).

7. L. Han, **I. A. Digdaya**, T. W. F. Buijs, F. F. Abdi, Z. Huang, R. Liu, B. Dam, M. Zeman, W. A. Smith and A. H. M. Smets *Gradient dopant profiling and spectral utilization of monolithic thin-film silicon photoelectrochemical tandem devices for solar water splitting.* Journal of Materials Chemistry A, **3**, 4155 (2015).

8. D. Zhang, **I. A. Digdaya**, R. Santbergen, R. A. C. M. M. van Swaij, P. Bronsveld, M. Zeman, J. A. M. van Roosmalen and A. W. Webber *Design and fabrication of a $SiO_x$/ITO double-layer anti-reflective coating for heterojunction silicon solar cells.* Solar Energy Materials & Solar Cells, **117**, 132 (2013).

9. P. Perez-Rodriguez, D. Cardenas-Morcoso, **I. A. Digdaya**, A. M. Raventos, P. Procel, O. Isabella, S. Gimenez, M. Zeman, W. A. Smith and A. H. M. Smets *Improving the back surface field on an amorphous silicon carbide (a-SiC:H) thin film photocathode for solar water splitting.* ChemSusChem, **11**, 1–9 (2018).

10. M. Valenti, E. Kontoleta **I. A. Digdaya**, T. M. P. Jonsson, G. Biskos, A. Schmidt-Ott, and W. A. Smith, *The Role of Size and Dimerization of Decorating Plasmonic Silver Nanoparticles on the Photoelectrochemical Solar Water Splitting Performance of $BiVO_4$ Photoanodes.* ChemNanoMat, **2**, 739 (2016).

11. R. Vasudevan, Z. Thanawala, L. Han, T. W. F. Buijs, H. Tan, D. Deligiannis, P. Perez-Rodriguez, **I. A. Digdaya**, W. A. Smith, M. Zeman and A. H. M. Smets, *A thin-film silicon/silicon hetero-junction hybrid solar cell for photoelectrochemical water-reduction applications.* Solar Energy Materials & Solar Cells, **150**, 82 (2016).